THE COMPLETE SECOND-ORDER DIFFRACTION AND RADIATION SOLUTIONS FOR A VERTICALLY AXISYMMETRIC BODY

by

Moo-Hyun KIM

B.S.E., Naval Architecture
Seoul National University, 1981

M.S.E., Naval Architecture
Seoul National University, 1983

SUBMITTED TO THE DEPARTMENT OF OCEAN ENGINEERING
IN PARTIAL FULFILLMENT OF THE REQUIREMENTS
FOR THE DEGREE OF

DOCTOR OF PHILOSOPHY

at the
MASSACHUSETTS INSTITUTE OF TECHNOLOGY
October 1988

Signature of Author ______________________
Department of Ocean Engineering
October, 1988

Certified by ______________________
Dick K.P. Yue
Thesis Supervisor

Accepted by ______________________
A. Douglas Carmichael
Chairman, Department Committee

THE COMPLETE SECOND-ORDER DIFFRACTION AND RADIATION SOLUTIONS FOR A VERTICALLY AXISYMMETRIC BODY

by
Moo-Hyun, KIM

Submitted to the Department of Ocean Engineering
in partial fulfillment of the requirements for the degree of
Doctor of Philosophy

ABSTRACT

The second-order sum- and difference-frequency wave excitations and resonant responses of moored vessels and compliant offshore platforms are important design considerations when their natural frequencies are substantially above or below that of significant ocean wave energy. In this thesis, the complete deterministic and stochastic analyses of second-order wave forces on large bodies are presented.

We study in Part One the second-order diffraction and radiation problem for vertical axisymmetric bodies in plane monochromatic and bichromatic waves. The second-order sum- and difference-frequency potentials and local quantities such as pressures and run-up as well as wave excitations and body responses are obtained. A sequence of boundary integral equations involving free-surface ring sources of general order are formulated and solved for each Fourier mode of the second-order potential. The solution is expedited by analytic integration in the entire local-wave-free outer field of a requisite free-surface integral. The method is validated by extensive convergence tests and comparisons to available semi-analytic solutions. The complete wave excitation quadratic transfer functions (QTF) are computed for a number of different geometries and compared to those of various aproximation methods.

In Part Two, the statistical properties of the sum- and difference-frequency wave forces are studied using the complete QTF's and a two-term Volterra series model. In particular, the probability density functions (PDF) and spectra of the second-order excitations in unidirectional Gaussian seas are derived. Comparisons of the present PDF's to those calculated from approximated QTF's reveal that the extreme and rms second-order forces can be severely underestimated by existing approximation methods. Finally, the theory is extended to multidirectional random seas, where it is found that unidirectionality is not necessarily a conservative assumption when second-order wave effects are included.

ACKNOWLEDGEMENTS

I wish to express my sincere gratitude to my advisor, Prof. Dick Yue, for his guidance, advice, and encouragement during my graduate studies. From him, I have learned not only general scientific knowledge but also how to approach the problem and present the result. I also direct my appreciation to Prof. J.N. Newman, P.D. Sclavounos, and C.C. Mei. My research has been immensely influenced by their teaching and research. Special thanks go to other members of my thesis committee, Prof. T.F. Ogilvie and M.S. Triantafyllou.

It was my pleasure to work with other members of Hydro group, especially Dr. Chang-Ho Lee. Their friendship and cooperative attitude made my stay at MIT enjoyable.

This thesis is dedicated to my wife, Mi-Hae, whose endless understanding and support made this work possible. Her sacrifices for me during the past several years leave debts I can only hope to repay. I am very grateful to my parents for their continuous support throughout my education. Through this work, I also want to express my love to my two sons, Sung-Won and Sung-Min.

This research is supported by the National Science Foundation and the office of Naval Research. The numerical computations have been made possible by the National Science Foundation's support of the following supercomputers: Minnesota Supercomputer Institute's CRAY-1 & CRAY-2, and Pittsburgh Supercomputer Center's CRAY X-MP.

CONTENTS

CHAPTER 0. GENERAL INTRODUCTION

> Of making many books there is no end,
> and much study wearies the body.
>
> - OLD TESTAMENT, Ecclesiastes 12:12 -

When nonlinear effects are included in the diffraction or radiation of waves by a body, there are, at second order, interactions at the sums and differences of the component frequencies of the incident waves. Although the magnitudes of these nonlinear effects are in general only second order, they act at frequencies away from that of the ambient wave energy, and may therefore be of primary concern especially when such excitations are near the natural periods of the body motions or where restoring or damping forces are small. Typical examples are the subharmonic resonance of moored vessels or offshore platforms, and the superharmonic resonance of tension-leg platforms. In certain other cases, such as for non-wall-sided geometries (e.g. conical gravity platforms, Jamieson et al, 1985), second-order effects may also be an appreciable part of the total excitation and are therefore important corrections to the linearized results.

Despite its importance, the consistent theoretical developments of the second-order wave body interaction problem have until recently been scant. The principal difficulties are the correct treatment of the second-order free-surface boundary conditions and a proper specification of the radiation condition for the second-order diffracted waves. In a monochromatic incident wave, the second-order pressure and the resulting force consist of mean and second-harmonic components. The mean drift force can be obtained entirely from the first-order potential, hence has been studied extensively (for a review, see Pinkster, 1980). The double-frequency force, however, includes contributions from the second-order potential, the solution of which was considered controversial even for the simplest case of diffraction by a vertical circular cylinder. Issacson (1977) maintained the insolvability of the second-order problem by the usual perturbation procedure, which was later found to be incorrect by Wehausen (1980) and Hunt & Baddour (1981). Most of the published results on this subject (e.g. Chakrabarti, 1978; Hunt & Baddour, 1981; Chen & Hudspeth, 1982; Rahman, 1983; Sabuncu & Goren, 1985; etc.) appear to be inconsistent, and their numerical results differ significantly. Among other shortcomings, a common difficulty is a failure to satisfy either the inhomogeneous free-surface condition or the second-order radiation condition or both.

A seminal work was that of Molin (1979), who by decomposing the second-order diffraction potential into free and forced terms satisfying respectively homogenous and inhomogenous free-surface conditions, obtained consistent radiation conditions for the separate components. These results have also been formally founded and extended to bichromatic waves by Wang (1987) who studied the long-time limit of the initial-value problem. To obtain integrated second-order quantities such as forces, Molin avoided the explicit solution of the double-frequency second-order potential by introducing a fictitious assisting radiation potential at that frequency. Applying Green's identity, an expression for the second-order force can be obtained in terms of the assisting potential and functions of first-order quantities. The method requires the vanishing of a far-field integral -- a weak radiation condition guaranteed by the asymptotic behaviors of the second-order potentials. The same approach was suggested independently by Lighthill (1979), and was in fact used by Faltinsen & Loken (1978) for the two-dimensional problem. Molin's solution has since been extended, for example, by Molin & Marion (1986), who obtained some results for second-order motions; by Loken (1986), who also attempted a solution of the second-order potential; and by Eatock Taylor & Hung (1987), who developed a method for the evaluation of the free-surface integral based on leading asymptotics.

In the presence of bichromatic waves, the second-order forces occur at the sum and difference frequencies, and are often called 'springing' and 'slowly-varying' forces, respectively. The complete solution of these forces for three-dimensional bodies was first attempted by Loken (1986), whose results suffer from a number of numerical difficulties, especially those associated with the poor convergence of the free-surface integral. Subsequently, the free-surface integrals for slowly-varying forces were treated more carefully by Benschop et al (1987) and Hung & Eatock Taylor (1987). In these treatments, however, the convergence with the free-surface truncation radius is still essentially algebraic. Recently, Sclavounos (1988) developed a new approach in infinite water depth based on 'second-order Green functions'. By using the second-order Green function on the body, the difficult free-surface integral is avoided. The

Green function itself, however, is quite complicated and the use of the approach for practical applications has not been attempted yet.

Because of the complexity of the complete solution, numerous approximation methods for slowly-varying drift forces (e.g. Newman, 1974; Pinkster, 1980; Standing & Dacunha, 1982; Marthinsen, 1983) and for springing forces (e.g. De Boom et al, 1983; Herfjord & Nielsen, 1986; Petrauskas & Liu, 1987) have been suggested and widely used in practical applications. Without the complete solutions, however, the superiority of one approximation over another and indeed the validity of a particular method cannot be established.

In Part One, we consider the solutions of the second-order diffraction and radiation problems for monochromatic (Chapter I) and bichromatic (ChapterII) incident waves. A Green's theorem integral equation is obtained for the second-order diffraction potential involving the linear (at sum or difference frequencies) wave-source Green function. This equation is similar to that for the linear problem with the exception of a slowly-converging integral over the entire free surface. An effective and accurate evaluation of this integral is essential to the solution of the problem and a detailed asymptotic method which performs the integration analytically in the entire local-wave-free outer domain is developed. Since the second-order potential is obtained explicitly, the complete second-order local quantities such as pressures, velocities, and surface elevations are readily available in addition to the forces and moments.

For simplicity, we consider bodies which possess vertical axes of symmetry. Expressing the potentials in terms of Fourier series in the circumferential coordinate, we obtain after integration a sequence of one-dimensional integral equations along the generator of the body for each Fourier component with free-surface ring-source kernels of the corresponding order. For linear problems involving axisymmetric bodies, the ring-source distribution method was used by Black (1975), and later by Fenton (1978), Hulme (1983), and Fernandes (1983), who gave particular attention to the treatment of singularities and the convergence of representations of the ring source and its derivatives. Their numerical examples are, however, limited to the first two Fourier modes. For the diffraction problem, we present here an analysis and numerical method for the arbitrary-order ring source potential and its gradient.

The validity and accuracy of the method is demonstrated by extensive results for convergence with respect to body discretizations, number of circumferential modes, and free-surface integral evaluation, as well as by comparisons to semi-analytic solutions for the second-order forces and moments on a vertical cylinder. Detailed results for the linear and second-order mean and double-frequency (or difference- and sum-frequency) forces, moments, pressure distributions and run-up on the bodies are presented and discussed. One of the most interesting results is that there are components of the second-order pressures which decay very slowly with depth. Newman (1988) formally found this algebraic attenuation of the second-order diffraction potential based on the asymptotic analysis which is valid at large depth. For vessels with large draft, the resulting contributions may dominate the first-order components.

Based on the quadratic transfer functions (QTF) computed in Part One, the stochastic properties of the second-order wave excitations and responses in Gaussian random seas are studied in Part Two. For this purpose, the two term Volterra's series (the nonlinear system with memory) is used as a mathematical model. The complete probabilistic distribution of this system was first developed in the communication field by Kac & Siegert (1947) and Bedrosian & Rice (1971), and introduced to ocean engineering applications by Neal (1974). Since then, the approach has received a lot of attention, and has been reexamined and applied to the stochastic analyses of second-order forces and responses (e.g. Vinje, 1983; Naess, 1986; Langley, 1987). Their numerical examples, however, were typically based on idealized QTF's or those of two-dimensional bodies (Faltinsen & Loken, 1978) only, and are therefore of limited practical applications.

In Chapter III, the theory of Bedrosian & Rice (1971) is reviewed, and the complete probabilty density functions of slowly-varying wave excitations on a large draft vertical cylinder are calculated for unidirectional random seas. The results are compared to those based on approximated QTF's. It is found that the probability of extreme forces can be substantially underestimated using the approximations of Newman (1974) and Standing et al (1982).

In Chapter IV, the theory developed in the earlier chapters is applied to the sum-frequency resonant vertical-plane responses of a tension-leg platform (TLP) in unidirectional random seas. Our numerical results reveal that the second-order sum-frequency potential contributes significantly to the total springing excitations due primarily to the deeply penetrating nonlinear potential pressures. It is shown that existing approximations, which exclude the contribution of the second-order potential (e.g. De Boom et al, 1983; Nordgren, 1986; Petrauskas & Liu, 1987), are inadequate for the prediction of springing excitations on a TLP. The resulting tendon-tension load rms obtained by the present complete theory is two to three times larger than that predicted without second-order potential contributions. This fact is also confirmed by large-scale TLP experiments (Petrauskas & Liu, 1987).

Several recent experimental and field reports have pointed to the importance of wave directional spreading on slowly-varying drift forces and motions. In a series of experiments on the tension-leg platform, Teigen (1983) observed considerable reductions of the main direction drift forces in short crested waves. Grancini et al (1984) reported severe dynamic responses in the field when their moored tanker encountered storm and swell seas at the same time from different directions. These reports motivate Chapter V, where the slowly-varying wave drift forces in short crested irregular seas are considered. As a preliminary study for this, we maintain Newman's (1974) frequency domain assumption, but treat the directional spreading exactly. The monochromatic bidirectional quadratic transfer functions are then developed for this purpose. Because the directional spreading is treated exactly, the present method has a wider range of validity for general short-crested seas than existing approximation methods (e.g. Marthinsen, 1983) but does not appreciably increase the computational effort. From our numerical example, a surprising result is found which indicates that the amplitude of the slowly-varying force can be substantially amplified when the wave systems are incident from opposing directions. We conclude that the unidirectionality of the sea is not necessarily a conservative assumption when the second-order effects are concerned (cf. Eatock Taylor et al, 1988).

This thesis is composed of two parts and a total of seven chapters. Part One contains Chapters I and II, and describes the second-order deterministic theory. Part Two contains Chapters III,IV and V, and addresses the second-order stochastic theory. For convenience, equations, tables, and figures in each chapter are numbered independently of other chapters (starting from (1) or (1.1) for section 1 etc.), and are differentiated by chapter number, if necessary. Figures for each chapter are located after the last page of the text of that particular chapter. References and appendices are placed at the end of the entire thesis.

PART ONE

THE SECOND-ORDER DETERMINISTIC THEORY

Singularity is almost invariably a clue.

\- Sir Arthur Conan Doyle -

CHAPTER I

THE COMPLETE SECOND-ORDER DIFFRACTION SOLUTION FOR AN AXISYMMETRIC BODY IN MONOCHROMATIC INCIDENT WAVES.

1. INTRODUCTION

In this chapter, we consider the direct solution of the second-order diffraction problem. A Green's theorem integral equation is obtained for the second-order diffraction potential involving the (double-frequency) wave-source Green function. This equation is similar to that for the linear problem with the exception of a forcing term involving products of first-order potentials which is a slowly-converging integral over the entire free surface. An effective evaluation of this integral is essential to the solution of the problem and a detailed asymptotic method which performs the integration analytically in the entire local-wave-free outer domain is developed. Since the second-order potential is obtained explicitly, complete second-order local quantities such as pressures, velocities and surface elevations are readily available in addition to integrated forces and moments.

For simplicity, we consider bodies which possess vertical axes of symmetry. Expressing the potentials in terms of Fourier series in the circumferential coordinate, we obtain after integration a sequence of one-dimensional integral equations along the generator of the body for each Fourier component with free-surface ring-source kernels of the corresponding order.

To illustrate the present method, we present computational results for a uniform vertical circular cylinder and for a truncated conical body both in finite depth. The validity and accuracy of the method is demonstrated by extensive results for convergence with respect to body discretizations, number of circumferential modes, and free-surface integral evaluation, as well as comparisons to semi-analytic solutions for the second-order forces and moments for the vertical cylinder derived in Appendix B. Detailed results for the linear and second-order mean and double-frequency forces, moments, pressure distributions and run-up on the bodies are presented and discussed in §4. Important features of second-order diffraction effects are summarized in §5.

We study in this chapter the diffraction by a single monochromatic wave. The solution of sum- and difference-frequency second-order diffraction in the presence of bichromatic incident waves as well as the radiation problem are considered in Chapter II. Many of the techniques developed here can be extended to general three-dimensional bodies (see Chapter VI).

2. FORMULATION OF THE SECOND-ORDER PROBLEM

2.1 The boundary-value problem

We consider the linear and second-order diffraction of a plane monochromatic incident wave, frequency ω, linear amplitude A, by a fixed three-dimensional body in constant water depth, h. Cartesian coordinates with the x-y plane in the quiescent free surface and z positive upward are chosen. Assuming potential flow and weakly nonlinear waves, we express the total velocity potential Φ as a perturbation series in the wave-slope parameter, $\epsilon \equiv kA \ll 1$:

$$\Phi = \epsilon\, \Phi^{(1)} + \epsilon^2\, \Phi^{(2)} + \cdots, \tag{2.1}$$

where k is the incident wavenumber given by the dispersion relationship $\omega^2 = gk \tanh(kh)$, g being the gravitational acceleration. For monochromatic incident waves, we separate the time dependencies explicitly and write

$$\Phi^{(1)}(x,y,z,t) = \mathrm{Re}\,\{\phi^{(1)}(x,y,z)\; e^{-i\omega t}\},$$

$$\Phi^{(2)}(x,y,z,t) = \mathrm{Re}\,\{\phi^{(2)}(x,y,z)\; e^{-i2\omega t}\} + \bar{\Phi}^{(2)}(x,y,z). \tag{2.2}$$

Note that the contribution of the steady part of the second-order potential in (2.2) to the pressure (hence forces) or free-surface elevation is at most $O(\epsilon^3)$. At each order, the boundary-value problem is linear and we decompose ϕ into incident(ϕ_I) and diffracted (ϕ_D) potentials: $\phi^{(i)} = \phi_I{}^{(i)} + \phi_D{}^{(i)}$, i=1,2. The incident potentials are given from Stokes' waves:

$$\phi_I^{(1)} = \frac{-igA}{\omega}\,\frac{\cosh k(z+h)}{\cosh kh}\, e^{ikx}, \tag{2.3a}$$

$$\phi_I^{(2)} = \frac{-3i\omega A^2}{8}\,\frac{\cosh 2k(z+h)}{\sinh^4 kh}\, e^{i2kx}, \tag{2.3b}$$

for a wave incident from $x\sim-\infty$. The boundary-value problems governing the first- and second-order diffraction potentials are respectively:

$$\nabla^2\phi_D^{(1)} = 0, \qquad \text{in the fluid } (z<0); \tag{2.4a}$$

$$(-\omega^2 + g\,\partial/\partial z)\,\phi_D^{(1)} = 0, \qquad \text{on } z=0\ (S_F); \tag{2.4b}$$

$$\partial\phi_D^{(1)}/\partial z = 0, \qquad \text{on } z=-h; \tag{2.4c}$$

$$\partial\phi_D^{(1)}/\partial n = -\,\partial\phi_I^{(1)}/\partial n, \qquad \text{on the body } (S_B); \tag{2.4d}$$

$$\lim_{k\rho\to\infty} \sqrt{\rho}\,(\partial/\partial\rho - ik)\,\phi_D^{(1)} = 0, \qquad k\rho\gg1\ (S_\infty); \tag{2.4e}$$

and

$$\nabla^2\phi_D^{(2)} = 0, \qquad \text{in the fluid } (z<0); \tag{2.5a}$$

$$(-4\omega^2+ g\,\partial/\partial z)\,\phi_D^{(2)} = q, \qquad \text{on } z=0\ (S_F); \tag{2.5b}$$

$$\partial\phi_D^{(2)}/\partial z = 0, \qquad \text{on } z=-h; \tag{2.5c}$$

$$\partial\phi_D^{(2)}/\partial n = -\,\partial\phi_I^{(2)}/\partial n, \qquad \text{on the body } (S_B); \tag{2.5d}$$

plus a suitable radiation condition at infinity. In the above $\rho\equiv(x^2+y^2)^{1/2}$ is the radial distance from the origin, and $\partial/\partial n$ the normal derivative into the body. The first-order problem (2.4) is classical, and a variety of numerical methods are now available (e.g., Mei, 1978).

The second-order problem is complicated by the inhomogeneous forcing term in the free-surface boundary condition (2.5b), which is given in terms of quadratic products of the first-order potential:

$$q = \left[-\frac{i\omega}{2g} \phi^{(1)} \left(-\omega^2 \frac{\partial \phi^{(1)}}{\partial z} + g \frac{\partial^2 \phi^{(1)}}{\partial z^2} \right) + i\omega (\nabla \phi^{(1)})^2 \right]_{z=0} - q_{II}, \tag{2.6}$$

where the contribution from quadratic products of the incident potential $\phi_I^{(1)}$ itself, q_{II}, is subtracted out due to the free-surface condition satisfied by (2.3b). The specific radiation condition for $\phi_D^{(2)}$ depends on the far-field behavior of q. In general, if the free-surface forcing is absolutely integrable, the validity of a Sommerfeld-like radiation condition (2.4e) follows directly from Cauchy-Poisson theory (Stoker, 1957). In the present case, q contains quadratic products of $\phi_D^{(1)}$ itself (q_{DD}), as well as products of $\phi_D^{(1)}$ and a non-diminishing $\phi_I^{(1)}$ (q_{ID}), and a more careful asymptotic analysis is necessary. From (2.4e), q_{DD} decays as $O(1/\rho)$ for $\rho \gg 1$, while the far-field asymptotic of q_{ID} is

$$q_{ID} \sim \rho^{-1/2} e^{ik\rho(1+\cos\theta)} + O(\rho^{-3/2}), \qquad \rho \gg 1. \tag{2.7}$$

Following Molin (1979), we decompose $\phi_D^{(2)}$ into a homogeneous (free waves), ϕ_H, and a particular (locked waves) solution, ϕ_P, which satisfy respectively the homogeneous and inhomogeneous free-surface conditions (2.5b), and jointly the inhomogeneous body boundary condition (2.5d). The boundary-value problem for ϕ_H is similar to (2.4) and its far-field behavior is given by:

$$\phi_H \sim \rho^{-1/2} e^{ik_2\rho} + O(\rho^{-3/2}), \qquad \rho \gg 1, \tag{2.8}$$

where k_2 is the double-frequency wavenumber satisfying $4\omega^2 = k_2 g \tanh(k_2 h)$. From (2.7), ϕ_P has the asymptotic form

$$\phi_P \sim \rho^{-1/2} P(\theta, z)\, e^{ik\rho(1+\cos\theta)} + O(1/\rho), \qquad \rho \gg 1, \tag{2.9}$$

where satisfying the bottom condition, and the field equation to leading order, $P(\theta,z)$ is given by

$$P(\theta,z) = p(\theta)\cosh\left[k\sqrt{2(1+\cos\theta)}\,(z+h)\right] + O(\rho^{-1/2}). \tag{2.10}$$

Note that this "forced" second-order potential does not attenuate with depth on the weather-side ray, $\theta=\pi$, far away from the body. The asymptotic forms (2.8,9) for the free and locked wave potentials were first obtained by Molin (1979) and subsequently confirmed by the analysis of Wang (1987) who considered the long-time limit of the initial-value problem.

2.2 The boundary-integral equation for the second-order potential

We introduce the linear wave-source Green function at double-frequency (2ω), $G^+(x,x')$, where x, x' represent respectively the field and source points. Applying Green's second identity to $\phi_D^{(2)}$ and G^+, and using (2.5) and the boundary conditions satisfied by G^+, we obtain for $x'\epsilon S_B$ a second kind Fredholm integral equation for $\phi_D^{(2)}$:

$$2\pi\,\phi_D^{(2)}(x') + \iint_{S_B} \phi_D^{(2)}\frac{\partial G^+}{\partial n}\,dx = -\iint_{S_B} G^+\frac{\partial\phi_I^{(2)}}{\partial n}\,dx + \frac{1}{g}\iint_{S_F} q\,G^+\,dx, \tag{2.11}$$

where the integral over the far-field vanishes as $\rho\to\infty$:

$$\iint_{S_\infty}\left(\frac{\partial\phi_D^{(2)}}{\partial n}G^+ - \phi_D^{(2)}\frac{\partial G^+}{\partial n}\right)dx = 0, \tag{2.12}$$

upon using the method of stationary phase in conjunction with the asymptotic results (2.8,9). From the point of view of the integral equation (2.11) (not considering irregular frequencies associated with

S_B), the "weak" radiation condition (2.12) is sufficient for the uniqueness of the diffraction problem (Finkelstein, 1957; Peters & Stokers, 1957). Interestingly, it can be shown that (2.12) holds for the diffraction potentials at all orders.

The integral equation (2.11) is identical in form to that for a linear diffraction problem with the exception of the free-surface integral which extends to infinity. From the far-field behaviors of q and G^+, the integrand diminishes only as ρ^{-1} for $\rho \gg 1$, and is highly oscillatory, being the product of three wave-like functions. An accurate and efficient evaluation of this slowly converging forcing term is essential to the solution of (2.11) and a procedure involving analytic integrations in the local-wave-free domain is developed in §2.3.

For bodies which are vertically axisymmetric about ρ=0, the integral equation (2.11) over a surface can be reduced to a sequence of boundary-integral problems over a line in the ρ-z plane. To accomplish this, we expand $\phi_I^{(2)}$, $\phi_D^{(2)}$, q and G^+ into Fourier-cosine series in the circumferential coordinate θ:

$$\left\{ \begin{array}{c} \phi_{I,D}^{(2)}(\rho,\theta,z) \\ q\ (\rho,\theta) \end{array} \right\} = \sum_{n=0}^{\infty} \left\{ \begin{array}{c} \phi_{I,Dn}^{(2)}(\rho,z) \\ q_n(\rho) \end{array} \right\} \cos n\theta,$$

$$G^+(\rho,\theta,z;\rho',\theta',z') = \sum_{n=0}^{\infty} \frac{\epsilon_n}{2\pi} G_n^+(\rho,z;\rho',z') \cos n(\theta-\theta'), \tag{2.13}$$

where ϵ_0=1, ϵ_n=2 for n≥1. Substituting (2.13) into (2.11), performing the integration in θ and equating Fourier coefficients in θ', we obtain a one-dimensional integral equations for each Fourier mode, $\phi_{Dn}^{(2)}$:

$$2\pi\, \phi_{Dn}^{(2)} + \int_{\partial B} dl\; \rho\, \phi_{Dn}^{(2)} \frac{\partial G_n^+}{\partial n} = - \int_{\partial B} dl\; \rho \frac{\partial \phi_{In}^{(2)}}{\partial n} G_n^+ + \frac{1}{g} \int_{\partial F} d\rho\; \rho\, q_n G_n^+ , \qquad (2.14)$$

where the line integrals are along the traces ∂B, ∂F of S_B and S_F respectively on (ρ,z). In the above, the n-th mode of the inhomogeneous free-surface forcing term, q_n, can be obtained from (2.6):

$$q_0 = \frac{i\omega}{2} \sum_{m=0}^{\infty} \frac{1}{\epsilon_m} \{ (\nu \frac{\partial \phi_m^{(1)}}{\partial z} - \frac{\partial^2 \phi_m^{(1)}}{\partial z^2}) \phi_m^{(1)} + 2[(\frac{\partial \phi_m^{(1)}}{\partial \rho})^2 + (\frac{\partial \phi_m^{(1)}}{\partial z})^2] + \frac{m^2 \epsilon_m}{\rho^2} \phi_m^{(1)2} \} - q_{II0}$$

$$\begin{aligned} q_n = \frac{i\omega}{2} \sum_{m=0}^{n} \{ & \frac{1}{2} (\nu \frac{\partial \phi_{n-m}^{(1)}}{\partial z} - \frac{\partial^2 \phi_{n-m}^{(1)}}{\partial z^2}) \phi_m^{(1)} + \frac{\partial \phi_{n-m}^{(1)}}{\partial \rho} \frac{\partial \phi_m^{(1)}}{\partial \rho} + \frac{\partial \phi_{n-m}^{(1)}}{\partial z} \frac{\partial \phi_m^{(1)}}{\partial z} - \\ & - \frac{(n-m)m}{\rho^2} \phi_{n-m}^{(1)} \phi_m^{(1)} \} \\ + \frac{i\omega}{2} \sum_{m=0}^{\infty} \{ & \frac{1}{2} (\nu \frac{\partial \phi_m^{(1)}}{\partial z} - \frac{\partial^2 \phi_m^{(1)}}{\partial z^2}) \phi_{n+m}^{(1)} + \frac{1}{2} (\nu \frac{\partial \phi_{n+m}^{(1)}}{\partial z} - \frac{\partial^2 \phi_{n+m}^{(1)}}{\partial z^2}) \phi_m^{(1)} \\ & + 2 (\frac{\partial \phi_m^{(1)}}{\partial \rho} \frac{\partial \phi_{n+m}^{(1)}}{\partial \rho} + \frac{\partial \phi_m^{(1)}}{\partial z} \frac{\partial \phi_{n+m}^{(1)}}{\partial z}) + \frac{2m(n+m)}{\rho^2} \phi_m^{(1)} \phi_{n+m}^{(1)} \} - q_{IIn} , \end{aligned}$$

$$n = 1, 2, \ldots, \qquad (2.15)$$

where $\nu \equiv \omega^2/g$, $\phi_m{}^{(1)}$ is the m-th Fourier coefficient of $\phi^{(1)}$, and all quantities are evaluated on z=0. Noting that $G^+(\rho,\theta,z;\rho',\theta',z') = G^+(\rho,z;\rho',z';\cos(\theta-\theta'))$, the n-th mode ring-source defined in (2.13) can also be expressed as

$$G_n^+(\rho,z;\rho',z') = \int_0^{2\pi} G^+(\rho,z;\rho' z';\cos(\theta-\theta'))\, \cos n(\theta-\theta')\; d(\theta-\theta'). \qquad (2.16)$$

2.3 Evaluation of the general-order ring-source potential and its derivatives

The ring-source potential and its normal derivative in (2.14) have been analysed by a number of investigators (Fenton, 1978; Hulme, 1983; Fernandes, 1983) although numerical results have usually been restricted to the zeroth and first mode only. In order to solve for the diffraction potential itself, we develop here a computational algorithm for the general-order problem.

The wave-source Green function $G(x;x')$ can be expressed as a sum of its Rankine source and image, and a regular part:

$$G = 1/r + 1/r' + W, \tag{2.17}$$

where $r^2 \equiv R^2+(z-z')^2$, $r'^2 \equiv R^2+(z+z')^2$, and $R^2 \equiv \rho^2+\rho'^2-2\rho\rho'\cos(\theta-\theta')$.

For the $1/r$ Rankine part of (2.17) (the analysis for $1/r'$ is analogous), the circumferential integration (2.16) can be obtained analytically for any n in terms of second-kind Legendre functions of integral-minus-half order (Abramowitz & Stegun, 1964):

$$R_n \equiv \int_0^{2\pi} \frac{\cos n(\theta-\theta')}{r}\, d(\theta-\theta') = \frac{2}{\sqrt{\rho\rho'}}\, Q_{n-1/2}(a_o/b_o), \qquad n=0,1,2,\ldots \tag{2.18}$$

where $a_0 \equiv \rho^2+\rho'^2+(z-z')^2$ and $b_0 \equiv 2\rho\rho'$. For the first two modes, $n=0,1$, (2.18) can be evaluated directly in terms of complete elliptic integrals of the first and second kind (K and E respectively):

$$R_0 = 2\,(X/\rho\rho')^{1/2}\,K(X),$$

$$R_1 = 2\,(\rho\rho')^{-1/2}\,[ZX^{1/2}K(X) - 2X^{-1/2}E(X)], \tag{2.19}$$

where $X \equiv 2b_0/(a_0+b_0)$ and $Z \equiv a_0/b_0$.

For the higher modes, evaluations using the forward recurrence relationship for $Q_{n-1/2}$ starting from (2.19) are unstable. Thus for $n\geq 2$, we utilize instead the hypergeometric function representation of Q:

$$Q_{n-1/2}(Z) = \frac{\sqrt{\pi}}{(2Z)^{n+1/2}} \frac{\Gamma(n+1/2)}{\Gamma(n+1)} F(\tfrac{n}{2}+\tfrac{3}{4},\tfrac{n}{2}+\tfrac{1}{4},n+1,\tfrac{1}{Z^2}), \tag{2.20}$$

where Γ and F are respectively gamma and hypergeometric functions, and $Z>1$ in (2.20). If the field point is not close to the ring source, the hypergeometric series representation:

$$F = \frac{\Gamma(n+1)}{\Gamma(\frac{n}{2}+\frac{3}{4})\Gamma(\frac{n}{2}+\frac{1}{4})} \sum_{m=0}^{\infty} \frac{\Gamma(m+\frac{n}{2}+\frac{3}{4})\Gamma(m+\frac{n}{2}+\frac{1}{4})}{\Gamma(m+n+1)\Gamma(m+1)} \frac{1}{Z^{2m}} \tag{2.21}$$

converges rapidly, and (2.20) can be evaluated accordingly. As the field point approaches the ring source, i.e. as $Z\to 1+$, the logarithmic singularity can be excluded explicitly:

$$F = \frac{\Gamma(n+1)}{\Gamma(n/2+3/4)\Gamma(n/2+1/4)} \sum_{m=0}^{\infty} \frac{(n/2+3/4)_m(n/2+1/4)_m}{\Gamma(m+1)^2} \cdot$$

$$[2\Psi(m+1)-\Psi(n/2+3/4+m)-\Psi(n/2+1/4+m)-\ln(1-1/Z^2)]\;(1-1/Z^2)^m, \tag{2.22}$$

where Ψ is Euler's psi function and $(x)_m\equiv\Gamma(x+m)/\Gamma(x)$; and (2.22) is useful for $Z-1\ll 1$.

The singularity of the n-mode ring source near the source ring is given by the asymptotic behavior of $Q_{n-1/2}$ as $Z\to 1$, which can be inferred from (2.22) for m=0:

$$Q_{n-1/2}(Z) \sim -\frac{1}{2}\ln(1-\frac{1}{Z^2}) + \Psi(1) - \Psi(n+1/2) + \ln 2\,, \qquad Z\to 1. \tag{2.23}$$

The corresponding behavior for R_n is

$$R_n \sim \frac{2}{\rho'} \{-\frac{1}{2} \ln[(\rho-\rho')^2+(z-z')^2] + \ln \rho + 3 \ln 2 - c_n\}, \qquad (2.24)$$

where c_n are constants given by $c_0=0$, and

$$c_n = 2\,[1 + 1/3 + 1/5 + \ldots + 1/(2n-1)], \qquad \text{for } n\geq 1.$$

It is of interest to note that the logarithmic singularity of R_n is the same for all n. For computations, the two complementary expressions (2.21,22) for the hypergeometric functions are first converted to economized Chebyshev polynomials for a specified equal-ripple error in the whole domain $Z>1$ (Luke, 1975).

The n-th mode Rankine kernel of the integral equation (2.14) can be obtained in a similar manner:

$$\begin{aligned}\frac{\partial}{\partial n} R_n &= (n_\rho \frac{\partial}{\partial \rho} + n_z \frac{\partial}{\partial z})\, R_n \\ &= -\frac{n_\rho}{\rho\sqrt{\rho\rho'}} \{\, Q_{n-1/2}(Z) + \frac{2n-1}{a_o+b_o} [a_o Q_{n-1/2}(Z) - b_o Q_{n-3/2}(Z)] \,\} \\ &\quad + \frac{2}{\sqrt{\rho\rho'}} \frac{2n-1}{a_o^2-b_o^2} [(\rho-\rho')n_\rho+(z-z')n_z]\, [a_o Q_{n-1/2}(Z)-b_o Q_{n-3/2}(Z)],\end{aligned} \qquad (2.25)$$

where n_ρ and n_z are respectively the components of the unit normal vector **n** in the ρ and z directions. The apparent Cauchy singularity in the last term of (2.25) vanishes identically when the source point approaches the interior of piece-wise linear segments approximating the body boundary ∂B, and is otherwise finite for a body contour with continuous slope.

The behavior of (2.25) as the field point approaches the source ring is given by

$$\frac{\partial R_n}{\partial n} \sim \frac{-n_\rho}{\rho\rho'} \{- \frac{1}{2} \ln[(\rho-\rho')^2+(z-z')^2] + \ln\rho + 3\ln 2 - d_n\}, \tag{2.26}$$

where d_n are constants given in terms of c_n: $d_0=1$, and

$$d_n = (n+1/2)c_n - (n-1/2)c_{n-1} , \qquad n\geq 1. \tag{2.27}$$

As before, the logarithmic singularity is identical for all n.

For the nonsingular part of the Green function (2.17), the n-th mode ring source, W_n, is simply the Fourier-series coefficient of W:

$$W_n(\rho,z;\rho',z') = \int_0^{2\pi} W(\rho,z;\rho',z';\cos(\theta-\theta')) \cos n(\theta-\theta') \, d(\theta-\theta'), \quad n\geq 0. \tag{2.28}$$

Since W is periodic in $(\theta-\theta')$, the convergence of W_n with n is a function only of the smoothness of W. For computations, we truncate the number of modes at n=N, and the W_n's are given by discrete inverse Fourier transform:

$$W_n = \frac{4\pi}{\epsilon_n \epsilon_n' N} \sum_{m=0}^{N} \frac{1}{\epsilon_m'} \cos\,(nm\pi/N)\; W(\cos(m\pi/N)) \;, \quad n=0,1,\ldots,N, \tag{2.28}$$

where $\epsilon_n'\equiv 2$ for n=0,N, and $\epsilon_n'\equiv 1$ for n=1,2,...,N-1. Thus, only N+1 evaluations of the Green function W are required to evaluate the N+1 modes of the regular ring source W_n, and the error is measured by the last term W_N. In practice, the convergence of W_n with n may be slower than that of the potentials so that more evaluations, say $N_W>N$, are used for the W_n, n=0,1,...,N. Efficient algorithms for the evaluation of W are now available (e.g., Newman, 1985a) and are not detailed here.

We now turn to the far-field behavior of the general-order ring source. For R/h>>1, a useful expression for G is (John, 1950)

$$G = 2\pi i C_0 \cosh k(z+h) \cosh k(z'+h)\, H_0(kR)$$

$$+ 4 \sum_{m=1}^{\infty} C_m \cos \kappa_m(z+h) \cos \kappa_m(z'+h)\, K_0(\kappa_m R), \tag{2.29}$$

where H_0, K_0 are the zeroth-order first kind Hankel function and second kind modified Bessel function,

$$C_0 = (\nu^2-k^2)/(k^2h-\nu^2h+\nu)\ , \qquad C_m = (\kappa_m^2+\nu^2)/(\kappa_m^2h+\nu^2h-\nu), \tag{2.30}$$

and κ_m, m=1,2,..., are the real roots of the equation

$$\omega^2 = -\kappa_m g \tan \kappa_m h, \qquad (m-\tfrac{1}{2})\pi \leq \kappa_m h \leq m\pi. \tag{2.31}$$

For finite depth, the second term in (2.29) are local (evanescent) modes which decays exponentially with radial distance, $\kappa_m R$, and the far-field asymptotic of G is given by the first term which represents outgoing waves:

$$G = 2\pi i C_0 \cosh k(z+h) \cosh k(z'+h)\, H_0(kR) + O(e^{-\kappa_1 R}). \tag{2.32}$$

The far-field asymptotic of the ring sources, upon using the addition theorem, is

$$G_n = -4\pi^2 i C_0 \cosh k(z+h) \cosh k(z'+h)\, J_n(k\rho')\, H_n(k\rho) + O(e^{-\kappa_1 R}). \tag{2.33}$$

We remark that as depth increases, the rate of exponential decay of the local modes decreases according to (2.31), and is only algebraic ($\sim R^{-2}$) for infinitely deep water (Newman, 1967):

$$G = 2\pi i\nu\, e^{\nu(z+z')} H_0(\nu R) + O(R^{-2}). \tag{2.34}$$

2.4 Evaluation of the free-surface integral in (2.14)

The most difficult and computationally expensive aspect of the solution of the integral equations (2.14) is the efficient and accurate evaluation of the free-surface integrals:

$$I_n(\rho',z') \equiv \frac{1}{g} \int_a^\infty d\rho\, \rho\, q_n(\rho)\, G_n^+(\rho,0,;\rho',z'), \tag{2.35}$$

where a is the radius of the waterplane. The forcing terms, q_n, are given in (2.15) in terms of first-order potentials, which may in turn be obtained through an integral equation of the form (2.14) (minus the free-surface integral). We use instead a source-distribution representation for the first-order potential:

$$\phi_{Dn}^{(1)}(x) = \int_{\partial B} dl'\, \rho' \sigma_n(x') G_n(x;x'), \tag{2.36}$$

where the ring-source strengths, σ_n, satisfy the second-kind Fredholm integral equation:

$$2\pi\sigma_n(x) + \int_{\partial B} dl'\, \rho' \sigma_n(x')\, \partial G_n/\partial n = -\, \partial\phi_{In}^{(1)}(x)/\partial n, \qquad n=0,1,\ldots \tag{2.37}$$

Eq.(2.36) is preferred over a mixed-distribution in evaluating (2.15) since it reduces by one the order of derivatives of the Green function required. Eq.(2.37) is solved numerically following a standard procedure of discretizing ∂B into linear segments, assuming a constant source strength over each panel, and selecting collocation points at the mid-points of the segments. The details are omitted. The derivatives of the potential in (2.15) are evaluated by successive differentiation of (2.36).

The free-surface integral, (2.35), is evaluated over two intervals, (a,b) and (b,∞), where the radius b is chosen so that the latter interval is evanescent wave free:

$$I_n = \frac{1}{g}\left[\int_a^b d\rho\ \rho q_n G_n^+ + \int_b^\infty d\rho\ \rho \hat{q}_n \hat{G}_n^+ + \int_b^\infty d\rho\ \rho(q_n G_n^+ - \hat{q}_n \hat{G}_n^+)\right] \tag{2.38}$$

In the above, (^) represents terms which contain contributions from propagating waves only. In our computations, the near-field integral in (2.38) over the finite interval (a,b) is computed by numerical quadrature (Romberg integration) with controlled tolerance. The last integral is made negligibly small by a suitable choice of the partition radius b according to (2.32).

We evaluate the second integral, which is over an infinite domain, analytically. The integrand consists of products of three propagating waves and has a decay rate of $\rho^{-1/2}$ for $\rho \gg 1$. The local-wave-free first-order potential is given by

$$\hat{\phi}_{Dn}^{(1)} = -4\pi^2 i C_o \cosh k(z+h)\ H_n(k\rho) \int_{\partial B} dl'\rho'\sigma_n(x')J_n(k\rho')\cosh k(z'+h), \tag{2.39}$$

where the integral over ∂B is simply the n-th mode Kochin function which we denote as L_n. Substituting (2.39) into (2.15), we obtain

$$\hat{q}_o = \frac{-ik^2g^2A^2\cosh^2 kh}{2\omega} \sum_{m=0}^{\infty} \frac{2}{\epsilon_m}\left[\left(\frac{3}{2}\tanh^2 kh - \frac{1}{2} + \frac{\epsilon_m m^2}{2(k\rho)^2}\right)S_{m,m}(k\rho) + T_{m,m}(k\rho)\right],$$

$$\hat{q}_n = \frac{-ik^2g^2A^2\cosh^2 kh}{2\omega} \left\{ \sum_{m=0}^{n} \left[\left(\frac{3}{2}\tanh^2 kh - \frac{1}{2} - \frac{(n-m)m}{(k\rho)^2}\right)S_{n-m,m}(k\rho) + T_{n-m,m}(k\rho)\right]\right.$$

$$\left. + 2\sum_{m=0}^{\infty} \left[\left(\frac{3}{2}\tanh^2 kh - \frac{1}{2} + \frac{(n+m)m}{(k\rho)^2}\right)S_{n+m,m}(k\rho) + T_{n+m,m}(k\rho)\right] \right\},$$

$$n=1,2,\ldots,$$

where,

$$S_{m,n}(k\rho) \equiv \alpha_m\alpha_n H_m(k\rho)H_n(k\rho)+\beta_m\alpha_n J_m(k\rho)H_n(k\rho)+\alpha_m\beta_n H_m(k\rho)J_n(k\rho),$$

$$T_{m,n}(k\rho) \equiv \alpha_m\alpha_n H_m'(k\rho)H_n'(k\rho)+ \beta_m\alpha_n J_m'(k\rho)H_n'(k\rho)+\alpha_m\beta_n H_m'(k\rho)J_n'(k\rho), \tag{2.40}$$

and primes denote derivatives with respect to argument. The coefficients α_n, β_n, are given by $\alpha_n \equiv -4\pi^2 i C_0 L_n$, and $\beta_n \equiv \epsilon_n i^n/\cosh(kh)$. Using (2.33) for $\hat{G}_n$, we obtain an expression for the local-wave-free integrand, $\rho\hat{q}_n\hat{G}_n$, of the free-surface integral consisting of triple products of Bessel and Hankel functions multiplied by powers of $k\rho$. The final outer-field integral can be expressed in terms of definite integrals of the forms:

$$I^s_{lmn}(kb) = \int_{kb}^{\infty} (k\rho)^s\, H_l(k\rho) \begin{bmatrix} H_m^*(k\rho) \\ H_m(k\rho) \end{bmatrix} H_n(k_2\rho)\, d(k\rho), \qquad s=0,\pm 1;\ l,m,n=0,1,\ldots \tag{2.41}$$

where $(\ )^*$ denotes complex conjugate. A method for the evaluation of these integrals is outlined in Appendix A.

We remark that the exact evaluation of the local wave free integral above is critical to the efficacy of the present method. Substituting (2.39) into (2.15), combining with (2.33), and using the leading asymptotics of J_n and H_n for large arguments, it is easy to show that the free-surface integrand has the leading behavior: $k\rho G_n^+ q_n \sim [\exp(i(2k+k_2)\rho)+\exp(ik_2\rho)](k_2\rho)^{-1/2}$ for $k\rho, k_2\rho \gg 1$. Thus if the free-surface integral is simply truncated at b (e.g., Loken, 1986), the truncation error decreases only as $b^{-1/2}$. For accurate results, the effort involved in numerical quadrature over a large domain becomes prohibitive. On the other hand, the convergence can be improved by evaluating the integral of the leading asymptotic term only from b to infinity in terms of Fresnel integrals (Eatock-Taylor & Hung, 1987). The neglected terms are then of $O[\rho^{-3/2}(k^{-1}k_2^{-1/2}+k_2^{-1}k^{-1/2})]$, so that the convergence with b is still only algebraic, in contrast to the exponential decrease of error with b associated only with the evanescent modes in the present case.

3. SECOND-ORDER EXCITING FORCES, MOMENTS AND SURFACE ELEVATION

The boundary-integral equation (2.14) for $\phi_{Dn}^{(2)}$ is solved using a discretization procedure similar to that for the first-order problem. The hydrodynamic pressure can be calculated from the first- and second-order potentials according to Bernoulli equation:

$$-p^{(1)}/\rho_o = \frac{\partial\Phi^{(1)}}{\partial t} ,$$

$$-p^{(2)}/\rho_o = \frac{\partial\Phi^{(2)}}{\partial t} + \frac{1}{2}(\nabla\Phi^{(1)})^2 , \qquad (3.1)$$

where ρ_o denotes the fluid density. The second-order forces and moments, $f_j^{(2)}(t)$, $j=1,2,\ldots,6$, can be obtained by integrating the pressure on the wetted body surface:

$$f_j^{(2)}(t) = \iint_{S_B} p^{(2)}n_j dS + \iint_{S_\epsilon(t)} (p^{(1)}-\rho_o gz)n_j dS, \qquad (3.2)$$

where $(n_1,n_2,n_3)=\mathbf{n}$, $(n_4,n_5,n_6)=\mathbf{r}\times\mathbf{n}$, and S_B and $S_\epsilon(t)$ are respectively the mean and time-varying portions of the instantaneous wetted body surface.

For a harmonic incident wave, the second-order forces and moments contain double-frequency and steady components:

$$f_j^{(2)}(t) = \mathrm{Re}\{F_j^{(2)} e^{-2i\omega t}\} + \bar{F}_j^{(2)}. \tag{3.3}$$

The double-frequency forces and moments can be further split into that due to contributions from the quadratic products of the first-order potential, $F_1^{(2)}$, and that due to the second-order potential, $F_2^{(2)}$; i.e., $F_j^{(2)} = F_{j1}^{(2)} + F_{j2}^{(2)}$. These are given, for wall-sided bodies, by:

$$F_{j1}^{(2)} = -\frac{\rho_0}{4} \left\{ \iint_{S_B} (\nabla\phi^{(1)})^2 n_j dS + \frac{\omega^2}{g} \int_{W_0} (\phi^{(1)})^2 n_j dl \right\}, \tag{3.4}$$

$$F_{j2}^{(2)} = 2i\omega\rho_0 \iint_{S_B} \phi^{(2)} n_j dS , \tag{3.5}$$

where W_0 is the mean waterline. The mean second-order component is:

$$\bar{F}_j^{(2)} = -\frac{\rho_0}{4} \left\{ \iint_{S_B} |\nabla\phi^{(1)}|^2 n_j dS - \frac{\omega^2}{g} \int_{W_0} |\phi^{(1)}|^2 n_j dl \right\}. \tag{3.6}$$

For vertically axisymmetric bodies, the surface integrals can be reduced to line integrals along ∂B by integrating in θ and using orthogonality. Thus, for example, the horizontal force component, $F_{11}^{(2)}$, can be written as:

$$\begin{aligned} F_{11}^{(2)} = &- \frac{\rho_0 a n_\rho \omega^2}{4g} \sum_{n=0}^{\infty} \frac{2\pi}{\epsilon_n} \phi_n^{(1)} \phi_{n+1}^{(1)} \Big|_{z=0} \\ &- \frac{\rho_0}{4} \sum_{n=0}^{\infty} \int_{\partial B} dl \; \rho n_\rho \left[\frac{2\pi}{\epsilon_n} \left(\frac{\partial\phi_n^{(1)}}{\partial\rho} \frac{\partial\phi_{n+1}^{(1)}}{\partial\rho} + \frac{\partial\phi_n^{(1)}}{\partial z} \frac{\partial\phi_{n+1}^{(1)}}{\partial z} \right) + \frac{\pi n(n+1)}{\rho^2} \phi_n^{(1)} \phi_{n+1}^{(1)} \right], \end{aligned} \tag{3.7}$$

If the body is not wall-sided, an extra factor, $(1-n_z^2)^{-1/2}$, appears in the waterline terms.

For the free-surface elevation, $\zeta(t)$, we expand the exact free-surface condition in a Taylor expansion about z=0, and obtain the second-order elevation

$$\zeta^{(2)}(t) = \left[\frac{-1}{2g} (\nabla\Phi^{(1)})^2 + \frac{1}{g^2} \frac{\partial\Phi^{(1)}}{\partial t} \frac{\partial^2\Phi^{(1)}}{\partial t\partial z} - \frac{1}{g} \frac{\partial\Phi^{(2)}}{\partial t} \right]_{z=0} . \tag{3.8}$$

As with the velocity potential, $\zeta^{(2)}(t)$ can be decomposed into a time-independent term, $\bar{\eta}^{(2)}$, and a double-frequency term of amplitude $\eta^{(2)}$, which in turn can be written as a sum of contributions from the first-order ($\eta_1{}^{(2)}$) and second-order ($\eta_2{}^{(2)}=\eta_D{}^{(2)}+\eta_I{}^{(2)}$) potentials:

$$\zeta^{(2)}(t) = \mathrm{Re}\ [(\eta_1^{(2)}+\eta_2^{(2)})e^{-2i\omega t}] + \bar{\eta}^{(2)}, \tag{3.9}$$

and from (3.8):

$$\eta_1^{(2)} = \left[\frac{-1}{4g} (\nabla\phi^{(1)})^2 - \frac{\omega^2}{2g^2} \phi^{(1)} \frac{\partial\phi^{(1)}}{\partial z} \right]_{z=0} \tag{3.10}$$

$$\eta_2^{(2)} = \eta_D^{(2)} + \eta_I^{(2)} = \frac{2i\omega}{g} [\phi_D^{(2)} + \phi_I^{(2)}]_{z=0} \tag{3.11}$$

$$\bar{\eta}^{(2)} = \left[\frac{-1}{4g} |\nabla\phi^{(1)}|^2 + \frac{\omega^2}{2g^2} \phi^{(1)} \frac{\partial\phi^{(1)*}}{\partial z} \right]_{z=0} \tag{3.12}$$

If only integrated second-order quantities such as forces are required, an alternative method (Molin, 1979; Lighthill, 1979), which does not require the solution for $\phi_D{}^{(2)}$ explicitly, is to apply Green's theorem with the use of an assisting radiation potential, ϕ_j, which satisfies the first-order boundary-value problem (2.4) at double-frequency, with the body boundary condition

$$\frac{\partial\phi_j}{\partial n} = n_j , \qquad \text{on the body } (S_B);\ j=1,2,\ldots,6. \tag{3.13}$$

Applying Green's identity to $\phi_D^{(2)}$ and ψ_j, and taking advantage of the boundary conditions they satisfy, we obtain:

$$\iint_{S_B} \phi_D^{(2)} n_j dS = - \iint_{S_B} \psi_j \frac{\partial \phi_I^{(2)}}{\partial n} dS + \frac{1}{g} \iint_{S_F} q \psi_j dS \, , \tag{3.14}$$

so that the second-order forces are expressed in terms of first-order potentials only. For axisymmetric bodies, the free-surface integral in (3.14) has similar properties to that in (2.14) and the techniques of §2.4 are directly applicable. We remark that the computational effort involved in this indirect approach is not significantly different from the direct solution of §2, since in both cases, an additional boundary-value problem at double-frequency (Eq.2.14 or that for ψ) and an evaluation of similar free-surface integrals are involved.

For a uniform bottom-extended vertical cylinder, the first-order potentials can be expressed in closed form, so that semi-analytic expressions (not involving solutions of integral equations) for the second-order forces and moments can be derived using (3.14). These are summarized in Appendix B, and provide useful comparisons for the numerical results of §2 for this geometry.

4. NUMERICAL RESULTS AND DISCUSSION

For illustration we consider the diffraction of plane monochromatic waves by two axisymmetric geometries: (a) a bottom-seated uniform vertical cylinder (radius a, depth h=a) for which semi-analytic solutions for the forces are available (Appendix B); and (b) a conical island or gravity platform (waterplane radius a, depth h=a, toe angle 60°) where second-order effects are expected to be particularly important.

The integral equations (2.14) and (2.37) for the second- and first-order problems respectively are discretized and solved numerically following a standard procedure: (i) approximate the body contour, ∂B, by Np straight line segments; (ii) assume constant values for the potential, $\phi_{Dn}^{(2)}$, or ring-source strength, σ_n, over each segment; (iii) collocate the equations at the center of each segment to obtain a system of linear algebraic equations for the segment unknowns, which is then solved. In calculating the influence coefficients, the singularities of the kernels in §2.2 are subtracted out and integrated analytically. The sources of numerical error are those associated with: (i) the truncation to a finite number, N, of Fourier modes in θ; (ii) the assumed constant variations of the unknowns over each segement; and (iii) the geometric approximation of the body contour by Np piece-wise linear segments.

For the present geometries, the body contours are described exactly by straight segements, and the numerical errors are controlled by proper choices of Np and N. Table 1 shows the errors in the modulus of the first-order horizontal diffraction force on the uniform cylinder as a function of Np (N_W=20 is used for the evaluation of the ring-source Green functions). To describe the more rapid variations near the free-surface (especially for the second-order potential), cosine-spaced segments (with smaller lengths near the surface) are used in all our calculations. The convergence with Np is approximately quadratic. Hereafter, Np=20 segments are used for both the first- and second-order problems.

Table 1. Magnitude of the first-order horizontal diffraction force, $|F_x^{(1)}|/\rho g a^2 A$, on a uniform vertical cylinder (a/h=1) for different frequencies, $\nu a \equiv \omega^2 a/g$, as a function of the number of cosine-spaced segments, N_p, on the body; compared to exact values.

νa =	1.2	2.0	2.8
exact	2.6282	1.6281	1.0529
N_p = 10	2.6250	1.6243	1.0481
20	2.6276	1.6271	1.0515
30	2.6281	1.6276	1.0520

To show the convergence with increasing numbers, $n \leq N$, of azimuthal Fourier modes, we tabulate the modal amplitudes of the first- and second-order potentials on the vertical cylinder at $(\rho,z)=(a,0)$ (which are proportional to the run-up) in Table 2. For comparison, the amplitudes of the modes of the second-order incident and diffraction potentials are given separately. From partial wave decompositions of the incident waves, it is clear that the mode number beyond which the amplitudes attenuate rapidly increases with increasing frequency. This is seen for the larger $\omega^2 a/g \equiv \nu a$ as well as for the double-frequency potentials. It is of interest to note the large magnitudes and relatively slow decrease of $|\eta_{Dn}^{(2)}|$ compared to the double-frequency incident wave. In all our calculations up to $\nu a \simeq O(3)$, N=9 and 14 are used respectively for the linear and second-order problems.

A significant portion of the computational effort is in the evaluation of the free-surface integral in (2.14). For the free-surface forcing pressure terms, q_n (2.15), $\phi^{(1)}$ is calculated from first-order

Table 2. Convergence of the linear and second-order surface elevation angular modal amplitudes (normalized by A and A^2/a respectively) on the circumference (ρ=a) of a uniform vertical cylinder (a/h=1) for νa=1.2,2.0 and 2.8. (* indicates values less than 1e-10).

νa =	1.2			2.0			2.8		
	$\lvert\eta_n^{(1)}\rvert$	$\lvert\eta_{Dn}^{(2)}\rvert$	$\lvert\eta_{In}^{(2)}\rvert$	$\lvert\eta_n^{(1)}\rvert$	$\lvert\eta_{Dn}^{(2)}\rvert$	$\lvert\eta_{In}^{(2)}\rvert$	$\lvert\eta_n^{(1)}\rvert$	$\lvert\eta_{Dn}^{(2)}\rvert$	$\lvert\eta_{In}^{(2)}\rvert$
n= 0	0.6339	0.3242	0.0966	0.5308	1.1600	0.0793	0.4704	0.4404	0.0024
1	1.3028	0.8133	0.5301	1.1048	1.1375	0.0471	0.9477	2.3280	0.0400
2	0.8704	0.7719	0.5810	1.1422	1.1666	0.1358	1.0170	1.9287	0.0191
3	0.2018	0.3300	0.3201	0.6365	0.9640	0.1786	1.0089	1.6163	0.0265
4	0.0339	1.4545	0.1215	0.1639	0.2415	0.1236	0.5051	1.2758	0.0473
5	0.0047	1.4183	0.0355	0.0338	0.8139	0.0608	0.1431	0.6720	0.0405
6	0.0005	0.5586	0.0085	0.0059	1.2414	0.0235	0.0341	0.3541	0.0246
7	0.0001	0.1152	0.0017	0.0009	1.0073	0.0076	0.0070	1.0061	0.0118
8	0.5E-5	0.0194	0.0003	0.0001	0.5904	0.0021	0.0013	1.0968	0.0048
9	0.3E-6	0.0029	0.5E-4	0.1E-4	0.2228	0.0005	0.0002	0.7860	0.0016
10	0.2E-7	0.0004	0.6E-5	0.1E-5	0.0490	0.0001	0.3E-4	0.4555	0.0005
11	0.1E-8	0.0001	0.8E-6	0.1E-6	0.0086	0.2E-4	0.4E-5	0.2263	0.0001
12	*	0.6E-5	0.9E-7	0.1E-7	0.0014	0.4E-5	0.5E-6	0.0862	0.3E-4
13	*	0.6E-6	0.1E-7	0.9E-9	0.0002	0.6E-6	0.5E-7	0.0208	0.8E-5
14	*	0.5E-7	0.1E-8	*	0.2E-4	0.9E-7	0.5E-8	0.0036	0.2E-5

source strengths via (2.36) and its first and second derivatives from direct differentiation of (2.36). The Rankine part and its derivatives are evaluated analytically from (2.18).

At the <u>free-surface body intersection point</u>, we encounter two types of difficulties. The first one is the mathematical weak singularity of the potential at that point due to the confluence of boundary conditions. For a vertical (wall-sided) intersection, it is shown that the linear potential for horizontal motions has a weak, $r^2 \ln r$ type, singularity, while those for vertical motions or wave diffraction are regular at the intersection point (Kravtchenko, 1954; Miloh, 1980; Sclavounos, 1988).

The type of singularity for a nonvertical intersection case has not been completely resolved yet. We are also interested in local results such as run-up on non-wall-sided bodies. In this case, the validity of our results is established through careful convergence tests. Table i) shows, for example, the convergence (with decreasing grid size) of the (first-order) run-up at a given point (ρ=a, θ=0, z=0) on a 60 degree cone. The convergence of the linear diffraction potential at the intersection point is quite evident.

Table i) Convergence of the linear diffraction potential (at ρ=a, z=0, & θ=0; νa=2) for a 60 degree cone (h=a) with increasing the number of panels.

N_p=	10	20	30
$\lvert\phi_D^{(1)}\rvert$	2.818	2.827	2.825

When the linear potential has a weak singularity given above (e.g. surge radiation potential), the second derivatives of the linear potential at that point are logarithmically singular but still integrable. Therefore, the evaluation of the free-surface integral presents no theoretical difficulties. To avoid evaluations of the second derivatives near the intersection point, a weaker formulation for the free-surface integral can be used, alternatively, after integration by parts (e.g. Chau & Eatock Taylor, 1988).

Another kind of singularity is also encountered when a body has sharp corners (e.g. $\Phi \sim r^{2/3}$, at the corner of a truncated vertical cylinder). To account for this behavior, the cosine-spaced segments near the corner are used whenever we have sharp corners (e.g. Newman, 1985b).

The second type of difficulty is rather a methodological one associated with a panel method. With the use of constant-strength segments, the potential and its derivatives on the free surface from (2.36) are not accurate in a small neighbourhood (of the order of a segment length) near the intersection with the body (e.g., Korsmeyer, 1988). This is clearly shown in Figure 1a, where the diffraction potential and its derivatives for a vertical cylinder near the intersection point are calculated by (2.36). Higher accuracy is obtained by using cosine spacing compared to regular spacing ($N_p=20$), especially close to the intersection point. For cosine-spaced body segments, the typical relative errors in ϕ and ϕ_ρ for $(\rho-a)\geq 0.02a$ are $O(0.1\%)$. The above trend is not sensitive to changing frequencies. In practice, we obtain $\phi_z^{(1)}(a,0)$ and $\phi_\rho^{(1)}(a,0)$ from $\phi^{(1)}(a,0)$ using free-surface and body boundary conditions, respectively; $\phi_{\rho\rho}^{(1)}(a,0)$ from three-point differencing of $\phi_\rho^{(1)}$ at $(a,0)$, $(l_G,0)$, and $(2l_G,0)$; and $\phi_{zz}^{(1)}(a,0)$ from applying Laplace's equation at the intersection point. The values for $a\leq\rho\leq 2l_G$ are then obtained by three-point quadratic interpolations. In the following table, the free-surface forcing pressure at the intersection point with changing the lower boundary (l_G) of using (2.36) are given.

Table ii) The free-surface forcing pressure $|q_1|$ at the intersection point, $\rho=a$ & $z=0$, of a vertical cylinder ($h=a$), and for $\nu a=3$, with varying l_G/a (Exact solution is $|q_1(0)|=2.550$).

$l_G/a=$	0.030	0.025	0.020	0.015
$\|q_1\|=$	2.526	2.530	2.540	2.568

As already observed in Figure 1a, $l_G \sim 0.02a$ is the optimum value in this case. The accuracy of q inside l_G is local and does not change global quantities such as $F_2^{(2)}$ significantly (typically O(0.1%) for the values of l_G in Table ii). A similar behavior is also observed for the 60 degree cone. In all our computations, then, $l_G=0.02a$ is used. Figure 1b shows the comparisons between computed results and analytic solutions (cf. Appendix B) for the first three modes of the forcing pressure outside a uniform cylinder for $\nu a=2$. Computed free-surface pressures even at the intersection point agree well with those of analytic solutions. The slowly decaying and oscillatory behaviour of the profiles are quite evident.

The free-surface integral in (2.14) is calculated using the method of §2.4. To estimate the convergence of the integral with the partition radius b, we consider a typical local mode in the second term of (2.29). Using the addition theorem for K_0:

$$K_0(\kappa_m R) = \sum_{n=0}^{\infty} \epsilon_n \, I_n(\kappa_m \rho') \, K_n(\kappa_m \rho) \cos n(\theta-\theta'), \tag{4.1}$$

it is clear that for ρ' on the body, the decay of the local modes with ρ is exponential with a rate given by $\kappa_m \rho$ or in fact ρ/h according to (2.31). In general, for a given tolerance, we select a fixed (b-a)/h to control the error associated with neglected evanescent waves in the outer integral. Table 3 shows typical convergence of results with (b-a)/h for the second-order potential horizontal force and overturning moment (with respect to the bottom) on a uniform vertical cylinder (a/h=1).

Table 3. Magnitude of the second-order potential horizontal force and overturning moment (normalized by ρgaA^2 and ρga^2A^2 respectively) on a uniform vertical cylinder, a/h=1. The results are for different partition radii b for the free-surface integral evaluation compared to semi-analytic solutions (Appendix B).

νa =	1.2		2.0		2.8	
	$\lvert F_2^{(2)}\rvert$	$\lvert M_2^{(2)}\rvert$	$\lvert F_2^{(2)}\rvert$	$\lvert M_2^{(2)}\rvert$	$\lvert F_2^{(2)}\rvert$	$\lvert M_2^{(2)}\rvert$
exact	2.263	1.239	2.694	1.439	4.229	2.429
(b-a)/h= 2	2.258	1.237	2.663	1.430	4.193	2.418
3	2.262	1.238	2.691	1.437	4.227	2.429
4	2.263	1.238	2.694	1.439	4.231	2.431

It is seen that a partition radius of b-a~3h is adequate for 3 significant decimals of accuracy and is used in later computations. The accuracy with relatively small numerical integration requirements again underscores the efficacy of the method of §2.3 compared to methods which have only algebraic convergence.

We now turn to the results for the two geometries. Table 4 shows the first- and second-order forces and moments on the uniform circular cylinder (computed from pressure integration on the body) compared to semi-analytic results derived using assisting potentials (Appendix B). For the evaluation of the second-order mean ($\bar{F}_x{}^{(2)}$ and $\bar{M}_y{}^{(2)}$) and that part of the double-frequency ($F_{x1}{}^{(2)}$ and $M_{y1}{}^{(2)}$) forces and moments given by the first-order potential, the gradients of the linear potential on the body are required and are calculated by 3-point centered-differences of collocation point values. The errors in Table 4 increase somewhat with frequency but are less than 1% for all the quantities shown. In all cases

Table 4. Real and imaginary parts (real,imag) of the first- and second-order horizontal force and overturning moment (with respect to the bottom) on a uniform vertical cylinder (a/h=1) obtained by direct pressure integration on the body. For comparison, semi-analytic solutions obtained using assisting potentials (Appendix B) are given on the first rows. (The quantities $F^{(1)}$, $M^{(1)}$, $F^{(2)}$ and $M^{(2)}$ are normalized by $\rho g a^2 A$, $\rho g a^3 A$, $\rho g a A^2$ and $\rho g a^2 A^2$ respectively.)

νa =	1.2	2.0	2.8
$F_x^{(1)}$	0.708,-2.531 0.708,-2.531	-0.264,-1.606 -0.264,-1.606	-0.746,-0.743 -0.745,-0.742
$\bar{F}_x^{(2)}$	0.826 0.826	0.711 0.711	0.656 0.655
$F_{x1}^{(2)}$	-1.648,-0.308 -1.648,-0.305	-1.094, 0.849 -1.076, 0.846	0.892, 1.341 0.887, 1.345
$F_{x2}^{(2)}$	2.259,-0.136 2.258,-0.135	1.972,-1.835 1.973,-1.830	-2.209,-3.606 -2.208,-3.604
$F_x^{(2)}$	0.611,-0.444	0.878,-0.986	-1.317,-2.265
$M_y^{(1)}$	0.401,-1.431 0.400,-1.431	-0.165,-1.004 -0.165,-1.003	-0.511,-0.509 -0.510,-0.509
$\bar{M}_y^{(2)}$	0.870 0.870	0.822 0.823	0.777 0.778
$M_{y1}^{(2)}$	-1.485,-0.385 -1.485,-0.382	-1.063, 0.801 -1.044, 0.797	0.835, 1.268 0.829, 1.272
$M_{y2}^{(2)}$ B	1.201,-0.303 1.200,-0.302	1.041,-0.993 1.042,-0.990	-1.360,-2.012 -1.360,-2.013
$M_y^{(2)}$	-0.284,-0.688	-0.022,-0.192	-0.525,-0.744

for the force, the contribution of the second-order potential is larger than that of quadratic products of first-order quantities. However, these two effects are generally out of phase so that the net second-order excitations are relative small compared to the linear quantities but increase with increasing wave frequency. Thus for moderately steep waves, say $kA \sim 0.2$, the double-frequency second-order force amplitude is only about 4~16% for $\nu a = 1.2 \sim 2.8$. The situation for the overturning moment is similar but with somewhat smaller ratios of $M_{y2}^{(2)}$ to $M_{y1}^{(2)}$. This is related to the relative centers of pressure of the different pressure components (see Figures 3 and 4).

The magnitudes of the first- and second-order force coefficients are plotted in Figures 2 as a function of incident frequency. The comparisons with semi-analytic results are uniformly good except for small discrepancies in a neighborhood of $\nu a \simeq 2.4$ which corresponds to the first irregular frequency of the integral equation (2.37). (The frequency is given by the homogeneous interior Dirichlet solution at the first zero of $J_0(ka)$ at $ka \simeq 2.405$ or $\nu a \simeq 2.366$. The effects of the irregular frequencies, ν, associated with (2.14) which are one-fourth those of (2.37) are much weaker.) The force components due to the second-order potential are major portions of the total second-order quantities and their magnitudes relative to the other second-order contributions increase with increasing frequency. Thus, in no situation is it valid to ignore $F_2^{(2)}$ in favor of quadratic contributions of the first-order potential. This invalidates many recent engineering estimates of second-order wave effects on structures (e.g., Herfjord & Nielsen, 1986; Petrauskas & Liu, 1987) wherein the second-order potentials were ignored. Note that both $F_2^{(2)}$ and $M_2^{(2)}$ blow up as $\nu a = \nu h \to 0$, and the second-order result becomes invalid. This is related to failure of Stokes' expansion (see Eq. 2.3) as $kh \ll 1$ for fixed kA. As pointed out earlier, $F_2^{(2)}$ and $F_1^{(2)}$ (as well as the moments) are generally out of phase, so that the net double-frequency excitation amplitude is usually smaller than that of $F_2^{(2)}$ and important only for steep incident waves.

Unlike earlier work such as Molin (1979) and Eatock-Taylor & Hung (1987), we obtain the second-order potential explicitly so that useful local second-order quantities such as pressure distribution, velocities and wave run-up are also available. Figures 3a,b show the amplitudes of the linear and components of the second-order pressure distributions on the cylinder on the lee (θ=0) and weather (θ=π) sides respectively for νa=2. Analytic results, where available (from Eq.B.1), are also shown. The pressures $p_1^{(2)}$ and $\bar{p}^{(2)}$ which are due to quadratic products of the first-order potential, as well as the pressure due to $\phi_I^{(2)}$ attenuate with depth with a rate of ~2k, whereas the pressure associated with the second-order double-frequency free waves (ϕ_H) has a decay rate given by k_2~4k. On the other hand, the portion of the nonlinear potential second-order pressure, $p_2^{(2)}$, which is forced by the inhomogenous surface term (2.6) has a much slower attenuation with depth dictated by (2.6). This is especially evident on the weather side. The phenomenon can be seen in general from the far-field behavior of ϕ_P (Eq.2.10), where the depth-dependence of the potential varies from being a constant on the weather side (θ=π) to cosh 2k(z+h) on the lee side.

For longer waves, the situation is even more interesting, where the pressure may not decrease (monotonically) with depth and the minimum $p_2^{(2)}$ may not in general be at the bottom. This is shown in Figure 4 for the case of νa=1.2 for different circumferential positions along the cylinder. Along the leeward (θ=0) edge, the second-order potential pressure first decreases with depth, reaching a minimum at around mid-draft and then begins to increase towards the bottom. At the waveward quarter ($\theta=3\pi/4$) the pressure has a minimum close to the surface and then increases monotonically with depth.

For deeper water, the total hydrodynamic pressure may be dominated by that due to the second-order potential. Figures 5 show the pressure distributions on a uniform cylinder of depth h=4a at $\nu a=2$. As expected, all pressure components given by $\phi^{(1)}$ ($\phi_I^{(2)}$ or ϕ_H) attenuate exponentially while $p_2^{(2)}$ (which is proportional to ϕ_P at deeper depths) has only an algebraic-like decay with depth. This has a very important consequence for the forces on deep-draft bodies. Figure 6 shows the horizontal force components on a uniform cylinder of varying depth h/a for $\nu a=2$. With the attenuation of linear-potential pressures with depth, the quantities $F_x^{(1)}$ and $F_{x1}^{(2)}$ (as well as forces due to $\phi_I^{(2)}$ and ϕ_H) reach constant values rapidly as h/a increases. The force due to the second-order potential, ϕ_P, however, continues to increase in magnitude and converges to a constant asymptotic very slowly. For information, the magnitudes of the first- and second-order components of the free-surface elevation on the cylinder (at $\theta=\pi$) are also plotted, which show that the increase in $F_{x2}^{(2)}$ is not due to the magnitude of the potential on the surface. For truncated cylindrical bodies, this phenomenon gives rise to unexpected second-order vertical forces even when $\nu H > O(1)$, where H is the draft of the body (see Chapter IV).

We next show the first- and second-order run-up on the uniform cylinder as a function of the azimuthal angle θ for $\nu a=2$ (Figure 7). The amplitudes of the run-up components generally increase from the lee ($\theta=0^\circ$)

to weather side, whereas $\eta_2^{(2)}$ has another maximum at the lee quarter. The relative magnitudes and phases between $\eta_1^{(2)}$ and $\eta_2^{(2)}$ depend on θ, and in general the total double-frequency run-up can be several times larger than the second-order mean set-up(down), which itself has a trend similar to $\eta_1^{(2)}$, with a maximum setup on the weather side and setdown along the leeward portion of the cylinder. The general behavior of the various run-up components is sensitive to the incident wave frequency. In Figure 8, we plot the maximum amplitude, over θ, and the position of the maximum (θ_{max}) of these components as a function of νa. Except for the lower frequency, the maximum $|\eta_1^{(2)}|$ is greater than $|\eta_2^{(2)}|$ by almost a constant factor, while both quantities as well as the maximum $|\bar{\eta}^{(2)}|$ (which are all for $\bar{\eta}^{(2)}>0$) tend to increase with frequency. The maximum net double-frequency amplitude $|\eta_1^{(2)}+\eta_2^{(2)}|$ is less sensitive to frequency as is the case for the linear run-up, $|\eta^{(1)}|$. The dependence on water depth has been plotted in Figure 6 for $\nu a=2$. In general, the amplitudes, including $|\eta_2^{(2)}|$, are not sensitive to increasing depth beyond $\nu h >\sim 2$. On the other hand $\eta_2^{(2)}$ increases rapidly in shallow water as a consequence of Stokes' expansion for long waves as pointed out earlier.

We next turn to results for a bottom-seated truncated vertical cone (waterplane radius a, water depth h=a, and a toe angle of 60°). Such a geometry has been proposed for gravity platforms in the Arctic (e.g., Sarpkaya & Isaacson, 1981), or may be considered as a model for a circular island. In this case, the non-vertical body wall is expected to lead to more important second-order effects.

Figures 9 show the magnitudes of the components of horizontal and vertical forces and overturning moment (with respect to the bottom center) on such a body. As a check, the results for $|F_{x2}^{(2)}|$ and $|F_{z2}^{(2)}|$ obtained independently using assisting potentials (Eq. 3.14) are also plotted. These second-order potential forces dominate all other second-order contributions throughout the frequency range. Although the relative phases between $F_1^{(2)}$ and $F_2^{(2)}$ still cause the amplitudes to partially cancel, the net second-order double-frequency forces on the cone may be an appreciable part of the total excitation especially for higher frequencies. For example, for wave slope of kA=0.2, $|F_{x1}^{(2)}+F_{x2}^{(2)}|$ at $\nu a \simeq 2.4$ and $|F_{z1}^{(2)}+F_{z2}^{(2)}|$ at $\nu a \simeq 2.8$ are respectively 60% and 180% of the corresponding linear amplitudes at those frequencies. For the overturning moment, $M_2^{(2)}$ is comparable in magnitude to $M_1^{(2)}$ and they both oscillate with frequency. In this case, however, the components are roughly in phase and the net double-frequency moment is comparable to the linear moment only for steep waves (say $kA \gtrsim .25$ at $\nu a \sim 2.5$).

The run-up along the circumference of the cone is plotted in Figure 10 for the first- and second-order double-frequency and steady components for $\nu a=2$. The double-frequency run-up is much greater than that for the vertical cylinder and shows large variations along the waterline. The net amplitude is given essentially by the second-order potential component and has a maximum at the sides of the cone where it may be comparable to the first-order run-up there for $kA \gtrsim .13$. Again the detail features depend very much on the specific incident frequency, and the results are summarized in Figure 11 where the maxima, over θ, of the amplitudes of the various run-up components are plotted as a function of νa together with the positions (θ_{max}) of the respective maxima. Comparing to Figure 8 for the vertical cylinder, we observe that: the magnitudes of the second-order components are <u>much</u> larger; $|\eta_1^{(2)}|_{max}$ is now quite small compared to $|\eta_2^{(2)}|_{max}$; the maximum total double-frequency run-up increases more rapidly with frequency; the locations of the maxima are more sensitive to frequency; and the interesting fact that the maxima of $|\bar{\eta}^{(2)}|$ are now all for mean set-down (i.e., $\bar{\eta}^{(2)}<0$).

We have also calculated the components of the pressure on the cone. With the exception of a sharper rise of $p_2^{(2)}$ towards the free surface, the qualitative features are similar to those for the vertical cylinder.

5. CONCLUSION

Using a general order ring-source boundary-integral equation method, the second-order diffraction problem for an axisymmetric body in the presence of plane monochromatic incident waves is solved for the nonlinear sum-frequency potential. An important part of the solution is the efficient and accurate calculation of the forcing term which requires the evaluation of an oscillatory and slowly decaying integral on the free surface. An approach which treats the entire local-wave-free outer region analytically is developed and shown to be efficacious. Although the second-order potential is solved explicitly, the present method is comparable in computational effort to existing approaches (Molin, 1979; Lighthill, 1979) which utilize fictitious assisting potentials to obtain global second-order quantities. An important benefit is that complete second-order local quantities such as pressure distributions and surface elevations are now available.

For illustration, the second-order diffraction problem for a uniform vertical cylinder and a truncated vertical cone are studied in some detail. In addition to convergence tests with respect to truncation and discretizations, comparisons of the second-order forces and moments for both geometries with independent results obtained using assisting potentials confirm the validity and accuracy of the present calculations.

From our numerical examples, several important second-order diffraction features are observed:

(1) The relative importance of second-order effects generally increase with frequency, $\omega^2 a/g$, and with the draft of the body, $\omega^2 H/g$.

(2) The second-order potential can not be neglected in favor of quadratic contributions of the linear potential. Double-frequency results obtained without accounting for this potential will likely be inadequate in all but very specialized cases.

(3) The second-order double-frequency diffraction potential can penetrate much deeper than even the linear (incident-frequency) potentials. The pressure or velocities associated with this nonlinear potential may not in general be negligible even for $|\omega^2 z/g| > O(1)$. In particular, the vertical force otherwise absent on a deep truncated cylinder can be nontrivial due to this potential.

(4) When the body side walls are outward sloping towards the bottom, such as in the case of a vertical cone, second-order effects such as run-up are amplified and may indeed be greater than first-order quantities for moderately steep incident waves.

The present method can be generalized to the case where the incident waves contain multiple frequency components as well as the radiation problem -- these are considered in Chapter II.

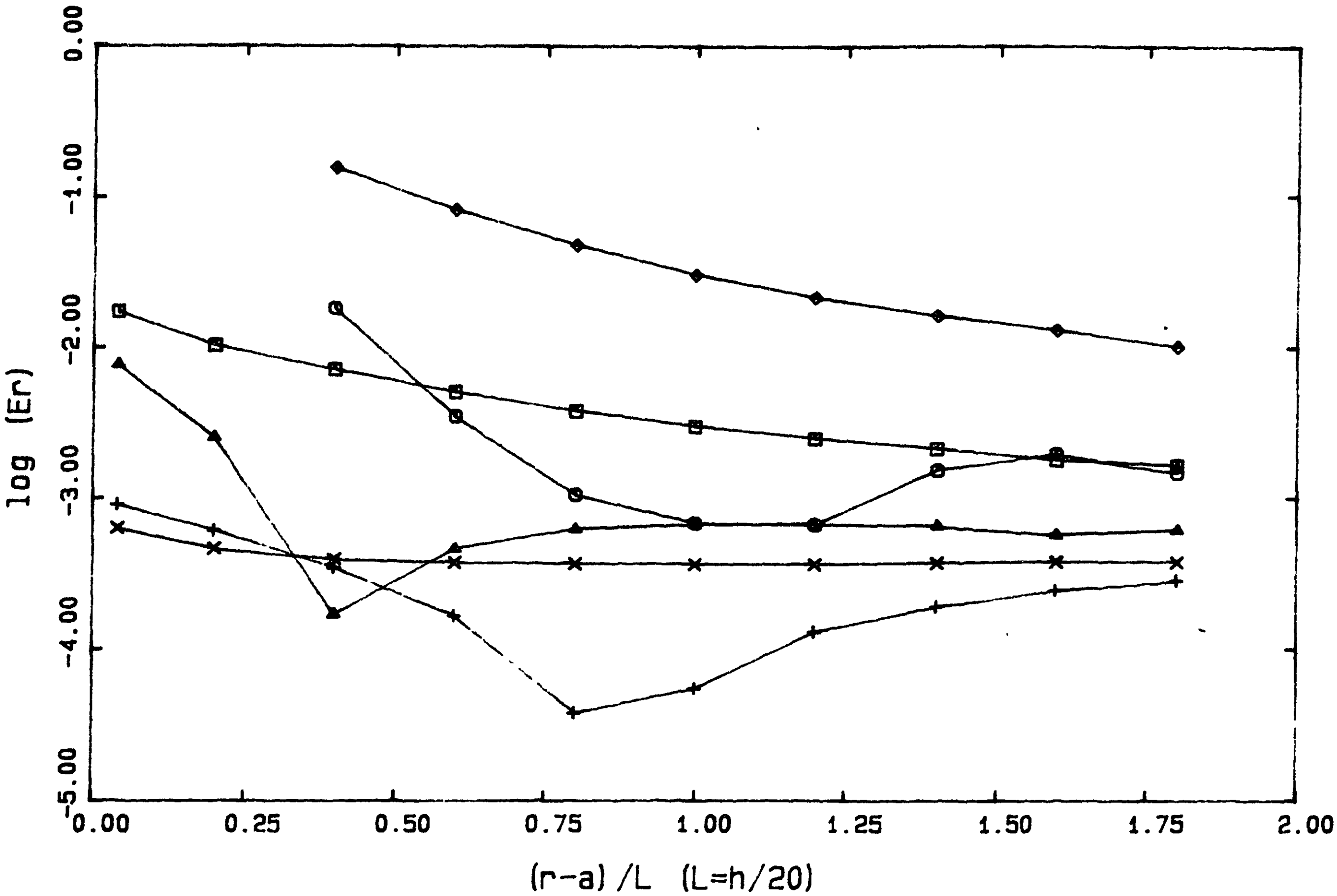

Figure 1a. Relative errors in computing linear diffraction potential and its derivatives for a bottom-mounted vertical cylinder of h=a & $\nu a=3$ near the free surface body intersection point. Computed values are for: ϕ_1 (x), $\phi_{1\rho}$ (□), & ϕ_{1zz} (◇) for regular spacing; and ϕ_1 (+), $\phi_{1\rho}$ (Δ), & ϕ_{1zz} (o) for cosine spacing.

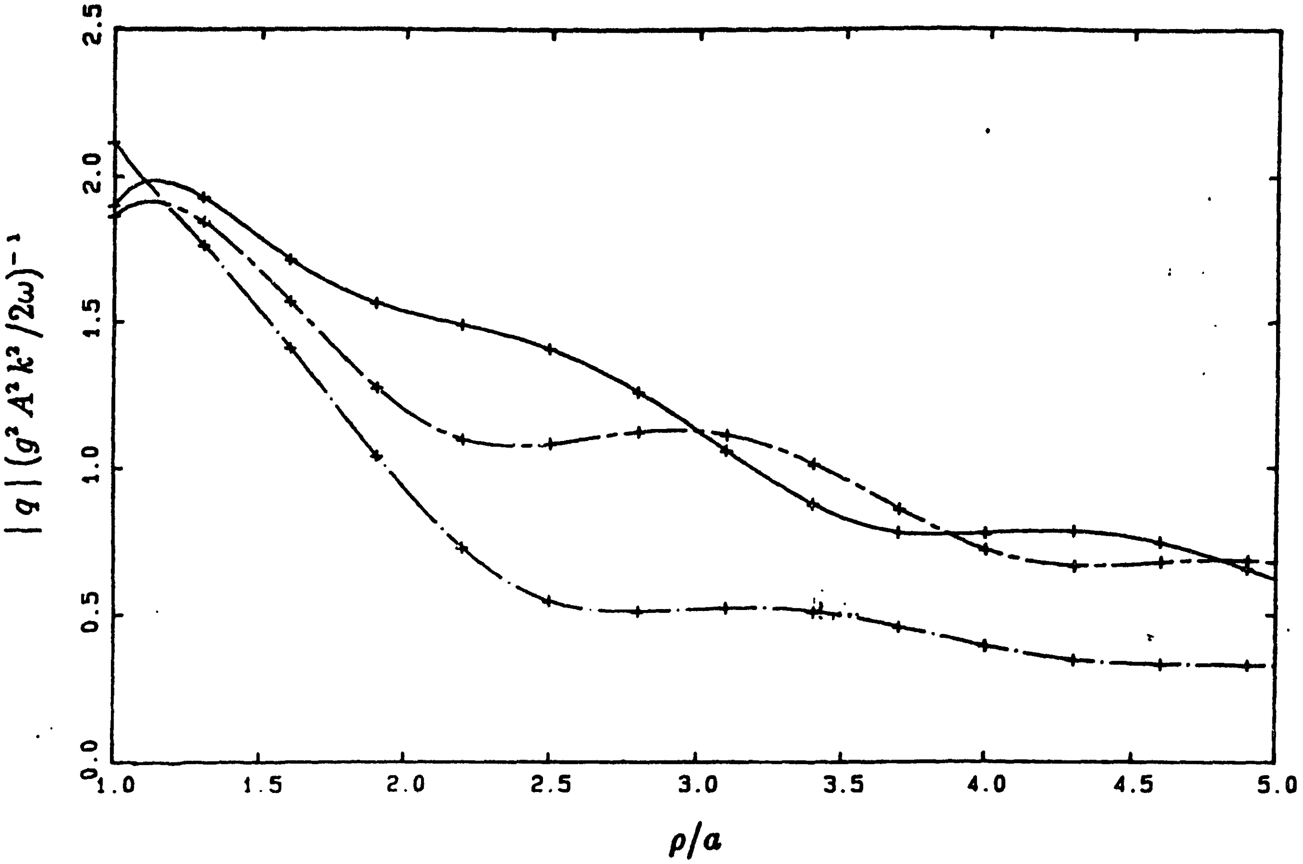

Figure 1b. Comparison between analytic and computed results (+) for the amplitude of the first three modes of the second-order free-surface forcing pressure outside a uniform vertical cylinder (h=a, νa=2) as a function of radial distance. The curves are analytic results for: q_o (—— • ——); q_1 (————); and q_2 (—— – ——).

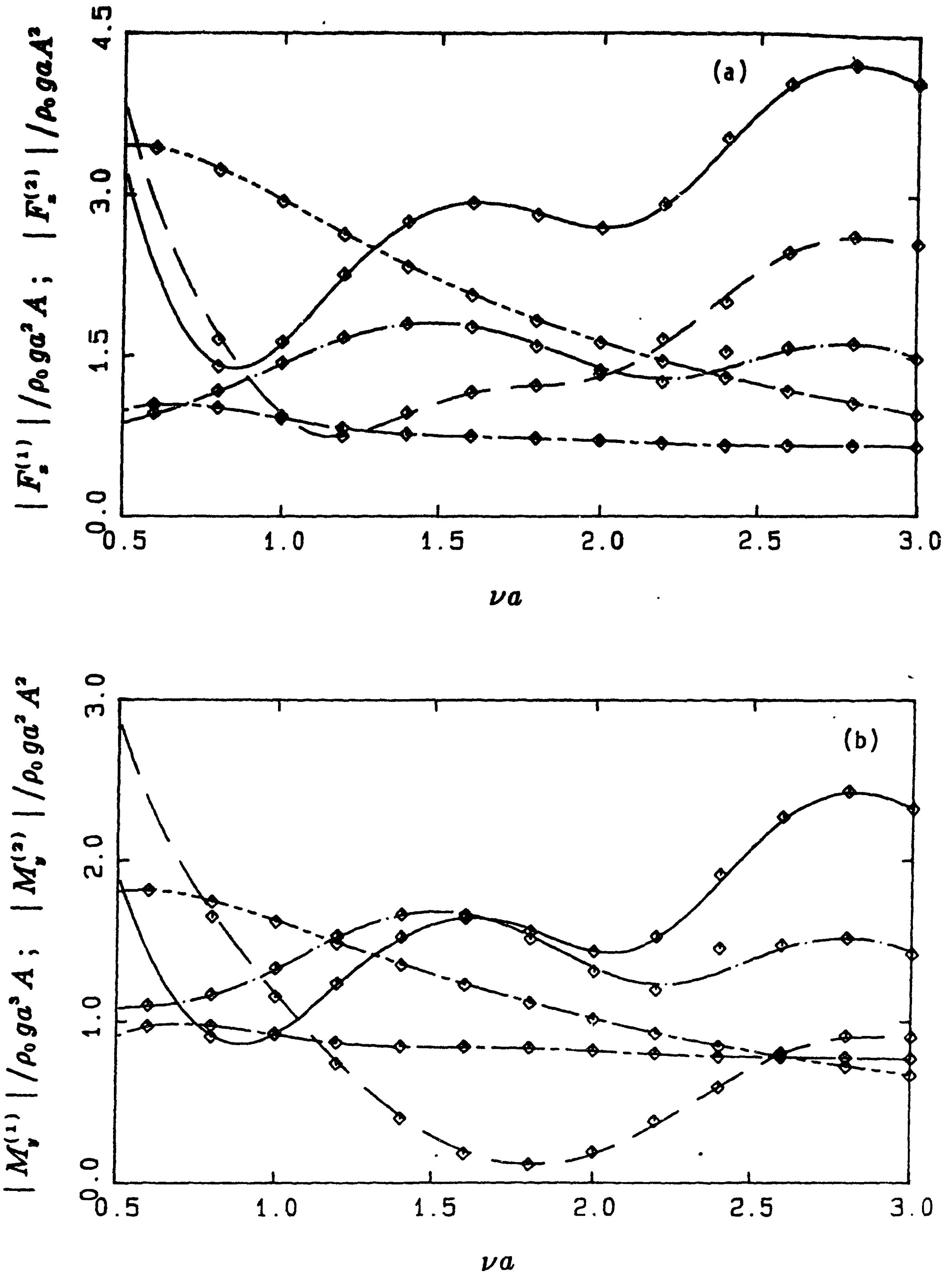

Figure 2. Amplitudes of the linear and components of second-order wave excitations on a uniform vertical cylinder (a=h) as a function of incident frequency, νa. The curves are for semi-analytic solutions for: $|F^{(1)}|$ (—— – – ——); $\bar{F}^{(2)}$ (—— – ——); $|F_1^{(2)}|$ (—— • ——); $|F_2^{(2)}|$ (————); and $|F_1^{(2)}+F_2^{(2)}|$ (—— — ——). Results from pressure integration are denoted by symbols (◇). (a) Horizontal force, F_x; and (b) pitch moment with respect to the bottom, M_y.

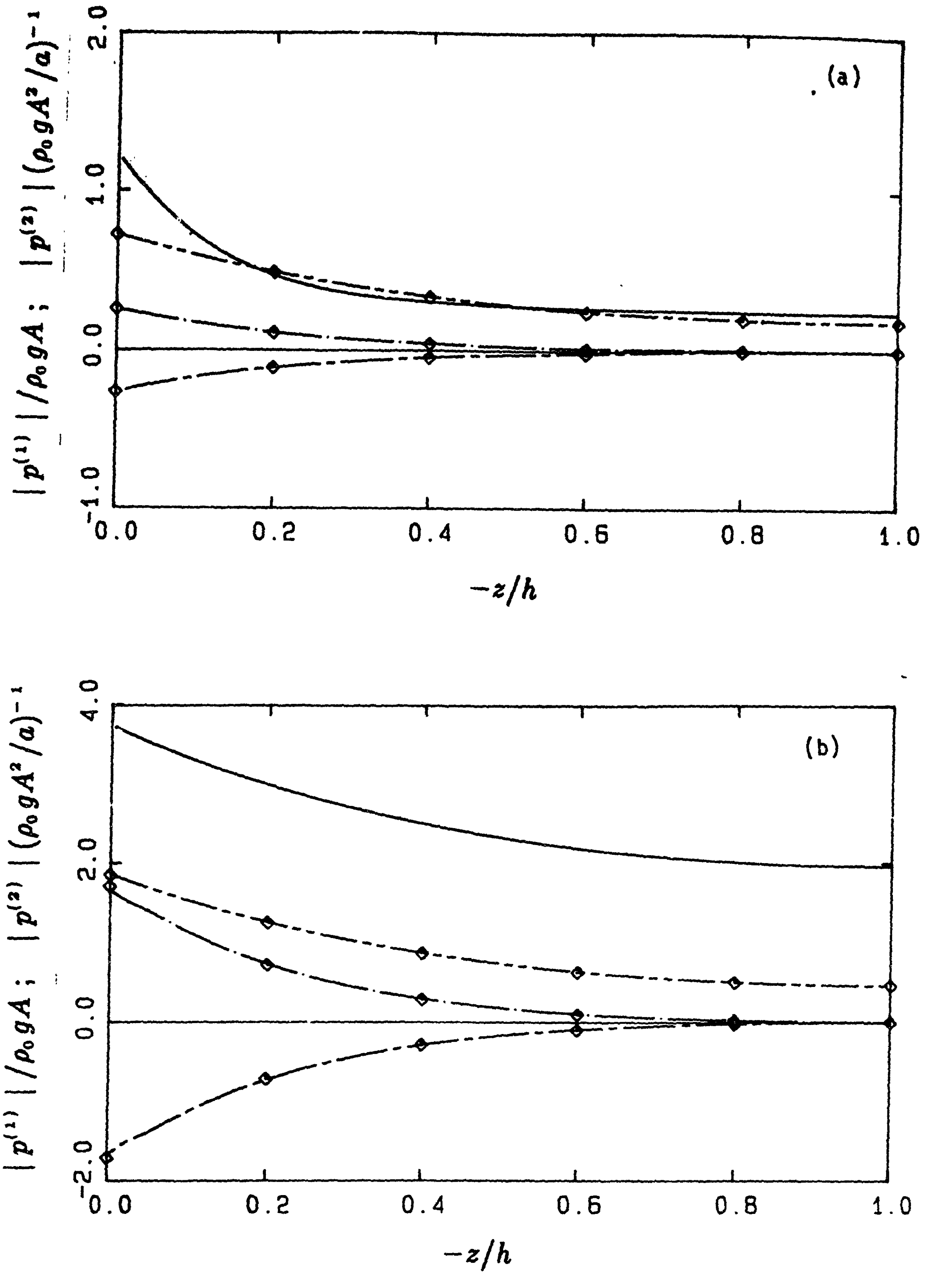

Figure 3. Modulus of the linear and components of second-order hydrodynamic pressure on the side of a uniform vertical cylinder (h=a, $\nu a=2$) on the (a) lee side ($\theta=0$); and (b) weather side ($\theta=\pi$). The curves are computed results for: $|p^{(1)}|$ (—— – – ——); $\bar{p}^{(2)}$ (—— – ——); $|p_1^{(2)}|$ (—— • ——); and $|p_2^{(2)}|$ (————). Analytic results obtained from the linear potential are denoted by symbols (◇).

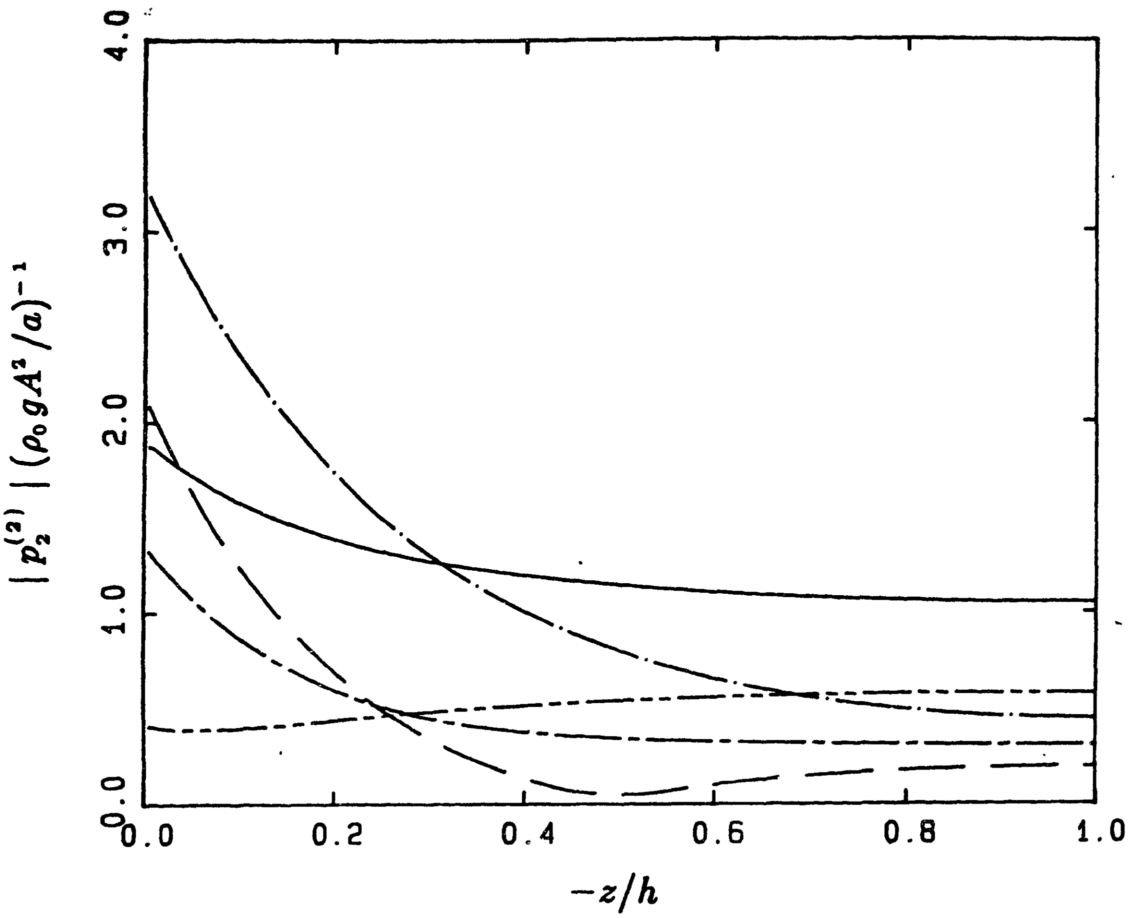

Figure 4. Modulus of the (double-frequency) hydrodynamic pressure due to the second-order potential on the side of a uniform vertical cylinder (h=a, $\nu a=1.2$) at different angular positions: $\theta=0$ (— — —); $\theta=\pi/4$ (—— • ——); $\theta=\pi/2$ (—— – ——); $\theta=3\pi/4$ (— – – —); and $\theta=\pi$ (————).

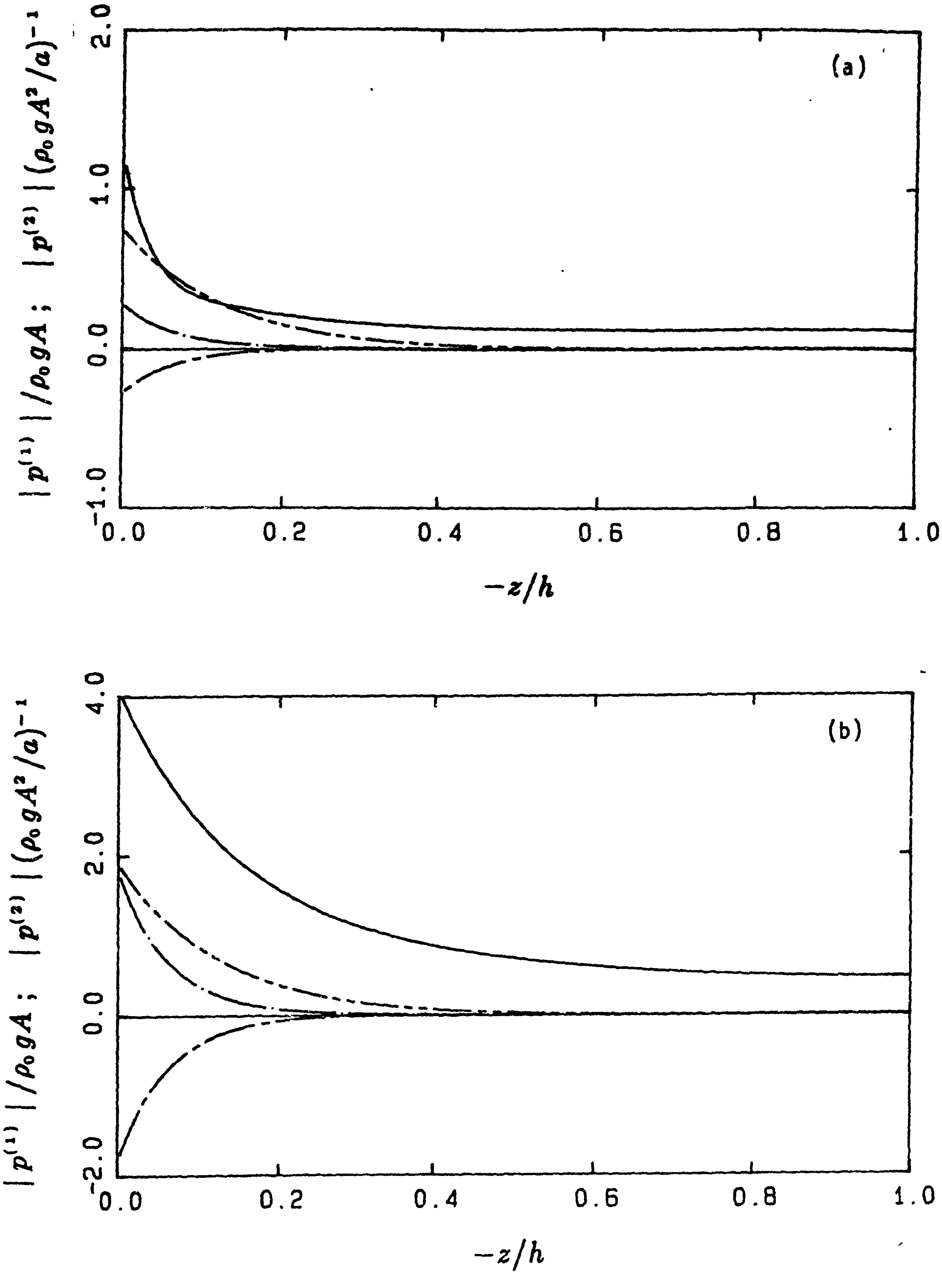

Figure 5. Modulus of the linear and components of second-order hydrodynamic pressure on the side of a uniform vertical cylinder ($h=4a$, $\nu a=2$) on the (a) lee side ($\theta=0$); and (b) weather side ($\theta=\pi$). The curves are computed results for: $|p^{(1)}|$ (—— – – ——); $\bar{p}^{(2)}$ (—— – ——); $|p_1^{(2)}|$ (—— • ——); and $|p_2^{(2)}|$ (————).

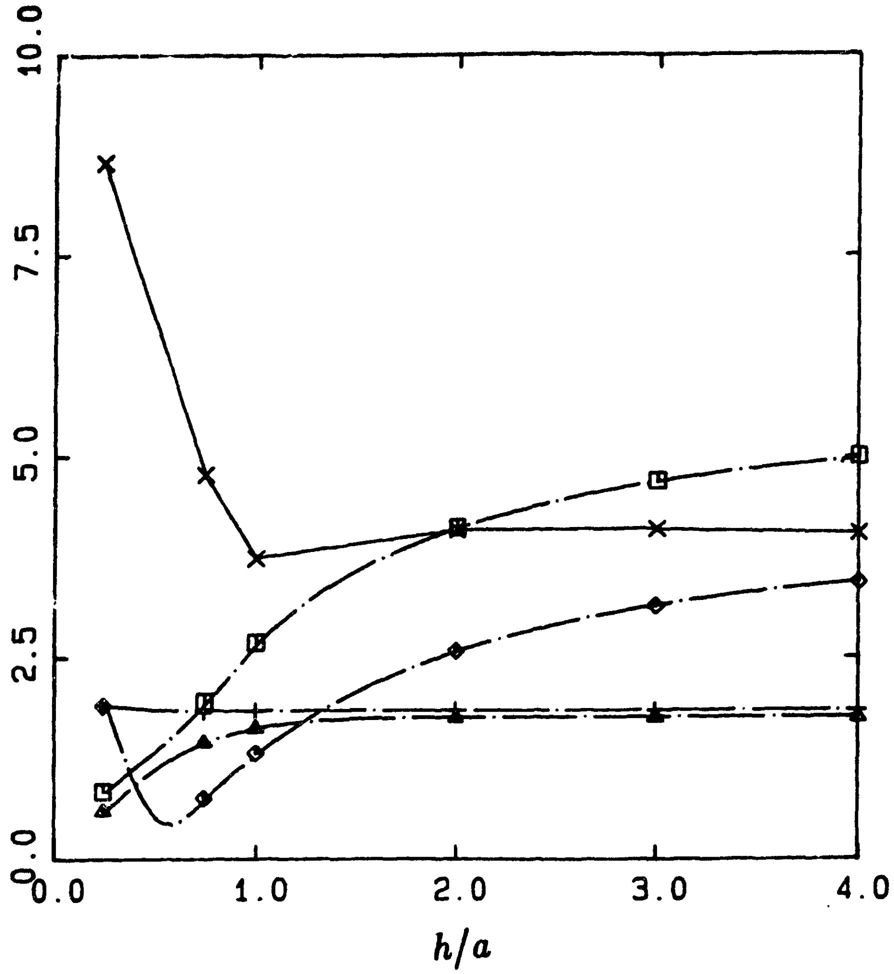

Figure 6. Amplitudes of the linear and components of second-order horizontal force and run-up (at $\theta=\pi$) for uniform vertical cylinders ($\nu a=2$) as a function of the depth, h. Connected symbols are for computed values of: $|F^{(1)}|/\rho_0 g a^2 A$ (Δ); $|F_2^{(2)}|/\rho_0 g a A^2$ (□); $|F_1^{(2)}+F_2^{(2)}|/\rho_0 g a A^2$ (◇); $|\eta^{(1)}|/A$ (+); and $|\eta_2^{(2)}|a/A^2$ (X). Analytic solutions are represented by the curves (—— • ——).

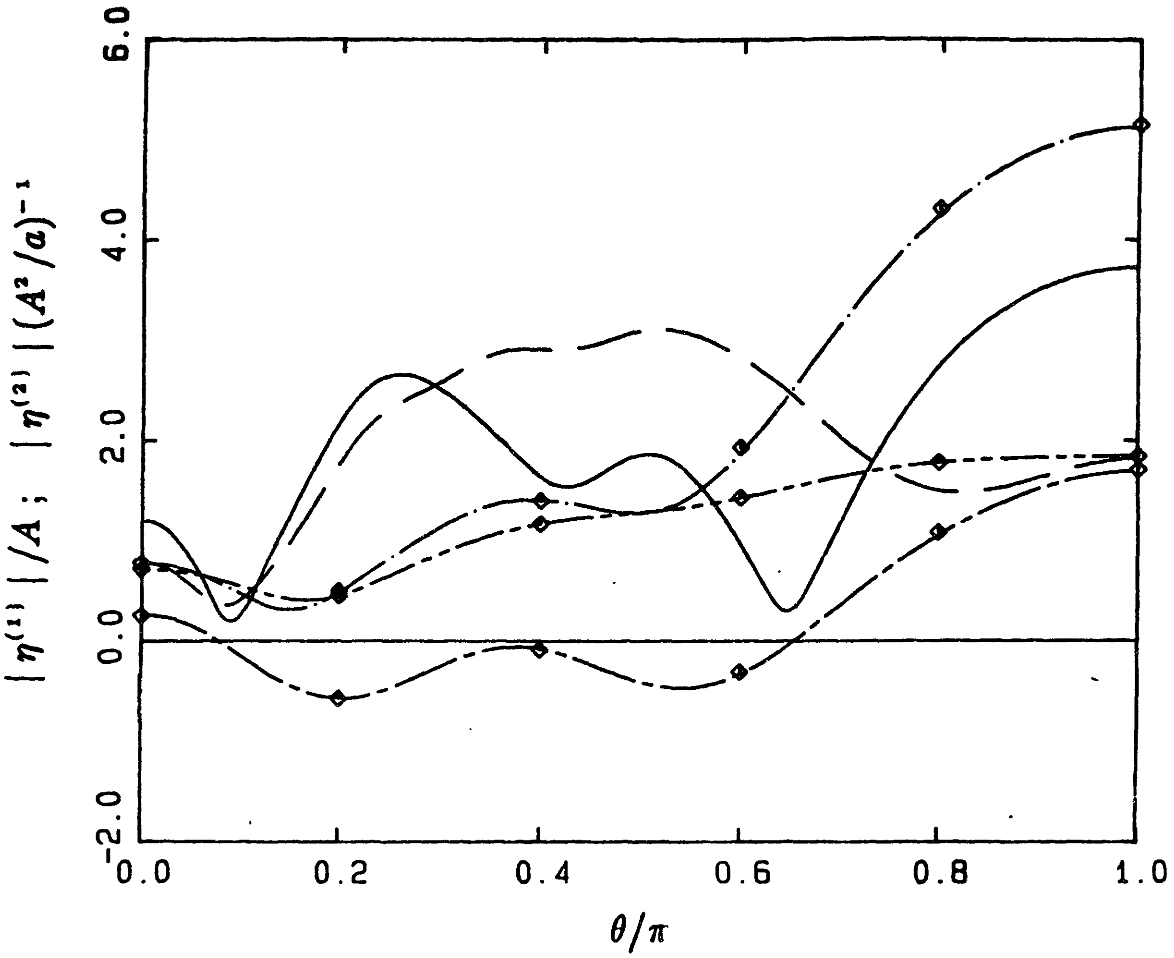

Figure 7. Amplitudes of the linear and components of second-order free surface elevations (run-up) on a uniform vertical cylinder ($h=a$, $\nu a=2$) as a function of the azimuthal angle, θ. The curves are for computed values for: $|\eta^{(1)}|$ (—— – – ——); $\bar{\eta}^{(2)}$ (—— – ——); $|\eta_1^{(2)}|$ (—— • ——); $|\eta_2^{(2)}|$ (————); and $|\eta_1^{(2)}+\eta_2^{(2)}|$ (— — —). Analytic results obtained from the linear potential are denoted by symbols (◇).

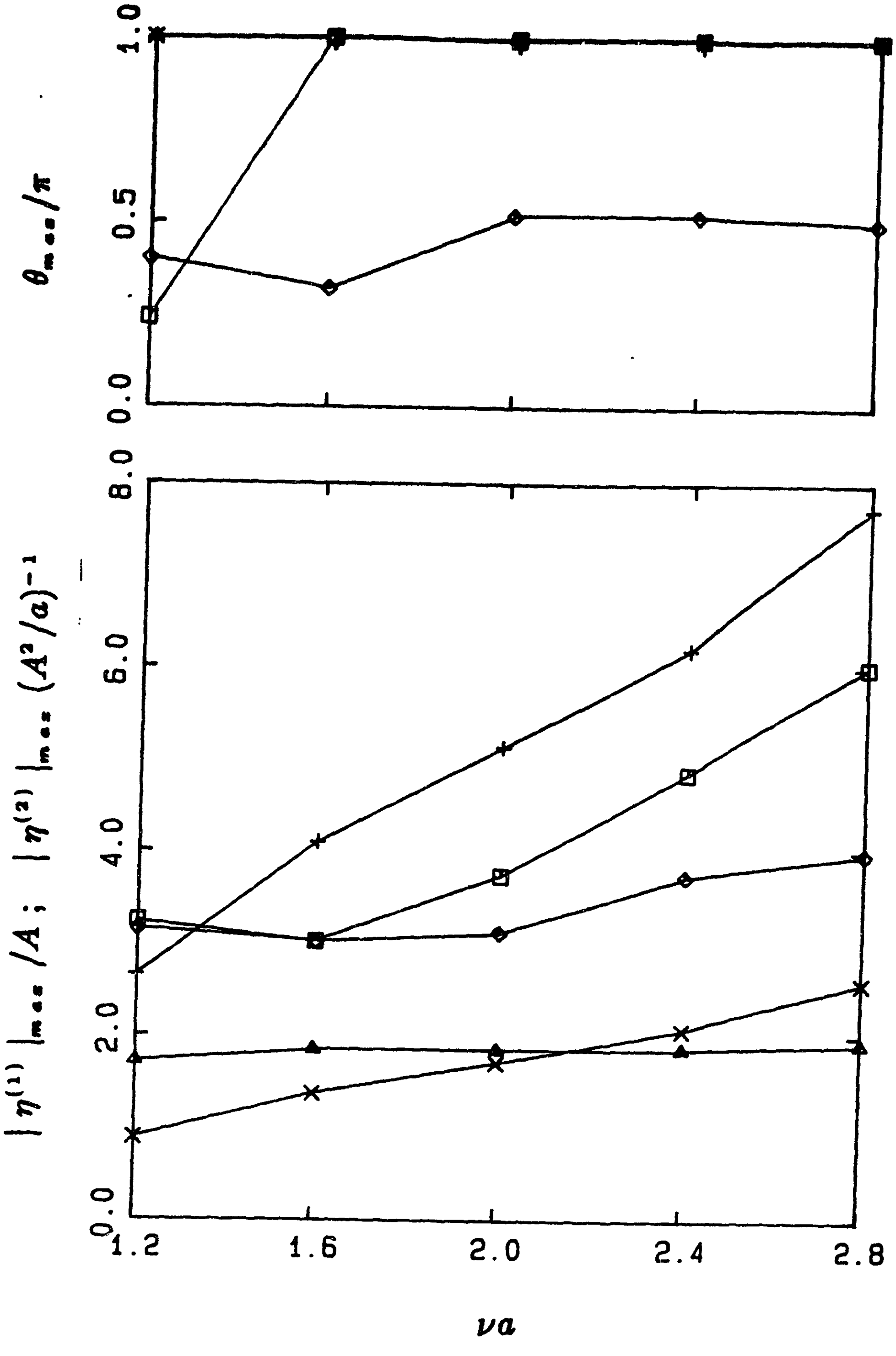

Figure 8. Maximum amplitudes (over θ) and the positions of the maxima (θ_{max}) of the linear and components of second-order wave run-up on a uniform vertical cylinder (h=a) as a function of incident frequency, νa. The symbols are for: $|\eta^{(1)}|$ (Δ); $\bar{\eta}^{(2)}$ (X); $|\eta_1^{(2)}|$ (+); $|\eta_2^{(2)}|$ (□); and $|\eta_1^{(2)}+\eta_2^{(2)}|$ (◇).

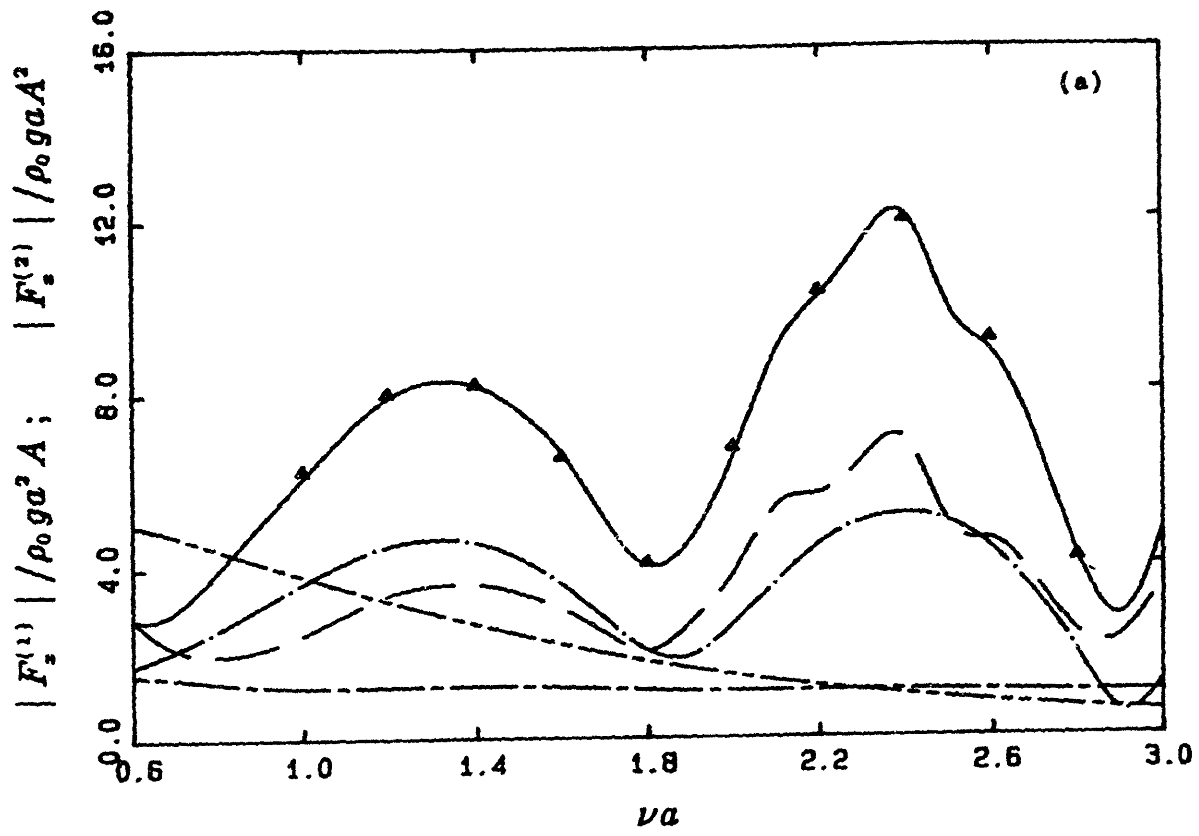

Figure 9. Amplitudes of the linear and components of second-order wave excitations on a truncated vertical cone (h=a, toe angle 60°) as a function of incident frequency, νa. The curves are for results computed from pressure integration for: $|F^{(1)}|$ (—— – – ——); $\bar{F}^{(2)}$ (—— – ——); $|F_1^{(2)}|$ (—— • ——); $|F_2^{(2)}|$ (————); and $|F_1^{(2)}+F_2^{(2)}|$ (— — —). The symbols (Δ) denote results calculated from (3.14). (a) Horizontal force, F_x; (b) vertical force, F_z; and (c) pitch moment with respect to the bottom, M_y.

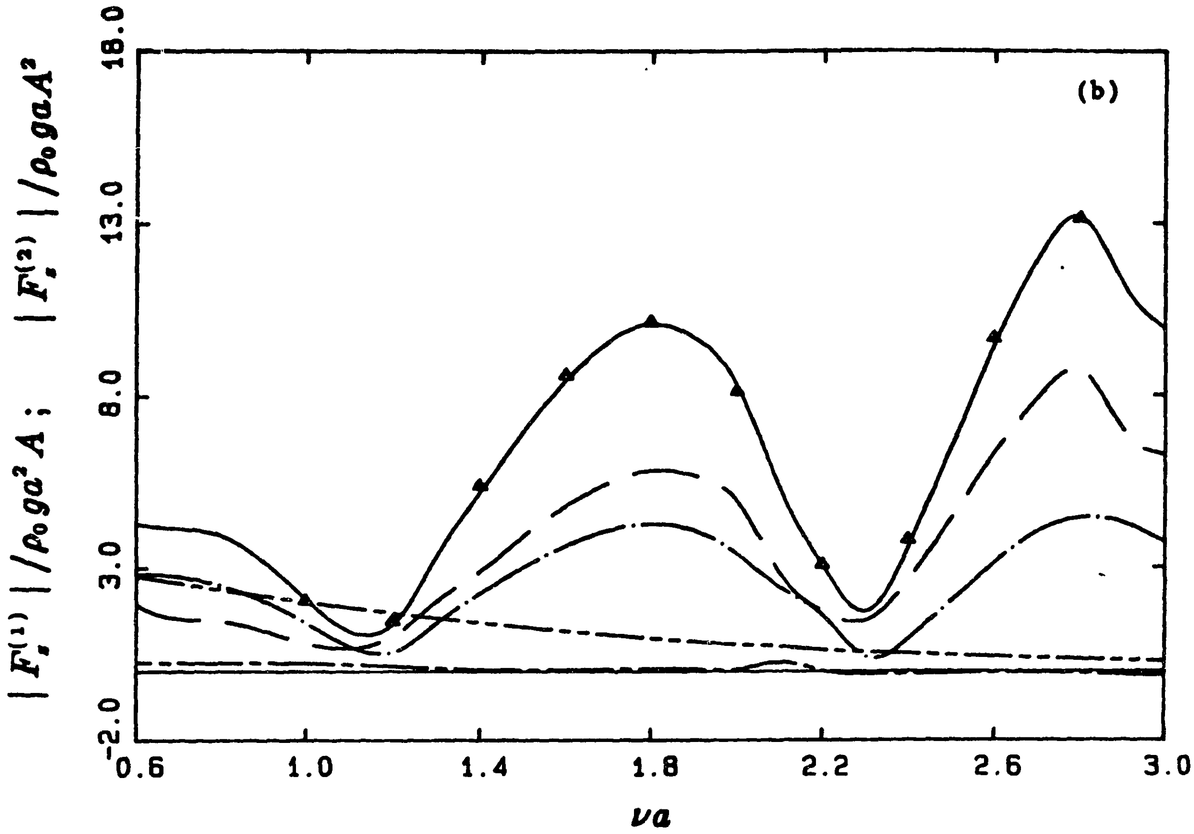

Figure 9. Amplitudes of the linear and components of second-order wave excitations on a truncated vertical cone (h=a, toe angle 60°) as a function of incident frequency, νa. The curves are for results computed from pressure integration for: $|F^{(1)}|$ (—— – – ——); $\bar{F}^{(2)}$ (—— - ——); $|F_1^{(2)}|$ (—— • ——); $|F_2^{(2)}|$ (————); and $|F_1^{(2)}+F_2^{(2)}|$ (— — —). The symbols (Δ) denote results calculated from (3.14). (a) Horizontal force, F_x; (b) vertical force, F_z; and (c) pitch moment with respect to the bottom, M_y.

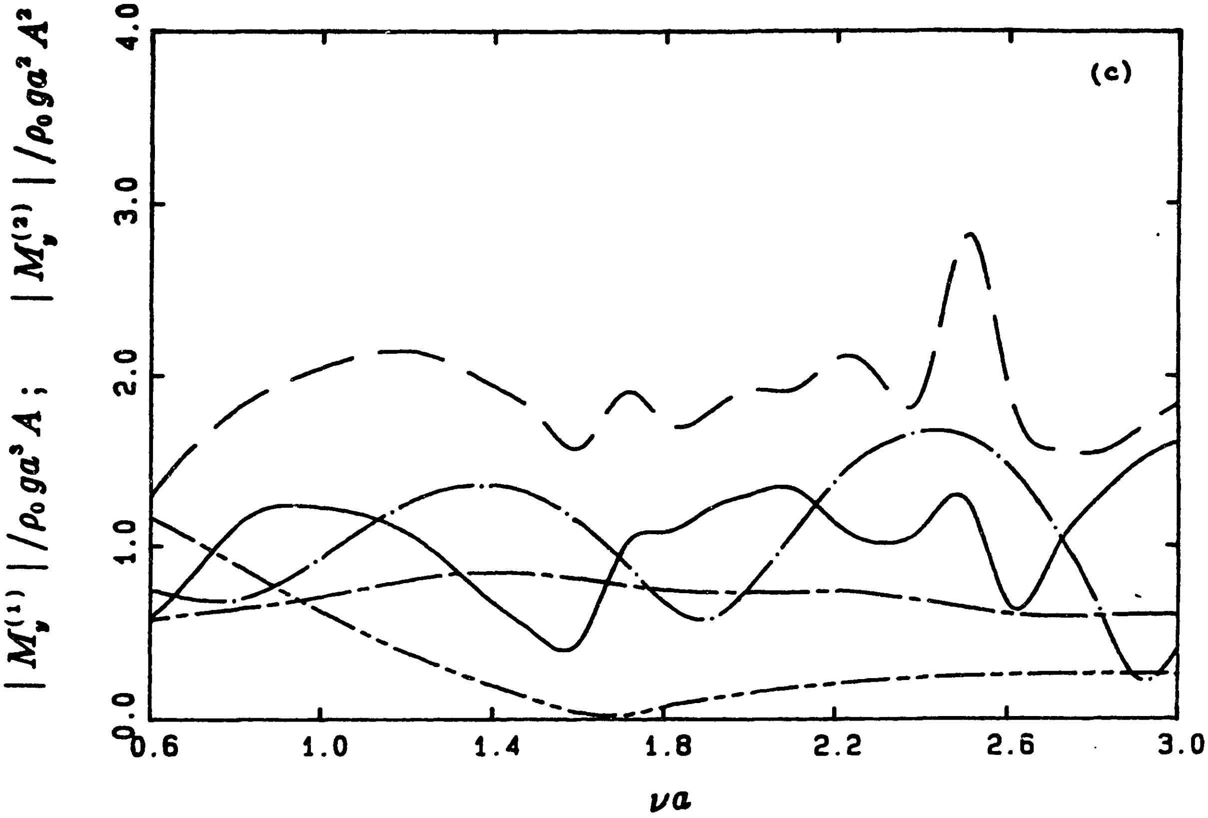

Figure 9. Amplitudes of the linear and components of second-order wave excitations on a truncated vertical cone (h=a, toe angle 60°) as a function of incident frequency, νa. The curves are for results computed from pressure integration for: $|F^{(1)}|$ (—— – – – ——); $\bar{F}^{(2)}$ (—— – ——); $|F_1^{(2)}|$ (—— • ——); $|F_2^{(2)}|$ (————); and $|F_1^{(2)}+F_2^{(2)}|$ (— — —). The symbols (Δ) denote results calculated from (3.14). (a) Horizontal force, F_x; (b) vertical force, F_z; and (c) pitch moment with respect to the bottom, M_y.

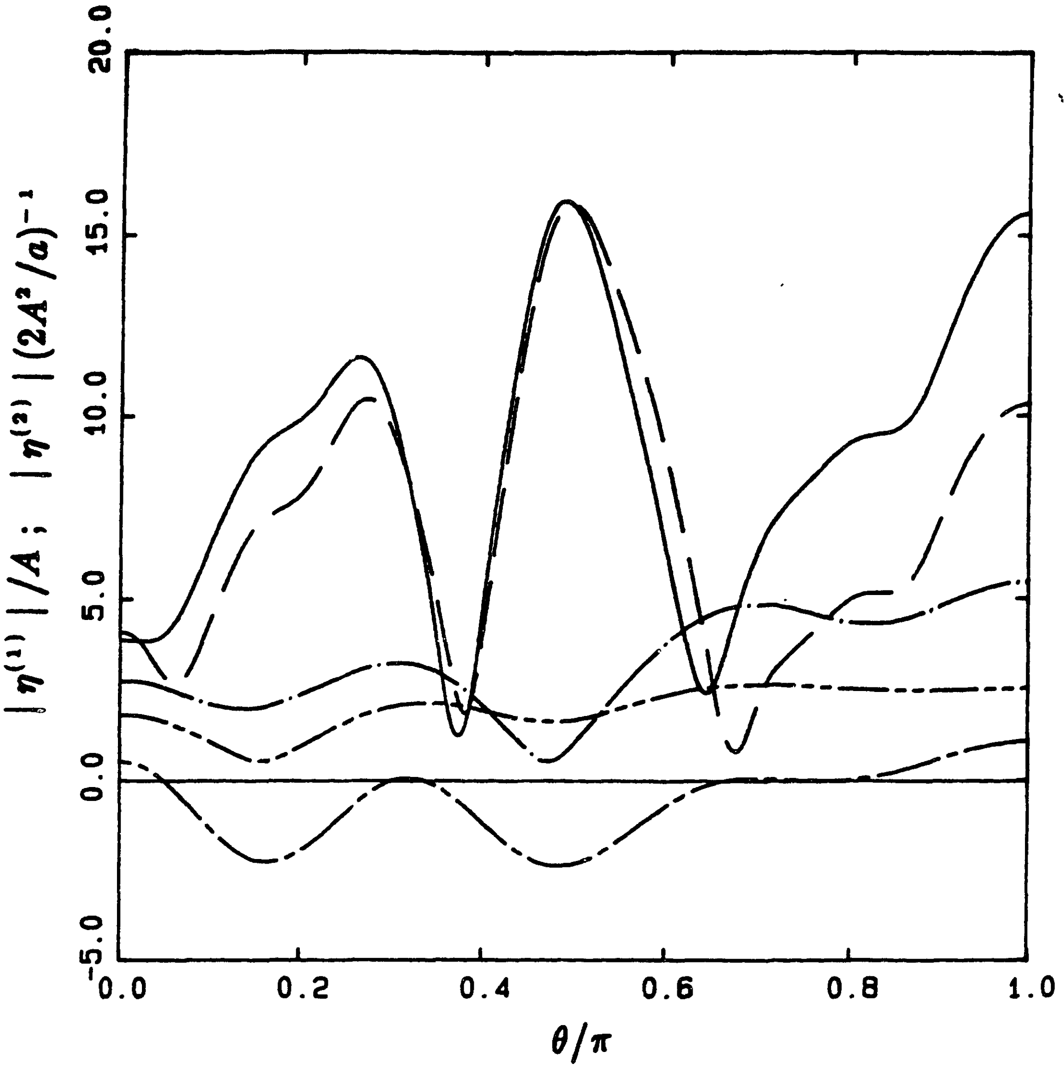

Figure 10. Amplitudes of the linear and components of second-order free surface elevations (run-up) on a truncated vertical cone (h=a, toe angle 60°, νa=2) as a function of the azimuthal angle, θ. The curves are for computed values for: $|\eta^{(1)}|$ (—— – – ——); $\bar{\eta}^{(2)}$ (—— – ——); $|\eta_1^{(2)}|$ (—— • ——); $|\eta_2^{(2)}|$ (————); and $|\eta_1^{(2)}+\eta_2^{(2)}|$ (— — —). Note that a different scale is used for plotting second-order amplitudes.

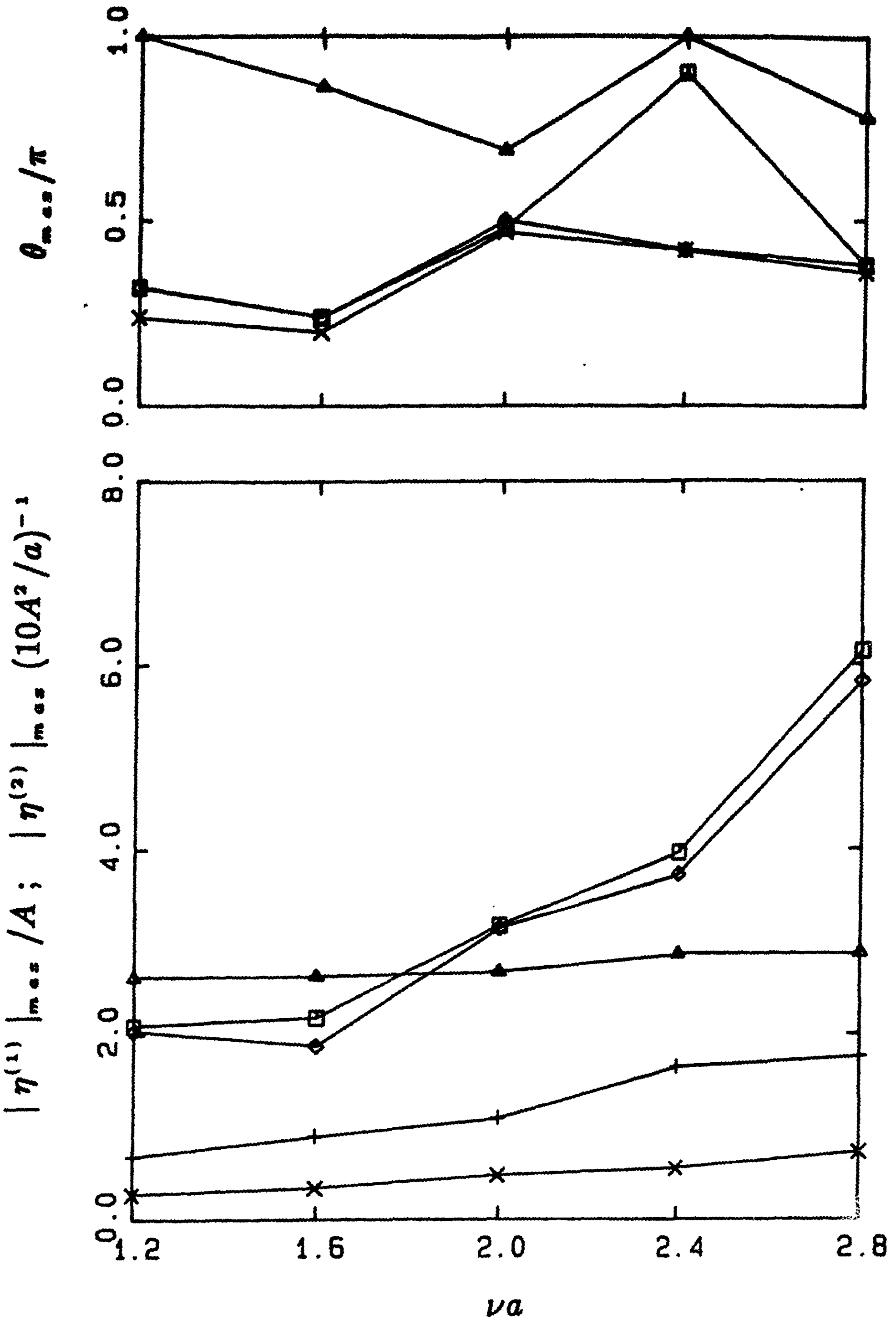

Figure 11. Maximum amplitudes (over θ) and the positions of the maxima (θ_{max}) of the linear and components of second-order wave run-up on a truncated vertical cone (h=a, toe angle 60°) as a function of incident frequency, νa. The symbols are for: $|\eta^{(1)}|$ (Δ); $\bar{\eta}^{(2)}$ (×); $|\eta_1^{(2)}|$ (+); $|\eta_2^{(2)}|$ (□); and $|\eta_1^{(2)}+\eta_2^{(2)}|$ (◇). Note that a different scale is used for plotting second-order amplitudes.

CHAPTER II

THE COMPLETE SECOND-ORDER DIFFRACTION AND RADIATION SOLUTIONS FOR AN AXISYMMETRIC BODY IN BICHROMATIC INCIDENT WAVES.

1. INTRODUCTION

Many compliant offshore platforms are designed so that their natural periods are substantially below or above that of significant ocean wave energy. As a result, second-order sum- (springing) and differrence-frequency (slowly-varying) wave excitations and the associated resonant responses are important design considerations. Theoretical developments and numerical results for the complete sum- and difference-frequency wave excitations and/or body responses in the presence of bichromatic waves are, however, still scarce. The major difficulty for a complete solution is the presence of complicated body boundary terms for floating bodies and the slowly-convergent free-surface integrals. As a result, a number of approximation methods for slowly-varying drift forces (Newman, 1974; Pinkster,1980; Standing & Dacunha, 1982; Marthinsen, 1983) and springing excitations (De Boom et al, 1983; Herfjord & Nielsen, 1986; Petrauskas & Liu, 1987) have been proposed and are widely used in practical applications. In the absence of the complete solutions, however, the validity and relative merit of each method have so far not been established.

In this chapter, the complete second-order diffraction method for axisymmetric bodies in a regular wave train, which is detailed in Chapter I, is extended to sum- and difference-frequency diffraction and radiation problems in bichromatic incident waves. A Green's theorem integral equation is obtained and solved for the second-order sum- and difference-frequency potentials, respectively. For illustration, the complete sum- and difference-frequency wave excitation QTF's as well as local quantity QTF's are calculated for bottom-mounted vertical cylinders in different water depths and for respectively fixed and freely-floating hemispheres. The validity and accuracy of the method are demonstrated by extensive results for convergence with respect to body discretizations, Fourier modes, and free-surface integral evaluations, as well as by comparison to semi-analytic solutions for the bottom-mounted vertical cylinder derived in Appendix C. Salient features of the second-order problem and especially the behaviors of local effects due to the second-order potential are discussed in §5. Based on this, the validity of various existing approximation methods is thoroughly examined. The deficiencies of these approximations are particularly severe for large draft bodies.

Given the complete excitation and response QTF's for bichromatic incident waves, the statistics of second-order excitations and responses in general Gaussian seas can be readily obtained. This will be considered in Part two.

2. FORMULATION OF THE PROBLEM

We consider the linear and second-order wave body interaction problems for fixed or freely-floating three-dimensional bodies in plane progressive bichromatic incident waves from $x=-\infty$. Cartesian coordinates with the x-y plane in the quiescent free surface and z positive upward are chosen. Assuming potential flow and weak nonlinearities, we write the total velocity potential as a purturbation series with respect to small wave slope ϵ:

$$\Phi = \epsilon\,\Phi^{(1)} + \epsilon^2\Phi^{(2)} + \cdots \tag{2.1a}$$

For each order, the related boundary value problem is linear and we can decompose Φ into the incident(Φ_I), diffraction(Φ_D), and radiation(Φ_R) potentials:

$$\Phi = \epsilon\,(\Phi_I^{(1)} + \Phi_D^{(1)} + \Phi_R^{(1)}) + \epsilon^2\,(\Phi_I^{(2)} + \Phi_D^{(2)} + \Phi_R^{(2)}) + \cdots \tag{2.1b}$$

At first order, the diffraction potential represents the scattered waves due to the presence of the fixed body, and the radiation potential the radiated waves due to first-order body motions. At second order, $\Phi_D^{(2)}$ represents the second-order diffraction potential for the body undergoing first-order motions, while $\Phi_R^{(2)}$ is the second-order radiation potential due to second-order motions in the absence of ambient waves.

In the presence of two frequency waves, we can write the first-order velocity potential as

$$\Phi^{(1)}(x,t) = \mathrm{Re}\,\{\sum_{j=1}^{2} \phi_j^{(1)}(x) \quad e^{-i\omega_j t}\} \tag{2.2}$$

and the second-order potential as a superposition of sum- and difference-frequency terms:

$$\Phi^{(2)}(x,t) = \mathrm{Re} \sum_{j=1}^{2} \sum_{l=1}^{2} \{ \phi^{-}(x)\, e^{-i\omega^{-}t} + \phi^{+}(x)\, e^{-i\omega^{+}t} \} \tag{2.3}$$

where $\omega^{-}=\omega_j-\omega_l$ and $\omega^{+}=\omega_j+\omega_l$. The difference-frequency potential, ϕ^{-} in (2.3), is related to the slowly-varying wave excitations and body responses, while the sum-frequency potential, ϕ^{+}, to the springing wave exitations and superharmonic responses. This sum- and difference-frequency potentials can be solved independently after formulating each boundary value problem seperately.

The first-order bichromatic incident wave potential with amplitude A and for water depth h is given by:

$$\phi_I^{(1)} = \sum_{j=1}^{2} \frac{-igA_j}{\omega_j} \frac{\cosh k_j(z+h)}{\cosh k_j h}\, e^{ik_j x} \tag{2.4}$$

where the frequency ω_j and wavenumber k_j satisfy dispersion relation; $\omega_j^2=k_j g \tanh k_j h$, g being the gravitational accelaration. The second-order bichromatic incident wave potential, $\Phi_I^{(2)}$, satisfies the Laplace equation in the fluid region, zero vertical velocity on the sea bottom (z=-h), and inhomogeneous free-surface condition given by:

$$\left(\frac{\partial}{\partial t^2} + g \frac{\partial}{\partial z} \right) \Phi_I^{(2)} = Q_{II} \equiv \frac{1}{g} \frac{\partial \Phi_I^{(1)}}{\partial t} \frac{\partial}{\partial z}\left(\frac{\partial^2 \Phi_I^{(1)}}{\partial t^2} + g \frac{\partial \Phi_I^{(1)}}{\partial z} \right) - \frac{\partial}{\partial t} (\nabla \Phi_I^{(1)})^2 \Big|_{z=0} \tag{2.5}$$

where (2.5) can be obtained from the Taylor's expansion of the exact free-surface condition about z=0. Upon substituting (2.2~4) into (2.5) and solving for $\Phi_I^{(2)}$, we obtain sum- and difference-frequency second-order incident wave potentials as follows:

$$\phi_I^+ = \left(\frac{\gamma_{jl}^+ + \gamma_{lj}^+}{2}\right) \frac{\cosh k^+(z+h)}{\cosh k^+h}\, e^{ik^+x} \tag{2.6a}$$

where $$\gamma_{jl}^+ = \frac{-igA_jA_l}{2\omega_j}\; \frac{k_j^2(1-\tanh^2 k_jh) + 2k_jk_l(1-\tanh k_jh \tanh k_lh)}{\nu^+ - k^+\tanh k^+h} \tag{2.6b}$$

and

$$\phi_I^- = \left(\frac{\gamma_{jl}^- + \gamma_{lj}^{-*}}{2}\right) \frac{\cosh k^-(z+h)}{\cosh k^-h}\, e^{ik^-x} \tag{2.7a}$$

where $$\gamma_{jl}^- = \frac{-igA_jA_l^*}{2\omega_j}\; \frac{k_j^2(1-\tanh^2 k_jh) - 2k_jk_l(1+\tanh k_jh \tanh k_lh)}{\nu^- - k^-\tanh k^-h} \tag{2.7b}$$

In above equations, * represents complex conjugate, and $\nu\pm$ and $k\pm$ are defined respectively by:

$$\nu^{\pm} = \frac{\omega^{\pm\,2}}{g} \qquad \text{and} \qquad k^{\pm} = k_j \pm k_l \tag{2.8}$$

When $\omega_j \to \omega_l$, ϕ_I^- becomes time independent and its contribution to force or surface elevation is at most $O(\epsilon^3)$, while ϕ_I^+ in (2.6) is reduced to well known second-order Stokes wave for a regular wave train:

$$\phi_I^+ = \frac{-3i\omega A^2}{8}\, \frac{\cosh 2k(z+h)}{\sinh^4 kh}\, e^{i2kx} \quad . \tag{2.9}$$

One can easily check from (2.6) that ϕ_I^+ vanishes for $k_jh \gg 1$, $k_lh \gg 1$. In this limit, ϕ_I^- still contributes and reduces to the form for $(k_j-k_l)h$ $=O(1)$:

$$\phi_I^- \sim \frac{iA_jA_l^* (\omega_l-\omega_j)\,\omega_j\omega_l}{(\omega_j-\omega_l)^2-(\omega_j^2-\omega_l^2)\tanh k^-h}\;\frac{\cosh k^-(z+h)}{\cosh k^-h}\;e^{ik^-x} \tag{2.10a}$$

and for $(k_j-k_l)h \gg 1$:

$$\phi_I^- \approx iA_jA_l^*\;\frac{(\omega_l-\omega_j)\,\omega_j\omega_l}{(\omega_j-\omega_l)^2-|\omega_j^2-\omega_l^2|}\;e^{\nu^-z+i\nu^-x} \tag{2.10b}$$

We next consider the interaction of the linear and second-order bichromatic incident waves with three-dimensional freely-floating bodies. Defining a body disturbance potential as a sum of the linear diffraction and radiation potentials; $\phi_B^{(1)}=\phi_D^{(1)}+\phi_R^{(1)}$, $\phi_B^{(1)}$ satisfies the Laplace equation in the fluid region, zero normal velocity on the bottom ($z=-h$), and following boundary conditions:

$$\left(-\omega^2+g\frac{\partial}{\partial z}\right)\phi_B^{(1)}=0 \qquad \text{on the free-surface } S_F \tag{2.11a}$$

$$\frac{\partial\phi_B^{(1)}}{\partial n}=-\frac{\partial\phi_I^{(1)}}{\partial n}-i\omega\,\mathbf{n}\cdot(\xi^{(1)}+\alpha^{(1)}\times \mathbf{r}) \qquad \text{on the body } S_B \tag{2.11b}$$

$$\lim_{\rho\to\infty}\sqrt{\rho}\left(\frac{\partial}{\partial\rho}-ik\right)\phi_B^{(1)}\to 0 \qquad \text{at infinity } S_\infty \tag{2.11c}$$

where r and ρ represent the position vector on the body surface and radial distance from the origin, respectively, and $n=(n_1,n_2,n_3)$ outward unit normal vector. The first righthand side term of the body boundary condition in (2.11b) is for the linear diffraction potential, $\phi_D^{(1)}$, and the second term for the linear radiation potential, $\phi_R^{(1)}$. The translational (Ξ) and rotational(α) first-order motions in the presence of two frequency waves are given by:

$$\Xi^{(1)}(x,t) = \mathrm{Re}\sum_{j=1}^{2}[\ \xi_j^{(1)}(x)\ e^{-i\omega_j t}\ ]\ ,\quad \xi_j^{(1)}=(\xi_{j1}^{(1)},\xi_{j2}^{(1)},\xi_{j3}^{(1)}) \tag{2.12a}$$

$$\alpha^{(1)}(x,t) = \mathrm{Re}\sum_{j=1}^{2}[\ \alpha_j^{(1)}(x)\ e^{-i\omega_j t}\ ]\ ,\quad \alpha_j^{(1)}=(\alpha_{j1}^{(1)},\alpha_{j2}^{(1)},\alpha_{j3}^{(1)}) \tag{2.12b}$$

where the subscript 1,2, and 3 in (2.12) represent the translational and rotational modes with respect to x, y, and z axis respectively. Solving (2.11) for $\phi_D{}^{(1)}$ and $\phi_R{}^{(1)}$ seperately, we obtain first-order wave exciting forces (or moments) and hydrodynamic coefficients (added mass & hydrodynamic damping) for six degree-of-freedom linear motions. For example, the added mass($\lambda_{kk'}$) and hydrodynamic damping($d_{kk'}$) in k-th direction due to k'-th mode can be obtained from the radiation potential, $\Psi_R{}^{(1)}$, for the unit velocity:

$$\lambda_{kk'}+\frac{i}{\omega}\,d_{kk'}=\rho_0\iint_{S_B}\Psi_{Rk'}^{(1)}\ n_k\ dS \qquad (\ k,k'=1\sim 6\ ) \tag{2.13a}$$

where

$$\phi_R^{(1)}= -i\omega\sum_{k=1}^{3}(\ \xi_k^{(1)}\Psi_{Rk}^{(1)}+\ \alpha_k^{(1)}\Psi_{R(k+3)}^{(1)}) \quad \text{and} \quad r\times n=(n_4,n_5,n_6) \tag{2.13b}$$

and the linear wave exciting force for k-th mode from:

$$F_{exk}^{(1)}= \mathrm{Re}\ \{\ \rho_0 i\omega\iint_{S_B}(\ \phi_I^{(1)}+\ \phi_D^{(1)})\ n_k\ dS\ \} \tag{2.14}$$

where ρ_0 is the fluid density.

After solving the first-order potentials and motions, we can calculate boundary forcing terms of the second-order diffraction problem, which are given in terms of quadratic products of linear solutions. The inhomogeneous free-surface and body-surface conditions for the second-order potential, $\Phi^{(2)}$, can be otained by using Taylor's expansion of the associated exact boundary conditions about respective quiescent positions. This procedure is detailed in Ogilvie(1983), and will not be elaborated here. We define the second-order diffraction potential, $\Phi_D^{(2)}$, as the solution which satisfies the following inhomogeneous free-surface and body-surface boundary conditions, where the body is undergoing linear motions but free from second-order motions:

$$\left(\frac{\partial}{\partial t^2}{}_2 + g \frac{\partial}{\partial z} \right) \Phi_D^{(2)} = Q \equiv \frac{1}{g} \left. \frac{\partial \Phi^{(1)}}{\partial t} \frac{\partial}{\partial z} \left(\frac{\partial^2 \Phi^{(1)}}{\partial t^2} + g \frac{\partial \Phi^{(1)}}{\partial z} \right) - \frac{\partial}{\partial t} (\nabla \Phi^{(1)})^2 \right|_{z=0} - Q_{II} \tag{2.15}$$

$$\frac{\partial \Phi_D^{(2)}}{\partial n} + \frac{\partial \Phi_I^{(2)}}{\partial n} = B \equiv$$

$$n \bullet \dot{H} r - n \bullet [(\Xi^{(1)} + \alpha^{(1)} x \ r) \bullet \nabla] \nabla \Phi^{(1)} + (\alpha^{(1)} x \ n) \bullet [(\dot{\Xi}^{(1)} + \dot{\alpha}^{(1)} x \ r) - \nabla \Phi^{(1)}] \tag{2.16}$$

where (upper •) denotes the derivative with respect to the time. In (2.16), H matrix, which is second order, is composed of the quadratic products of the first-order rotational motions:

$$H = -\frac{1}{2} \begin{bmatrix} (\alpha_2^2 + \alpha_3^2) & 0 & 0 \\ -2\alpha_1\alpha_2 & (\alpha_1^2 + \alpha_3^2) & 0 \\ -2\alpha_1\alpha_3 & -2\alpha_2\alpha_3 & (\alpha_1^2 + \alpha_2^2) \end{bmatrix} \tag{2.17}$$

As pointed out by Ogilvie (1983), H matrix depends on the sequence of rotation, and the order roll-pitch-yaw is used here. In the absence of linear rotational motions, the body forcing term B in (2.16) can be simplified as

$$B(x,t) = -\,n\cdot(\Xi^{(1)}\cdot\nabla)\nabla\phi^{(1)} \qquad (2.18)$$

Being quadratic product of the linear solutions, the free-surface and body-surface forcing terms, Q and B in (2.15,16), have the forms:

$$\begin{matrix} Q(x,t) \\ B(x,t) \end{matrix} = \mathrm{Re}\sum_{j=1}^{2}\sum_{l=1}^{2}\left[\begin{matrix} Q^{+}(x) \\ B^{+}(x) \end{matrix}\, e^{-i\omega^{+}t} + \begin{matrix} Q^{-}(x) \\ B^{-}(x) \end{matrix}\, e^{-i\omega^{-}t} \right] \qquad (2.19)$$

Then, each of the sum- and difference-frequency second-order diffraction potentials satisfies the following boundary value problem respectively, and can be solved independently:

$$\nabla^2\phi_D^{\pm} = 0 \qquad \text{in the fluid} \qquad (2.20a)$$

$$\left(-\omega^{\pm 2} + g\frac{\partial}{\partial z}\right)\phi_D^{\pm} = Q^{\pm} \qquad \text{at } z=0 \qquad (2.20b)$$

$$\partial\phi_D^{\pm} / \partial z = 0 \qquad \text{at } z=-h \qquad (2.20c)$$

$$\frac{\partial\phi_D^{\pm}}{\partial n} = -\frac{\partial\phi_I^{\pm}}{\partial n} + B^{\pm} \qquad \text{at } S_B \qquad (2.20d)$$

$$\text{condition at infinity} \qquad \text{as } \rho\to\infty \qquad (2.20e)$$

In (2.20b), the sum- and difference-frequency free-surface forcing terms can be written in symmetric forms as follows:

$$Q^{+} = (\,q_{jl}^{+} + q_{lj}^{+})\,/\,2 \qquad \text{and} \qquad Q^{-} = (\,q_{jl}^{-} + q_{lj}^{-*}\,)\,/\,2 \qquad (2.21)$$

$$q^{+}_{jl} = \frac{-i\omega_l}{2g}\,\phi^{(1)}_{l}\left(-\omega_j^2 \frac{\partial\phi^{(1)}_{j}}{\partial z} + g\,\frac{\partial^2\phi^{(1)}_{j}}{\partial z^2} \right) + i\omega_l \nabla\phi^{(1)}_{j}\cdot\nabla\phi^{(1)}_{l} \quad - q^{+}_{IIjl} \qquad (2.22)$$

$$q^{-}_{jl} = \frac{i\omega_l}{2g}\,\phi^{(1)*}_{l}\left(-\omega_j^2 \frac{\partial\phi^{(1)}_{j}}{\partial z} + g\,\frac{\partial^2\phi^{(1)}_{j}}{\partial z^2} \right) - i\omega_l \nabla\phi^{(1)}_{j}\cdot\nabla\phi^{(1)*}_{l} - q^{-}_{IIjl} \qquad (2.23)$$

The free-surface forcing, $Q_{\pm}$, contains all kinds of possible interaction of incident, diffracted, and radiated waves, which can be symbolized as (IR,ID,RD,RR,DD). (IR,ID) and (RD,RR,DD) decay at rates of $1/\sqrt{\rho}$ and $1/\rho$, respectively as $\rho\to\infty$. For the second-order scattering problem by fixed bodies, terms involving R vanish, while for the forced oscillation problem, all interaction terms except RR are zero. The sum- and difference-frequency body-surface forcing terms can be obtained in a similar way, and equation (2.18), for example, has the form:

$$B^{+} = (b^{+}_{jl} + b^{+}_{lj}) \;/\; 2 \qquad \text{and} \qquad B^{-} = (b^{-}_{jl} + b^{-*}_{lj}) \;/\; 2 \qquad (2.24)$$

$$b^{+}_{jl} = -\frac{1}{2}\, n\cdot(\xi^{(1)}_{l}\cdot \nabla)\nabla\phi^{(1)}_{j} \qquad (2.25)$$

$$b^{-}_{jl} = -\frac{1}{2}\, n\cdot(\xi^{(1)*}_{l}\cdot \nabla)\nabla\phi^{(1)}_{j} \qquad (2.26)$$

With these forcing terms, we can solve boundary value problem (2.20) for $\phi_{D\pm}$, and resulting sum- and difference-frequency second-order wave excitations.

Finally, the sum- and difference-frequency second-order radiation potentials associated with corresponding second-order motions satisfy the Laplace equation, bottom condition, and following boundary conditions:

$$\left(-\omega^{\pm 2} + g\frac{\partial}{\partial z} \right) \phi_R^{\pm} = 0 \qquad \text{at } z=0 \tag{2.27a}$$

$$\frac{\partial \phi_R^{\pm}}{\partial n} = -i\omega^{\pm}\, n \cdot (\xi^{\pm} + \alpha^{\pm} \times r) \qquad \text{at } S_B \tag{2.27b}$$

$$\lim_{\rho \to \infty} \sqrt{\rho} \left(\frac{\partial}{\partial \rho} - ik_2^{\pm} \right) \phi_R^{\pm} \to 0 \qquad \text{at } S_\infty \tag{2.27c}$$

where $k_2^{\pm}$ are the wavenumbers associated with sum and difference frequencies $\omega^{\pm}$. The total second-order motions, in (2.27b), can be written in the form:

$$\begin{matrix} \Xi^{(2)}(x,t) \\ \alpha^{(2)}(x,t) \end{matrix} = \mathrm{Re} \sum_{j=1}^{2} \sum_{l=1}^{2} \left\{ \begin{matrix} \xi^{+}(x) \\ \alpha^{+}(x) \end{matrix} e^{-i\omega^{+}t} + \begin{matrix} \xi^{-}(x) \\ \alpha^{-}(x) \end{matrix} e^{-i\omega^{-}t} \right\} \tag{2.28}$$

The boundary value problem of the second-order radiation potential, $\phi_R^{\pm}$, associated with second-order motions is identical to that of the linear radiation potential except for the shift of the pertinent frequency. The added mass and hydrodynamic damping for second-order motions can be obtained exactly the same way as the linear problem.

So far, we set up the entire linear and second-order boundary value problems clearly except for the radiation condition of the second-order diffraction potential in (2.20e). The radiation condition of the second-order diffraction potential for monochromatic waves was first obtained by Molin (1979), and is extended here to bichromatic waves. Considering the boundary value problem (2.20) is still linear, we decompose the second-order diffraction potential, $\phi_D^{\pm}$, into a homogeneous, $\phi_H^{\pm}$, and particular solution, $\phi_P^{\pm}$, which satisfy homogeneous and inhomogeneous free-surface conditions respectively, and inhomogeneous body-boundary condition jointly. The homogeneous second-order diffraction potential, $\phi_{H\pm}$, has the conventional asymptotic behavior as $\rho \to \infty$:

$$\phi_H^{\pm} \sim \frac{e^{ik_2^{\pm}\rho}}{\sqrt{\rho}} + O(\rho^{-3/2}) \qquad (2.29)$$

The asymptotic form of the particular second-order diffraction potential, $\phi_{P\pm}$, can be obtained from that of the free-surface forcing pressure, which is composed of quadratic products of the linear body disturbance potentials, Q_{BB}, and cross products of the linear incident and body disturbance potentials, Q_{IB}. Using asymptotic forms of the linear potentials,

$$\phi_{B\,j}^{(1)} \sim e^{ik_j\rho} / \sqrt{\rho} + O(\rho^{-3/2}) \qquad (2.30a)$$

$$\phi_{I\,j}^{(1)} \sim e^{ik_j\rho\cos\theta} \qquad (2.30b)$$

we can easily see that Q_{BB} decays as fast as $O(1/\rho)$, while Q_{IB} at a rate of $O(1/\sqrt{\rho})$, and Q_{IB} has the following asymptotic form:

$$Q_{IB}^{\pm} \sim e^{i\rho(k_j \pm k_1\cos\theta)} / \sqrt{\rho} + O(1/\rho) \qquad (2.31)$$

For the particular second-order diffraction potential to satisfy the inhomogeneous free-surface condition up to the leading order, $O(1/\sqrt{\rho})$, as $\rho \to \infty$, we write:

$$\phi_P^{\pm} \sim E_{j1}^{\pm}(\theta,z)\, e^{i\rho(k_j \pm k_1\cos\theta)} / \sqrt{\rho} + O(1/\rho) \qquad (2.32)$$

Furthermore, this asymptotic form should satisfy the bottom condition and leading order Laplace equation at infinity. Then, we can determine $E_{\pm}$ in the form:

$$E^{+}_{\bar{j}l}(\theta,z) = \Theta^{+}_{\bar{j}l}(\theta) \cosh \{(k_j^2 + k_l^2 \pm 2k_j k_l \cos\theta)^{1/2}(z+h)\} \qquad (2.33)$$

Finally, $\Theta(\theta)$ can be obtained from the free-surface condition. This condition for a infinite depth was also derived by Wang (1987). When j=l, the sum-frequency part reduces to the same asymptotic form given in Molin (1979).

3. SOLUTIONS FOR THE SUM- AND DIFFERENCE-FREQUENCY SECOND-ORDER POTENTIALS.

In this section, we solve the linear and second-order boundary value problems formulated in Section 2 by the boundary integral equation method/ ring source distribution method. Let's first consider the boundary value problem (2.20) for the second-order diffraction potential, $\phi_{D}{}^{+}_{-}$, and introduce the sum- and difference-frequency linear pulsating source potentials, $G_{\pm}$, associated with frequencies ω^{+}_{-}. Applying Green's theorem for $\phi_{D}{}^{+}_{-}$ and G^{+}_{-}, we obtain Fredholm integral equation of the second kind for $\phi_{D}{}^{+}_{-}$:

$$2\pi\, \phi^{+}_{\bar{D}} + \iint_{S_B} \phi^{+}_{\bar{D}} \frac{\partial G^{\pm}}{\partial n}\, dS = \iint_{S_B} G^{\pm} \left\{ B^{\pm} - \frac{\partial \phi^{+}_{\bar{I}}}{\partial n} \right\} dS + \frac{1}{g} \iint_{S_F} Q^{\pm}\, G^{\pm}\, dS \qquad (3.1)$$

where the source strengths on the body- and free-surface in the right hand side are known a priori and given by the body- and free-surface forcing terms, respectively. In deriving (3.1), the vanishment of the far field integral ("weak radiation condition" for the sum- and difference-frequency second-order diffraction potentials) can be proved by the method of stationary phase integral using asymptotic forms for $\phi_{D\pm}^{+}$ and G_{-}^{+}.

In solving the integral equation (3.1) numerically, as was already adressed in Chapter I, the most difficult task is the evaluation of the right hand side integrals, particularly the slowly convergent free-surface integral. In difference-frequency problems, the composite wavenumber of free-surface integrands for $\rho >> 1$ is $k_j - k_1 \cos\theta + k_2^-$, hence associated wavelength is in general much longer than that of sum-frequency problem whose characteristic wavenumber is $k_j + k_1 \cos\theta + k_2^+$. Despite small amplitudes, the resulting relative convergence of difference-frequency free-surface integrals with increasing ρ are extremely slow especially when two frequencies are close. In sum-frequency cases, the decaying rate of the free-surface integral is faster but the integrand becomes more highly oscillatory with larger amplitudes compared to the difference-frequency problem. Therefore, any simple truncation (e.g. Loken, 1986) of these integrals are computationally prohibitive. Furthermore, the moving average technique (e.g. Molin & Marion, 1986) is expected to be ineffective for bichromatic waves because of the non-uniform oscillaion of the integrands. An elaborate method involving analytic integrations in entire local-wave-free domain was developed in Chapter I for monochromatic waves, and extended here to bichromatic waves.

If the body has a vertical axis of symmetry, we integrate (3.1) first with respect to θ and obtain a sequence of one dimensional integral equations for each Fourier mode. For this purpose, we expand the second-order diffraction potential $\phi_{D\pm}^{+}$, free-surface and body-surface forcings Q_{-}^{+} and B_{-}^{+}, and linear pulsating Green function G_{-}^{+} by Fourier cosine series:

$$\begin{matrix} \phi_D^{+}(\rho,\theta,z) \\ Q^{\pm}(\rho,\theta) \\ B^{\pm}(\rho,\theta,z) \end{matrix} = \sum_{n=0}^{\infty} \begin{matrix} \phi_{Dn}^{+}(\rho,z) \\ Q_n^{\pm}(\rho) \\ B_n^{\pm}(\rho,z) \end{matrix} \cos n\theta \tag{3.2a}$$

$$\text{and} \quad G^{\pm}(\rho,\theta,z;\rho',\theta',z'), = \sum_{n=0}^{\infty} \frac{\epsilon_n}{2\pi} G_n^{\pm}(\rho,z;\rho',z') \cos n(\theta-\theta') \tag{3.2b}$$

where $\epsilon_n=1$ for $n=0$ and 2 for $n\geq 1$. Substituting (3.2) into (3.1) and using orthogonality of the trigonometric functions in θ integration, we obtain a one dimensional integral equations for each n:

$$2\pi \phi_{Dn}^{+} + \int_{\partial_B} \rho \, dl \, \phi_{Dn}^{+} \frac{\partial G_n^{\pm}}{\partial n} = \int_{\partial_B} \rho \, dl \left(B_n^{\pm} - \frac{\partial \phi_{In}^{+}}{\partial n} \right) G_n^{\pm} + \frac{1}{g} \int_{\partial_F} \rho \, d\rho \, Q_n^{\pm} G_n^{\pm} \tag{3.3}$$

where the line integrals are along the traces $\partial B, \partial F$ of S_B and S_F respectively, and outward unit normal vector along ∂_B is given by $n=(n_\rho,n_z)$. The n-th mode sum-frequency free-surface forcing, Q_n^+, can be obtained by rearranging the double products of Fourier series (2.22) as follows:

$$q_{0jl}^{+} = \sum_{m=0}^{\infty} \frac{2}{\epsilon_m} \Big[\Big(\frac{\tanh^2 k_j h}{2} + \frac{k_l}{k_j} \tanh k_j h \tanh k_l h + \frac{k_l}{k_j} \frac{\epsilon_m}{2} \frac{m^2}{(k_j\rho)(k_l\rho)} \Big) \phi_m^j \phi_m^l$$
$$- \frac{1}{2} \frac{\partial^2 \phi_m^j}{\partial (k_j z)^2} \phi_m^l + \frac{k_l}{k_j} \frac{\partial \phi_m^j}{\partial (k_j \rho)} \frac{\partial \phi_m^l}{\partial (k_l \rho)} \Big] \Big|_{z=0} \tag{3.4a}$$

$$q_{njl}^{+} = \frac{-ig^2 A_j A_l k_j^2}{2\omega_j} \Big[\sum_{m=0}^{n} \Big\{ \chi_{jl} \phi_{n-m}^{j} \phi_m^l - \frac{1}{2} \frac{\partial^2 \phi_{n-m}^{j}}{\partial (k_j z)^2} \phi_m^l + \frac{k_l}{k_j} \frac{\partial \phi_{n-m}^{j}}{\partial (k_j \rho)} \frac{\partial \phi_m^l}{\partial (k_l \rho)} \Big\}$$

$$+\sum_{m=0}^{\infty}\{\hat{\chi}_{jl}(\phi_{n+m}^{j}\phi_{m}^{l}+\phi_{m}^{j}\phi_{n+m}^{l}) - \frac{1}{2}\left(\frac{\partial\ \phi_{n+m}}{\partial(k_j z)^2}\phi_m^l + \frac{\partial\ \phi_m}{\partial(k_j z)^2}\phi_{n+m}^l\right) +$$

$$\frac{k_l}{k_j}\left(\frac{\partial\phi_{n+m}^{j}}{\partial(k_j\rho)}\frac{\partial\phi_m^l}{\partial(k_l\rho)} + \frac{\partial\phi_m^j}{\partial(k_j\rho)}\frac{\partial\phi_{n+m}^{l}}{\partial(k_l\rho)}\right)\Bigg|_{z=0} \qquad (3.4b)$$

$$\text{where}\quad \begin{matrix}\chi_{jl}\\ \hat{\chi}_{jl}\end{matrix} = \frac{\tanh^2 k_j h}{2} + \frac{k_l}{k_j}\tanh k_j h\ \tanh k_l h \mp \frac{k_l}{k_j}\frac{(n \mp m)m}{(k_j\rho)(k_l\rho)} \qquad (3.5)$$

In above equations, ϕ_m^j represents the m-th Fourier mode of the total linear potential of frequency ω_j and normalized by $-igA_j/\omega_j$. The free-surface condition for ϕ has already been exploited in deriving (3.4). The n-th mode difference-frequency free-surface forcing, Q_n^-, can also be obtained similarly using (3.2) and (2.23). We also express the n-th mode sum- and difference-frequency body-surface forcings, $B_{\pm}$, in terms of single Fourier cosine series. For example, in the absence of rotational modes, the sum-frequency body-boundary forcing term (2.25) has the following expression:

$$-2\ b_{jl}^{+} = \qquad (3.6)$$

$$n_\rho\left(\xi_{\rho l}^{(1)}\frac{\partial^2\phi_j^{(1)}}{\partial\rho^2} + \frac{\xi_{\theta l}^{(1)}}{\rho}\frac{\partial^2\phi_j^{(1)}}{\partial\rho\partial\theta} + \xi_{zl}^{(1)}\frac{\partial^2\phi_j^{(1)}}{\partial\rho\partial z}\right) + n_z\left(\xi_{\rho l}^{(1)}\frac{\partial^2\phi_j^{(1)}}{\partial z\partial\rho} + \frac{\xi_{\theta l}^{(1)}}{\rho}\frac{\partial^2\phi_j^{(1)}}{\partial z\partial\theta} + \xi_{zl}^{(1)}\frac{\partial^2\phi_j^{(1)}}{\partial z^2}\right)$$

where $\xi_\rho{}^{(1)}=\xi_x{}^{(1)}\cos\theta$, $\xi_\theta{}^{(1)}=-\xi_x{}^{(1)}\sin\theta$, and we set $\xi_y{}^{(1)}$ to be zero without loss of generality for axisymmetric bodies. Then, above equation can be rearranged as a single Fourier series as follows:

$$b^{+}_{0j1} = -\frac{\xi^{(1)}_{x1}}{4}\left[n_\rho \frac{\partial^2\phi^{(1)}_{1j}}{\partial\rho^2} + n_z \frac{\partial^2\phi^{(1)}_{1j}}{\partial z\,\partial\rho} + \frac{1}{\rho}\frac{\partial\phi^{(1)}_{1j}}{\partial n}\right] - \frac{\xi^{(1)}_{z1}}{2}\left[n_\rho \frac{\partial^2\phi^{(1)}_{0j}}{\partial\rho\,\partial z} + n_z \frac{\partial^2\phi^{(1)}_{0j}}{\partial z^2}\right] \tag{3.7}$$

$$b^{+}_{nj1} = -\frac{\xi^{(1)}_{x1}}{4}\left[n_\rho\left(\frac{\partial^2\phi^{(1)}_{n-1j}}{\partial\rho^2} + \frac{\partial^2\phi^{(1)}_{n+1j}}{\partial\rho^2}\right) + n_z\left(\frac{\partial^2\phi^{(1)}_{n-1j}}{\partial z\,\partial\rho} + \frac{\partial^2\phi^{(1)}_{n+1j}}{\partial z\,\partial\rho}\right) - \frac{n-1}{\rho}\frac{\partial\phi^{(1)}_{n-1j}}{\partial n} + \frac{n+1}{\rho}\frac{\partial\phi^{(1)}_{n+1j}}{\partial n}\right] - \frac{\xi^{(1)}_{z1}}{2}\left[n_\rho \frac{\partial^2\phi^{(1)}_{nj}}{\partial\rho\,\partial z} + n_z \frac{\partial^2\phi^{(1)}_{nj}}{\partial z^2}\right] \tag{3.8}$$

The other terms including rotational modes or the corresponding expression for B_n^- can be treated in a similar way.

The sum- and difference-frequency ring sources used in (3.3) can be obtained from:

$$G^{\pm}_{n}(\rho,z;\rho',z') = \int_0^{2\pi} G^{\pm}(\rho,z;\rho',z';\cos(\theta-\theta'))\,\cos(n(\theta-\theta'))\,d(\theta-\theta') \tag{3.9}$$

The method for the evaluation of general order ring sources, $G_n\pm$, and their normal derivatives, $G_n\pm/\partial n$, as well as their important asymptotic properties are detailed in Chapter I.

For the second-order diffraction problem, we have used Green's theorem directly to derive the pertinent integral equation for $\phi_D\pm$. For the linear problem, however, we used ring source distribution method in preference to the combined distribution since it reduces the order of derivatives of the Green function by one in calculating velocitites and accelerations. Then, the linear body disturbance potential, $\phi_{Bn}^{(1)} = \phi_{Dn}^{(1)} + \phi_{Rn}^{(1)}$, is obtained by distributing ring sources ($\sigma_n = \sigma_{Dn} + \sigma_{Rn}$) on ∂B:

$$\phi^{(1)}_{Bn}(x) = \int_{\partial_B} \rho' dl' \, \sigma_n(x') \, G_n(x;x') \tag{3.10}$$

where the diffraction ring source strength, σ_{Dn}, is determined from the following integral equation (for σ_{Rn}, the right hand side is replaced by the associated term in (2.11b)):

$$2\pi \, \sigma_{Dn}(x) + \int_{\partial_B} \rho' dl' \, \sigma_{Dn}(x') \, \frac{\partial G_n(x;x')}{\partial n_x} = - \frac{\partial \phi^{(1)}_{I\,n}(x)}{\partial n_x} \tag{3.11}$$

The integral eqations (3.3) and (3.11) are solved numerically following a standard procedure of discretizing ∂B into linear segments, assuming constant source strength or potential over each panel, and selecting colocation points at the mid points of the segments.

As was pointed out earlier, the most difficult and computationally expensive part in solving second-order diffraction potential $\phi_{Dn}^{\pm}$ in (3.3) is the evaluation of the free-surface integrals given by:

$$I_n(\rho', z') = \frac{1}{g} \int_a^{\infty} d\rho \, \rho \, Q_n^{\pm}(\rho) \, G_n^{\pm}(\rho, z=0; \rho', z') \tag{3.12}$$

where a is the radius of the waterplane. The free-surface forcings, $Q_n^{\pm}$, are given on the entire free surface (a,∞) in terms of first-order potentials of frequencies ω_j and ω_l and their derivatives, which may in turn be obtained through (3.10) and its differentiations. In the present method, the free-surface integral (3.12) is evaluated in two intervals, (a,b) & (b,∞), where partition radius b is chosen so that the latter interval is entirely local-wave-free:

$$I_n = \frac{1}{g} \left[\int_a^b d\rho\, \rho\, Q_n^{\pm} G_n^{\pm} + \int_b^{\infty} d\rho\, \rho\, \hat{Q}_n^{\pm} \hat{G}_n^{\pm} \right] \tag{3.13}$$

The first integral is numerically evaluated by Romberg quadrature with controlled tollerence, while the second integral, where all local modes are exponentially small, is treated anallytically. In the above, (^) represents terms which contain contributions from propagating wave only and these are given by:

$$\hat{G}_n^{\pm} = -4\pi^2 i c^{\pm} \cosh k_2^{\pm}(z+h) \cosh k_2^{\pm}(z'+h)\, J_n(k_2^{\pm}\rho')\, H_n(k_2^{\pm}\rho) \tag{3.14}$$

$$\hat{q}^{+}_{0jl} = \frac{-ig^2 A_j A_l k_j^2}{2\omega_j} \cosh k_j h \cosh k_l h \sum_{m=0}^{\infty} \frac{2}{\epsilon_m} \left[\left(\Lambda_{jl} + \frac{\epsilon_m k_l}{2\,k_j} \frac{m^2}{k_j\rho\; k_l\rho} \right) S^{+j,l}_{m,m} + \frac{k_l}{k_j} T^{+j,l}_{m,m} \right] \tag{3.15a}$$

$$\hat{q}^{+}_{njl} = \frac{-ig^2 A_j A_l k_j^2}{2\omega_j} \cosh k_j h \cosh k_l h \left\{ \sum_{m=0}^{n} \left[\left(\Lambda_{jl} - \frac{k_l}{k_j} \frac{(n-m)m}{k_j\rho k_l\rho} \right) S^{+\,j,l}_{n-m,m} + \frac{k_l}{k_j} T^{+\,j,l}_{n-m,m} \right] \right.$$

$$\left. + \sum_{m=0}^{\infty} \left[\left(\Lambda_{jl} + \frac{k_l}{k_j} \frac{(n+m)m}{k_j\rho\; k_l\rho} \right) \left(S^{+\,j,l}_{n+m,m} + S^{+\,j,l}_{m,n+m} \right) + \frac{k_l}{k_j} \left(T^{+\,j,l}_{n+m,m} + T^{+\,j,l}_{m,n+m} \right) \right] \right\} \tag{3.15b}$$

where $$\Lambda_{jl} = \frac{\tanh^2 k_j h}{2} + \frac{k_l}{k_j} \tanh k_j h \tanh k_l h - \frac{1}{2} \tag{3.16}$$

$$S^{+j,l}_{K,m} = \left(\alpha_K^j \alpha_m^l + \alpha_K^j \beta_m^l + \beta_K^j \alpha_m^l \right) H_K^j H_m^l + \alpha_K^j \beta_m^l H_K^j H_m^{l*} + \beta_K^j \alpha_m^l H_K^{j*} H_m^l \tag{3.17}$$

$$T^{+j,l}_{K,m} = \left(\alpha_K^j \alpha_m^l + \alpha_K^j \beta_m^l + \beta_K^j \alpha_m^l \right) H_K^{'j} H_m^{'l} + \alpha_K^j \beta_m^l H_K^{'j} H_m^{'l*} + \beta_K^j \alpha_m^l H_K^{'j*} H_m^{'l} \tag{3.18}$$

In the above, J and H are the Bessel and Hankel functions of the first kind respectively, and (') in (3.18) represents differentiation with respect to the arguments. The coefficients α, β used in (3.17,18) are given respectively by:

$$\alpha_K^j = -4\pi^2 i c_j \; L_K^j \qquad \text{and} \qquad \beta_K^j = \epsilon_K i^K / 2 \cosh k_j h \tag{3.19}$$

The function L is the Kochin function which describes the far-field behavior of the linear disturbance potential in (3.10), and is given by:

$$L_m^j = \int_{\partial_B} dl' \; \rho' \; \sigma_n^j(x') \; J_n(k_j \rho') \cosh k_j (z'+h) \tag{3.20}$$

The coefficient c in (3.19) is $c=(\nu^2-k^2)/(k^2h-\nu^2h+\nu)$; $\nu \equiv \omega^2/g$, and $c_\pm$ in (3.14) can be obtained from the same equation ν and k replaced by $\nu_\pm$ and $k_{2\pm}$. From (3.14,15), we easily see that the local-wave-free integrand, $\rho \hat{Q}_n \hat{G}_n$, is basically composed of triple product of Hankel functions. One of such integrals has the form:

$$I_1 = \int_b^\infty d\rho \; \rho \; H_K(k_j \rho) \; H_m(k_1 \rho) \; H_n(k_2^\pm \rho) \tag{3.21}$$

A method for accurate evaluation of highly oscillatory and slowly convergent integrals, such as I_1, for monochromatic waves is outlined in Chapter I. In sum-frequency problem, the characteristics of free-surface integrals are in general similar to those of double frequency problem. For the difference-frequency problem, however, the oscillation and relative decay of the free- surface integrand (or the resulting integral) become much slower than that of sum-frequency problem especially when two incident wave frequencies are close. In this case, relative convergence of leading asymptotic method (e.g. Eatock Taylor & Hung, 1987) is extremely slow. With the present method, this slow decay of the propagating waves does not cause any problem since we only concern about the decaying rate of the local waves, which is not very sensitive to changing propagating wave frequencies but depends primarily on the ratio ρ/h.

4. THE COMPLETE SUM- AND DIFFERENCE-FREQUENCY QUADRATIC TRANSFER FUNCTIONS

In previous sections, we described boundary value problems and solution methods for the sum- and difference-frequency second-order potentials. As a result, we can calculate not only second-order forces and moments but also local quantities such as pressures and free-surface elevations. The hydrodynamic pressure(P) and free-surface elevation(ς) can be expanded as a purturbation series like Φ in (2.1a), and the linear and second-order terms are given respectively by:

$$P^{(1)} = -\rho_0 \frac{\partial\Phi^{(1)}}{\partial t} \quad , \quad P^{(2)} = -\rho_0 \frac{\partial\Phi^{(2)}}{\partial t} - \frac{\rho_0}{2} (\nabla\Phi^{(1)})^2 \tag{4.1}$$

$$\varsigma^{(1)} = \frac{-1}{g} \frac{\partial\Phi^{(1)}}{\partial t}\Big|_{z=0} \quad , \quad \varsigma^{(2)} = \frac{-1}{2g} (\nabla\Phi^{(1)})^2 + \frac{1}{g^2} \frac{\partial\Phi^{(1)}}{\partial t} \frac{\partial^2\Phi^{(1)}}{\partial t\partial z} - \frac{1}{g} \frac{\partial\Phi^{(2)}}{\partial t}\Big|_{z=0} \tag{4.2}$$

In the presence of bichromatic waves, the second-order terms in (4.1) & (4.2) can be written in the form:

$$(P^{(2)}(t), \varsigma^{(2)}(t)) = \mathrm{Re} \sum_{j=1}^{2} \sum_{l=1}^{2} [\, A_j A_l (p^{+}_{jl}, \eta^{+}_{jl})\, e^{-i\omega^{+}t} + A_j A^{*}_l (p^{-}_{jl}, \eta^{-}_{jl})\, e^{-i\omega^{-}t}] \tag{4.3}$$

where $p_{jl\pm}$ and $\eta_{jl\pm}$ are quadratic transfer functions for pressures and free-surface elevations. The complete pressure and free-surface run-up QTFs consist of the linear quadratic term, (p_q, η_q), and second-order potential contribution, (p_p, η_p):

$$(p^+_{jl},\ \eta^+_{jl}) = (p^+_{qjl},\ \eta^+_{qjl}) + (p^+_{pjl},\ \eta^+_{pjl}) \tag{4.4}$$

Each component for sum-frequency problem has the form:

$$p^+_{qjl} = [\, - \frac{\rho_o}{4} \nabla\phi^{(1)}_j \bullet \nabla\phi^{(1)}_l] \,/\, A_j A_l \quad , \quad p^+_{pjl} = \rho_o i \omega^+ \phi^+ / \, A_j A_l \tag{4.4}$$

$$\eta^+_{qjl} = [- \frac{1}{4g} \nabla\phi^{(1)}_j \bullet \nabla\phi^{(1)}_l - \frac{\omega_j \omega_l \, (\nu_j + \nu_l)}{4\, g^2} \phi^{(1)}_j \phi^{(1)}_l] \,/\, A_j A_l \quad , \quad \eta^+_{pjl} = \frac{i\omega^+ \phi^+}{g\, A_j A_l} \tag{4.5}$$

The wave forces and moments on a body can be obtained by integrating the fluid pressure over the instantaneous wetted-body surface, S(t):

$$(F(t), M(t)) = \iint_{S(t)} P \, (n, r \times n) \, dS \tag{4.6}$$

Hereafter, we will only give expressions for the forces, and the corresponding moment expressions can be readily obtained by replacing n by rxn. Using Taylor's expansion for both the pressure and unit normal vector of the instantaneous position S(t) in (4.6) with respect to the body surface at rest (S_B), the above pressure integral over S(t) can be transformed to surface- and waterline- integrals of the quiescent body position, S_B, as detailed in Ogilvie (1983). After collecting the first- and second-order contributions, we can write the complete first- and second-order hydrodynamic forces as follows:

$$F^{(1)} = F_R^{(1)} + F_I^{(1)} + F_D^{(1)} + F_{HS}^{(1)} \tag{4.7}$$

$$F^{(2)} = F_R^{(2)} + F_I^{(2)} + F_D^{(2)} + F_{HS}^{(2)} + F_q^{(2)} \tag{4.8}$$

At first order, $F_R^{(1)}$ gives added mass and hydrodynamic damping forces, $F_{HS}^{(1)}$ the hydrostatic restoring forces for the first-order motions, whereas $F_I^{(1)}$ & $F_D^{(1)}$ are acting as the linear wave exciting force. Each force is given by:

$$F^{(1)}_{R,I,D} = -\rho_0 \iint_{S_B} \frac{\partial\Phi^{(1)}_{R,I,D}}{\partial t}\, n \, dS \tag{4.9}$$

$$F^{(1)}_{HS} = -\rho_0 g A_w \left(\Xi_3^{(1)} + y_f \alpha_1^{(1)} - x_f \alpha_2^{(1)} \right) k \tag{4.10}$$

where A_w is the waterplane area, k the unit vector in z direction, and x_f & y_f are the locations of the longitudinal and transverse center of floatations. Similarly at second order, $F_R^{(2)}$ & $F_{HS}^{(2)}$ are the radiation- and hydrostatic- forces for the second-order motions, while the other forces, $F_I^{(2)}$, $F_D^{(2)}$, and $F_q^{(2)}$, contribute as the second-order wave exciting force. Each forces are given by:

$$F^{(2)}_{R,I,D} = -\rho_0 \iint_{S_B} \frac{\partial\Phi^{(2)}_{R,I,D}}{\partial t}\, n \, dS \tag{4.11}$$

$$F^{(2)}_{HS} = -\rho_0 g A_w \left(\Xi_3^{(2)} + y_f \alpha_1^{(2)} - x_f \alpha_2^{(2)} \right) k \tag{4.12}$$

$$F_q^{(2)} = -\rho_0 \iint_{S_B} [\{\tfrac{1}{2} \nabla\phi^{(1)^2} + (\Xi^{(1)} + \alpha^{(1)} \times r) \bullet \frac{\partial}{\partial t}(\nabla\phi^{(1)})\} n + (\alpha^{(1)} \times n) \frac{\partial}{\partial t}\phi^{(1)}] dS$$

$$+ \frac{\rho_0 g}{2} \int_{WL} \{ \zeta^{(1)^2} - 2\zeta^{(1)} (\Xi_3^{(1)} + y\, \alpha_1^{(1)} - x\, \alpha_2^{(1)}) \} N\, dl$$

$$- \rho_0 g A_w \{ \alpha_3^{(1)} (x_f \alpha_1^{(1)} + y_f \alpha_2^{(1)}) \} k \tag{4.13}$$

where $N = n/\sqrt{(1-n_3^2)}$, and for the wall-sided geometry at $z=0$; $N=n$. The equivalent expression of (4.13) using relative wave heights can be readily obtained after rearranging (4.13). The force, $F_q^{(2)}$, represents the contribution from quadratic products of the linear solutions. The first- and second-order motions can then be obtained from the eqilibrium of the enertia force and the forces given above. For example, the translational motions at each order can be calculated from:

$$M (\ddot{\Xi}^{(1)} + \ddot{\alpha}^{(1)} \times r_G) = F^{(1)} \tag{4.14}$$

$$M (\ddot{\Xi}^{(2)} + \ddot{\alpha}^{(2)} \times r_G) = F^{(2)} - M \ddot{H}\, r_G \tag{4.15}$$

where M is the mass of the body and r_G the position vector of the center of gravity. As pointed out earlier, the second-order radiation problem, for $\phi_R^{(2)}$, is identical to that of the linear problem except for the shift of frequency, hence the added mass and hydrodynamic damping for the second-order motions can be obtained like (2.13a). We consider here second-order wave exciting forces somewhat detail, where all interesting nonlinear aspects are included.

The second-order exciting forces are given by the terms in (4.11,13):

$$F_{ex}^{(2)} = F_{I}^{(2)} + F_{D}^{(2)} + F_{q}^{(2)} \tag{4.16}$$

In the presence of the bichromatic waves, the second-order wave excitation (4.16) has the form:

$$F_{ex}^{(2)}(t) = \mathrm{Re} \sum_{j=1}^{2} \sum_{l=1}^{2} \left[A_j A_l f_{jl}^{+} e^{-i\omega^{+} t} + A_j A_l^{*} f_{jl}^{-} e^{-i\omega^{-} t} \right] \tag{4.17}$$

$$f_{jl}^{\pm} = f_{qjl}^{\pm} + f_{pjl}^{\pm} \tag{4.18}$$

where $f^{\pm}$ are the complete sum- and difference-frequency force quadratic transfer function(QTF). In (4.18), $f_q^{\pm}$ represents contribution from quadratic products of linear solutions, while $f_p^{\pm}$ from the second-order potential. For example, these forces, for the case of fixed bodies, are given by (More general expression for freely-floating bodies can readily be derived from (4.11) and (4.13)):

$$f_{qjl}^{+} = \left[-\frac{\rho_0}{4} \iint_{S_B} \nabla\phi_j^{(1)} \cdot \nabla\phi_l^{(1)} \, n \, dS - \frac{\rho_0 \omega_j \omega_l}{4g} \int_{WL} \phi_j^{(1)} \phi_l^{(1)} N \, dl \right] / A_j A_l \tag{4.19}$$

$$f_{qjl}^{-} = \left[-\frac{\rho_0}{4} \iint_{S_B} \nabla\phi_j^{(1)} \cdot \nabla\phi_l^{(1)*} \, n \, dS + \frac{\rho_0 \omega_j \omega_l}{4g} \int_{WL} \phi_j^{(1)} \phi_l^{(1)*} N \, dl \right] / A_j A_l^{*} \tag{4.20}$$

$$f_{pjl}^{\pm} = \left[\rho_0 i\omega^{\pm} \iint_{S_B} (\phi_I^{\pm} + \phi_D^{\pm}) \, n \, dS \right] / (A_j A_l, A_j A_l^{*}) \tag{4.21}$$

For later discussion, we further split $f_p = f_I + f_B + f_F$, where f_I represents the second-order Froude-Krilov term, and f_B and f_F are contributions due to body and free-surface forcings respectively.

For vertically axisymmetric bodies, the θ integrals in (4.19~21) can be integrated explicitly. For example, the horizontal component of f_{qjl}^+ in (4.19) has the form upon integrating with respect to θ:

$$f_{xqjl}^{+} = \frac{\rho_0 ga\, n_\rho}{4(1-n_z^2)^{1/2}} \sum_{n=0}^{\infty} \frac{\pi}{\epsilon_n} (\psi_n^j \psi_{n+1}^l + \psi_n^l \psi_{n+1}^j) \Big|_{z=0} + \frac{\rho_0\, g^2}{4\, \omega_j \omega_l} \sum_{n=0}^{\infty} \int \rho n_\rho dl \times$$

$$\Big[\frac{\pi}{\epsilon_n} \Big(\frac{\partial \psi_n^j}{\partial \rho} \frac{\partial \psi_{n+1}^l}{\partial \rho} + \frac{\partial \psi_n^l}{\partial \rho} \frac{\partial \psi_{n+1}^j}{\partial \rho} + \frac{\partial \psi_n^j}{\partial z} \frac{\partial \psi_{n+1}^l}{\partial z} + \frac{\partial \psi_n^l}{\partial z} \frac{\partial \psi_{n+1}^j}{\partial z}\Big) + \frac{\pi n(n+1)}{2\, \rho^2} (\psi_n^j \psi_{n+1}^l + \psi_n^l \psi_{n+1}^j)\Big] \tag{4.22}$$

The previous equations for bichromatic waves can easily be generalized to irregular seas after summing up all wave components in (4.3) and (4.17).

If only integrated quantities such as second-order forces are required, an alternative method (Molin, 1979; Lighthill, 1979), which does not require the solution for $\phi_{D\pm}$ explicitly, can be used as follows:

$$\iint_{S_B} \phi_D^{\pm} n_k dS = \iint_{S_B} \Psi_k^{\pm} \Big(B^{\pm} - \frac{\partial \phi_I^{\pm}}{\partial n} \Big) dS + \frac{1}{g} \iint_{S_F} Q^{\pm} \Psi_k^{\pm} dS \tag{4.23}$$

where $\Psi_{k\pm}$ are the linear assisting radiation potentials for k mode associated with $\omega_\pm$, and satisfy the body boundary condition $\partial \Psi_{k\pm}/\partial n = n_k$. In (4.23), $B_\pm$ contain the second spatial derivatives of the linear potential on the body, which are difficult to calculate with sufficient accuracy. To circumvent this problem, an alternative expression of $f_{BBjl\pm}$ which is free from the second spatial derivatives can be derived using Stoke's theorem and some vector identities as follows:

$$\iint_{S_B} \mathbf{n}\bullet\Psi^{\pm}[(\boldsymbol{\xi}_1^{(1)}+\boldsymbol{\alpha}_1^{(1)}\times \mathbf{r})\circ\nabla]\nabla\phi_j^{\pm}\, dS =$$

$$\int_{\Gamma} d\mathbf{l}\circ[\Psi^{\pm}\, \nabla\phi_j^{(1)}\times\, (\boldsymbol{\xi}_1^{(1)}+\boldsymbol{\alpha}_1^{(1)}\times \mathbf{r})] - \iint_{S_B} \mathbf{n}\bullet\nabla\Psi^{\pm}\times\, [\nabla\phi_j^{(1)}\times\, (\boldsymbol{\xi}_1^{(1)}+\boldsymbol{\alpha}_1^{(1)}\times \mathbf{r})]\, dS \tag{4.24}$$

where Γ is the surounding boundary of S_B. For a uniform bottom-mounted vertical cylinder, the first-order diffraction and radiation potentials can be expressed in closed forms, so that semi-analytic expressions for the second-order forces and moments can be derived using (4.23). These are summarized in Appendix C, and provide useful benchmark for the second-order numerical results.

5. NUMERICAL RESULTS AND DISCUSSION

For illustration, we consider the diffraction of plane bichromatic waves by the bottom-seated uniform vertical cylinder (radius a, depth h=a,4a) for which semi-analytic expressions for forces are available (Appendix C). We also calculated the second-order wave excitations and responses of the fixed or freely-floating hemispheres (radius a, depth h=3a) in the presence of bichromatic incident waves.

The numerical procedure for solving integral equations (3.1) and (3.11) for the second- and first-order problems is in general same as Chapter I, say: (i) approximate the body contour, ∂B, by N_p straight line segments; (ii) assume constant values for the potential $\phi_{Dn}^{\pm}$, or ring source strength σ_n, over each segment; (iii) colocate the equations at the center of each segment to obtain a system of linear algebraic equations for the segment unknowns, which is then solved. Then, the numerical errors are controlled by the number of panels and azimuthal Fourier modes. In the following, we present the convergence of the second-order sum- and differency-frequency calculations with respect to the number of panels (N_p), Fourier modes(N), and partition radius(b) of the free surface integral. For comparison, two typical frequency pairs, which are close and far apart, respectively, are chosen.

Table 1 shows the convergence of the nonlinear potential force QTF, $f_{pjl}\pm$, with increasing the number of panels. To describe the more rapid variations near the free-surface (especially for the second-order potential), cosine-spaced segments (with smaller lengths near the free surface) are used in all our calculations. As expected, we achieve faster convergences for f_{pjl}^-, and hence may use less number of segments in the difference-frequency problem. In the following calculation, N_p=20 segments are used for both the linear and second-order sum- and diffferency-frequency calculations.

Table 1. Magnitudes of the second-order potential horizontal force QTF, $|f_{pjl}\pm/\rho gaA_jA_l|$, on a uniform vertical cylinder (h/a=1) with increasing the number of cosine-spaced segments, N_p, on a body; (Partition radius (b-a)/h=3 is used)

	Difference-frequency		Sum-frequency	
$(\nu_j a, \nu_l a)$	(1.0,2.0)	(1.4,1.6)	(1.0,2.0)	(1.4,1.6)
semi-analytic	1.936	0.435	2.656	2.875
N_p=10	1.935	0.435	2.664	2.876
20	1.936	0.435	2.661	2.876
30	1.936	0.435	2.660	2.875

To show the convergence of $\phi^{\pm}$ with increasing numbers, $n \leq N$, of azimuthal Fourier modes, the modal amplitudes of sum- and difference-frequency potentials at $(\rho, z) = (a, 0)$ (which are proportional to the run-up) are given in Table 2. It was already pointed out in Chapter I that the mode number beyond which the amplitudes attenuate rapidly increases with increasing mean frequency. For the same frequency pair, much faster convergences are obtained in the difference-frequency problem. The convergence rate of ϕ^- becomes faster as the frequency difference

Table 2. The convergence of the sum- and difference-frequency potential modal amplitudes normalized by $|\phi_n^{\pm}/(gA_jA_l/2i\omega_j\omega_l a)|$ on the circumference (ρ=a) of a uniform vertical cylinder (h/a=1). (* indicates values less than 1.E-4).

	Difference-frequency		Sum-frequency	
$(\nu_j a, \nu_l a)$	(1.0,2.0)	(1.4,1.6)	(1.0,2.0)	(1.4,1.6)
n=0	2.4178	12.5268	0.2368	0.2015
1	4.2202	4.1827	1.2925	1.3914
2	1.3129	0.2759	0.6589	0.7688
3	0.2763	0.0118	0.1915	0.0446
4	0.0361	0.0036	1.0461	1.0093
5	0.0169	0.0039	1.5603	1.4606
6	0.0016	0.0001	1.1920	1.1262
7	0.0010	0.0001	0.4556	0.4683
8	0.0001	*	0.0969	0.1027
9	*	*	0.0168	0.0177
10	*	*	0.0023	0.0026
11	*	*	0.0002	0.0003
12	*	*	*	*
13	*	*	*	*
14	*	*	*	*

decreases, however, that of ϕ^+ is not sensitive to changing frequency differences. The convergence of the sum-frequency second-order potential, ϕ^+, is generally slow and requires more Fourier modes when compared to linear potentials. From the slower and less uniform decrease of ϕ^+ with increasing n, we expect large variations of the sum-frequency wave run-up in the circumferential direction, which will be shown later. In the following calculations, N=9 and N=(14,9) are used respectively in the linear and second-order sum- and difference-frequency problems.

The free-surface integral given in (3.13), which is extremely expensive in computations and crucial for the accuracy, is calculated using the method described in section 3, and its convergence is checked with increasing the partition radius b. As pointed out in Chapter I, the decay rate of local waves primarily depends on the ratio ρ/h. Table 3 shows the typical convergence of the sum- and difference-frequency second-order potential force QTFs, $f_{pjl\pm}$, on a uniform vertical cylinder (a/h=1) with increasing partition radius. We can see much weaker influence of local waves, in the difference-frequency problem, with increasing distance from the body (equivalently, much faster convergences of the free-surface integrals). This was also pointed out by Kagemoto & Yue (1986) in the study of multiple-body interactions including evanescent waves. It is seen that a partition radius of (b-a)~3h is sufficient for 3 significant decimals of accuracy and used in later computations. The accuracy with relatively small numerical integration requirements again underscore the efficacy (particularly in the difference-frequency problem where the propagating waves decay very slowly) of the entire local-wave-free method.

Table 3. **Magnitudes** of the second-order sum- and difference-frequency potential force QTFs, $|f_{pjl}^{\pm}/\rho g a A_j A_l|$, on a uniform vertical cylinder ($h/a=1$). The results for different partition radius b are compared to semi-analytic solutions (Appendix C).

	Difference-frequency		Sum-frequency	
$(\nu_j a, \nu_l a)$	(1.0,2.0)	(1.4,1.6)	(1.0,2.0)	(1.4,1.6)
exact	1.936	0.435	2.656	2.875
$(b-a)/h=2$	1.936	0.435	2.668	2.861
3	1.936	0.435	2.661	2.876
4	1.936	0.435	2.659	2.877

Until recently, numerous approximation methods for sum- (springing) and difference-frequency (slowly-varying) wave excitations and resulting responses have been suggested and widely used primarily due to the difficulty in calculating the second-order potential contributions. In the absence of the complete QTF, the preference for one method over the others, or even the validity of each method (which is clearly a function of frequency combinations, body geometries, and water depths) have been quite controversial (Ogilvie, 1983). With the complete sum- and difference-frequency wave excitation and response QTFs available by the present method, we investigate the general behavior of the springing and slowly-varying excitation QTFs in the bifrequency domain, and examine the validity of various approximation methods. For this purpose, (i) bottom-mounted vertical cylinders of two different drafts; h/a=1 & 4, and (ii) fixed and freely-floating hemispheres for h/a=3 are selected. In addition to the force and moment QTFs, interesting local quantity QTFs such as pressures and run-up are also available by the present method. Many interesting nonlinear aspects of the integrated quantities can be clearly understood with the behavior of these local solutions, as will be shown later.

(i) Difference-frequency problem

For the approximate estimation of the slowly-varying wave excitations in irregular seas, Newman (1974) used the mean drift force operator, f_{qjj}^{-}, based on the narrow band assumption of the input spectrum. Marthinsen (1983) suggested a similar approximation method using the slowly-varying wave envelope concept. These methods greatly simplify the problem and are most widely used in engineering applications even though the validity depends critically on the narrow-bandedness of the input spectrum and the slope of QTF near the diagonal. Other existing approximation methods include partly the contributions of the second-order potential. For example, the incomplete QTF operators ($f_{qjl}^{-}+f_{Ijl}^{-}$) and ($f_{qjl}^{-}+f_{Ijl}^{-}+f_{BIjl}^{-}$) were used by Standing et al (1982) and Pinkster (1980), respectively.

In Table 4, the complete second-order slowly-varying force QTF on a bottom-seated vertical cylinder and each of its components are given for two water depths (h/a=1, 4) and various combinations of incident frequencies. In the vicinity of the diagonal (small frequency difference, $\Delta\nu a$), the linear quadratic term, f_{qjl}^{-}, dominates other contributions. For the larger frequency difference, however, the contributions due to the second-order incident wave (f_{Ijl}^-,f_{Bjl}^-) are greatly increased and become dominant over f_{qjl}^-. The free-surface contribution, f_{Fjl}^-, remains small overall. The contributions, f_{Ijl}^- and f_{Bjl}^-, are nearly in phase, and hardly cancel each other. For fixed sum-frequency and increasing frequency difference, all contributions from the second-order potential, ϕ^-, increase almost linearly starting from zero for $(\nu_j-\nu_l)a = \Delta\nu a = 0$. The slopes of f_{Bjl}^- and f_{Ijl}^- with increasing direction of $\Delta\nu a$ are much larger than f_{Fjl}^-. The linear square term, f_{qjl}^-, is less sensitive to changing frequency differences. Interestingly, the magnitudes of all second-order components become smaller with increasing water depth or cylinder draft. For fixed $\Delta\nu a$ and varying sum frequency, f_{Ijl}^- and f_{Bjl}^- continue to increase with decreasing sum frequency, while f_{Fjl}^- increases slowly with increasing sum frequency.

These results show that the validity of Newman's or Marthinsen's approximation methods is very sensitive to the narrow bandedness of the input spectrum due to the large slope of f_{Ijl}^- and f_{Bjl}^- near the diagonal $\omega_j=\omega_l$. While, Pinkster's (QIB)** approximation is expected to give better results for a broader class of input spectra without considerable increase of the computing time. This is also pointed out by Eatock Taylor et al (1988). Fortunately, the small contribution from the free-surface forcing makes it possible to avoid the most cumbersome free-surface integral in many engineering applications.

** Pinkster used only f_{BI} as a body-forcing contribution even for freely-floating bodies. In this sense, the QIB approximation, which includes both f_{BI} and f_{BB} as a body-forcing contribution, is more general.

Table 4. Magnitudes of the complete second-order slowly-varying force QTF, $|f_{jl}^{-}/\rho g a A_j A_l^{*}|$, and each of its components on a uniform vertical cylinder. The upper triangular matrix is for h/a=1, and lower part for h/a=4. On the diagonal, $f_{qjl}^{-} = f_{jl}^{-}$, and () for h/a=4. Each element satisfies the symmetry relation $f_{jl}^{-} = f_{lj}^{-*}$. Computed values are for: first row; $|f_{qjl}^{-}|$, second row; $|f_{Ijl}^{-}|$, third row; $|f_{Bjl}^{-}|$, fourth row; $|f_{Fjl}^{-}|$, and fifth row; the complete QTF $|f_{jl}^{-}|$.

$\nu_j a=$	1.0	1.2	1.4	1.6	1.8	2.0
$\nu_l a=$ 1.0	0.918 (0.666)	0.864 0.297 0.302 0.037 0.982	0.811 0.550 0.568 0.097 1.163	0.765 0.770 0.794 0.166 1.347	0.722 0.963 0.966 0.229 1.489	0.680 1.131 1.063 0.273 1.575
1.2	0.647 0.168 0.167 0.034 0.689	0.826 (0.636)	0.791 0.255 0.259 0.036 0.870	0.758 0.481 0.493 0.097 1.011	0.723 0.683 0.697 0.166 1.165	0.685 0.864 0.854 0.226 1.294
1.4	0.612 0.337 0.331 0.088 0.763	0.612 0.166 0.165 0.034 0.640	0.772 (0.603)	0.753 0.229 0.231 0.036 0.810	0.729 0.437 0.445 0.099 0.925	0.698 0.626 0.632 0.166 1.054
1.6	0.578 0.504 0.481 0.150 0.856	0.588 0.332 0.325 0.093 0.701	0.594 0.164 0.164 0.035 0.615	0.748 (0.600)	0.735 0.211 0.213 0.037 0.777	0.712 0.406 0.411 0.101 0.867
1.8	0.552 0.664 0.602 0.208 0.943	0.567 0.497 0.471 0.158 0.788	0.583 0.329 0.322 0.096 0.678	0.602 0.163 0.163 0.037 0.619	0.732 (0.615)	0.717 0.198 0.200 0.038 0.749
2.0	0.534 0.809 0.676 0.243 1.009	0.547 0.653 0.586 0.215 0.877	0.566 0.491 0.463 0.161 0.765	0.593 0.327 0.319 0.099 0.678	0.615 0.163 0.162 0.038 0.629	0.711 (0.624)

Table 5 shows the slowly-varying pitch moment QTF on the uniform vertical cylinders with respect to the center of the waterplane. In this table, the behavior of the body-surface forcing contribution, M_{Bjl}^-, is very similar to that of M_{Ijl}^-, as in Table 4, hence is not given separately. From Table 5, the pitch-roll moment QTFs associated with ϕ_I^-, M_{Ijl}^- and M_{Bjl}^-, in general dominate other contributions due to the slow depth attenuation of ϕ_I^- predicted by (2.7a). Despite decreasing amplitudes of ϕ_I^- for larger h, M_{Ijl}^- and M_{Bjl}^- for h/a=4 are even more important due to the lower pressure center (equivalently, larger moment arm) associated with ϕ_I^-. As $\Delta\nu a$ approaches zero, the magnitude of the second-order potential pressure, which is proportional to ω^-, decreases but penetrates even deeper, hence the resulting pitch moment QTF close to the diagonal is still appreciable. To show these phenomena more clearly, we present in Figure 1a,b the second-order potential pressure QTF, p_{pjl}^-, as well as linear quadratic term, p_{qjl}^-, along the vertical cylinder of h/a=4 for two incident frequency combinations; $(\nu_j,\nu_l)=(1,2)$ and (1.4,1.6). The behavior of the second-order potential pressure, p_{pjl}^-, is dominated by ϕ_I^- and its diffracted free waves, hence its depth decaying rate is characterized by the wavenumber k_j-k_l or k_2^-. For smaller $\Delta\nu a$, p_{pjl}^- becomes smaller in magnitude but penetrates deeper on both sides of the cylinder as shown in Figure 1. When $\Delta\nu a$ is small, ϕ_I^- behaves like shallow water long waves, and the pressures are almost uniform to the bottom. These deeply penetrating local pressures contribute significantly to the pitch moment because of their large moment arms. However, p_{qjl}^- attenuates much faster than p_{pjl}^- according to the rate k_j+k_l and does not contribute appreciably to the pitch moment. As a result of the above discussion, for fixed sum-frequency and increasing frequency differences, M_{Ijl}^- and M_{Bjl}^- have the largest slope near the diagonal. It is interesting to note that relative magnitudes of M_{Fjl}^- near the diagonal are also appreciably increased due to the slow depth attenuation of locked waves at the lee side, which can be expected from (2.33).

Due to these behaviors of the second-order incident wave or free waves associated with it, the validity of Newman's or Marthinsen's aproximation methods should be carefully examined, particularly for the pitch-roll excitations of large draft bodies. The results above have important applications for the prediction of the slowly-varying pitch moments on offshore platforms, particularly when the center of pitch rotation is located close to free-surface. In this case, Newman's or Marthinsen's approximation methods are expected to underestimate the total pitch-moment QTF substantially, so do not lead to a safe design.

In Figure 2, the second-order potential pressure QTFs, p_{pjl}^-, for h/a=1 and $(\nu_j a, \nu_l a)=(1,2)$ are plotted along the five angular positions of a vertical cylinder. Due to dominant contributions from ϕ_I^-, behaviors of p_{pjl}^- around the circumference of the cylinder are quite uniform in contrast to those of the sum-frequency case which will be shown later. The free-surface forcing term, whose decaying rate is angularly dependent and given by (2.33), has a minimum attenuation on the lee side ($\theta=0$). This contribution, however, is not important compared to the sum-frequency problem where deeply penetrating pressures on the weather side ($\theta=\pi$) contribute significantly.

Table 5. Magnitudes of the complete second-order pitch moment QTF, $|M_{jl}^- / \rho g a^2 A_j A_l^*|$, and each of its components, on a uniform vertical cylinder with respect to the center of waterplane. The upper triangular matrix is for h/a=1, and lower part for h/a=4. On the diagonal, $M_{qjl}^- = M_{jl}^-$, and () is for h/a=4. Computed values are for: first row; $|M_{qjl}^-|$, second row; $|M_{Ijl}^-|$, third row; $|M_{Fjl}^-|$, and the complete QTF in fourth row; $|M_{jl}^-|$.

$\nu_j a=$	1.0	1.2	1.4	1.6	1.8	2.0
$\nu_l a=$ 1.0	0.003 (0.173)	0.063 0.148 0.018 0.345	0.115 0.272 0.048 0.624	0.155 0.377 0.080 0.848	0.185 0.464 0.110 1.016	0.207 0.533 0.130 1.126
1.2	0.203 0.318 0.055 0.729	0.044 (0.173)	0.080 0.127 0.017 0.303	0.120 0.238 0.047 0.548	0.154 0.334 0.080 0.750	0.182 0.415 0.108 0.908
1.4	0.257 0.559 0.130 1.232	0.196 0.315 0.055 0.708	0.076 (0.178)	0.099 0.114 0.018 0.281	0.128 0.216 0.048 0.500	0.157 0.306 0.080 0.687
1.6	0.299 0.702 0.197 1.539	0.235 0.552 0.133 1.184	0.194 0.312 0.056 0.690	0.096 (0.181)	0.111 0.105 0.018 0.267	0.134 0.201 0.049 0.469
1.8	0.321 0.766 0.249 1.682	0.264 0.691 0.207 1.465	0.218 0.546 0.138 1.144	0.188 0.310 0.058 0.673	0.106 (0.176)	0.117 0.099 0.018 0.259
2.0	0.325 0.782 0.268 1.717	0.282 0.753 0.258 1.597	0.240 0.683 0.211 1.412	0.205 0.542 0.143 1.113	0.178 0.309 0.060 0.661	0.112 (0.165)

In Figure 3, we present the second-order potential run-up QTF, η_{pjl}^-, and linear quadratic contribution, η_{qjl}^-, around the uniform vertical cylinder of h/a=1 for two incident frequency combinations. The variation of η_{pjl}^- with respect to the angular position is much smoother than that of η_{qj1}^-, which can be expected from the behavior of ϕ_I^-. For smaller $\Delta\nu a$, the free-surface elevation, η_{pj1}^-, is more invariant in the circumferential direction.

We next consider slowly-varying wave excitations on the fixed and freely-floating hemispheres of radius a (h=3a) in bichromatic incident waves. We first present in Table 6 the complete slowly-varying force QTF and each of its components for a fixed hemisphere. In contrast to the cylinder case, f_{qj1}^- is the most important contribution in all frequency ranges considered, especially for horizontal forces. The components f_{Ij1}^- and f_{BIj1}^- also contribute appreciably but their effects are much alleviated compared to those of the vertical cylinders in Table 4. The free-surface contribution again remains small, hence the QIB approximation is expected to give fair results for a broad range of input spectra. For slowly-varying vertical forces, f_{qj1}^- and $(f_{Ij1}^-+f_{Bj1}^-)$ are in general reinforcing each other so that the complete QTF, f_{j1}^-, is always larger than individual contributions; however, the opposite trend is found for horizontal forces. For fixed νa and increasing sum frequency, f_{pj1}^- has milder variations compared to f_{qj1}^-, but the opposite trend results for fixed sum frequency and increasing $\Delta\nu a$.

For fixed sum frequency and increasing $\Delta\nu a$, $(f_{Ixj1}^-+f_{Bxj1}^-)$ increases according to the increase of associated pressures, while $(f_{Izj1}^-+f_{Bzj1}^-)$ decreases due to the shallower penetration of ϕ_I^- for larger $\Delta\nu a$.

Table 6. Magnitudes of the complete second-order force QTF, $|f_{jl}^-/\rho g a A_j A_l^*|$, and each of its components for a fixed hemisphere of h/a=3. The upper triangular matrix is for horizontal forces, and lower part for vertical forces. On the diagonal, $|f_{qjl}^-|=|f_{jl}^-|$, and () for vertical mean forces. Each element satisfies the symmetry relation $f_{jl}^-=f_{lj}^{-*}$. Computed values are for: first row; $|f_{qjl}^-|$, second row; $|f_{Ijl}^- + f_{Bjl}^-|$, third row; $|f_{Fjl}^-|$, and fourth row; the complete QTF $|f_{jl}^-|$.

$\nu_j a=$	1.0	1.2	1.4	1.6	1.8	2.0
$\nu_l a=$ 1.0	0.471	0.493	0.498	0.497	0.495	0.494
	(0.538)	0.061	0.140	0.246	0.369	0.495
		0.014	0.038	0.070	0.104	0.132
		0.482	0.459	0.415	0.360	0.304
1.2	0.512	0.513	0.517	0.516	0.515	0.513
	0.280	(0.499)	0.060	0.138	0.241	0.362
	0.011		0.013	0.038	0.069	0.102
	0.803		0.505	0.472	0.422	0.362
1.4	0.478	0.477	0.523	0.525	0.526	0.525
	0.258	0.272	(0.468)	0.059	0.136	0.238
	0.040	0.012		0.013	0.037	0.069
	0.770	0.760		0.511	0.478	0.428
1.6	0.440	0.449	0.450	0.531	0.536	0.538
	0.232	0.250	0.267	(0.442)	0.059	0.135
	0.082	0.042	0.013		0.012	0.037
	0.731	0.734	0.728		0.522	0.489
1.8	0.398	0.414	0.424	0.425	0.545	0.551
	0.211	0.222	0.245	0.264	(0.417)	0.058
	0.137	0.087	0.044	0.013		0.012
	0.681	0.701	0.706	0.701		0.536
2.0	0.356	0.376	0.392	0.401	0.401	0.560
	0.225	0.201	0.215	0.241	0.262	(0.392)
	0.203	0.144	0.090	0.045	0.013	
	0.621	0.655	0.676	0.681	0.675	

As a result, the slope of the vertical force QTF near the diagonal is very steep with positive sign. Therefore, a severe underestimation of slowly-varying vertical forces by Newman's approximation is expected. The mean vertical drift force, which is given on the diagonal, has a minus sign and is comparable in magnitude with the horizonal mean drift force.

For freely-floating bodies, we separate contributions due to body forcing into two terms, f_{BIjl}^- and f_{BBjl}^-, where f_{BIjl}^- represents the diffraction effect of ϕ_I^-, and f_{BBjl}^- the contribution from the first-order motions. The contribution f_{BBjl}^- is calculated from (4.24) which is free from the second spatial derivatives on the body, hence, is numerically more favorable. For the contribution $f_{Ijl}^-+f_{BIjl}^-$, there is no difference between fixed and freely-floating bodies, hence is not given separately in Table 7. The general tendency for relative magnitudes of individual contributions is similar to that of the fixed hemisphere. As expected, the effect of the first-order motions decreases with increasing sum frequency. The contribution of the body forcing due to linear motions, f_{BBjl}^-, as well as the free-surface contribution, f_{Fjl}^-, are found to be less important especially near the diagonal. However, due to the possible phase cancellation among the contributions, neglecting f_{Fjl}^- or f_{BBjl}^- for certain cases may not lead to reasonable approximation particularly for large $\Delta\nu a$. For example, when $(\nu_j a,\nu_l a)=(2,1)$ in Table 7, the horizontal force QTF from the free-surface integral reaches 70% of total QTF. For difference-frequency forces, no dramatic change of the QTFs is observed after including linear motions. This effect is more significant for the sum-frequency problem as will be shown later.

Table 7. Magnitudes of the complete second-order force QTF, $|f_{jl}^-/\rho g a A_j A_l^*|$, and each of its components for a freely-floating hemisphere of $h/a=3$. The upper triangular matrix is for horizontal forces, and lower part for vertical forces. On the diagonal, $|f_{qjl}^-|=|f_{jl}^-|$, and () for vertical forces. Each element satisfies the symmetry relation $f_{jl}^-=f_{lj}^{-*}$. Computed values are for: first row; $|f_{qjl}^-|$, second row; $|f_{BBjl}^-|$, third row; $|f_{Fjl}^-|$, and fourth row; the complete QTF $|f_{jl}^-|$.

$\nu_j a=$	1.0	1.2	1.4	1.6	1.8	2.0
$\nu_l a=$ 1.0	0.519 (0.306)	0.719 0.015 0.028 0.709	0.619 0.026 0.072 0.591	0.534 0.040 0.129 0.483	0.482 0.060 0.189 0.407	0.447 0.084 0.247 0.354
1.2	0.189 0.030 0.023 0.469	0.878 (0.494)	0.783 0.004 0.020 0.766	0.718 0.010 0.060 0.660	0.681 0.020 0.109 0.570	0.653 0.036 0.160 0.487
1.4	0.376 0.063 0.039 0.630	0.526 0.018 0.015 0.817	0.717 (0.488)	0.677 0.005 0.015 0.658	0.660 0.010 0.047 0.598	0.648 0.019 0.087 0.529
1.6	0.430 0.090 0.061 0.681	0.516 0.040 0.040 0.820	0.457 0.014 0.012 0.742	0.652 (0.426)	0.645 0.003 0.013 0.627	0.639 0.008 0.042 0.581
1.8	0.447 0.113 0.098 0.694	0.499 0.060 0.077 0.813	0.434 0.028 0.039 0.730	0.407 0.012 0.011 0.686	0.644 (0.392)	0.643 0.002 0.013 0.626
2.0	0.448 0.134 0.150 0.680	0.476 0.077 0.126 0.788	0.409 0.043 0.080 0.713	0.386 0.023 0.041 0.676	0.378 0.010 0.012 0.655	0.646 (0.370)

The mean drift forces for a freely-floating hemisphere are given in Table 7 along the diagonal and they interestingly change signs from + to - in the vicinity of the heave resonance ($\nu a \sim 1$). This was also observed by

Pinkster (1980) and Molin (1983).

We next consider the second-order motion transfer function of a freely-floating hemisphere. Having obtained the complete force QTF, f_{jl}^{-}, heave and surge response QTFs can readily be calculated from (4.15). Interestingly, the second-order heave and surge motions are uncoupled but each of them is affected by first-order surge and heave motions via second-order wave exciting forces. If any pair of bichromatic waves is such that their frequency sum or difference falls on the heave natural frequency, second-order heave resonance occurs. A typical example of the difference-frequency resonance of a freely-floating hemishere is given in Table 8. There, we observe a resonance for a wave pair, $(\nu_j a, \nu_l a)=(1,4)$, whose frequency difference is close to the heave natural frequency. Because of the substantial hydrodynamic damping at that frequency the resonance is weak, as shown in Table 8. In this frequency range, the surge response QTF is much smaller than that of heave, although the horizontal and vertical force QTFs are comparable. Any pair of long waves can generate similar types of sum-frequency resonances. If the natural frequency (ω_n) of the system is very low or high, the corresponding wave damping and linear exciting force are typically small near ω_n. We may then have prominent second-order resonances, which may be more important than the linear one. Typical examples are slowly-varying large-amplitude platform surge motions or the superharmonic vertical plane resonance of Tension-Leg Platforms.

Table 8. Difference-frequency heave and surge response QTFs, $|\xi_{jl}^{-}a/A_jA_l^*|$, of a freely-floating hemisphere of h/a=3. Computed values are for; first row: the complete exciting force QTF, second row: the complete response QTF. Values in () are for surge excitiing force and response QTFs.

$\nu_j a=$	0.6	1.0	1.4
$\nu_l a=$	0.161 (0.175)	0.378 (0.188)	0.366 (0.133)
3.6	0.207 (0.049)	0.455 (0.067)	0.240 (0.075)
	0.150 (0.230)	0.373 (0.170)	0.338 (0.103)
4.0	0.112 (0.051)	0.684 (0.050)	0.298 (0.044)
	0.144 (0.205)	0.333 (0.219)	0.300 (0.029)
4.4	0.071 (0.041)	0.495 (0.056)	0.390 (0.010)

(ii) Sum-frequency problem

For an estimation of sum-frequency (springing) wave excitations in irregular long-crested seas, Herfjord & Nielsen (1986) and Petrauskas & Liu (1987) used a linear quadratic operator, f_{qjl}^+, to approximate the complete sum-frequency QTF, f_{jl}^+. More terms ($f_{qjl}^+ + f_{Ijl}^+ + f_{BIjl}^+$) are included by De Boom et al (1983) with the exception of the free-surface contributions. The weakness of these approximation methods will be discussed in the following.

In Table 9, we present the sum-frequency horizontal force QTF on a bottom-mounted vertical cylinder for two different water depths. Unlike the difference-frequency problem, components relating to the second-order incident wave, f_{Ijl}^+ and f_{Bjl}^+, are almost negligible in the frequency range considered, and hence are not given separately. Actually, ϕ_I^+ and its contributions vanish in infinitely deep water. Therefore, we presume that most of the contributions of f_{pjl}^+ are from the free-surface integral, f_{Fjl}^+, which is larger than f_{qjl}^+ in the frequency range considered. This free-surface term becomes more important for deeper water depths (or larger drafts) due to the deep penetration of the associated second-order potential pressure, as shown in Table 9. For fixed $\Delta\nu a$ and increasing sum-frequency, f_{pjl}^+ increases fast in an oscillatory manner, especially for h/a=4. This accounts for the relative importance of second-order potential contributions for larger sum frequency. For a fixed sum-frequency and increasing frequency differences, f_{pjl}^+ decreases rapidly (especially for h/a=4) due to the expected cancellations in the interaction between long and short waves. This phenomenon is mainly due to the particular behavior of the second-order potential pressure predicted by (2.33), whose effects become more clear and important for the pitch moment QTF. It is noteworthy that f_{qjl}^+ and f_{pjl}^+ are in most cases 180 degrees out of phase, hence decreasing each other. This fact was also addressed in Chapter I for the case of monochromatic waves. From these results, we can conclude that any approximation methods used for sum-frequency excitations without involving free-surface contributions should be very restrictive regardless of the shape of the input spectra.

Table 9. Magnitudes of the complete sum-frequency force QTF, $|f_{jl}^{+}/\rho g a A_j A_l|$, and each of its components for uniform vertical cylinders. The upper triangular matrix is for h/a=1, and lower part for h/a=4. On the diagonal, () for h/a=4. Each element satisfies the symmetry relation $f_{jl}^{+}=f_{lj}^{+}$. Computed values are for: first row; $|f_{qjl}^{+}|$, second row; $|f_{pjl}^{+}|$, and third row; $|f_{jl}^{+}|=|f_{qjl}^{+}+f_{pjl}^{+}|$.

$\nu_j a=$	1.0	1.2	1.4	1.6	1.8	2.0
$\nu_l a=$	1.440(1.493)	1.577	1.709	1.802	1.828	1.778
1.0	1.636(3.004)	1.963	2.308	2.582	2.710	2.661
	0.939(1.518)	0.782	0.778	0.850	0.903	0.886
	1.546	1.676(1.641)	1.764	1.813	1.797	1.709
1.2	3.179	2.262(3.723)	2.549	2.752	2.807	2.682
	1.641	0.752(2.084)	0.847	0.959	1.013	0.973
	1.681	1.774	1.805(1.868)	1.808	1.753	1.634
1.4	3.408	4.035	2.754(4.472)	2.876	2.857	2.671
	1.748	2.262	0.971(2.612)	1.074	1.105	1.037
	1.850	1.909	1.945	1.772(1.957)	1.689	1.556
1.6	3.685	4.211	4.654	2.930(4.975)	2.872	2.668
	1.853	2.302	2.714	1.160(3.021)	1.184	1.114
	1.969	1.981	1.957	1.910	1.593(1.820)	1.467
1.8	3.769	4.162	4.454	4.843	2.816(5.097)	2.688
	1.809	2.182	2.505	2.935	1.226(3.277)	1.227
	1.995	1.959	1.878	1.786	1.677	1.368(1.544)
2.0	3.613	3.852	3.961	4.159	4.695	2.693(5.043)
	1.620	1.899	2.094	2.375	3.018	1.334(3.502)

In Table 10, the complete sum-frequency pitch moment QTF (M_{jl}^{+}) as well as linear quadratic (M_{qjl}^{+}) and second-order potential terms (M_{pjl}^{+}) with respect to the center of waterplane are given for the cases where h/a=1 and 4. In this case, M_{pjl}^{+} is generally much larger than M_{qjl}^{+} especially for deeper water. This is attributable to the deep penetration of the sum-frequency second-order potential. To show this more clearly, we have plotted the pressure distributions on the lee(θ=0) and weather side($\theta=\pi$) of the vertical cylinder, as a function of depth, in Figure 4a,b for two different combinations of incident wave frequencies. In this figure, a dominant second-order potential pressure on the weather side can be noted. The linear quadratic pressures, p_{qjl}^+, attenuate according to wavenumber (k_j+k_l), while the nonlinear potential pressures, p_{pjl}^+, appear to decrease only algebraically with depth. Due to this slow attenuation of p_{pjl}^+, the pressures on a deeply submerged portion of large-draft bodies are still nontrivial and contribute significantly to the pitch moment through a large moment arm. Appreciable heave excitations on a large draft TLP leg, which have been reported in experiments but cannot be predicted by the linear theory, can be attributed to above phenomena. For fixed sum-frequency, p_{pjl}^+ penetrates deepest on the weather side of the cylinder (especially when two frequencies are close), as shown in Figure 4. This interesting phenomenon can partly be explained by the asymptotic behavior of ϕ_p^+ given in (2.32,33). The decay rate of ϕ_p^+ with increasing depth is characterized by the angular dependent wavenumber $k_\theta= (k_j^2+k_l^2+2k_jk_l\cos\theta)^{1/2}$, which has a minimum (maximum) for $k_j=k_l$ and $\theta=\pi(0)$ and increases with increasing $k_j-(+)k_l$. Due to this interesting behavior of ϕ_p^+, the pitch moment QTF decreases rapidly for a fixed sum frequency and increasing $\Delta\nu a$, as shown in Table 10, especially for the case h/a=4.

The above discussion emphasizes the importance of second-order potential contributions and/or the weakness of existing approximation methods used in the estimation of sum-frequency wave excitations on large draft bodies. An important example of this is superharmonic wave excitations and resulting resonant responses of a Tension-Leg Platform in vertical plane motions (see Chapter IV). Interestingly, it was reported in Petrauskas & Liu (1987) that large scale experiments tended to give 3~4 times larger rms tendon loads than their predictions entirely based on f_{qjl}^+. This large discrepancy may be attributable to the contributions of the second-order potential.

Table 10. Magnitudes of the complete sum-frequency pitch moment QTF, $|M_{jl}^+/\rho g a^2 A_j A_l|$, and each of its components for uniform vertical cylinders with respect to the center of waterplane. The upper triangular matrix is for h/a=1, and lower part for h/a=4. On the diagonal, () is for h/a=4. Each element satisfies symmetry relation, $M_{jl}^+=M_{lj}^+$. Computed values are for: first row; $|M_{qjl}^+|$, second row; $|M_{pjl}^+|$, and third row $|M_{qjl}^+ + M_{pjl}^+|$.

$\nu_j a$=	1.0	1.2	1.4	1.6	1.8	2.0
$\nu_l a$= 1.0	0.217(0.235) 0.785(4.472) 0.635(4.309)	0.199 0.942 0.794	0.184 1.089 0.939	0.166 1.194 1.048	0.145 1.228 1.094	0.121 1.179 1.063
1.2	0.254 4.220 4.028	0.181(0.262) 1.071(4.934) 0.927(4.738)	0.164 1.181 1.039	0.147 1.252 1.117	0.126 1.256 1.136	0.103 1.180 1.079
1.4	0.272 3.762 3.524	0.267 4.777 4.554	0.147(0.259) 1.251(5.237) 1.116(5.011)	0.130 1.285 1.162	0.109 1.262 1.156	0.086 1.167 1.082
1.6	0.279 3.481 3.219	0.264 4.333 4.092	0.245 5.079 4.851	0.112(0.223) 1.295(5.580) 1.185(5.364)	0.094 1.265 1.173	0.073 1.179 1.106
1.8	0.270 3.088 2.829	0.248 3.739 3.505	0.223 4.332 4.120	0.196 5.231 5.037	0.078(0.168) 1.255(6.037) 1.178(5.869)	0.063 1.217 1.155
2.0	0.246 2.569 2.331	0.221 3.008 2.798	0.191 3.351 3.168	0.164 3.983 3.821	0.138 5.421 5.283	0.058(0.116) 1.254(6.502) 1.198(6.387)

In Figure 5, the second-order potential pressure QTFs, p_{pjl}^+, along the vertical cylinder of h/a=1 are given for five angular positions. In this case, variations in p_{pjl}^+ for different angular positions are large due to the dominant contribution from angular-dependent free-surface pressures. The decay rate at the waveward side is much slower than that of leeward side. Along the leeward edge(θ=0), the nonlinear potential pressure initially decreases with depth, reaches a minimum, and then begins to increase towards the bottom. We also see that a minimum of p_{pjl}^+ may not occur at the bottom of the cylinder. Similar trends were given for monochromatic waves in Chapter I.

In Figure 6, we present the second-order potential run-up QTF, η_{pjl}^+, as well as the linear quadratic contribution, η_{qjl}^+, around a vertical cylinder of h/a=1, for two different incident frequency combinations; $(\nu_j a, \nu_l a)=(1,2)$ and (1.4,1.6). Both η_{pjl}^+ and η_{qjl}^+ are not sensitive to changes in $\Delta\nu a$ when compared with the difference-frequency case (see Figure 2). The magnitude of η_{qjl}^+ generally increases from the lee(θ=0) to weather side($\theta=\pi$), whereas η_{pjl}^+ has two peaks near $\theta=\pi/4$ and π, which are comparable in magnitude.

We next consider, in Table 11, the horizontal and vertical sum-frequency force QTFs on a fixed hemisphere of h/a=3. Again, contributions associated with ϕ_I^+, f_{Ijl}^+ and f_{BIjl}^+, are negligible in the bifrequency range considered, and hence are not given separately. In the horizontal direction f_{qjl}^+ and f_{pjl}^+ are comparable in magnitude, but in the vertical direction, f_{pjl}^+ is dominant over f_{qjl}^+. This is due to appreciable second-order potential pressures on the bottom of the sphere, which was previously observed. For both horizontal and vertical forces, f_{qjl}^+ and f_{pjl}^+ are generally out of phase, and hence the complete QTF is much smaller than the individual sum. Interestingly, the complete vertical sum-frequency forces are large and become even more important with increasing sum frequency.

In Figure 7, we present the sum- and difference-frequency potential run-up, $\eta_p^{\pm}$, around a fixed sphere for two frequency combinations. The general trend for η_p^- is very close to that of the vertical cylinder given in Figure 3. For η_{pjl}^+, the trend is similar to Figure 6 with the exception that we have a more dominant peak on the weather side.

Table 11. Magnitudes of the complete sum-frequency force QTF, $|f_{jl}^+/\rho g a A_j A_l|$, and each of its components for a fixed hemisphere of h/a=3. The upper triangular matrix is for horizontal forces, and lower part for vertical forces. On the diagonal, () is for vertical forces. Each element satisfies the symmetry relation $f_{jl}^+=f_{lj}^+$. Computed values are for: first row; $|f_{qjl}^+|$, second row; $|f_{pjl}^+|$, and third row; the complete QTF $|f_{jl}^+|$.

$\nu_j a=$	1.0	1.2	1.4	1.6	1.8	2.0
$\nu_l a=$ 1.0	1.247(0.320)	1.268	1.317	1.399	1.485	1.538
	1.104(1.229)	1.249	1.412	1.594	1.747	1.830
	0.730(0.914)	0.704	0.692	0.681	0.655	0.610
1.2	0.278	1.333(0.237)	1.409	1.496	1.569	1.600
	1.192	1.426(1.182)	1.604	1.777	1.905	1.954
	0.918	0.663(0.948)	0.642	0.628	0.603	0.560
1.4	0.230	0.191	1.488(0.147)	1.560	1.607	1.607
	1.055	1.055	1.774(0.937)	1.918	2.006	2.015
	0.827	0.865	0.614(0.790)	0.600	0.579	0.541
1.6	0.187	0.151	0.114	1.604(0.094)	1.617	1.586
	0.909	0.968	0.859	2.024(0.874)	2.079	1.995
	0.722	0.819	0.745	0.592(0.781)	0.585	0.518
1.8	0.157	0.126	0.100	0.096	1.598(0.108)	1.545
	0.816	0.812	0.836	0.971	2.057(1.187)	2.032
	0.660	0.687	0.736	0.877	0.563(1.083)	0.570
2.0	0.139	0.116	0.102	0.107	0.122	1.484(0.133)
	0.759	0.789	0.859	1.055	1.342	2.017(1.572)
	0.620	0.673	0.758	0.951	1.225	0.606(1.444)

We next investigate how the trend of sum-frequency excitation is changed when we allow first-order motions. In contrast to the difference-frequency case, displayed in Table 7, the body-surface forcing term due to linear motions; f_{BBjl}^{+}, contributes significantly and this effect is even stronger for vertical forces. The linear square term, f_{qjl}^{+}, is amplified in both the horizontal and vertical directions when we include linear motions, especially near the heave resonance frequency. Major contributions in this case, as shown in Table 12, are f_{qjl}^{+}, f_{BBjl}^{+}, and f_{Fjl}^{+}. These forces generally do not act in phase, hence the magnitude of the total QTF is much less than the individual sum. Nevertheless, magnitudes of the complete horizontal and vertical force QTFs are increased by first-order body motions. With increasing sum-frequency and fixed $\Delta\nu a$, f_{Fjl}^{+} continues to increase its relative importance over the other contributions, while f_{BBjl}^{-} decreases, and f_{qjl}^{-} approaches the result of the fixed sphere due to the decreasing effects of linear motion. As a result, f_{qjl}^{+} and f_{BBjl}^{+} are the most important contributions in the small sum-frequency region, $(\nu_j+\nu_l)a < 2.8$, but f_{Fjl}^{+} dominates other contributions for $(\nu_j+\nu_l)a > 2.8$. It is also noticible that f_{qjl}^{+} and f_{BBjl}^{+} are greatly increased near the heave resonance frequency, which was not conspicuous in the difference-frequency case.

Table 12. Magnitudes of the complete sum-frequency force QTF, $|f_{jl}^{+}/\rho g a A_j A_l|$, and each of its components for a freely-floating hemisphere of h/a=3. The upper triangular matrix is for horizontal forces, and lower part for vertical forces. On the diagonal, () is for vertical forces. Each element satisfies the symmetry relation, $f_{jl}^{+}=f_{lj}^{+}$. Computed values are for: first row; $|f_{qjl}^{+}|$, second row; $|f_{BBjl}^{+}|$, third row; $|f_{Ijl}^{+}+f_{BIjl}^{+}+f_{Fjl}^{+}|$, and fourth row; $|f_{jl}^{+}|$.

$\nu_j a$=	1.0	1.2	1.4	1.6	1.8	2.0
$\nu_l a$=	2.646(3.467)	2.551	2.107	1.916	1.797	1.677
1.0	1.198(4.427)	0.999	0.762	0.682	0.648	0.623
	1.573(0.984)	1.767	1.568	1.459	1.357	1.226
	1.041(1.461)	0.977	0.812	0.733	0.678	0.632
	2.702	2.871(2.085)	2.548	2.373	2.263	2.151
1.2	3.826	1.031(3.219)	0.829	0.727	0.675	0.642
	0.778	2.336(1.204)	2.282	2.233	2.169	2.060
	1.877	1.067(2.338)	0.948	0.879	0.822	0.761
	1.539	1.200	2.302(0.720)	2.154	2.061	1.965
1.4	2.459	2.034	0.653(1.254)	0.555	0.504	0.474
	0.565	1.134	2.293(1.142)	2.266	2.216	2.117
	1.517	1.866	0.857(1.516)	0.806	0.760	0.705
	0.962	0.771	0.496	2.010(0.378)	1.916	1.823
1.6	1.747	1.483	0.897	0.458(0.638)	0.409	0.368
	0.517	1.109	1.180	2.249(1.331)	2.215	2.079
	1.280	1.632	1.372	0.778(1.383)	0.759	0.694
	0.656	0.553	0.393	0.330	1.822(0.307)	1.735
1.8	1.356	1.102	0.697	0.502	0.348(0.399)	0.322
	0.522	1.022	1.204	1.456	2.169(1.696)	2.141
	1.159	1.375	1.305	1.451	0.752(1.653)	0.766
	0.473	0.431	0.340	0.306	0.295	1.665(0.284)
2.0	1.103	0.901	0.575	0.419	0.338	0.291(0.288)
	0.493	0.994	1.191	1.473	1.786	2.178(1.977)
	1.051	1.278	1.254	1.450	1.734	0.829(1.918)

6. CONCLUSION

The second-order diffraction and radiation problems for fixed or freely-floating axisymmetric bodies in the presence of plane bichromatic incident waves are solved by the ring-source integral equation method. An important part of the solution is the efficient and accurate evaluation of the boundary forcing terms, particularly the poorly convergent free-surface integrals. An approach which treats the entire local-wave-free outer region analytically is developed and shown to be efficacious for both sum- and difference-frequency problems. Although the second-order sum- and difference-frequency potentials and associated local solutions are solved explicitly, the present method is comparable in computational effort to existing approaches (Eatock Taylor et al, 1988; Matsui, 1988) which utilize fictitious radiation potentials to obtain global second-order quantities. On the other hand, the availability of the second-order potential allows us to discover and explain many important local second-order phenomena associated with the pressures and free-surface elevations.

For illustration, the sum- and difference-frequency problems for bottom-mounted vertical cylinders of h/a=1 and 4, and fixed and freely-floating hemispheres, are studied in some detail. Convergence tests with respect to truncations and discretizations, as well as, comparisons to semi-analytic solutions for the vertical cylinders (Appendix C), confirm the validity and accuracy of the present calculations.

From our numerical examples, several important features of the second-order solutions have been observed:

(1) Difference-frequency problem: Among the individual contributions to the second-order force, the linear quadratic term, f_{qj1-}, and second-order incident wave contributions, f_{Ij1}^- & f_{BIj1}^-, are found to be the most important. The second-order difference-frequency incident potential,

ϕ_I^-, attenuates slowly with depth especially for small frequency differences. As a result, f_{Ijl}^- & f_{BIjl}^- have large slopes near the diagonal and are particularly important when the draft of a body is large, or when major portions of the body are deeply submerged. The resulting slowly-varying vertical forces for these bodies may be appreciable. In this case, the validity of Newman's or Marthinsen's approximation methods may no longer be justified. On the other hand, Pinkster's (or QIB) approximation is expected to give good engineering results for a broad class of input spectra without a substantial increase in computing time. The pressures and run-up associated with ϕ^- are found to be relatively constant around the body, especially when the two frequencies are close. Any pairs of waves in a sea spectrum, which satisfy $\omega^-=\omega_n$, can excite slowly-varying resonant responses, and are particularly important when damping forces are small at that frequency.

(2) Sum-frequency problem: In contrast to the difference-frequency problem, the second-order locked wave potential, ϕ_p^+, plays an important role. This free-surface contribution cannot be neglected in favor of other contributions, and hence any approximation method excluding this term will likely be inadequate regardless of the shape of the input spectra. On the other hand, contributions associated with ϕ_I^+ are negligible except for the long wave (or equivalently, shallow water) regime. The body-boundary forcing contribution due to linear motions, f_{BBjl}^+, is found to be much more important in the sum-frequency problem. The second-order sum-frequency potential, ϕ^+, attenuates slowly with depth, especially on the weather side. Interestingly, this second-order potential pressure, p_{pjl}^+, penetrates deeper for smaller frequency difference pairs. Because of these phenomena, pitch-roll moments of large draft bodies can be greatly magnified particularly when the center of rotation is close to the free surface. A typical example is the superharmonic pitch-roll excitation and response of a TLP. Petrauskas & Liu's (1987) method, which is based on an approximated QTF f_{qjl}^+, substantially underestimates the springing motions of the TLP when compared to experimental measurements. This large discrepancy may be attributed to contributions from the second-order potential (see Chapter IV). The sum-frequency second-order potential pressures and run-up have large variations around the body due to significant contributions from the free-surface forcing pressures.

The present theory and numerical results for bichromatic waves can be easily applied to the estimation of the slowly-varying or springing wave excitations and responses in irregular seas. This will be studied in Part two.

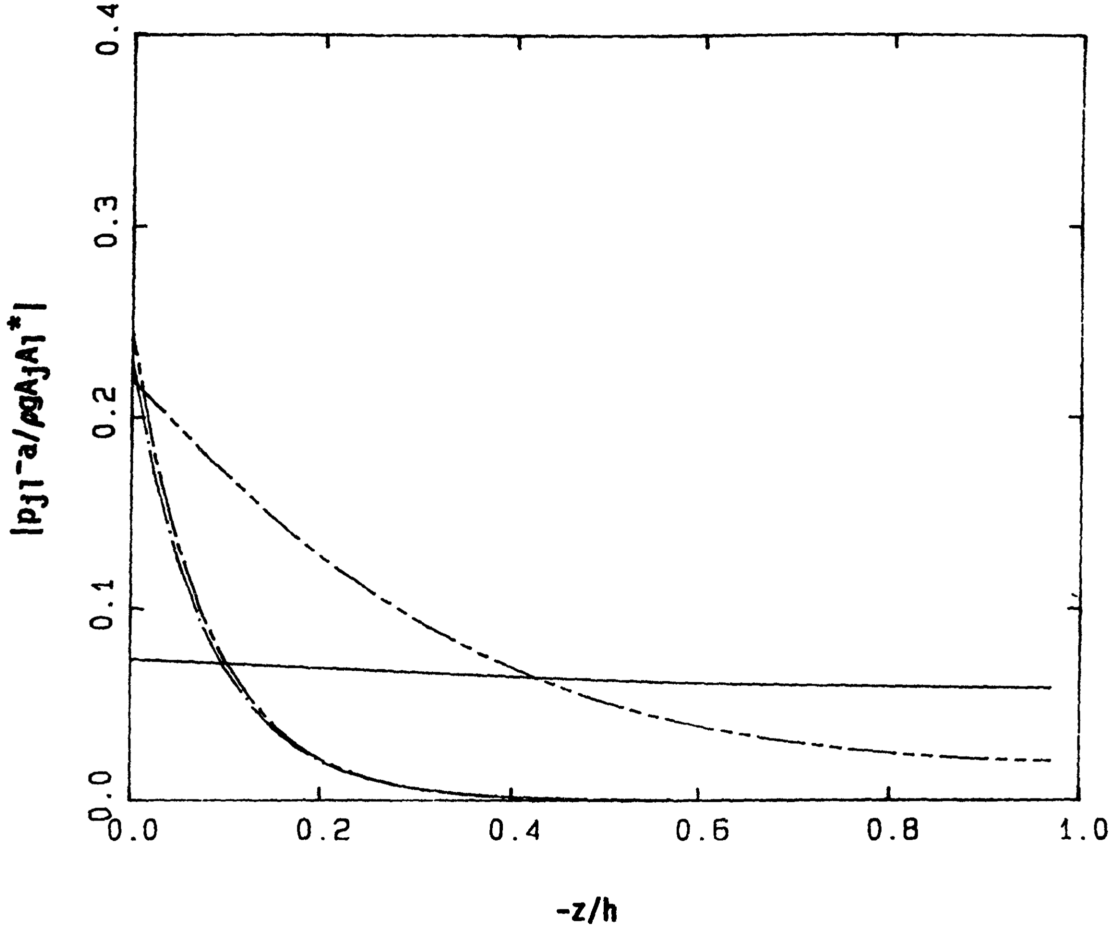

Figure 1a. The second-order slowly-varying pressure QTFs at the lee side (θ=0) of a vertical cylinder of h/a=4. The curves are for: $|p_{qjl}^-|$ for $\nu_j a, \nu_l a$= 1,2 (—— • ——); 1.4,1.6 (—— - ——), and $|p_{pjl}^-|$ for $\nu_j a, \nu_l a$= 1,2 (—— - - ——); 1.4,1.6 (————).

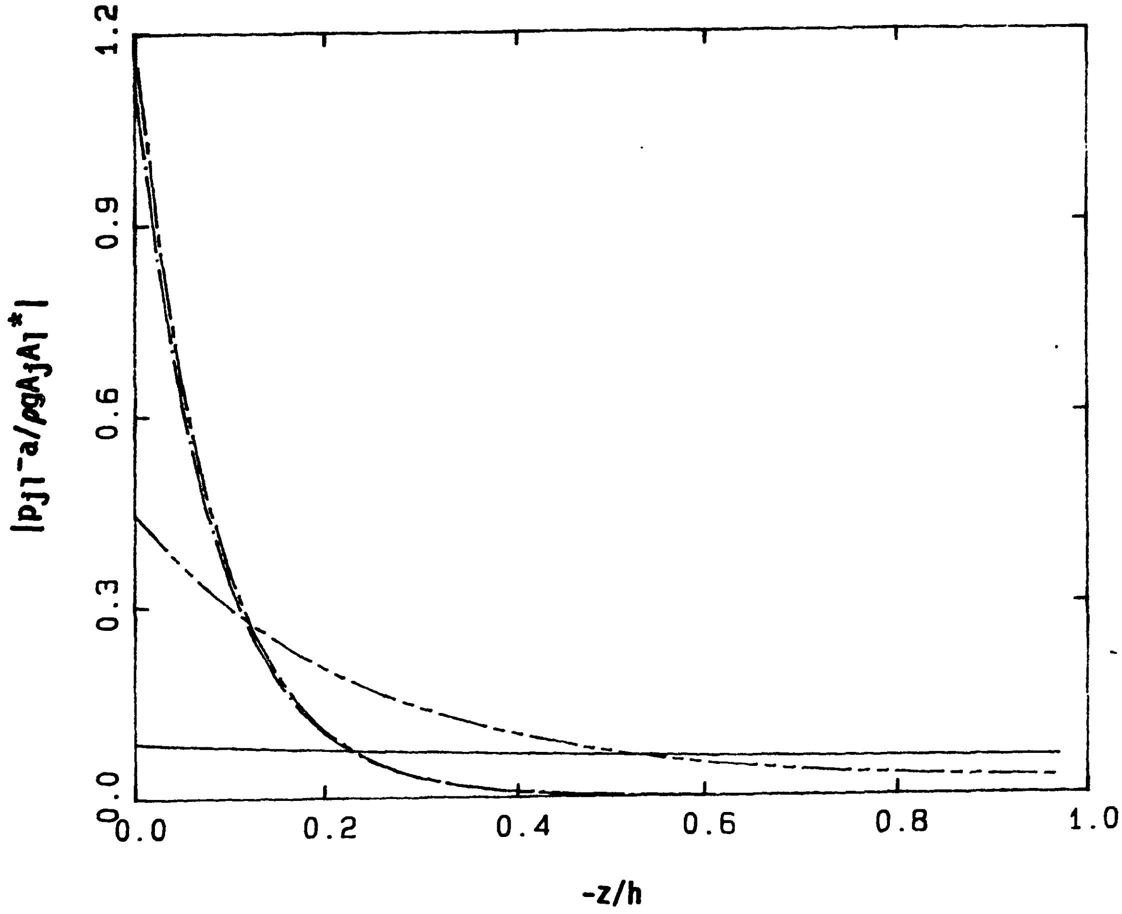

Figure 1b. The second-order slowly-varying pressure QTFs at the weather side ($\theta=\pi$) of a vertical cylinder of h/a=4. The curves are for: $|p_{qj1}^-|$ for $\nu_j a, \nu_1 a$= 1,2 (—— • ——); 1.4,1.6 (—— - ——), and $|p_{pj1}^-|$ for $\nu_j a, \nu_1 a$= 1,2 (—— - - - ——); 1.4,1.6 (————).

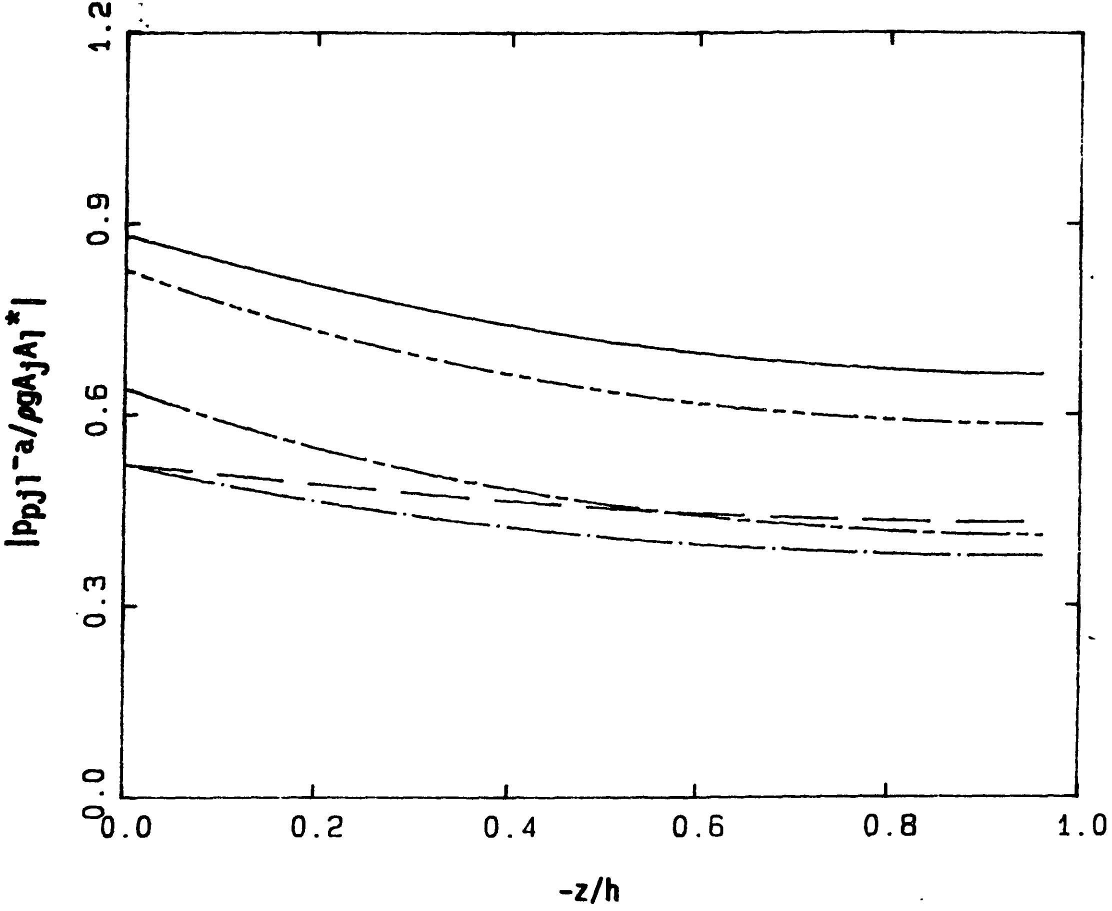

Figure 2. The slowly-varying second-order potential pressure QTFs, $|p_{pjl}^{-}|$, for $(\nu_j a, \nu_l a)=(1,2)$ around a vertical cylinder of h/a=1. The curves are for: $\theta=0$ (------), $\theta=\pi/4$ (—— • ——), $\theta=\pi/2$ (—— - ——), $\theta=3\pi/4$ (—— - - ——), and $\theta=\pi$ (————).

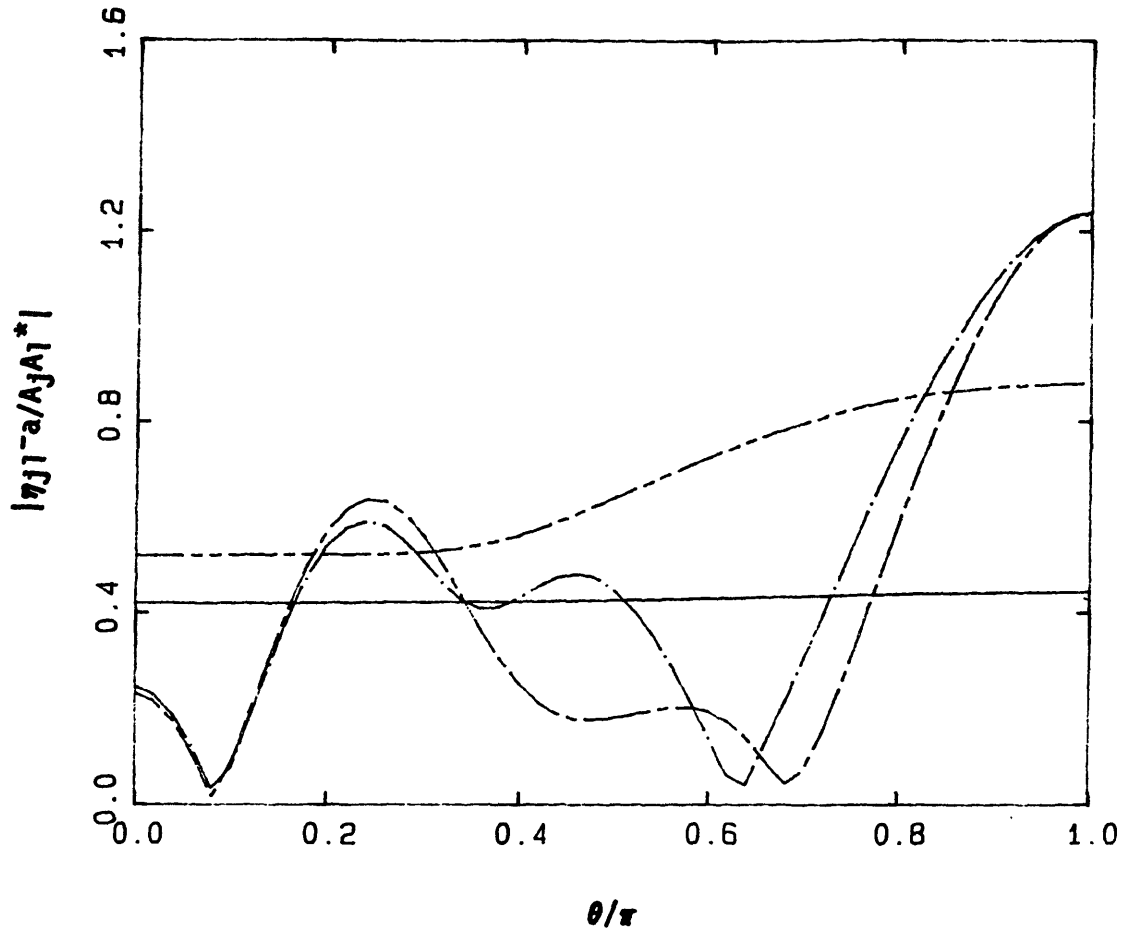

Figure 3. The second-order slowly-varying run-up QTFs, η_{qjl}^- and η_{pjl}^-, around a vertical cylinder of h/a=1. The curves are for: $|\eta_{qjl}^-|$ for $\nu_j a, \nu_l a$= 1,2 (—— • ——); 1.4,1.6 (—— – ——), and $|\eta_{pjl}^-|$ for $\nu_j a, \nu_l a$= 1,2 (—— – – ——); 1.4,1.6 (————).

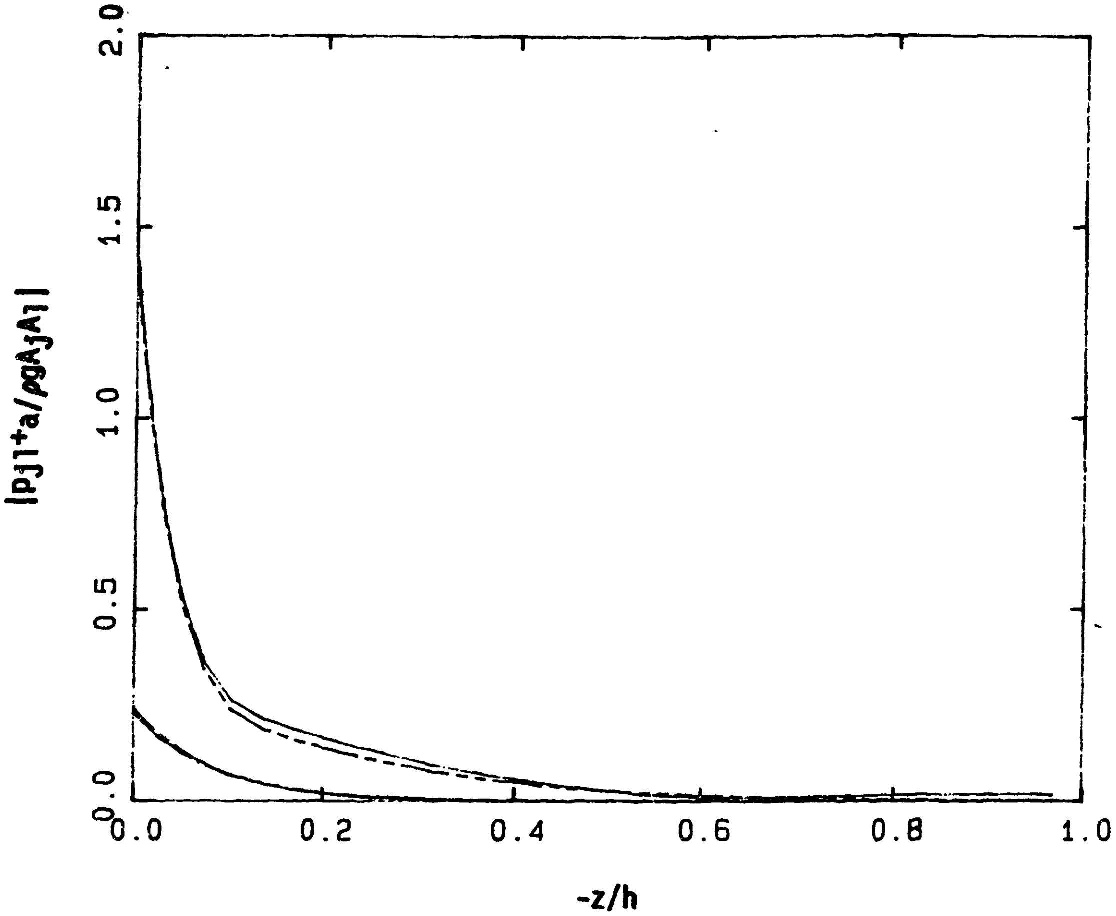

Figure 4a. The second-order sum-frequency pressure QTFs at the lee side (θ=0) of a vertical cylinder of h/a=4. The curves are for: $|p_{qj1}^{+}|$ for $\nu_j a,\nu_1 a$= 1,2 (—— • ——); 1.4,1.6 (—— - - ——), and $|p_{pj1}^{+}|$ for $\nu_j a,\nu_1 a$= 1,2 (—— - - - ——); 1.4,1.6 (————).

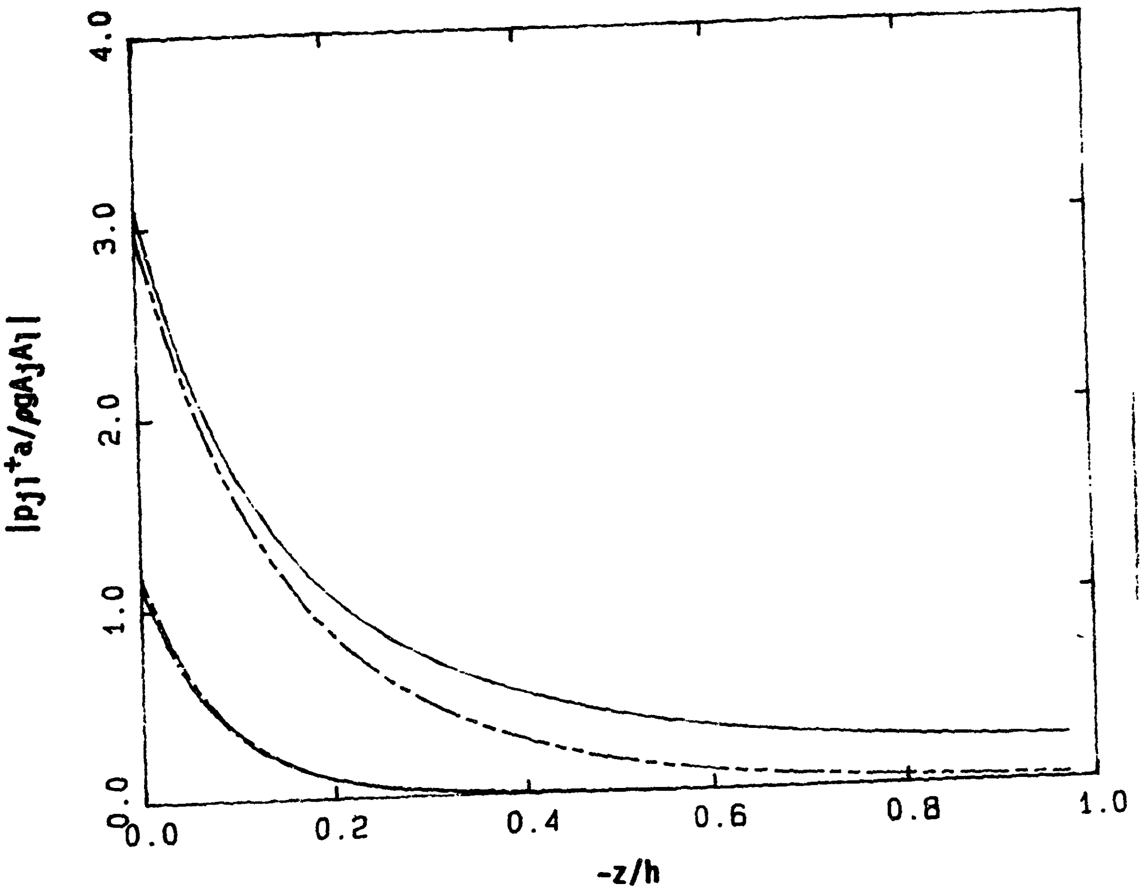

Figure 4b. The second-order sum-frequency pressure QTFs at the weather side ($\theta=\pi$) of a vertical cylinder of h/a=4. The curves are for: $|p_{qjl}^{+}|$ for $\nu_j a, \nu_l a$= 1,2 (—— • ——); 1.4,1.6 (—— – ——), and $|p_{pjl}^{+}|$ for $\nu_j a, \nu_l a$= 1,2 (—— – – ——); 1.4,1.6 (————).

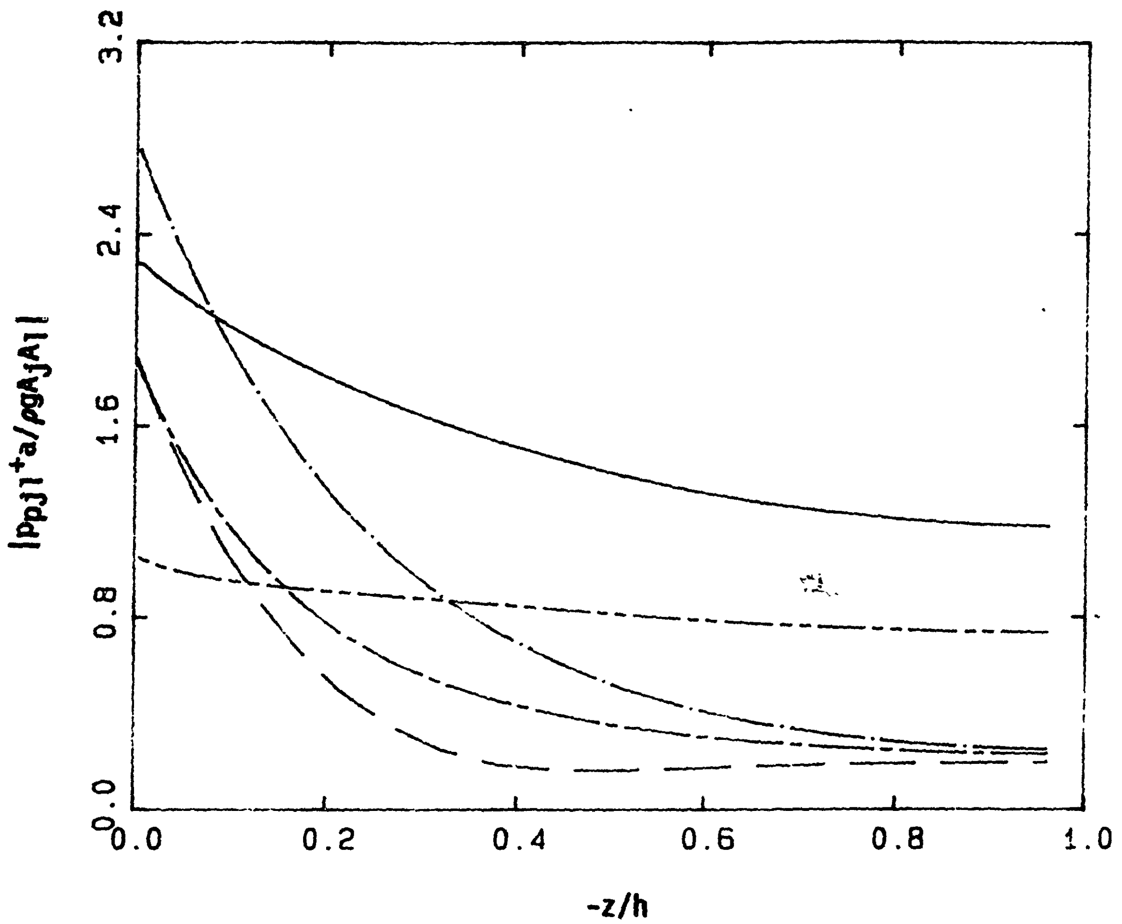

Figure 5. The sum-frequency second-order potential pressure QTFs, $|p_{pjl}{}^{+}|$, for $(\nu_j a, \nu_l a)=(1,2)$ around a vertical cylinder of h/a=1. The curves are for: $\theta=0$ (------), $\theta=\pi/4$ (—— • ——), $\theta=\pi/2$ (—— – ——), $\theta=3\pi/4$ (—— – – ——), and $\theta=\pi$ (————).

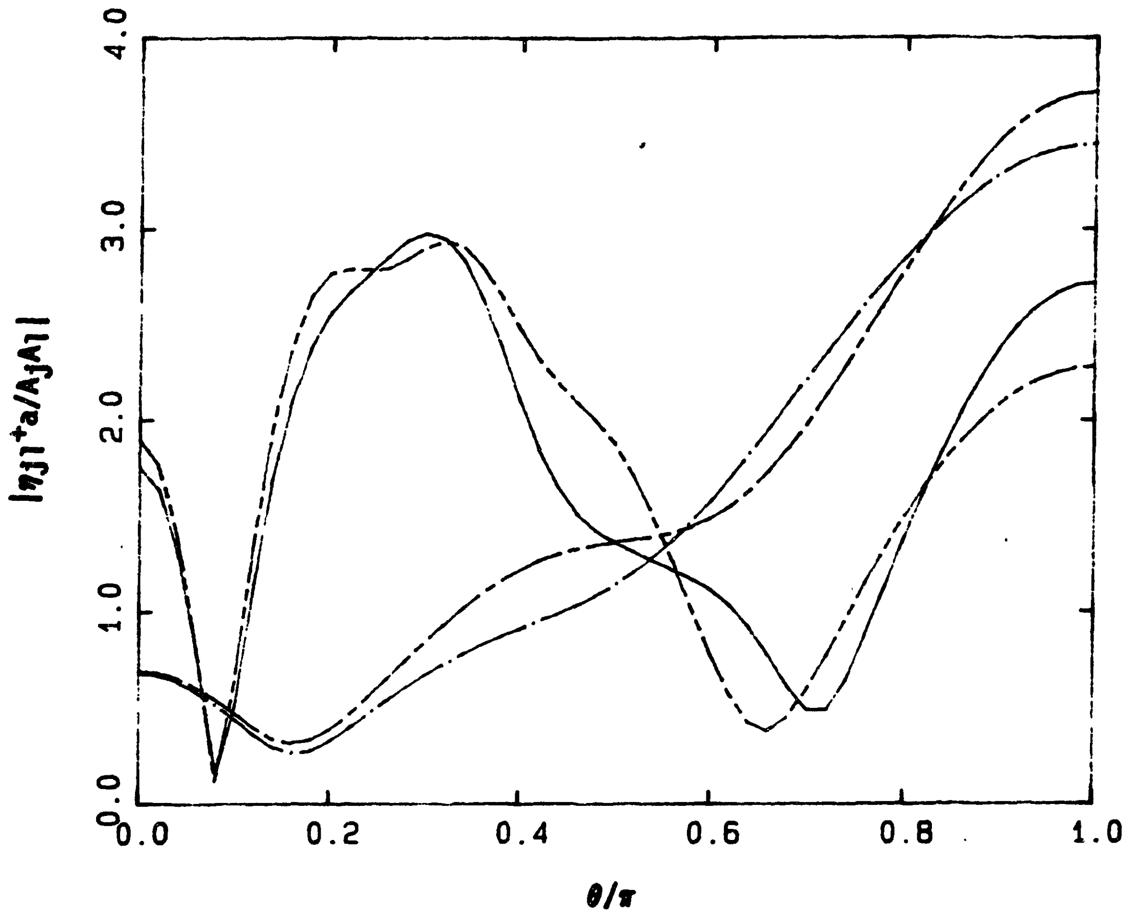

Figure 6. The second-order sum-frequency run-up QTFs, $\eta_{qjl}{}^{+}$ and $\eta_{pjl}{}^{+}$, around a vertical cylinder of h/a=1. The curves are for: $|\eta_{qjl}{}^{+}|$ for $\nu_j a, \nu_l a$= 1,2 (—— • ——); 1.4,1.6 (——— - - ——), and $|\eta_{pjl}{}^{+}|$ for $\nu_j a, \nu_l a$= 1,2 (—— - - - ——); 1.4,1.6 (————).

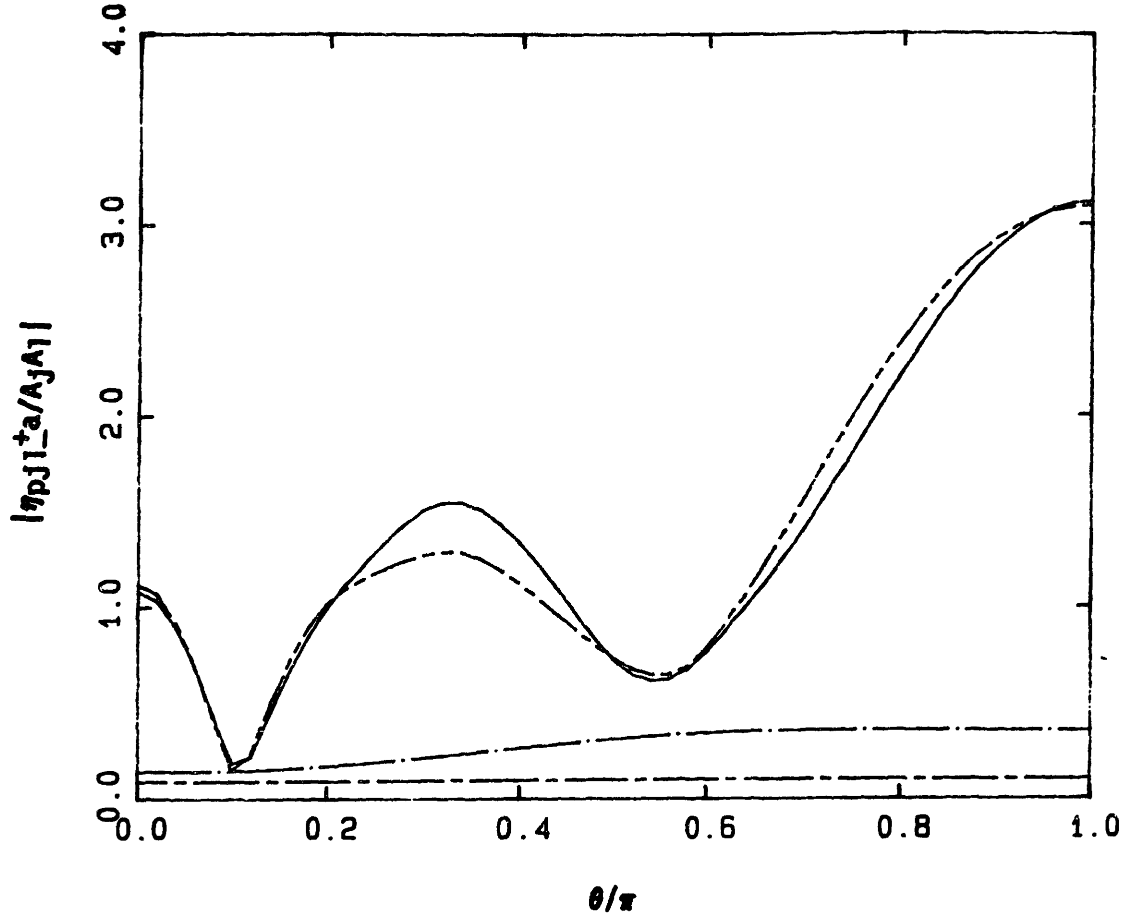

Figure 7. The sum- and difference-frequency second-order potential run-up QTFs, $\eta_{pjl}{}^{+}_{-}$, around a fixed hemisphere of h/a=3. The curves are for: $|\eta_{pjl}{}^{-}|$ for $\nu_j a, \nu_l a$= 1,2 (—— • ——); 1.4,1.6 (—— – ——), and $|\eta_{pjl}{}^{+}|$ for $\nu_j a, \nu_l a$= 1,2 (—— – – ——); 1.4,1.6 (————).

PART TWO

APPLICATION TO RANDOM SEAS AND STATISTICS

There are three kinds of lies; lies, damned lies, and statistics

- Benjamin Disraeli -

CHAPTER III

THE STATISTICAL DISTRIBUTION OF SECOND-ORDER WAVE EXCITATIONS IN UNIDIRECTIONAL RANDOM SEAS.

1. INTRODUCTION

When the natural frequency of a offshore structure is much lower or higher than the appreciable wave energy band of the input spectrum, the second-order wave forces and responses may dominate linear quantities and become critical to engineering design. Typical examples are the resonant vertical-plane springing motions of tension-leg platforms and the large-amplitude slowly-varying surge motions of moored vessels.

It is well known that for time-invariant linear system the output due to a Gaussian input is also Gaussian, and the output spectrum gives sufficient information for its statistical distribution. For nonlinear systems with memory (e.g. a two-term Volterra series), the output process due to a Gaussian input is non-Gaussian, and hence the spectral analysis gives only limited information about the probabilty distribution. In general, then, the probability density functions of second-order forces and responses in Gaussian random seas must be derived based on the input wave spectrum and the quadratic transfer function(QTF) of a system.

In Chapter II, we obtained the complete force quadratic transfer functions(QTF) for bichromatic incident waves. Based on this information, we consider in this chapter the complete statistical properties of the second-order forces in unidirectional Gaussian random seas. The most widely used mathematical model for the present problem is a two-term Volterra functional polynomial expansions (or Volterra series). The complete probabilistic distribution of this model was first developed in the communication field by Kac & Siegert(1947) and Bedrosian & Rice(1971), and introduced to ocean engineerng applications by Neal(1974). Since then, the theory has been reexamined and applied mainly to the study of slowly-varying wave forces (e.g. Pinkster, 1980; Vinje, 1983; Naess, 1986).

Despite the progress made in the statistical theory, the Volterra model has so far only been applied to some two-dimensional geometries because complete QTFs for three-dimensional bodies have not been available until recently. In view of the theoretical and numerical difficulties associated with the second-order problem, numerous approximation methods based on approximated QTFs (see Chapter II) have been widely used in engineering applications without necessarily any confidence that they will lead to a safe design.

In this chapter, we study the statistical properties of the second-order wave excitations in unidirectional random seas (for multidirectional seas, see Chapter V). For illustration, we calculate the complete difference-frequency force PDFs and spectra for a large-draft truncated vertical cylinder, and compared them to those based on approximated QTFs (e.g. Newman, 1974; Pinkster, 1980; Standing & Dacunha, 1982). Our numerical results reveal that some approximation methods may substantially underestimate the probabilty of difference-frequency extreme loads.

For the related sum-frequency problem, the analysis follows closely with the exception that explicit expressions for the probability distribution are in general not possible and numerical evaluations are required. As is commonly known, the PDF's themselves are typically not so important for springing forces in view of practical applications where information on the spectra and variance (rms) are more relevant, for example, for the fatigue design of mooring cables. This is addressed in the case of a tension-leg platform in Chapter IV.

2. THE COMPLETE PROBABILITY DISTRIBUTION OF A TWO-TERM VOLTERRA SERIES

We consider the general statistical properties of the second-order wave loads on a body due to stationary Gaussian random seas. A two-term Volterra series is used as a mathematical model for this problem. Then, the total wave force F(t) has the following expression:

$$F(t) = F^{(1)}(t) + F^{(2)}(t) =$$

$$\int_{-\infty}^{\infty} h^{(1)}(\tau)\, \varsigma(t-\tau)\, d\tau + \int_{-\infty}^{\infty}\int_{-\infty}^{\infty} h^{(2)}(\tau_1,\tau_2)\, \varsigma(t-\tau_1)\, \varsigma(t-\tau_2)\, d\tau_1 d\tau_2 \tag{2.1}$$

where $h^{(1)}(\tau)$ and $h^{(2)}(\tau_1,\tau_2)$ are respectively the linear and quadratic impulse response functions. The unidirectional (Gaussian with zero mean) random sea surface $\varsigma(t)$ at some reference point can be expressed as a sum of component waves:

$$\varsigma(t) = \sum_j a_j \cos(\omega_j t + \epsilon_j) = \mathrm{Re} \sum_j A_j\, e^{i\omega_j t}$$

(2.2)

where a_j, ω_j, and ϵ_j are the amplitude, frequency, and phase of the j-th wave component, and ϵ_j is a uniformly distributed random variable in $[0,2\pi]$. Substituting (2.2) into (2.1), we obtain an equivalent expression of F(t) in the frequency domain:

$$F^{(1)}(t) = \mathrm{Re} \sum_j A_j \; H^{(1)}(\omega_j) \; e^{i\omega_j t} \tag{2.3}$$

$$F^{(2)}(t) = F^{-}(t) + F^{+}(t) =$$

$$\mathrm{Re} \sum_j \sum_k \left[A_j A_k^* \; H^{(2)}(\omega_j,-\omega_k) \; e^{i(\omega_j-\omega_k)t} + A_j A_k H^{(2)}(\omega_j,\omega_k) \; e^{i(\omega_j+\omega_k)t} \right] \tag{2.4}$$

where $()^*$ represents the complex conjugate of a quantity. The first term of (2.4) describes the difference-frequency (slowly-varying) forces, and the second term the sum-frequency (springing) forces. $H^{(1)}$ and $H^{(2)}$ are the linear and quadratic transfer functions of $F^{(1)}$ and $F^{(2)}$, respectively. These are given by the Fourier transforms of $h^{(1)}$ and $h^{(2)}$:

$$H^{(1)}(\omega) = \int_{-\infty}^{\infty} h^{(1)}(\tau) \; e^{-i\omega\tau} \, d\tau$$

$$H^{(2)}(\omega_j,\omega_k) = \int\!\!\int_{-\infty}^{\infty} h^{(2)}(\tau_1,\tau_2) \; e^{-i(\omega_j\tau_1+\omega_k\tau_2)} \; d\tau_1 d\tau_2 \tag{2.5}$$

The quadratic impulse response or transfer functions may, without loss of generality, be assumed to be symmetrical. The quadratic transfer function $H^{(2)}$, for example, satisfies the following symmetric conditions:

$$H^{(2)}(\omega_j,-\omega_k) = H^{(2)*}(\omega_k,-\omega_j) \quad , \quad H^{(2)}(\omega_j,\omega_k) = H^{(2)}(\omega_k,\omega_j) \tag{2.6}$$

The complete probabilistic theory for a nonlinear time-invariant Volterra system represented by (2.1) or (2.4) was first obtained by Kac & Siegert (1947), and later reexamined by Bedrosian & Rice (1971) and Neal (1974). As shown in the above references, F(t) may be decomposed in the following way:

$$F(t) = \sum_n [\, c_n W_n(t) + \lambda_n W_n^2(t) \,] \tag{2.7}$$

where $W_n(t)$ are normalized Gaussian variables which are mutually independent. The coefficients λ_n are the eigenvalues of the following integral equation:

$$\int_{-\infty}^{\infty} K(\omega,\omega') \, \gamma(\omega') \, d\omega' = \lambda \, \gamma(\omega) \tag{2.8}$$

The Hermitian kernel $K(\omega,\omega')$ is given by:

$$K(\omega,\omega') = \sqrt{s(\omega)} \, H^{(2)}(\omega,-\omega') \, \sqrt{s(\omega')} \tag{2.9}$$

where $s(\omega)$ is a two-sided input wave spectrum. From the properties of a Hermitian kernel, λ_n are real, and the orthonormal eigenfunctions, γ_n, satisfy $\gamma_n(-\omega)=\gamma_n^*(\omega)$. The coefficients c_n in (2.7) are given by:

$$c_n = \int_{-\infty}^{\infty} H^{(1)}(\omega) \, \sqrt{s(\omega)} \, \gamma_n(\omega) \, d\omega \tag{2.10}$$

Then, the characteristic function of F(t) is given by:

$$\Theta_F(\theta) = \frac{1}{\prod_n (1 - i2\lambda_n\theta)^{1/2}} \operatorname{Exp}\left[- \sum_n \frac{\theta^2 c_n^2}{2(1 - i2\lambda_n\theta)} \right] \tag{2.11}$$

and the corresponding probability density function of F(t) can be obtained from the inverse Fourier transform of (2.11):

$$p(F) = \frac{1}{2\pi} \int_{-\infty}^{\infty} \Theta(\theta)\, e^{-i\theta F}\, d\theta \tag{2.12}$$

In general, (2.12) can only be computed numerically except for some special cases, as shown in the next section.

3. THE EXPLICIT PROBABILITY DENSITY FUNCTION OF THE DIFFERENCE-FREQUENCY WAVE EXCITATIONS

If we only consider the second-order term, $F^{(2)}(t)$, $c_n=0$ in (2.11), and we obtain a simpler form:

$$\Theta_{F^{(2)}}(\theta) = \frac{1}{\prod_n (1 - i2\lambda_n\theta)^{1/2}} \tag{3.1}$$

The probability distributions of the slowly-varying extreme forces and corresponding large-amplitude motions are important design considerations, and we focus hereafter on the second-order difference-frequency wave forces represented by the first term of (2.4):

$$F^{-}(t) = \operatorname{Re} \sum_j \sum_k A_j A_k^* D_{jk}\, e^{i(\omega_j - \omega_k)t} \tag{3.2}$$

For convenience, we use the notation; $D_{jk} \equiv f_{jk}^{-} \equiv 2H^{(2)}(\omega_j, -\omega_k)$ for $\omega_j, \omega_k \geq 0$, where $D_{jk} = D_{kj}^*$. The mean of $F^{-}(t)$ is obtained when j=k in (3.2):

$$E(F^-) = \sum_j a_j^2 D_{jj} = 2\int_0^\infty S(\omega)\; D(\omega,\omega)\; d\omega \tag{3.3}$$

where $S(\omega)$ is a one-sided input wave spectrum ($S(\omega) = 2s(\omega)$ for $\omega \geq 0$, and $S(\omega)=0$ for $\omega < 0$). The one-sided spectrum of $F^-(t)$ can be obtained from the continuous form of the autocorrelation function of (3.2) after using Wiener-Kinchin relation (see Chapter V) as follows:

$$S_{F^-}(\mu) = 8\int_0^\infty S(\omega)\; S(\omega+\mu)\; |D(\omega,\omega+\mu)|^2\; d\omega \tag{3.4}$$

The variance of $F^-(t)$ is then simply given by the area of S_{F^-}. As pointed out by Naess (1986), the probability density function of F^- can be derived in an explicit form. For difference-frequency excitations only, we set $H^{(2)}(\omega,\omega')=0$ for $\omega \cdot \omega' > 0$. The integral equation (2.8) then generates a set of double eigenvalues, $\lambda_{2n-1}=\lambda_{2n}=\nu_n$, and can be rewritten in the form:

$$\int_0^\infty K(\omega,\omega')\; \beta(\omega')\; d\omega' = \nu\; \beta(\omega) \qquad (\, \omega \geq 0 \,) \tag{3.5}$$

where $K(\omega,\omega') \equiv \sqrt{S(\omega)}\; D(\omega,\omega')\; \sqrt{S(\omega')}$. Again, the eigenvalue problem (3.5) must in general be solved numerically given $D(\omega,\omega')$.

From (3.1) and the independence property of $W_n(t)$, we obtain:

$$\Theta_{F^-}(\theta) = \frac{1}{\prod_n (\, 1 - i2\nu_n\theta \,)} \tag{3.6}$$

Using residue theorem, (3.6) can be inverted analytically leading to the following explicit probability density function of $F^-(t)$:

$$p(F^-) = \sum_{n=1}^{M} \frac{A_n}{2\nu_n} \text{Exp} \left[-\frac{F^-}{2\nu_n} \right] \qquad \text{for } F^- \geq 0$$

$$p(F^-) = \sum_{n=M+1}^{N} \frac{A_n}{2|\nu_n|} \text{Exp} \left[\frac{F^-}{2|\nu_n|} \right] \qquad \text{for } F^- < 0 \tag{3.7}$$

where N is the total number of eigenvalues, and $\nu_n > 0$ for n=1,•••,M and $\nu_n < 0$ for n=M+1,•••,N. The coefficients A_n are given by:

$$A_n = \prod_{m=1,(m \neq n)}^{N} \frac{\nu_n}{\nu_n - \nu_m} \tag{3.8}$$

The mean and variance of $F^-(t)$ can be obtained from the eigenvalues of (3.5) as follows:

$$E(F^-) = 2 \sum_{n=1}^{N} \nu_n \quad , \qquad \sigma_{F^-}^2 = 4 \sum_{n=1}^{N} \nu_n^2 \tag{3.9}$$

If the input spectrum is sufficiently narrow banded and the slope of the QTF with respect to the frequency difference is small near the diagonal, $\omega_j = \omega_k$, we may write; $D_{jk} = D_{jj} + O(\omega_j - \omega_k)$, and the exact expression (3.2) can be approximated by (Newman, 1974):

$$F^-(t) = \text{Re} \sum_j \sum_k A_j A_k^* D_{jj} e^{i(\omega_j - \omega_k)t} \tag{3.10}$$

If Newman's approximation is employed, the eigenvalue problem (3.5) can be solved explicitly, as shown in Chapter V. In this case, (3.5) has only two eigenvalues, $\nu_{\pm}$, and they are given by:

$$\nu_{\pm} = \frac{1}{2} \left[\frac{E(F^-)}{2} \pm \left\{ M_0 \int_0^{\infty} S(\omega) D^2(\omega,\omega) \, d\omega \right\}^{1/2} \right] \tag{3.11}$$

where M_0 is the zeroth moment of the input spectrum, $S(\omega)$, and $E(F^-)$ is given in (3.3). The probabilistic distribution of (3.10) then has the following form:

$$p(F^-) = \frac{1}{2} \text{Exp} \left[- \frac{|F^-|}{2|\nu^\pm|} \right] \qquad \text{where} \quad \begin{matrix} \nu^+ \text{ for } F^- \geq 0 \\ \nu^- \text{ for } F^- < 0 \end{matrix} \tag{3.12}$$

The variance of (3.10) can be obtained from (3.9):

$$\sigma^2_{F^-} = 2 M_0 \int_0^\infty S(\omega) D^2(\omega,\omega) \, d\omega + \frac{E(F^-)^2}{2} \tag{3.13}$$

The spectrum (one-sided) of (3.10) is given by (see Chapter V):

$$S_{F^-}(\mu) = 2 \int_0^\infty S(\omega) S(\omega+\mu) \left[D(\omega,\omega) + D(\omega+\mu,\omega+\mu) \right]^2 d\omega \tag{3.14}$$

4. NUMERICAL RESULTS AND DISCUSSION

As an application of the theory in the previous section, we consider the second-order difference-frequency wave excitations on a large-draft truncated vertical cylinder (radius a=15m, draft H=4a) in unidirectional irregular seas in water depth h=2H. A two parameter Pierson-Moskovitz spectrum of significant wave height $H_{1/3}$=6m and mean period T_m= 8 sec is used as the input spectrum. For computations, the small wave energy outside the frequency band $0.4 \leq \omega \leq 1.15$ is assumed to be zero.

$$S(\omega) = \frac{\omega_m^4 \, H_{1/3}^2}{4\pi \, \omega^5} \text{Exp} \left[- \left(\frac{\omega_m}{\omega}\right)^4 / \, \pi \right] \tag{4.1}$$

where mean frequency $\omega_m = 2\pi/T_m$.

The complete difference-frequency wave excitation QTFs, $D(\omega_j,\omega_k)$, for the truncated vertical cylinder are calculated by the numerical method detailed in Chapter II, and are given in Table 1. For comparison, those of Standing et al's (1982) and Pinkster's (1980) approximation methods are also given (see Chapter II).

Table 1a shows the horizontal force QTFs for various combinations of incident frequencies. For Newman's (1974) approximation, only mean drift data on the diagonal are necessary. As pointed out in Chapter II, the

Table 1a. The difference-frequency horizontal-force QTFs for a truncated vertical cylinder of radius a=15m, draft H=4a. Computed values (Re,Im) are for first row: $f_{qjk}^{-}+f_{Ijk}^{-}$ (Standing et al, 1982); second row: $f_{qjk}^{-}+f_{Ijk}^{-}+f_{Bjk}^{-}$ (Pinkster, 1980); and third row: $f_{qjk}^{-}+f_{pjk}^{-}$ (complete theory).

ω_j=	0.40	0.55	0.70	0.85	1.00	1.15
ω_k= 0.40	0.04,0.00	0.13,0.02 0.13,0.13 0.12,0.13	0.28,0.25 0.27,0.65 0.19,0.60	0.33,0.64 0.22,1.41 0.10,1.23	0.22,0.91 -0.16,1.70 -0.33,1.43	0.05,0.97 -0.06,1.07 -0.43,0.81
0.55		0.23,0.00	0.40,0.15 0.40,0.31 0.37,0.29	0.46,0.52 0.44,0.99 0.35,0.89	0.36,0.79 0.26,1.54 0.09,1.37	0.22,0.86 -0.01,1.33 -0.24,1.15
0.70			0.56,0.00	0.61,0.24 0.61,0.45 0.57,0.40	0.52,0.53 0.51,1.07 0.39,0.93	0.37,0.67 0.27,1.34 0.14,1.12
0.85				0.65,0.00	0.58,0.19 0.58,0.44 0.51,0.38	0.46,0.44 0.44,1.02 0.31,0.82
1.00					0.59,0.00	0.56,0.19 0.56,0.49 0.47,0.41
1.15						0.62,0.00

components due to the second-order incident wave potential, f_{Ijk}^- and f_{Bjk}^-, contribute significantly, and they are equally important. Due to these terms, the slope of QTF (especially the imaginary part) near the diagonal is very steep. Therefore, neither Newman's nor Standing et al's method, which neglect both or one of these terms respectively, is expected to give fair results compared to the complete theory. On the other hand, the contribution from the free-surface integral is generally small except for large ω^+ and ω^- ($\omega^+=\omega_j+\omega_k$, $\omega^-=\omega_j-\omega_k$), hence Pinkster's method which excludes only this contribution seems to be more robust.

The vertical force QTFs are given in Table 1b, where we see that there is a small pressure on the bottom of the cylinder even for the high frequency pairs. Because of the fast depth-attenuation of the linear potential, the linear square term, f_{qjk}^-, is almost negligible except for very low frequency pairs. In contrast, ϕ^- penetrates to large depths, particularly for smaller ω^- (see Chapter II), and cause the large gradients near the diagonal. Due to these combined effects, Newman's approximation is expected to underestimate severely the difference-frequency vertical force of large-draft bodies. Interestingly, the free-surface contribution, f_{Fjk}^-, is equally important in this case compared to the other contributions.

Table 1b. The difference-frequency vertical-force QTFs for a truncated vertical cylinder of radius a=15m, draft H=4a. Computed values (Re,Im) are for first row: $f_{qjk}^- + f_{Ijk}^-$ (Standing et al, 1982); second row: $f_{qjk}^- + f_{Ijk}^- + f_{Bjk}^-$ (Pinkster, 1980); and third row: $f_{qjk}^- + f_{pjk}^-$ (complete theory).

ω_j=	0.40	0.55	0.70	0.85	1.00	1.15
ω_k= 0.40	-0.08,0.00	-0.15,0.00 -0.14,0.00 -0.14,0.00	-0.09,0.00 -0.05,0.02 -0.05,0.00	-0.03,0.00 -0.02,0.06 -0.01,0.01	-0.01,0.00 -0.04,0.06 0.00,0.01	0.00,0.00 -0.06,0.03 0.00,0.00
0.55		-0.02,0.00	-0.10,0.00 -0.08,0.01 -0.08,0.00	-0.05,0.00 -0.01,0.04 -0.02,0.00	-0.01,0.00 -0.01,0.08 0.00,0.01	0.00,0.00 -0.06,0.07 0.00,0.01
0.70			0.00,0.00	-0.08,0.00 -0.05,0.01 -0.06,0.00	-0.03,0.00 0.01,0.05 -0.01,0.00	-0.01,0.00 -0.01,0.11 0.00,0.00
0.85				0.00,0.00	-0.07,0.00 -0.03,0.01 -0.05,0.00	-0.02,0.00 0.03,0.07 0.00,0.00
1.00					0.00,0.00	-0.06,0.00 -0.02,0.02 -0.04,0.00
1.15						0.00,0.00

The pitch moment QTFs with respect to the center of waterplane are given in Table 1c. The fast increase of QTF (especially the imaginary part) near the diagonal with increasing frequency difference is noteworthy. As pointed out earlier, this is due to the slower attenuation of ϕ^- for smaller ω^-. The deeply penetrating pressure associated with ϕ^- greatly magnifies the pitch moment through its large moment arm. Consequently, Newman's or Standing's approximations are hardly applicable in this case even for a sufficiently narrow banded input spectrum.

Table 1c. The difference-frequency pitch-moment (with respect to the center of waterplane) QTFs for a truncated vertical cylinder of radius a=15m, draft H=4a. Computed values (Re,Im) are for first row: $M_{qjk}^{-}+M_{Ijk}^{-}$ (Standing et al, 1982); second row: $M_{qjk}^{-}+M_{Ijk}^{-}+M_{Bjk}^{-}$ (Pinkster, 1980); and third row: $M_{qjk}^{-}+M_{pjk}^{-}$ (complete theory).

ω_j=	0.40	0.55	0.70	0.85	1.00	1.15
ω_k= 0.40	0.04,0.00	0.09,-0.48 0.09,-0.68 0.11,-0.68	0.16,-1.02 0.18,-1.60 0.25,-1.53	0.17,-1.30 0.34,-2.25 0.41,-2.04	0.15,-1.28 0.63,-2.05 0.72,-1.82	0.08,-1.04 0.20,-1.11 0.52,-0.87
0.55		0.14,0.00	0.18,-0.53 0.18,-0.79 0.22,-0.76	0.19,-1.03 0.22,-1.69 0.28,-1.55	0.18,-1.21 0.36,-2.08 0.42,-1.90	0.13,-1.09 0.42,-1.51 0.57,-1.36
0.70			0.19,0.00	0.19,-0.57 0.19,-0.89 0.23,-0.82	0.19,-1.03 0.21,-1.73 0.27,-1.55	0.14,-1.10 0.30,-1.83 0.30,-1.59
0.85				0.18,0.00	0.18,-0.60 0.18,-0.98 0.24,-0.89	0.16,-0.97 0.18,-1.69 0.23,-1.44
1.00					0.18,0.00	0.17,-0.62 0.17,-1.06 0.24,-0.93
1.15						0.17,0.00

Based on the QTF data given in Table 1 and the input spectrum (4.1), the eigenvalue problem (3.5) and the corresponding PDF (3.7) are calculated for each method. For this calculation, the QTFs are linearly interpolated using the values given in Table 1. First of all, the convergence of (3.7) with increasing number of eigenvalues (equivalently, the number of frequency discretizations) is tested. As shown in Table 2 or Figure 2, we obtain rapid convergences with increasing N_ω, which shows the efficacy of the complete theory for such applications. Similar rates of convergences are also obtained for the other approximations, and $N_\omega=20$ is used for all later results.

Table 2. Convergences of the mean and variance of the complete horizontal force PDF with increasing number of eigenvalues, N_ω.

	Mean ($E(F^-)$)	Variance ($\sigma_{F^-}^2$)
$N_\omega=$ 5	1.681	8.486
10	1.678	8.330
20	1.678	8.315
30	1.678	8.312

Figures 3a~c show the PDFs of the difference-frequency wave excitations obtained using the complete theory as well as those of existing approximation methods. The overall results confirm the earlier observations regarding the QTFs. It is seen that the PDFs based on Newman's approximation differ significantly from the exact solutions and greatly underestimate the probability of extreme values. Futhermore, the large probability of negative horizontal forces and positive vertical forces can not predicted by Newman's approximation. Pinkster's approximation, which includes all but free-surface contributions, slightly overestimates the exact solution, and appears acceptable for engineering applications. In Table 3, we summarize the mean and standard deviation of each method obtained from (3.9).

Table 3. **The mean and standard deviation of the difference-frequency wave excitation.**

	horizontal force		vertical force		pitch moment	
	$E(F^-)$	σ_{F-}	$E(F^-)$	σ_{F-}	$E(M^-)$	σ_{M-}
Newman:	1.678	1.768	-0.076	0.095	0.636	0.646
Standing:	1.678	2.239	-0.077	0.263	0.636	2.932
Pinkster:	1.678	3.260	-0.077	0.239	0.636	4.679
complete:	1.678	2.884	-0.077	0.212	0.636	4.351

From this table, we see that the mean drift forces can be obtained correctly by any method. On the other hand, Newman's approximation severely underestimate (e.g. 61%, 45%, and 15%, respectively, for the horizontal and vertical forces and pitch moment) the exact standard deviation.

The variances of the difference-frequency excitations can also be obtained from the area under the associated spectra given by (3.4) or (3.14). We present in Figures 4a~c these spectra for each method. The results are again consistent with the earlier observations. As expected, all the curves converge to the exact value as $\omega^- \to 0$, but differ signifficantly for large ω. When the natural frequency of a system is very low (e.g. $\omega_n \ll 0.1$) and associated damping is small, the slowly-varying response spectra based on approximation methods may be obtained more correctly because of the filtering by the motion transfer function.

5. CONCLUSION

In this chapter, we review the general statistical properties of a two-term Volterra series and obtain explicitly the PDFs and spectra of the second-order difference-frequency wave excitations in unidirectional Gaussian seas. Specifically, we calculated the complete probability distributions of the difference-frequency wave excitations on a large-draft truncated vertical cylinder, and compared them with those based on approximated QTFs.

From our numerical results, we found that Newman's (1974) and Standing et al's (1982) approximation methods severely underestimate the variance and the probability of extreme forces and may, therefore, not be acceptable for many engineering applications. This emphasizes the necessity of the use of complete theory, or at least Pinkster's (1980) approximation which appears to be more robust than the other aproximation methods.

The present complete theory is directly applicable to predictions of the probability distributions of the second-order responses as long as the equation of motion is assumed to be a time invariant linear system. When nonlinear damping or restoring forces are present, however, the two-term Volterra model is not adequate for the statistical analysis of the nonlinear responses (Naess, 1986).

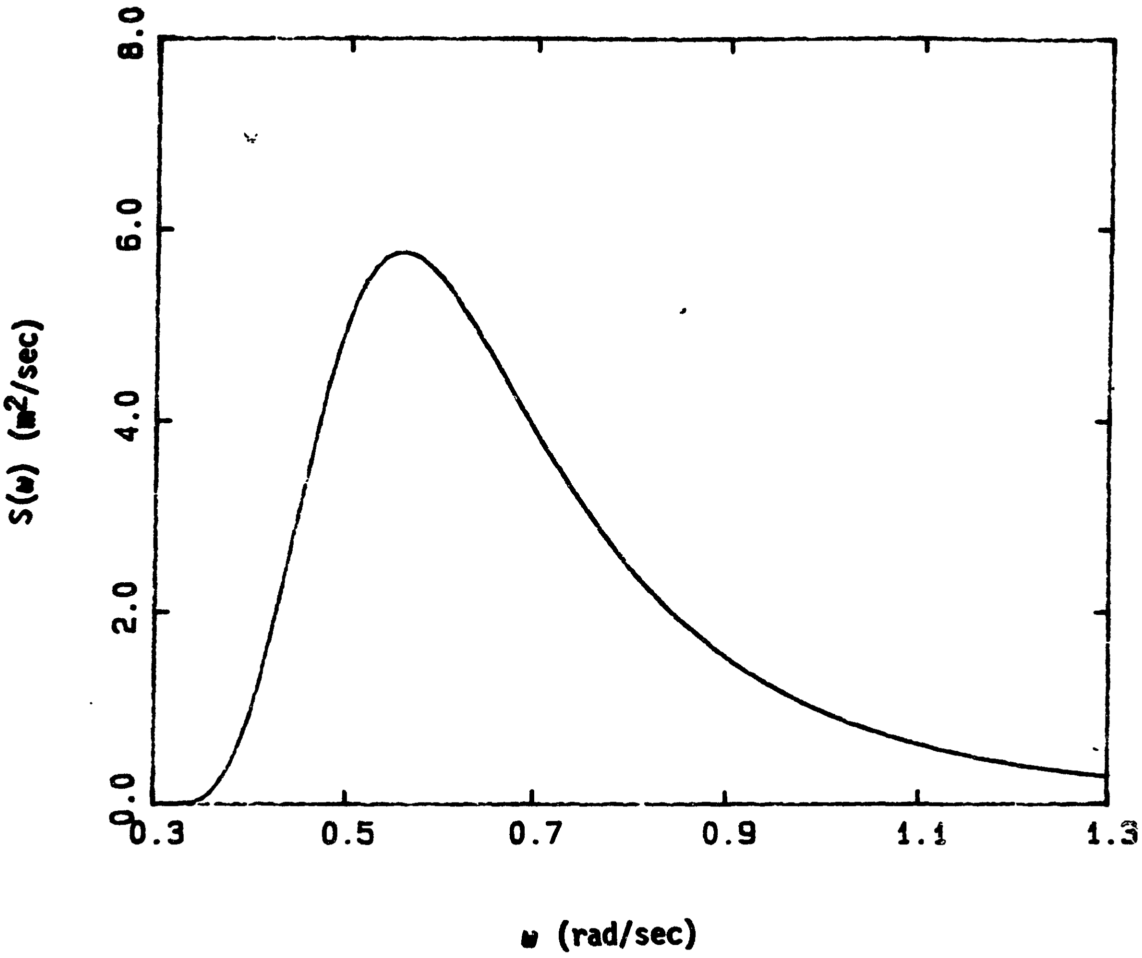

Figure 1. Two parameter ($H_{1/3}$=6m, T_m=8sec) Pierson-Moskovitz input amplitude spectrum.

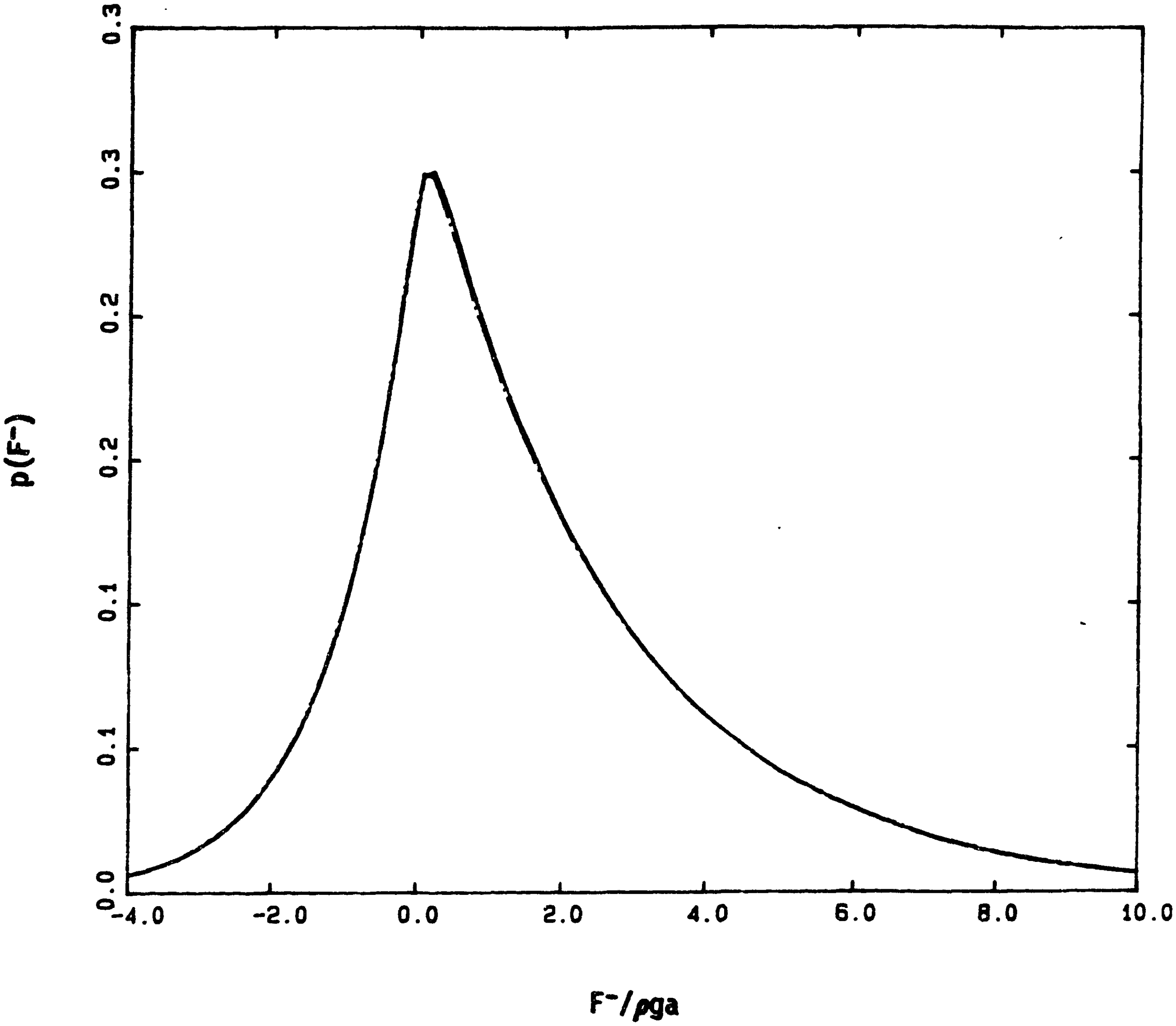

Figure 2. Convergence of the complete PDF for slowly-varying horizontal forces with increasing number of eigenvalues.

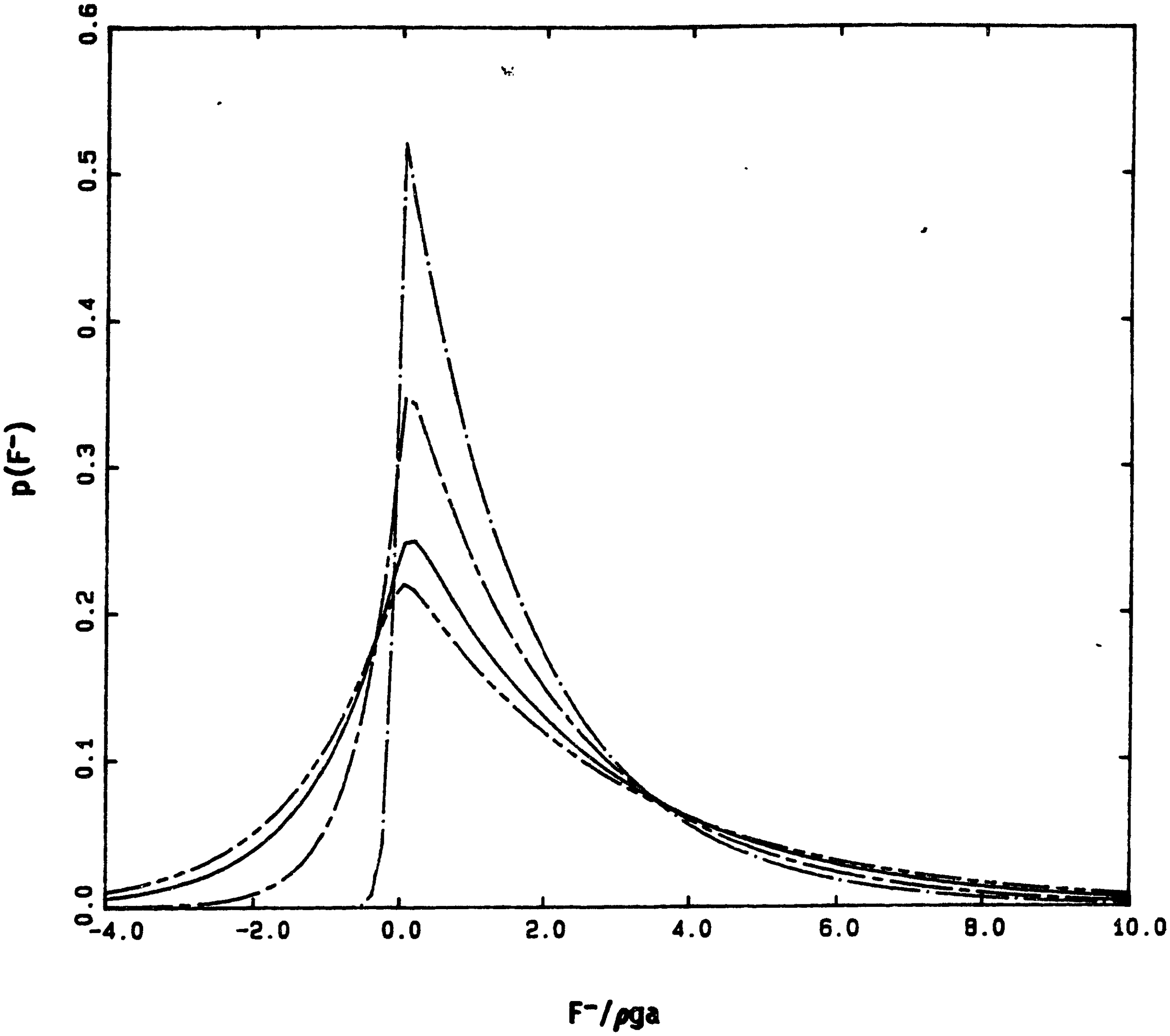

Figure 3a. PDFs of the difference-frequency horizontal force on a truncated vertical cylinder (radius a=15m, draft H=4a) obtained using: Newman's(—— • ——), Standing's(—— – ——) and Pinkster's(—— – – – ——) approximations, and the complete theory(————).

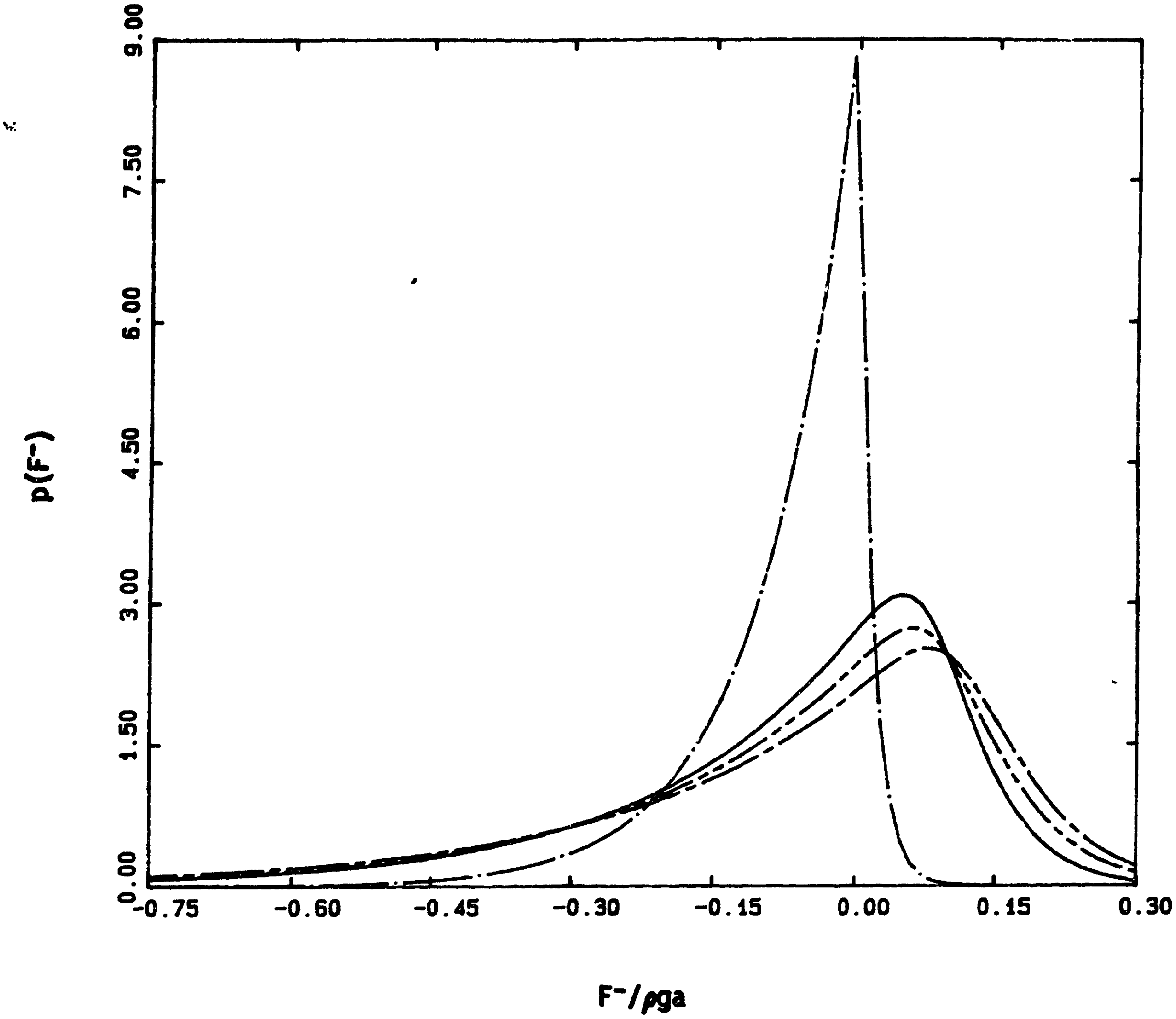

Figure 3b. PDFs of the difference-frequency vertical force on a truncated vertical cylinder (radius a=15m, draft H=4a) obtained using: Newman's (—— • ——), Standing's(—— – ——) and Pinkster's(—— – – ——), approximations, and the complete theory(————).

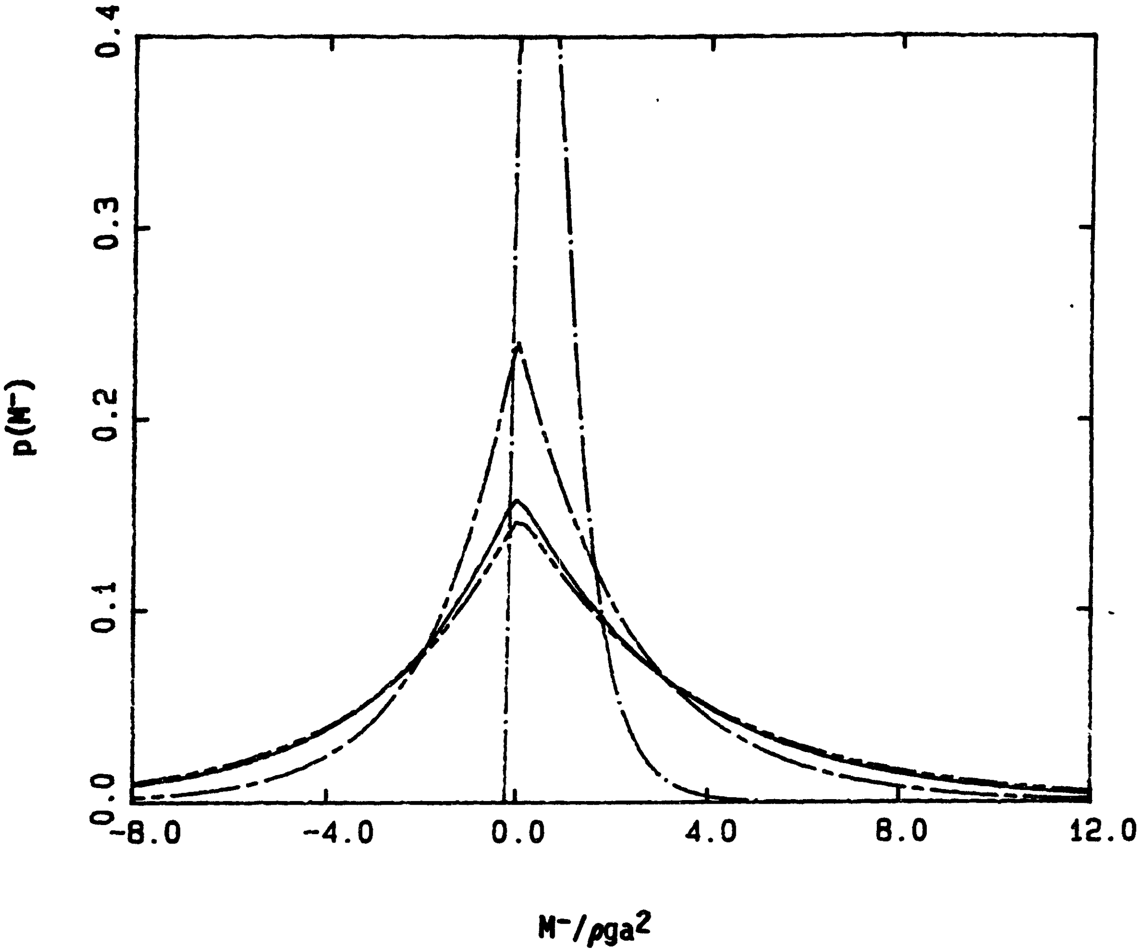

Figure 3c. PDFs of the difference-frequency pitch moment on a truncated vertical cylinder (radius a=15m, draft H=4a) obtained using: Newman's (—— • ——), Standing's(—— – ——) and Pinkster's(—— – – – ——) approximations, and the complete theory(————).

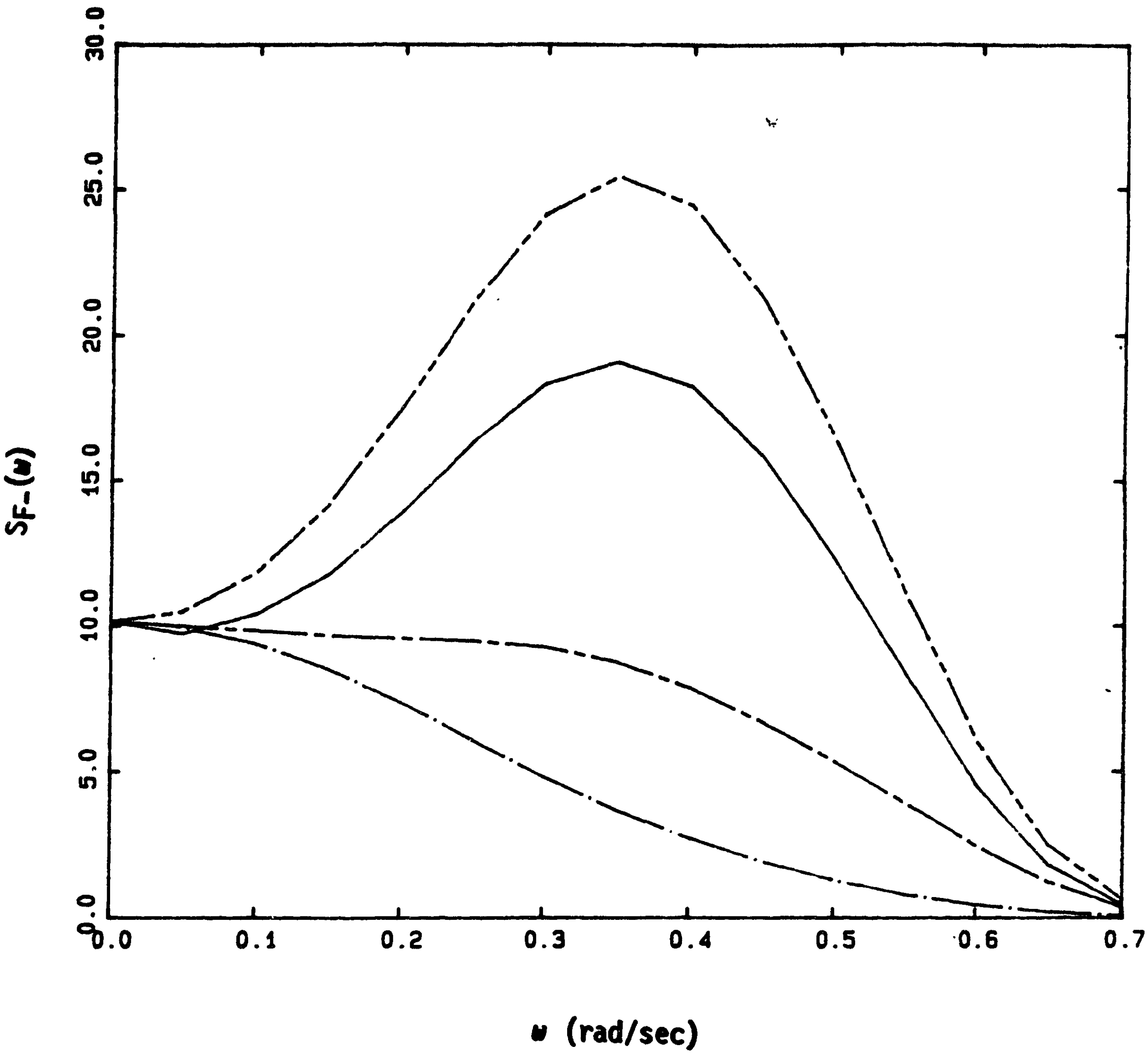

Figure 4a. One-sided amplitude spectra of the difference-frequency horizontal force on a truncated vertical cylinder (radius a=15m, draft H=4a) obtained using: Newman's(—— · ——), Standing's(—— – ——), and Pinkster's(—— – – – ——) approximations, and the complete theory(————).

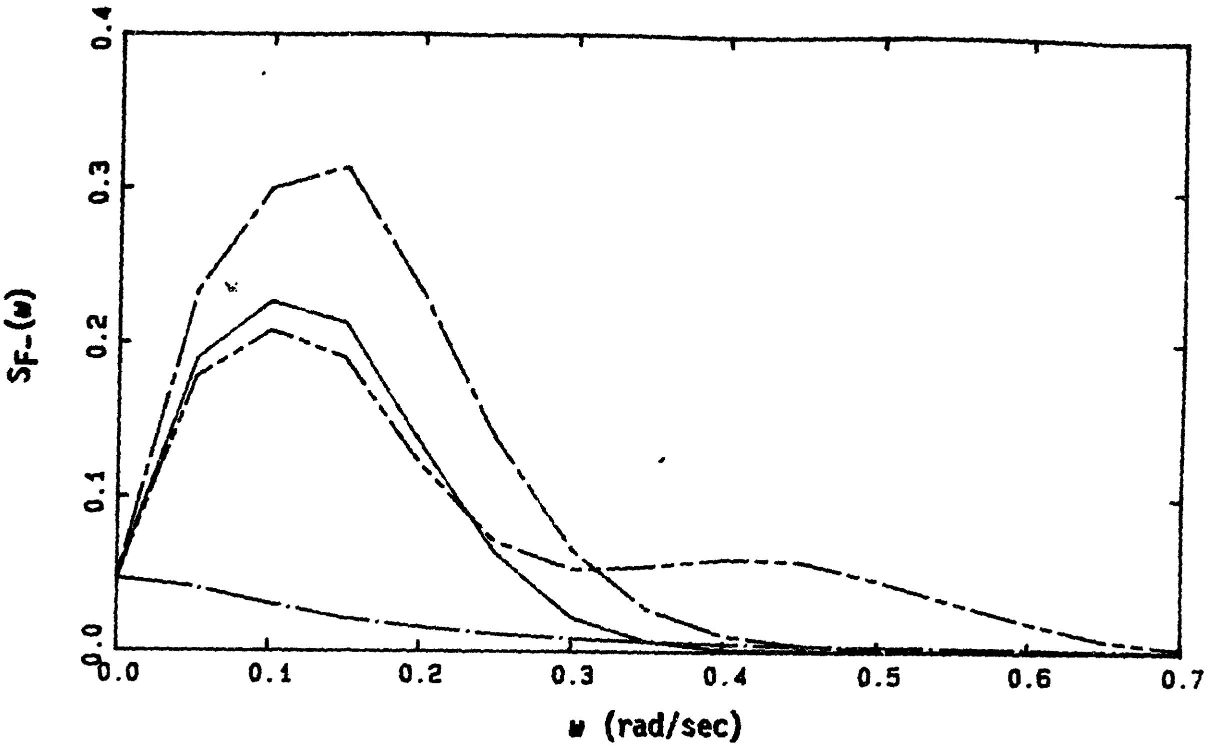

Figure 4b. One-sided amplitude spectra of the difference-frequency vertical force on a truncated vertical cylinder (radius a=15m, draft H=4a) obtained using: Newman's(—— • ——), Standing's(—— – ——), and Pinkster's(—— – – – ——) approximations, and the complete theory(————).

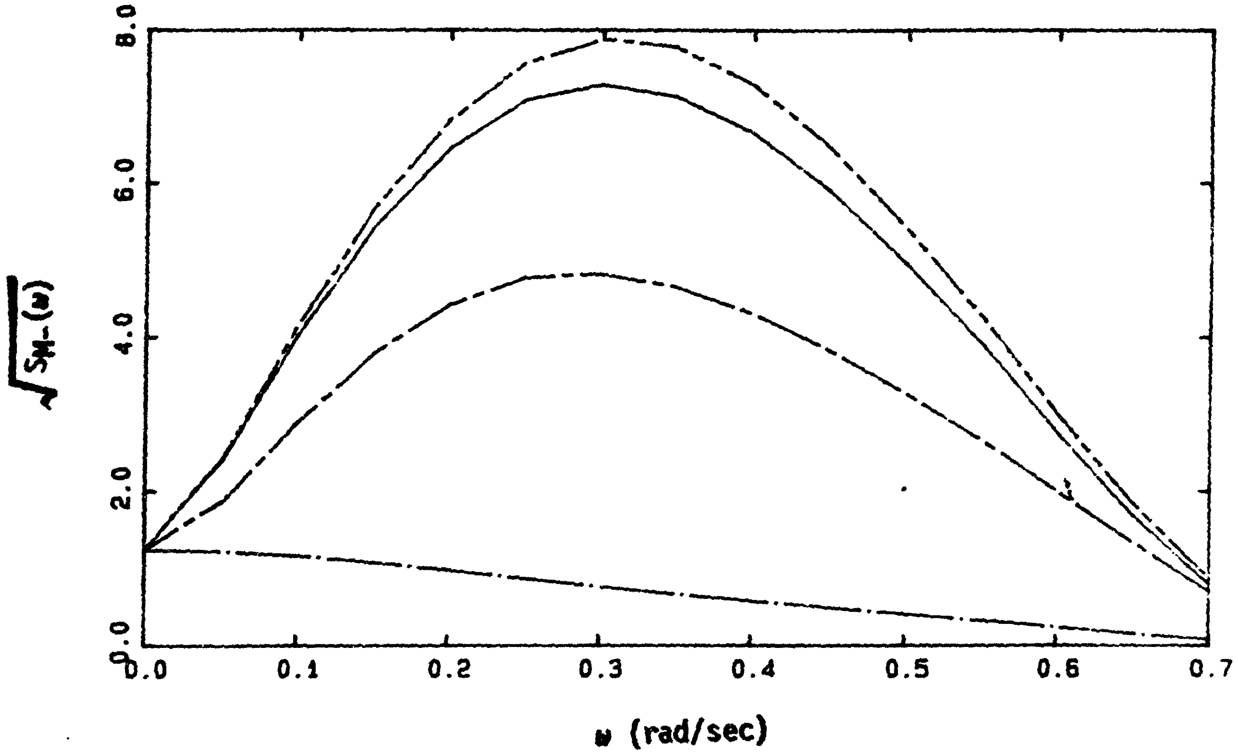

Figure 4c. One-sided amplitude spectra of the difference-frequency pitch moment on a truncated vertical cylinder (radius a=15m, draft H=4a) obtained using Newman's(—— • ——), Standing's(—— – ——), and Pinkster's(—— – – – ——) approximations, and the complete theory(————).

CHAPTER IV.

THE SECOND-ORDER SUM-FREQUENCY WAVE EXCITATION AND RESPONSE OF A TENSION-LEG PLATFORM.

1. INTRODUCTION

The deep water tension-leg platform (TLP) is designed so that the natural periods of the vertical-plane motions (typically 1~4 seconds) are substantially below that of most of the ocean wave energy. In the absence of appreciable damping mechanisms, the resonant TLP responses and resulting tension-leg loads depend critically on any source of high-frequency excitations. It is now widely accepted that higher-order sum-frequency wave exciting forces, often called 'springing' forces, are important mechanisms for the vertical-plane resonant excitation of a TLP. In addition to the need for better estimates of damping forces, a reliable calculation of these nonlinear wave loads in irregular seas is critical for the design of the tension leg tendons.

Despite the progress in second-order wave-diffraction theory and computations in recent years, there has not been a complete calculation of the sum-frequency forces on a TLP in the presence of bichromatic incident waves. A main reason is the theoretical and computational difficulties in obtaining the general sum-frequency force quadratic transfer function (QTF) associated with the nonlinear potential. Thus, recent calculations of springing forces on TLPs have relied on simplifying approximations whose validity cannot in general be justified. For example, Nordgren (1986) neglected nonlinear effects completely, while Petrauskas & Liu (1987) included second-order contributions due to the first-order potential only. The comparisons to experiments are, overall, not satisfactory. For example, measured rms values of tendon loads which are factors of three or more higher than predictions using experimental damping values are reported in Petrauskas & Liu (1987).

In previous chapters, we developed a complete second-order diffraction-radiation method for the calculation of sum- and difference-frequency forces on an axisymmetric body for any combination of incident frequencies (ω_j,ω_l). The nonlinear sum- and difference-frequency potentials are obtained explicitly so that in addition to the forces and moments, important local quantities, such as second-order pressures, particle velocities, and surface elevations are also available.

In this chapter, we apply the method to calculate the springing resonant tendon loads of a TLP in irregular seas. In §2, the exact second-order sum-frequency forces and moments on a single TLP leg are obtained in terms of the QTF for a general combination of incident wave frequencies. These results are used in a model for a typical four-leg four-pontoon TLP in §3. A number of damping ratios and wave spectrum parameters are considered in calculating the resultant rms tendon-tension loads. Several important conclusions are given in the final section.

2. SPRINGING WAVE EXCITING FORCES AND MOMENTS ON A SINGLE TLP LEG.

We first consider the springing excitations on a fixed single TLP leg in this section. The complete theory for second-order sum-frequency diffraction problem was already detailed in Chapter II and will not be elaborated here. In the presence of bichromatic incident waves, (ω_j,ω_l), we can write the total sum-frequency wave excitation in the form:

$$f^+(t) = \mathrm{Re} \sum_{j=1}^{2} \sum_{l=1}^{2} A_j A_l \, f_{jl}^+ \, e^{-i(\omega_j + \omega_l)t} \tag{2.1}$$

$$f_{jl}^+ = f_{qjl}^+ + f_{pjl}^+ \tag{2.2}$$

where the complete sum-frequency force QTF, f_{jl}^+, consists of two components; that due to quadratic products of the linear potential, f_{qjl}^+, and that due to the second-order potential itself f_{pjl}^+.

For long-crested irregular seas, the incident wave elevation can be expressed as a sum of regular wave components:

$$\eta(t) = \mathrm{Re} \sum_{j=1}^{N} A_j \, e^{-i\omega_j t} \qquad (A_j = a_j \, e^{i\epsilon_j}) \tag{2.3}$$

where a_j and ϵ_j are the amplitude and phase of the j-th component wave, and the random phase ϵ_j is uniformly distributed in 0 and 2π. The component amplitude is given by $a_j=\sqrt{2S(\omega_j)\Delta\omega}$, where $S(\omega)$ is the (one-sided) input amplitude spectrum. The total second-order springing forces due to all the components in (2.3) is given by:

$$f^+(t) = \mathrm{Re} \sum_{j=1}^{N} \sum_{l=1}^{N} A_j A_l \, f_{jl}^+ \, e^{-i(\omega_j + \omega_l)t} \tag{2.4}$$

From (2.4), it is clear that $f^+(t)$ is a zero-mean process. Upon deriving its autocorrelation function in continuous form and using the Wiener-Kinchin relation, the spectrum (one-sided) of the springing force can be expressed in the form:

$$S_f(\omega^+) = 8 \int_0^{\omega^+/2} S(\frac{\omega^+}{2} + \mu)\, S(\frac{\omega^+}{2} - \mu)\, \left| f^+_{jl}(\frac{\omega^+}{2} + \mu\, ,\, \frac{\omega^+}{2} - \mu) \right|^2 d\mu \qquad (2.5)$$

We now present results for a single TLP leg. For definiteness, we consider a circular cylindrical leg of radius a, draft H = 4a, in deep water. This radius-draft ratio is the same as the bottom-seated (h = H) cylinder in the single-leg experiment of Petrauskas & Liu (1987). For this bottom-seated geometry, Figure 1 shows a comparison of the horizontal springing force due to a regular incident wave of wavenumber ka. Despite fairly large scatter in the experimental data, the improved overall correlation of the present complete theory with measurements is evident.

For the actual deep-water TLP leg, we present in Tables 1 the sum-frequency QTF for a broad range of bichromatic wave combinations (ω_j,ω_l). In most cases, $f_{pjl}{}^+$ is greater in magnitude than $f_{qjl}{}^+$, but the two are generally out of phase. For the horizontal force (and pitch moment) in regular waves $\omega_j \simeq \omega_l$, the relative contributions of the second-order potential increase dramatically with higher sum frequencies, and account for the general increase of the total springing force amplitude with frequency. In general, for fixed $\omega^+=\omega_j+\omega_l$, the amplitude of the QTF decreases rapidly with the difference of the component frequencies, $2\mu = \omega_j-\omega_l$, due to expected cancellations in the interaction between long and short waves. The gradient of the total QTF with respect to μ near the diagonal is typically larger for increasing ω^+.

A surprising result is found for the vertical force in Table 1(b). For all but the lowest frequency incident waves, the effect of the first-order pressure at the bottom of the leg is very small. For free waves at the sum frequency ω^+, and for products of the first-order potentials, it is clear that the wavenumbers must be greater than k_j or k_l so that contributions to the vertical force are negligible. On the other hand, the nonlinear locked potential which is forced by the inhomogeneous surface pressure decays slowly, and the effect on the bottom of the leg can be appreciable (cf. Newman, 1988), and in fact may increase with sum frequency ω^+. To show this more clearly, we plot the pressure distributions on the lee (θ=0) and weather side (θ=π) of the leg as a function of depth in Figure 2 for two different combinations of incident wave frequencies. The linear quadratic potential pressures, $p_{qjl}{}^+$, attenuate exponentially with a wavenumber $k^+=k_j+k_l$, but the nonlinear potential pressures, $p_{pjl}{}^+$, appears to decrease only algebraically with depth. For fixed ω^+, $p_{pjl}{}^+$ penetrates deepest for $\omega_j=\omega_l$, even though longer incident wavelengths are involved when $\mu>0$. On the lee side, the second-order pressure is generally smaller and attenuates more rapidly, but shows an interesting non-monotonic behavior for the case $\omega_j=\omega_l$. Some of these features, as already adressed in Chapter II, can be seen from the far-field asymptotic behavior of the nonlinear potential. For deep water, the decay of far-field locked potential with depth is exponential with a rate $(k_j{}^2+k_l{}^2+2k_jk_l\cos\theta)^{1/2}$, which has a minimum (maximum) for $k_j=k_l$ and $\theta=\pi$ (0) and increases with increasing k_j-(+)k_l.

Table 1. Magnitude of the second-order sum-frequency force QTF for a TLP leg (a=25 ft, H=4a) for incident wave frequencies ω_j, ω_l for a) horizontal force $F_{xjl}^+/\rho g a A_j A_l$; b) vertical force $F_{zjl}^+/\rho g a A_j A_l$; and c) pitch moment with respect to the center of the waterplane $M_{yjl}^+/\rho g a^2 A_j A_l$. For comparison, three quantities, $|F_{qjl}^+|$ (first row); $|F_{pjl}^+|$ (second row); and $|F_{qjl}^+ + F_{pjl}^+|$ (third row) are shown. Due to symmetry, only upper half of the table is given

Table 1a

ω_j=	0.8	1.0	1.2	1.4	1.6	1.8	2.0
ω_l= 0.8	1.503	1.505	1.215	1.172	1.410	1.376	1.248
	1.523	1.469	0.913	1.433	1.875	1.832	1.619
	0.406	0.299	0.585	0.923	0.845	0.602	0.508
1.0		1.560	1.434	1.620	1.893	1.754	1.533
		2.186	2.093	2.697	3.306	2.622	1.951
		0.714	0.822	1.258	1.208	0.888	0.430
1.2			1.561	1.835	1.990	1.685	1.421
			3.159	3.784	3.762	2.707	1.925
			1.601	1.953	1.773	1.060	0.504
1.4				1.949	1.838	1.398	1.324
				4.544	4.003	2.468	2.165
				2.598	2.179	1.074	0.879
1.6					1.573	1.363	1.576
					4.625	3.893	3.927
					3.054	2.540	2.357
1.8						1.530	1.639
						5.895	5.225
						4.371	3.588
2.0							1.433
							6.263
							4.821

The center-of-pressure of f_{pjl}^+ is deeper compared to f_{qjl}^+, so that the second-order potential pitch moment, M_{pjl}^+, with respect to the center of the leg waterplane is also greater(cf. Table 1c).

Table 1b

$\omega_j=$	0.8	1.0	1.2	1.4	1.6	1.8	2.0
$\omega_l=$ 0.8	0.014 0.249 0.239	0.005 0.154 0.150	0.001 0.039 0.039	0.000 0.006 0.006	0.000 0.002 0.002	0.000 0.001 0.001	0.000 0.000 0.000
1.0		0.002 0.419 0.418	0.000 0.152 0.152	0.000 0.029 0.029	0.000 0.007 0.007	0.000 0.002 0.002	0.000 0.000 0.000
1.2			0.000 0.392 0.392	0.000 0.105 0.105	0.000 0.026 0.026	0.000 0.005 0.005	0.000 0.001 0.001
1.4				0.000 0.313 0.313	0.000 0.105 0.105	0.000 0.017 0.017	0.000 0.003 0.003
1.6					0.000 0.567 0.567	0.000 0.100 0.100	0.000 0.013 0.013
1.8						0.000 0.491 0.491	0.000 0.086 0.086
2.0							0.000 0.665 0.665

As will be seen later (§3), the small nonlinear potential vertical force can have an appreciable effect on the total pitch moment on the TLP, since its moment arm is typically greater than that of the horizontal forces with respect to the center of rotation. Furthermore, the wave effects on other structural members such as horizontal pontoons may not be negligible depending on the gradients of these nonlinear potentials which persist with depth.

Table 1c.

$\omega_j=$	0.8	1.0	1.2	1.4	1.6	1.8	2.0
$\omega_l=$ 0.8	0.277 1.767 1.489	0.195 1.554 1.364	0.144 0.734 1.608	0.213 1.022 0.811	0.212 1.019 0.808	0.151 0.728 0.578	0.103 0.505 0.402
1.0		0.213 2.911 2.723	0.226 2.387 2.197	0.277 2.290 2.023	0.259 1.919 1.664	0.179 1.188 1.011	0.121 0.730 0.610
1.2			0.255 3.951 3.759	0.273 3.673 3.426	0.235 2.778 2.553	0.146 1.441 1.299	0.099 0.842 0.744
1.4				0.241 4.607 4.379	0.177 3.384 3.211	0.097 1.476 1.380	0.092 1.108 1.018
1.6					0.119 5.309 5.190	0.096 3.455 3.361	0.114 2.472 2.360
1.8						0.112 6.142 6.040	0.107 4.125 4.020
2.0							0.079 6.684 6.605

In the analysis of lightly-damped vertical motions of a TLP, we are primarily concerned with the details of the excitation near the heave-pitch natural frequency ω_n. In Figure 3, we plot the springing force and moment ROA's for $\omega^+=2.6,3.0$, as a function of the difference of the interacting frequencies, $2\mu=\omega_j-\omega_l$. For comparison, the second-order contribution from quadratic products of first-order potentials only are also shown. In all cases, the first-order potential approximations are inadequate, underpredicting the horizontal force for lower values of μ and substantially underpredict the vertical force and pitch moment. For the horizontal force and moment, there is a gradual decrease of the total RAO with μ, although the first-order potential component appears almost constant with increasing frequency difference. For the vertical force, f_{qjl}^{+} is almost zero, while f_{pjl}^{+} decreases rapidly with increasing μ, so that the penetration of ϕ^{+} with depth is primarily due to waves which are relatively close in frequency.

3. RESONANT VERTICAL-PLANE MOTIONS AND TENDON TENSIONS OF A TLP IN LONG-CRESTED IRREGULAR SEAS.

In this section, we consider the resonant wave excitations and tendon loads of a TLP in irregular seas. The incident waves are assumed to be unidirectional, although it is now known (e.g. Kim & Yue; 1988a) that this is not necessarily a conservative assumption when second-order effects are concerned.

For numerical illustration, we use a simplified TLP model consisting of four circular cylindrical legs (radius a=25', draft H=100') connected by four circular cylindrical horizontal pontoons (radius 12.5', length 150', and centerline depth 82.5'). The legs form a square with center-to-center distance 2L=200' and the TLP is symmetric with respect to the x and y axes which are fixed at the center of the platform in the quiescent free surface and z is positive upwards. The main particulars of the TLP are summarized in Table 2.

Table 2. Main particulars of the TLP.

Total mass:	$M_o = 1.8 \times 10^6$ slugs
Total displaced mass:	$\Delta_B = 2.14 \times 10^6$ slugs
Total moment of inertia:	$I_{xx} = I_{yy} = 1.5 \times 10^{10}$ slug-ft^2
Location of the center of gravity:	$z_G = 20$ ft
Location of the center of buoyancy:	$z_B = -60$ ft
Number of tendons:	16 tendons, 4 on each leg
Individual tendon stiffness:	$k_t = 1.2 \times 10^6$ lbf/ft
Tendon length:	$l_t = 1400$ ft
Total submerged weight of tendons:	$W_t = 5 \times 10^6$ lbf
Total tendon pretension:	$T_o = 1.1 \times 10^7$ lbf

We focus on the motions of the platform near its vertical-plane natural periods, ω_n. While the calculation for the single leg in §2 is accurate and exact in the context of a complete second-order theory, we make several important simplifications in this section whose validity must be tested against experiments and three-dimensional computations for the whole TLP. In view of the high natural frequencies compared to draft , and the rapid decrease of the QTF with frequency difference μ (Figure 3) (i.e, longer waves do not contribute appreciably), we ignore wave effects on the pontoons and include only their infinite-fluid properties. As pointed out earlier, this may not be fully justified in view of the penetration of the nonlinear potential in depth. Similarly, since $\omega_n^2 L/g >> 1$, we ignore hydrodynamic interactions among the legs (including phasing), which may be conservative. For this problem, an exact interaction theory for first-order effects (Kagemoto & Yue; 1986), and a wide-spacing approximation for second-order diffraction (Abul-Azm & Williams; 1988) can be applied, but is not pursued here in view of the other simplifying assumptions and uncertainties (for example, damping).

For a perpendicular incidence angle, the yaw and roll motions are not involved and we consider the three degree-of-freedom linearized equation of motion of the TLP:

$$(\mathbf{m}+a)\ddot{x} + b\dot{x} + cx = f \tag{3.1}$$

where $x^T=(x_1,x_2,x_3)$ are the displacements in surge, heave and pitch; $\mathbf{m}$,a, b,c the mass, added mass, (linearized) damping, and linear restoring (stiffness) matrices; and f the exciting force vector.

For the wave exciting forces, we ignore hydrodynamic interactions and relative phases and write $f_1 = 4F_1$, $f_3 = 4F_3$, and $f_5 = 4(F_5+LF_3)$, where F_i are the single-leg results including both first-order excitation at wave frequency and all second-order sum-frequency contributions. The mass matrix, $\mathbf{m}$, is given in Table 2, and the added mass matrix, a, is obtained by the sum of the frequency-dependent added masses of the legs (ignoring interactions), A_{ij}, plus the infinite-fluid added mass of the pontoons, A^P: $a_{11} = 4A_{11} + A^P_{11}$; $a_{33} = 4A_{33} + A^P_{33}$; $a_{15} = a_{51} = 4A_{15} + A^P_{15}$; and $a_{55} = 4(A_{55} + L^2 A_{33}) + A^P_{55}$. Assuming vertical-plane natural frequencies in the range of 2.5~3 rad/sec, (first order) radiation calculations give $A_{11} \simeq .24 \times 10^6$ slugs, $A_{33} \simeq .06 \times 10^6$ slugs, $A_{15} \simeq -.13 \times 10^8$ slug-ft and $A_{55} \simeq .08 \times 10^{10}$ slug-ft^2, which remain fairly constant over the frequency range. The linear restoring matrix coefficients can be calculated from Table 2: $c_{11} = (T_0 - W_t/2)/l_t$; $c_{33} = 16\, k_t + 4\pi\rho g a^2$; $c_{15} = -H\, c_{11}$; and $c_{55} = H^2\, c_{11} + L^2\, c_{33} - z_G\, (M_0 g) + z_B\, (\Delta_B g)$.

For high-frequency motions of the TLP, the damping is very small and estimation of b in (3.1) is at the same time difficult and important. The total damping is, in general, a sum of wave radiation damping, viscous damping and mechanical damping. For wave damping, an estimate can be obtained from four times that of individual leg damping, B. From linear radiation calculations, we have $4B_{11} = (7.6 \sim 2.4) \times 10^4$ slug/sec; $4B_{15} = (-3.8 \sim -0.9) \times 10^5$ slug-ft/sec and $4B_{55} = (5 \sim 1) \times 10^5$ slug-ft^2/sec for frequencies in the range of $2.5 \sim 3$ rad/sec. The viscous drag is associated with boundary-layer friction, separation and vortex shedding. For TLP vertical motions, the amplitudes are small (relevant Keulegan-Carpenter number $\ll 1$) and the viscous effects are dominated by skin-friction drag. We estimate these forces for small Keulegan-Carpenter numbers from empirical models (e.g. Pearcy; 1979, Jonsson; 1978), corresponding to flows such as perpendicular cross flows over cylindrical members, parallel flows on side walls, and vertical flows against the bottom of the legs. We obtain the following estimates of viscous damping, b^v, for the TLP: $b^v_{11} \simeq 8 \times 10^2$ slug/sec, $b^v_{33} \simeq 9 \times 10^3$ slug/sec, $b^v_{15} \simeq - 6 \times 10^4$ slug-ft/sec and $b^v_{55} \simeq 8 \times 10^7$ slug-ft^2/sec. These damping coefficients are obtained after equivalent linearization for motion amplitudes of ~0.5 ft at the corner legs, and decrease approximately linearly with decreasing motion amplitudes in that vicinity. From the above, we observe that for heave and pitch motions, viscous damping dominates wave damping while the opposite is true for surge motions. Hydrodynamic estimates of damping coefficients represent lower-bound values, since they must, in general, be augmented by mechanical/material damping, especially when external damping devices are employed. On the other hand, the present viscous damping coefficients are probably high (by a factor of about 5) since the actual vertical leg displacement rms (from Table 3, say) is only O(0.1').

The heave motion in (3.1) is uncoupled and we have:

$$(M_o + a_{33})\ddot{x}_3 + b_{33}\dot{x}_3 + c_{33}x_3 = f_3 \tag{3.2}$$

The natural heave frequency is given by $\omega_3 = (c_{33}/(M_o+a_{33}))^{1/2} \simeq 2.74$ rad/sec, and the heave response RAO is

$$Z_3 = | x_3/f_3 | = \frac{1/c_{33}}{[\ \{1-(\omega/\omega_3)^2\}^2 + (2\varsigma_3\omega/\omega_3)^2]^{1/2}} \tag{3.3}$$

where the damping ratio in heave is defined by $\varsigma_3 \equiv b_{33}/2\sqrt{(M_o+a_{33})c_{33}}$.

The equation for the surge-pitch coupled motion is given by:

$$\begin{bmatrix} M_o + a_{11} & M_o z_G + a_{15} \\ M_o z_G + a_{15} & I_{yy} + a_{55} \end{bmatrix} \begin{bmatrix} \ddot{x}_1 \\ \ddot{x}_5 \end{bmatrix} + \begin{bmatrix} b_{11} & b_{15} \\ b_{15} & b_{55} \end{bmatrix} \begin{bmatrix} \dot{x}_1 \\ \dot{x}_5 \end{bmatrix} + \begin{bmatrix} c_{11} & c_{15} \\ c_{15} & c_{55} \end{bmatrix} \begin{bmatrix} x_1 \\ x_5 \end{bmatrix} = \begin{bmatrix} f_1 \\ f_5 \end{bmatrix} \tag{3.4}$$

Considering the undamped homogeneous equation of (3.4), we obtain the two natural frequencies and eigen-modes: (i) $\omega_n^+ \simeq 2.86$ rad/sec, $x_1 \simeq 0.16\ Lx_5$; and (ii) $\omega_n^- \simeq 0.046$ rad/sec, $Lx_5 \simeq 2.6 \times 10^{-4}\ x_1$. The first mode is a high-frequency surge-pitch coupled motion with a center of rotation at $z_c \simeq -.16L$; while the second mode is essentially a slowly-varying surge motion which does not contribute to springing tendon tension loads and will be ignored hereafter. For the high-frequency mode (hereafter referred to as 'pitch' mode), we substitute $x_1 = .16Lx_5$ in (3.4) and obtain the pitch modal equation:

$$m_o\ddot{x}_5 + b_o\dot{x}_5 + c_o x_5 = f_o \tag{3.5}$$

where the modal total mass, damping and restoring coefficients are given by $m_o = (I_{yy} + a_{55}) + .16L\ (M_o z_G + a_{15}) \simeq 2.35 \times 10^{10}$ slug-ft^2; $b_o = b_{55} + .16\ L\ b_{15}$; $c_o = c_{55} + .16Lc_{15} \simeq 19.2 \times 10^{10}$ lbf-ft; and $f_o = f_5 - z_c\ f_1$. The modal response RAO is then given by:

$$Z_o \equiv \left| \frac{x_5}{f_o} \right| = \frac{1/c_o}{[\ \{1 - (\omega/\omega_n^+)^2\}^2 + (2\varsigma_o\omega/\omega_n^+)^2]^{1/2}} \tag{3.6}$$

where the modal damping ratio is $\varsigma_o \equiv b_o/2\sqrt{m_o c_o}$.

The tendon tension load RAO's for heave, H_3, and ``pitch'', H_o, motions are simply $k_t Z_3$ and $k_t L Z_o$. These are plotted in the neighborhood of the natural frequencies for a range of damping ratios 0.05%, .1%, and .2%, in Figure 4. Note that our earlier estimates for wave plus viscous damping give values of $\varsigma \simeq 0.06\%$ for b_{33} and b_{55}. From (3.3) and (3.6), we see that the peak response amplitudes are inversely proportional to the damping ratio.

In (3.2) and (3.5), the modal exciting forces are respectively $f_3 = 4F_z$ and $f_o = f_5 - z_c f_1 = 4\ (M_y + LF_z - z_c F_x)$ for the heave and pitch motions. The single-leg forces consist of a first-order linear component due to incident waves near the natural frequencies, and second-order sum-frequency components due to combinations of longer waves whose sum of the frequencies are resonant. From linear diffraction calculations, the first-order force and moment RAO's for a single leg are: $|F_x^{(1)}|/\rho g a^2 A \simeq .336$; $F_z^{(1)} \simeq 0$; and $|M_y^{(1)}|/\rho g a^3 A \simeq 0.051$; at $\omega \simeq 2.8$ rad/sec. For typical ocean spectra, the second-order contributions dominate (see Table 3). From Figures 3 for the case $\omega^+ = 3$ rad/sec and $\mu = 0$, we see that $LF_z^{(2)}$ and $z_c F_x^{(2)}$ contribute up to 25% and 20%, respectively of the total `pitch' moment f_o. Surprisingly, for small μ, the heave force $F_z^{(2)}$ has a greater effect than the surge force $F_x^{(2)}$ because of the longer moment arm L compared to z_c. On the other hand, $F_z^{(2)}$ decreases rapidly with μ, so that its overall contribution to the total pitch moment is smaller than $F_x^{(2)}$ for a typical spectrum.

We now consider the heave-pitch response of the TLP in irregular waves. As input, we use the two-parameter Pierson-Moskowitz spectrum for fully-developed seas:

$$S(\omega) = \frac{\omega_m^4 \; H_{1/3}^2}{4\pi \; \omega^5} \, \mathrm{Exp} \left[- \left(\frac{\omega_m}{\omega} \right)^4 / \, \pi \right] \tag{3.7}$$

where ω_m and $H_{1/3}$ are the mean frequency and significant wave height, respectively. For numerical illustration, two different conditions are considered – sea state A: $H_{1/3}$= 20', $T_m \equiv 2\pi/\omega_m$= 8 sec; and sea state B: $H_{1/3}$= 8', T_m= 6 sec.

From (2.5), we see that the quadratic input wave energy at springing frequency ω^+ due to two components in the spectrum frequencies 2μ apart is $S(\omega^+/2+\mu)S(\omega^+/2-\mu)$. This is plotted in Figure 5 for the two spectra A, B, for ω^+= 2.6 and 3.0 rad/sec respectively, as a function of the frequency difference μ. Note that the maximum quadratic input is, in general, not at μ= 0 but increases with μ, reaching a peak before rapidly diminishing. Taking into account the rapid attenuation with μ of the square of the exciting force QTF (Figure 3) in the integrand in (2.5), however, the final contribution to the resonant response from long and short wave interactions (large μ) is still relatively small.

Performing the integral (2.5) for the full TLP, we obtain the spectra of the second-order sum-frequency modal excitation in heave, S_{f3}, and pitch, S_{f0}. Figures 6 show these results in the vicinity of the respective natural frequencies. The results are compared to the approximation of Petrauskas & Liu (1987) in which contributions of the second-order potentials are excluded. The excitation spectra are underestimated by a factor of 5 or more in the approximate theory.

Finally we calculate the TLP motion response and the resulting tension loads. The total tendon response is given by $x_3 + Lx_5$. For simplicity, we consider the heave and pitch modes separately and calculate the spectra of the tendon-tension load due to these uncoupled motions: $S_{\tau 3}(\omega)= |H_3(\omega)|^2 S_{f3}(\omega)$, and $S_{\tau 0}(\omega)= |H_0(\omega)|^2 S_{f0}(\omega)$, respectively. The variances of the tendon-tension loads, σ^2, are simply the areas under the curves:

$$\sigma^2 = \int_0^\infty S_\tau(\omega)\, d\omega = \int_0^\infty |H(\omega)|^2\, S_f(\omega)\, d\omega \tag{3.8}$$

Since the damping ratios are small, the width of the peak in $H(\omega)$ is narrow compared to the rate of variation of the excitation spectrum and (3.8) can be approximated by:

$$\sigma^2 \simeq S_f(\omega_n) \int_0^\infty |H(\omega)|^2\, d\omega = S_f(\omega_n)\ \left(\frac{k_t}{m}\right)^2 \frac{\pi}{4}\, \frac{1}{\varsigma\, \omega_n^3} \tag{3.9}$$

upon evaluating the definite integral analytically. Thus the variance of the tendon load is proportional to the value of the excitation spectrum at natural frequency and inversely proportional to the damping ratio.

Table 3. Summary of tendon tension load rms (in kips) for a damping ratio of $\zeta = 0.05$ %.

	Spectrum A	Spectrum B
first-order excitation only		
heave mode: σ_3^L	0	0
pitch mode: σ_0^L	10	7
approximate theory without ϕ^+		
heave mode: σ_3^+	0	0
pitch mode: σ_0^+	47	21
$\sigma^+ + \sigma^L$	57	28
complete second-order theory		
heave mode: σ_3^+	12	6
pitch mode: σ_0^+	111	51
$\sigma^+ + \sigma^L$	133	64

Table 3 summarizes the tendon-tension load rms (for $\zeta=0.05\%$) for the present complete theory compared to that obtained by ignoring the contributions of the second-order potentials, as well as linearized first-order results. By including the contributions of the second-order sum-frequency potentials from all bichromatic frequency pairs in the spectrum, the present estimates of the tendon load rms are two to three times greater than those using quadratic contributions of first-order potentials only, while the results from first-order theory only are totally inadequate. In the complete theory, the tendon load rms due to second-order sum-frequency heave forces is only slightly over 10% of that due to pitch, although the result may be quite sensitive to the draft/radius ratio of the legs.

We have considered only normal (0 degree) wave incidence here. The calculation for other incidence angles is similar. For 45 degree incidence, the restoring moment is provided by only two of the four legs, and may be the more critical case for tendon design. For short-crested irregular seas, the present analysis can be readily extended. Without a careful analysis, however, it is unclear whether ignoring the wave directionality will necessarily result in a more conservative design.

4. CONCLUSION

The complete second-order sum-frequency diffraction theory for axisymmetric bodies is applied to a TLP leg to obtain the second-order sum-frequency wave force quadratic-transfer functions for an arbitrary pair of incident wave frequencies. Ignoring hydrodynamic interactions among the major member and wave effects on the pontoons, these QTF's are used in the motion analysis of a four-leg four-pontoon TLP in the presence of an irregular sea. Some of the major findings are:

i) The effect of the second-order sum-frequency potential is a major part of the total second-order forces and moments on a leg. As the difference between the two incident frequencies increases, this effect is decreased but may still be comparable to quadratic contributions of the first-order potential.

ii) The second-order potential attenuates slowly with depth. The vertical forces on a leg even at high frequencies may not be small and contributes measurably (~10% in this case) to the tendon loads. This effect is more important for small frequency differences of the incident waves. The effects of the second-order potential velocity and pressure on the pontoons may not be negligible in general.

iii) The springing excitation spectra in irregular waves is increased by a factor of five or six when effects of the nonlinear sum-frequency potentials are included.

iv) The tendon-tension load rms is two to three times larger than that predicted by an approximate second-order theory using only first-order potentials. This explains the large discrepancies between TLP measurements and the approximate wave-theory predictions reported by Petrauskas & Liu (1987).

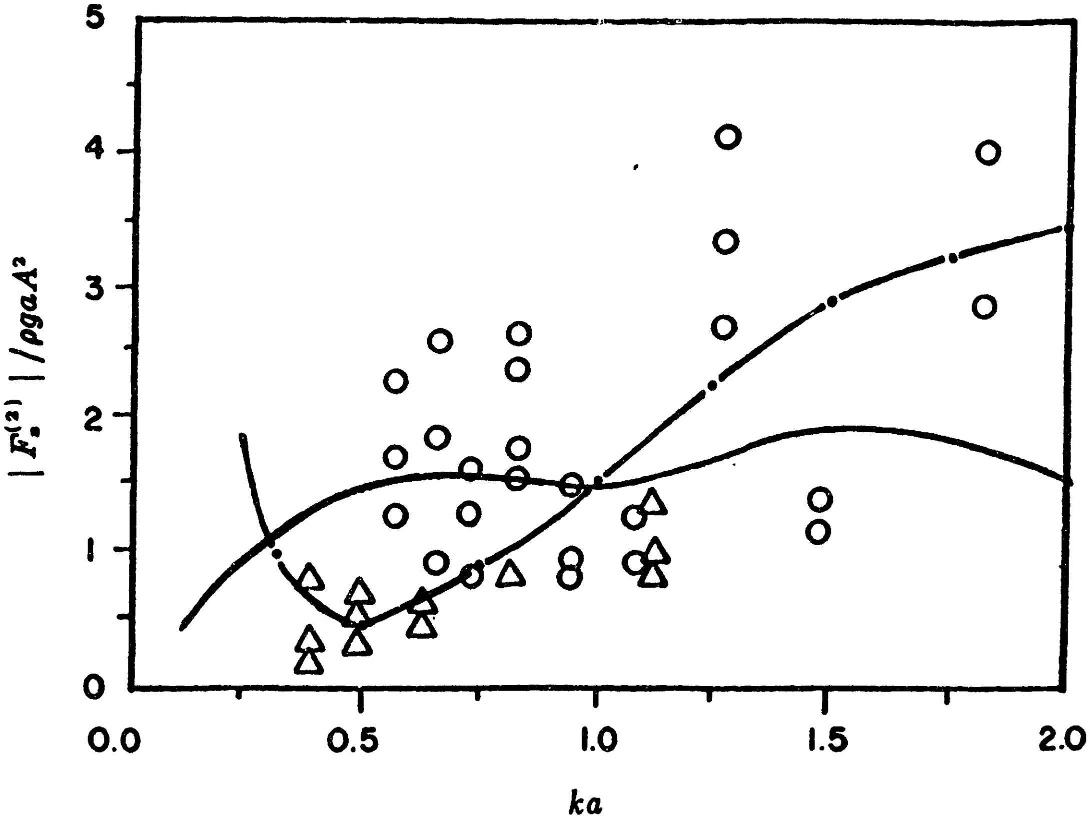

Figure 1. The second-order double-frequency horizontal force on a bottom-seated vertical cylinder, radius a, depth $4a$, due to a regular incident wave, wavenumber ka, amplitude A. The present complete theory (— · —) is compared to the measurements (O) and approximate theory (——) of [4], as well as experimental data (Δ) attributed to [12] (from [4]).

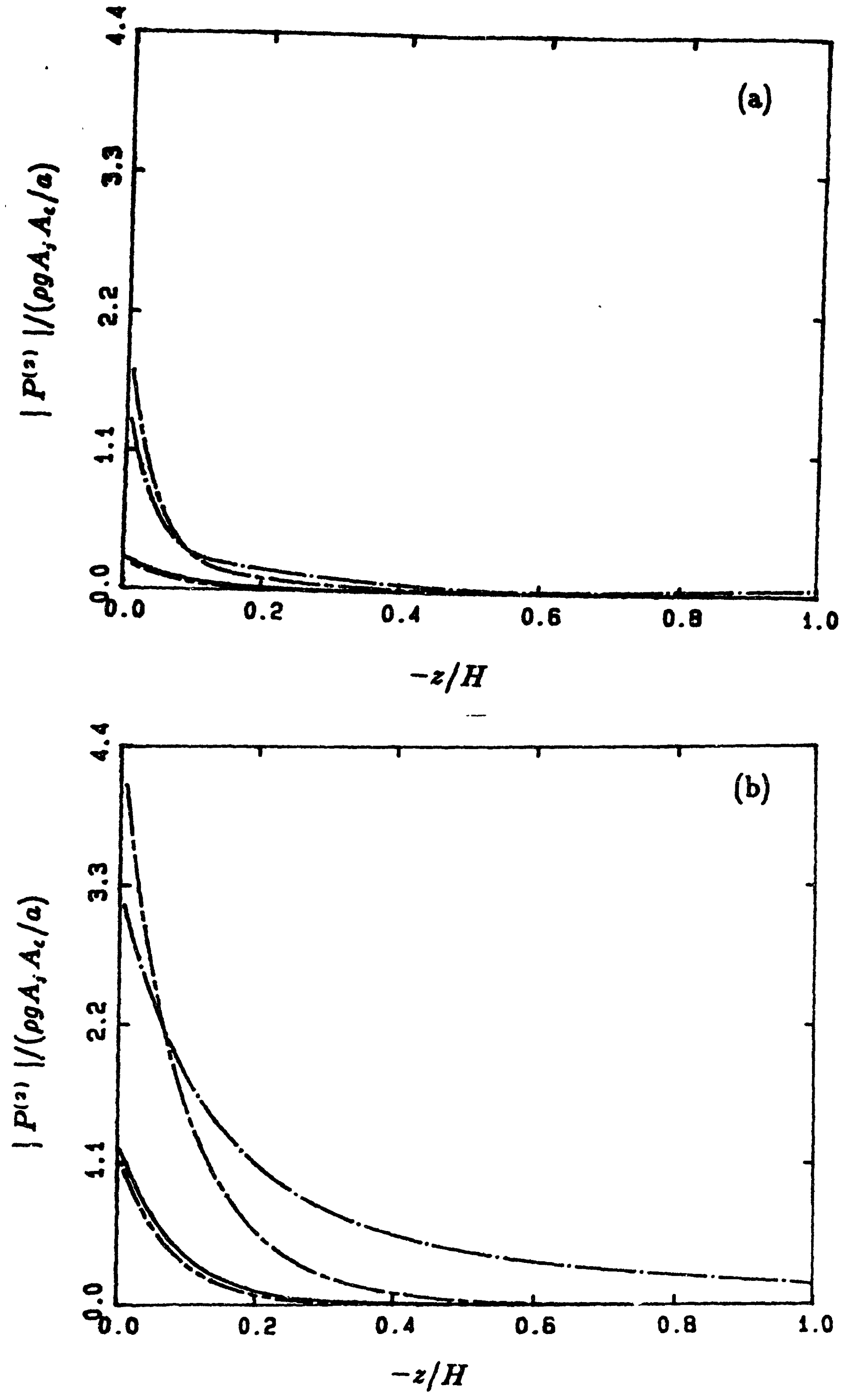

Figure 2. The second-order pressure on a TLP leg, radius a=25', draft H=4a, in deep water, plotted against depth for two azimuthal positions: (a) $\theta=0$ (lee side); and (b) $\theta=\pi$ (weather side). The curves are for: $|p_{pjl}{}^{+}|$ for ω_j,ω_l=1.4,1.4 (—— • ——); 1.0,1.8 (—— – ——); and $|p_{qjl}{}^{+}|$ for ω_j,ω_l= 1.4,1.4 (————); 1.0,1.8 (—— – – ——).

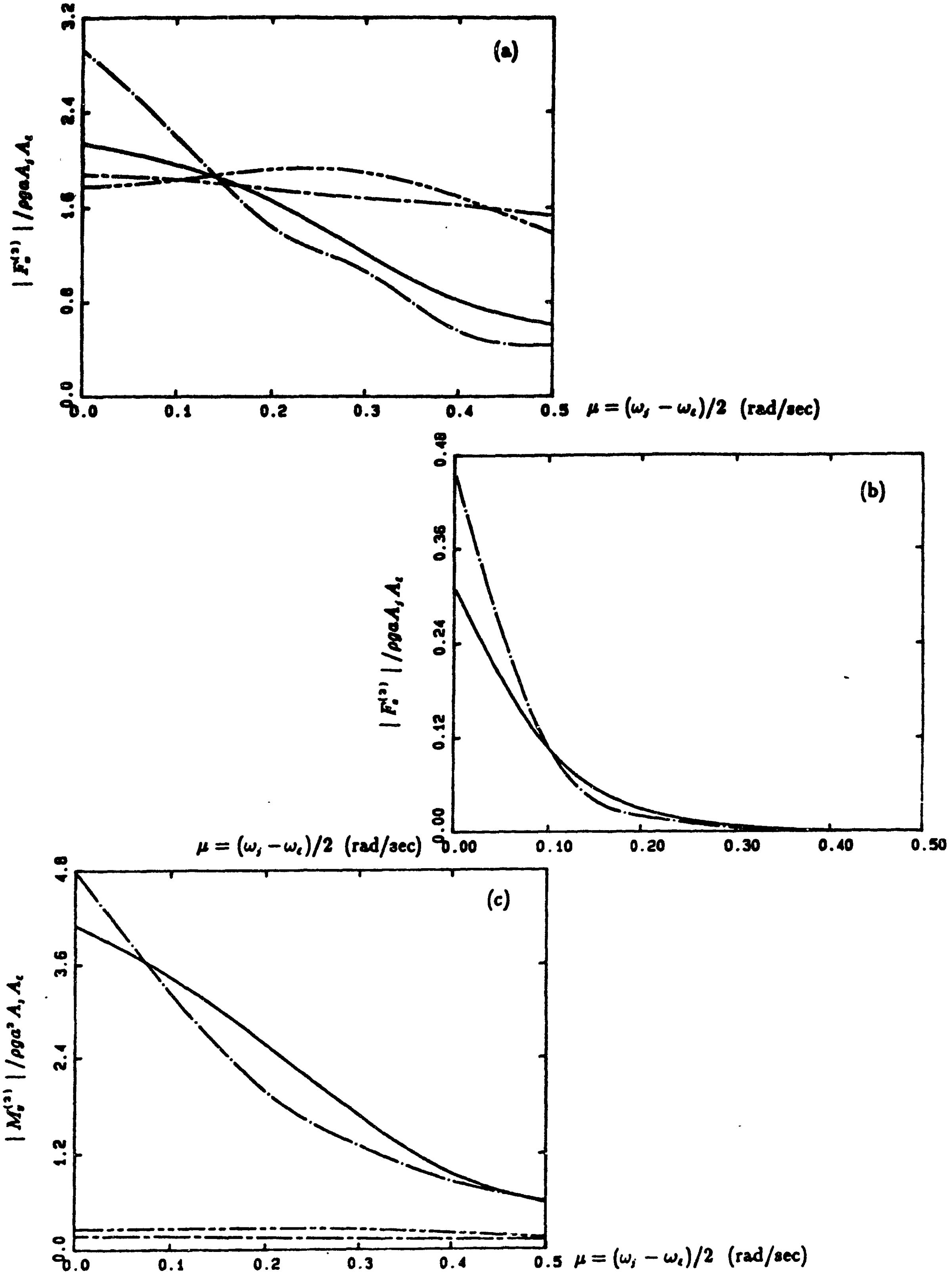

Figure 3. The second-order sum-frequency force QTFs on a TLP leg ((a) horizontal force, (b) vertical force, and (c) pitch moment). The curves are for: $|f_{pj1}{}^{+}|$ for ω^+=2.6 (———); and 3.0 (— • —), and $|f_{qj1}{}^{+}|$ for ω^+=2.6 (— – – —); and 3.0 (— – —).

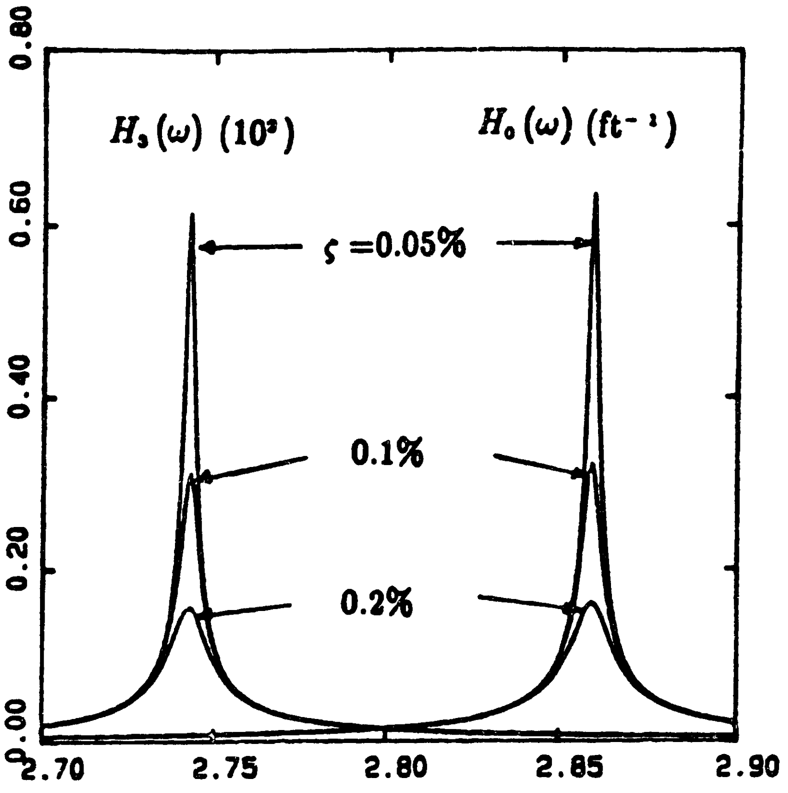

Figure 4. Tendon tension load RAO for the heave $H_3(\omega)$ and "pitch" mode $H_0(\omega)$ of the TLP for a range of damping ratios ς =0.05%, 0.1%, 0.2%.

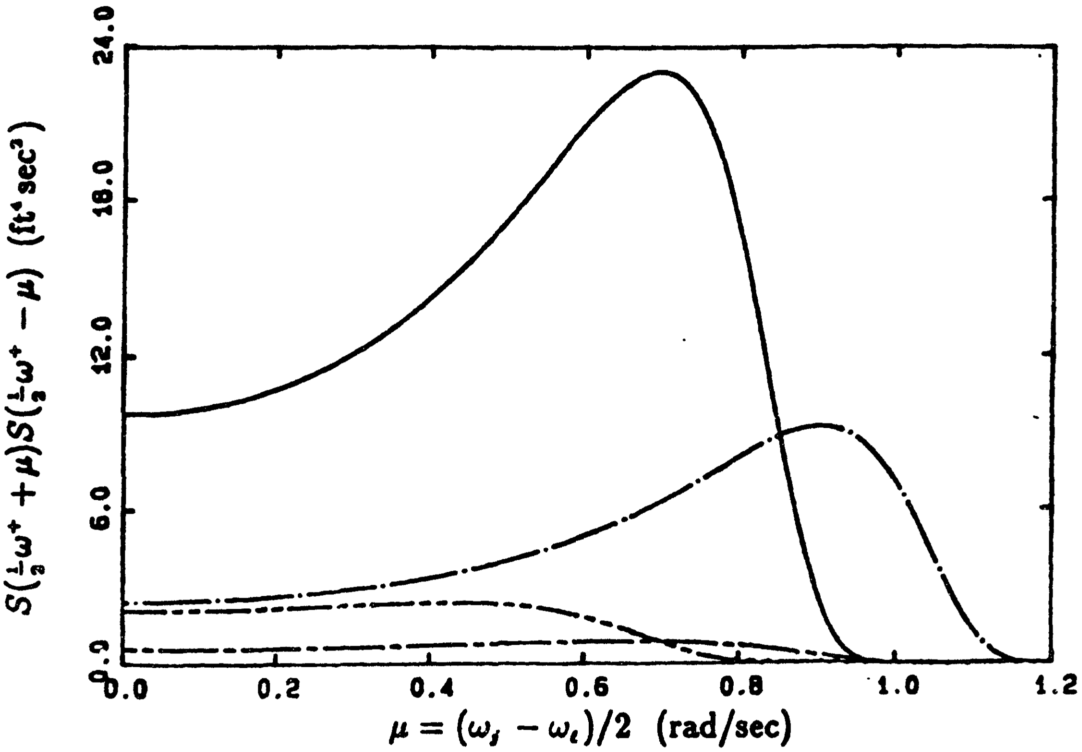

Figure 5. Quadratic wave input energy at sum frequency ω^+ due to two components in the spectrum frequency 2μ apart. The curves are for Spectrum A for $\omega^+ = 2.6$ (——), and 3.0 (— · —); and Spectrum B for $\omega^+ = 2.6$ (— - - - —), and 3.0 (— - —) (rad/sec).

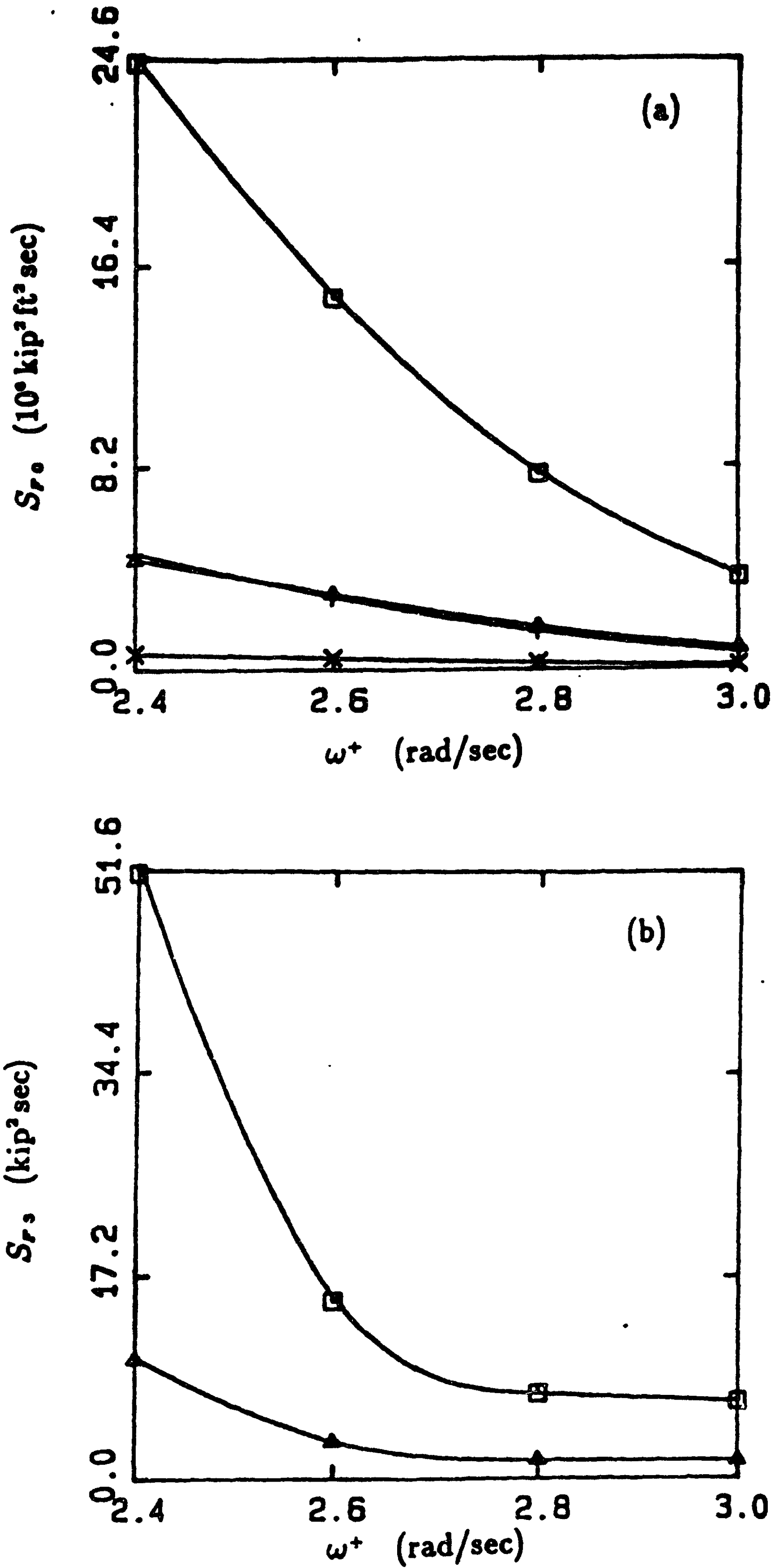

Figure 6. Second-order sum-frequency excitation spectrum for a full TLP for (a) "pitch" mode, and (b) heave. The curves are plotted against sum-frequency ω^+ for wave spectrum A: complete theory (□), approximation without $\phi^{(2)}$ (+) (≃ 0 for heave); and wave spectrum B: complete theory (Δ), approximation without $\phi^{(2)}$ (×) (≃ 0 for heave).

CHAPTER V

SLOWLY-VARYING WAVE DRIFT FORCES IN MULTIDIRECTIONAL IRREGULAR SEAS.

1. INTRODUCTION

Compliant deep-water structures and moored vessels often have very small restoring forces, and are susceptible to large resonant responses due to higher-order slowly-varying wave drift excitations. There have been many investigations of the second-order slowly-varying phenomena in the past decade, but they are mostly limited to unidirectional irregular waves, while studies of the more realistic short-crested seas are surprisingly rare.

A main difficulty of predicting second-order forces in general is the need to include the contribution of the second-order potential which is computationally difficult to obtain especially for three-dimensional bodies. For slowly-varying excitations, a number of engineering approximations have been proposed which include the index approximation of Newman (1974) and the envelope method of Marthinsen (1983a). These approximations assume that the spectra are narrow banded so that the exact quadratic transfer function (QTF) can be approximated by its monochromatic (mean drift force) value which is given from the first-order potential only. For many applications, the validity of a narrow-band frequency assumption is confirmed, for example in the numerical work of Faltinsen and Loken (1978) for two-dimensional bodies.

For multidirectional seas which are narrowly spread, the index and envelope approximations can be extended in a straightforward manner, although the additional assumption of narrow spreading can often be overly restrictive as pointed out by Marthinsen (1983b).

The fact that the inherent difficulty in solving for the exact QTF is not due to multi-directionality but to multiple frequencies leads us to the present approach, where Newman's narrow frequency band approximation is retained but the directional spreading is treated exactly. This is a useful approximation since in practice wave energies are typically fairly narrow banded and drift response periods very long, while on the other hand wave directional spreadings are often not narrow especially when more than one wave system is present. Thus the present work has a wider range of validity for general short-crested seas, but is otherwise not appreciably different from existing approximations in terms of analytical complexity or computational effort.

To provide some understanding of slowly-varying forces in short-crested seas, time-series simulations and spectral analyses of the forces are performed for the present method and for the index and envelope approximations. The statistics obtained from simulations agree well with those from the power spectra. For the probability distribution of the slowly-varying drift force, existing theories for the index and envelope methods are reexamined and generalized. In the index approximation, a remarkably simple closed-form probability density function (PDF) is obtained after taking advantage of the separability of summation expressions, which can be interpreted as a special case of the more general theory of Bedrosian and Rice (1971). This problem was also investigated in Vinje (1983), which unfortunately contained an important error. For the method of envelope, Langley(1984) derived the PDF for long-crested waves, which we extend to multidirectional seas and obtain also the probability distributions of related local variables such as the local amplitude, frequency, wavenumber and direction. All these results are confirmed by histograms obtained from direct numerical simulations of the processes.

For illustration, we consider the special case of a uniform vertical circular cylinder in the presence of combined storm and swell seas from different directions. A surprising result is obtained which indicates that the amplitude of the slowly-varing force can be substantially amplified when the wave systems are from opposing directions. This previously unreported phenomenon may be related to the field experience of Grancini et al (1984). Definitive experimental investigations are much needed.

2. SLOWLY-VARYING DRIFT FORCES

We consider the second-order slowly-varying drift forces on a body in the presence of irregular seas. The linear and second-order hydrodynamic forces on a body due to stationary Gaussian random seas can be in general expressed as a two-term Volterra series:

$$F_1(t) + F_2(t) = \int_{-\infty}^{\infty} h_1(\tau)\varsigma(t-\tau)\, d\tau + \int_{-\infty}^{\infty}\int_{-\infty}^{\infty} h_2(\tau_1,\tau_2)\varsigma(t-\tau_1)\varsigma(t-\tau_2)\, d\tau_1 d\tau_2 \tag{2.1}$$

where $h_1(\tau)$ and $h_2(\tau_1,\tau_2)$ are respectively the linear and quadratic impulse response functions. For example, $h_2(t-\tau_1,t-\tau_2)$ is the second-order exciting force at time t due to two unit-amplitude inputs at times τ_1 and τ_2 respectively. $\varsigma(t)$ is the ambient wave free-surface position at some reference point.

For unidirectional seas, the surface elevation $\varsigma(t)$ can be expressed as a sum of frequency components:

$$\varsigma(t) = \sum_i a_i \cos(\omega_i t + \epsilon_i) = \mathrm{Re} \sum_i A_i\, e^{i\omega_i t} \tag{2.2}$$

where a_i, ω_i, and ϵ_i are the amplitude, frequency, and phase of the i-th wave component, and ϵ_i is in general a uniformly-distributed random variable. We can rewrite the second term of (2.1) in an equivalent form in bifrequency domain:

$$F_2(t) = \mathrm{Re} \sum_{ij}\sum A_i A_j^* D_{ij}\, e^{i(\omega_i-\omega_j)t} + \mathrm{Re} \sum_{ij}\sum A_i A_j S_{ij}\, e^{i(\omega_i+\omega_j)t} \tag{2.3}$$

where $()^*$ represents complex conjugate of the quantity. $D_{ij} \equiv D(\omega_i,\omega_j)$ and $S_{ij} \equiv D(\omega_i,-\omega_j)$ are respectively the difference- and sum-frequency quadratic transfer functions (QTF), defined as the double Fourier transform of $h_2(\tau_1,\tau_2)$:

$$D(\omega_i,\omega_j) = \int_{-\infty}^{\infty}\int_{-\infty}^{\infty} h_2(\tau_1,\tau_2)\, e^{-i(\omega_i\tau_1-\omega_j\tau_2)}\, d\tau_1 d\tau_2 \tag{2.4}$$

Hereafter, we focus only on the slowly-varying (difference-frequency) part of the second-order force, $\tilde{F}(t)$, represented by the first term of (2.3):

$$\tilde{F}(t) = \text{Re} \sum_{i}\sum_{j} A_i A_j^* D_{ij} \, e^{i(\omega_i - \omega_j)t} \tag{2.5}$$

and D_{ij} satisfies the symmetry relation:

$$D_{ij} = D_{ji}^* \tag{2.6}$$

Note that (2.6) implies that $h_2(\tau_1,\tau_2)=h_2(\tau_2,\tau_1)$ which may not be true in general for a quadratic system. However, such a symmetry can always be achieved without loss of generality resulting in a simpler analysis. The time-average of $\tilde{F}(t)$ which gives the mean drift force $\bar{F}$, is obtained by setting i=j in (2.5):

$$\bar{F} = \sum_i a_i^2 D_{ii} = 2 \int_0^\infty S(\omega)\, D(\omega,\omega)\, d\omega \tag{2.7}$$

where $S(\omega)$ is the (one-sided) wave amplitude spectrum.

The exact QTF, D_{ij}, in general depends on quadratic combinations of the first-order potential, and also on the nonlinear potential of the second-order problem. Since the seminal work of Molin(1979) and Lighthill(1979), a satisfactory treatment of the second-order problem is now available (e.g. Kim & Yue;1988c,d, Eatock Taylor et al.;1988), although the computational effort is still quite substantial especially for multidirectinal sea application. For monochromatic incident waves, the difference-frequency component of the second-order force is steady, and the single-frequency QTF, D_{ii}, can be obtained in terms of first-order potentials only. For very low frequency excitations, such as those relevant to the horizontal motions of a moored ship or deep-water compliant platform, this fact can be exploited in a narrow-band approximation, wherein the bi-frequency QTF, D_{ij}, which depends on the second-order potential is replaced by the single-frequency QTF, D_{ii}, which does not depend on the second-order problem:

$$D_{ij} = D_{ii} + O(\omega_i - \omega_j)$$

so that (2.5) can be approximated as:

$$\tilde{F}(t) \simeq \mathrm{Re} \sum_{ij}\sum A_i A_j^* D_{ii} e^{i(\omega_i - \omega_j)t} \tag{2.8}$$

This approximation will be termed "index approximation" hereafter. For narrow-banded wave spectra and/or for slowly-varying excitations due to wave components close to each other in frequency, (2.8) should be useful provided that the gradient of D_{ij} with respect to frequency difference is sufficiently small near the diagonal D_{ii} (Ogilvie; 1983). Numerically, the validity of (2.8) has been investigated by Faltinsen & Loken(1978) for certain two-dimensional bodies and by Kim & Yue(1988d), Eatock Taylor et al(1988) for three dimensional bodies.

For <u>multidirectional</u> irregular seas, we can write $\zeta(t)$ as a double summation with respect to both frequency and incident direction:

$$\zeta(t) = \sum_{ik}\sum a_{ik} \cos(\omega_i t + \epsilon_{ik}) = \mathrm{Re} \sum_{ik}\sum A_{ik} e^{i\omega_i t} \tag{2.9}$$

where a_{ik} is the amplitude of a wave component of frequency ω_i and incidence angle β_k, and ϵ_{ik} its uniformly distributed random phase. The difference-frequency drift force in this case is given by:

$$\tilde{F}(t) = \mathrm{Re} \sum_{ijkl}\sum\sum\sum A_{ik}A_{jl}^{*} D_{ijkl} \, e^{i(\omega_i-\omega_j)t} \tag{2.10}$$

where $D_{ijkl} \equiv D(\omega_i,\omega_j,\beta_k,\beta_l)$ is the bichromatic-bidirectional quadratic transfer function, i.e., the (complex) second-order slowly-varying force due to the simultaneous incidence of two unit amplitude regular waves of frequency and direction ω_i, β_k and ω_j, β_l respectively. As before, D_{ijkl} satisfies the symmetry relation:

$$D_{ijkl} = D_{jilk}^{*} \tag{2.11}$$

The mean force with respect to time can be obtained when i=j in (2.10):

$$\bar{F} = \mathrm{Re} \sum_{ikl}\sum\sum a_{ik}a_{il} D_{iikl} \, e^{i(\epsilon_{ik}-\epsilon_{il})} \tag{2.12}$$

where the time average $\bar{F}$ still depends on the set of random phases for a specific realization. Upon taking the ensemble average with respect to the phases, we have:

$$E(\bar{F}) = \sum_{ik}\sum a_{ik}^{2} D_{iikk} = 2\int_{0}^{2\pi}\int_{0}^{\infty} S(\omega,\beta)\, D(\omega,\omega,\beta,\beta)\, d\omega d\beta \tag{2.13}$$

If the input spectrum is narrow in directional spreading in addition to narrow-banded in frequency, Newman's index approximation can be extended to the angular spreading and we write:

$$\tilde{F}(t) \simeq \mathrm{Re} \sum_{ijkl}\sum\sum\sum A_{ik}A_{jl}^{*} D_{iikk} \, e^{i(\omega_i-\omega_j)t} \tag{2.14}$$

where D_{iikk}, the QTF for a monochromatic wave with direction β_k, can again be obtained in terms of the linear wave-body interaction problem only.

Although the assumptions of narrow input frequency band and/or slowly-varying motion responses are usually quite acceptable, the analogous requirement of narrow spreading in incidence direction is often overly restrictive, and the approximation clearly fails when one is interested in two or more storms or storm-swell combinations from different directions. A much more reasonable approach is to assume narrow-bandedness for the frequency only but leave the directional spreading arbitrary in (2.10):

$$\tilde{F}(t) \simeq \mathrm{Re} \sum_{ijkl}\sum\sum\sum A_{ik}A_{jl}^{*}\, D_{iikl}\, e^{i(\omega_i-\omega_j)t} \tag{2.15}$$

This is the basis of our present approximation which has a larger range of validity than (2.14) for general short-crested seas, yet the analytical complexity or computational effort required are in fact not appreciably different. This is due to the fact that the major difficulty in calculating the exact QTF in (2.10) arises from bichromaticity and not the directional spreading. Thus, the monochromatic-bidirectional QTF D_{iikl} can still be evaluated in terms of the first-order potential only. A derivation of D_{iikl} utilizing the far-field approach is given in the Appendix D. D_{iikl} can be interpreted as the mean drift force due to an arbitrary combination of two waves of the same frequency from different directions.

Equation (2.13) for the ensemble-averaged mean drift force can be recovered identically from either (2.14) or (2.15), and the reduction of the mean drift force in the main direction due to directional spreading is given by the ratio of (2.7) and (2.13):

$$R_m = \int_0^{2\pi}\int_0^{\infty} S(\omega,\beta)\, D(\omega,\omega,\beta,\beta)\, d\omega d\beta \;\Big/\; \int_0^{\infty} S(\omega) D(\omega,\omega)\, d\omega \qquad (2.16)$$

An alternative but similar approach to the index approximation is the "envelope method" first suggested by Hsu and Blenkarn(1970) who regarded each element of a time series as part of a regular wave so that the slowly-varying drift force could be obtained from successive mean drift calculations within each element. This approach was placed on a somewhat more rigorous basis by Marthinsen(1983) using the concept of a modulated incident wave. For later reference, the formulation of the envelope method is outlined here. Consider the Hilbert transform pair for the ambient wave:

$$\begin{Bmatrix} \varsigma(t) \\ \eta(t) \end{Bmatrix} = \sum_i a_i \begin{Bmatrix} \cos \\ \sin \end{Bmatrix} (\omega_i t + \epsilon_i) \qquad (2.17)$$

If the input spectrum is narrow-banded, $\varsigma(t)$ and $\eta(t)$ can be rewritten in the form of a slowly-modulated wavetrain:

$$\begin{Bmatrix} \varsigma(t) \\ \eta(t) \end{Bmatrix} = \begin{Bmatrix} \mathrm{Re} \\ \mathrm{Im} \end{Bmatrix} \sum_i a_i\, e^{i((\omega_i - \omega_p)t + \epsilon_i)}\, e^{i\omega_p t} = \begin{Bmatrix} \mathrm{Re} \\ \mathrm{Im} \end{Bmatrix} a(t)\, e^{i(\omega_p t + \theta(t))} \qquad (2.18)$$

where $a(t)$ and $\theta(t)$ are the amplitude and phase of the slowly-varying envelope, and ω_p the frequency of the carrier wave:

$$\begin{aligned} a^2(t) &= \varsigma^2(t) + \eta^2(t) \\ \theta(t) + \omega_p t &= \tan^{-1}[\eta(t)/\varsigma(t)] \end{aligned} \qquad (2.19a,b)$$

Using the local frequency, ω_L, defined as the time derivative of the phase:

$$\omega_L(t) = \omega_p + \frac{d\theta(t)}{dt} \tag{2.20}$$

the slowly-varying drift force can then be approximated by:

$$\tilde{F}(t) \simeq a^2(t)\, D(\omega_L(t),\omega_L(t)) \tag{2.21}$$

Note that since D_{ii} is always positive, according to (21), $\tilde{F}(t)$ is also positive definite.

If the input directional spectrum is narrow-banded in both frequency <u>and</u> direction, this envelope method idea can be extended directly to multidirectional random seas by considering the Hilbert transform pair:

$$\begin{Bmatrix}\zeta(x,t)\\ \eta(x,t)\end{Bmatrix} = \sum_{ik}\sum a_{ik} \begin{Bmatrix}\cos\\ \sin\end{Bmatrix} (\omega_i t - k_i \bullet x + \epsilon_{ik}) \tag{2.22}$$

which can be rewritten in the form:

$$\begin{Bmatrix}\zeta(x,t)\\ \eta(x.t)\end{Bmatrix} = \begin{Bmatrix}\mathrm{Re}\\ \mathrm{Im}\end{Bmatrix} a(x,t)\, e^{i[\omega_p t - k_p \bullet x + \theta(x,t)]} \tag{2.23}$$

In this case, the amplitude and phase of the envelope are slowly-varying functions of both time and direction. The local frequency and local wavenumber vector are defined as:

$$\omega_L(x,t) = \omega_p + \frac{\partial\theta(x,t)}{\partial t} \tag{2.24}$$

$$k_L(x,t) = (k_L\cos\beta_L, k_L\sin\beta_L) = k_p - \nabla\theta(x,t) \tag{2.25}$$

where the local direction $\beta_L(x,t)$ is given by:

$$\beta_L(x,t) = \tan^{-1}\left[(k_p\sin\beta_p - \partial\theta/\partial y)/(k_p\cos\beta_p - \partial\theta/\partial x)\right] \tag{2.26}$$

If we choose x=0 as the reference point (for the definition of the QTF), the slowly-varying drift force is now given by:

$$\tilde{F}(t) \simeq a^2(t)\ D(\omega_L,\omega_L,\beta_L,\beta_L) \tag{2.27}$$

where ω_L and β_L are evaluated at x=0 from (2.24) and (2.26), and $\tilde{F}(t)$ acts instantaneously in the direction β_L.

We point out that although in certain applications it may be more convenient to use the local wavenumber k_L instead of the local frequency ω_L in (2.21) and (2.27); this cannot be done by direct substitution of the (deterministic) dispersion relation which is no longer valid between the random variables.

3. TIME-SERIES SIMULATION AND SPECTRAL ANALYSIS

For a given input amplitude spectrum $S(\omega)$, a time-series for the zero-mean Gaussian unidirectional seas can be realized by summing a large number of wave components with random phases[1]:

$$\zeta(t) = \sum_{i=1}^{N} \sqrt{2\ S(\omega_i)\Delta\omega}\ \cos(\omega_i t+\epsilon_i) \tag{3.1}$$

Here N and $\Delta\omega$ are the number and interval of frequency divisions, and ϵ_i is a random phase uniformly distributed between 0 and 2π. The time series

---

[1] As pointed out by Tucker et al(1984), the component amplitudes must in general be calcuated from the Rayleigh distribution, while (3.1) relies on the central limit theorem to guarantee the Gaussian property of $\zeta(t)$ in the limit. In this work, we use the latter for the sake of more direct results such as (3.7).

(3.1) has a periodicity of $2\pi/\Delta\omega$, so that a sufficiently small $\Delta\omega$(large N) is necessary for long-time simulations. This can be prohibitive for the direct simulation of $\tilde{F}(t)$ where the operation count typically increases as N^2. Thus, for long simulations, we adopt a modified method and write:

$$\zeta(t) = \sum_{i=1}^{N} \sqrt{2\, S(\omega_i)\Delta\omega}\ \cos(\omega_i' t+\epsilon_i) \tag{3.2}$$

where $\omega_i'=\omega_i+\delta\omega_i$, and $\delta\omega_i$ is a random perturbation uniformly distributed between $-\Delta\omega/2$ and $\Delta\omega/2$.

Short-crested irregular seas can be simulated in a similar way:

$$\zeta(t) = \sum_{i=1}^{N} \sum_{k=1}^{K} \sqrt{2\, S(\omega_i,\beta_k)\Delta\omega\Delta\beta}\ \cos(\omega_i' t+\epsilon_{ik}) \tag{3.3}$$

where in addition the incident directions are subdivided into K intervals of increment angle $\Delta\beta$, and ϵ_{ik} is a random phase uniformly distributed between 0 and 2π in ω-β space.

For a given realization of $\zeta(t)$, a simulation of $\tilde{F}(t)$ can be obtained from the QTF by evaluating the series (2.5) or (2.8), or the expression (2.21), at each time instant for unidirectional seas; or alternatively (2.10,14,15) or (2.27) for short-crested seas. If direct summation is used (eqs. 2.5,8,10,14,15), the QTF is calculated once for all arguments and stored for later times. When the envelope method is employed (eqs. 2.21,27), however, the QTF need to be calculated at each time instant for the instantaneous local frequency and direction. To avoid possible bias in $\tilde{F}(t)$ due to a particular sets of random phases, several simulations with different sets of random phases are typically made, and their statistics averaged (Jefferys; 1987).

For the input directional spectrum, we use a Pierson-Moskowitz spectrum with cosine-powered directional spreading where the separability with respect to frequency and direction is assumed:

$$S(\omega,\beta) = S(\omega)\, S_n(\beta)$$

$$S(\omega) = \frac{.0081\, g^2}{\omega^5}\, e^{-0.74(g/\omega U)^4}$$

$$S_n(\beta) = C_n \cos^{2n}\beta \qquad n=0,1,2,\ldots; \quad -\pi/2 \le \beta \le \pi/2 \tag{3.4}$$

Here g is the gravitational acceleration, U the wind speed, and the normalization C_n in (3.4) is chosen so that $\int S_n(\beta)d\beta = 1$. As n approaches infinity, the unidirectional spectrum $S(\omega)$ is recovered.

For the given directional spreading (3.4), the spreading reduction factor R_m in (2.16) can be obtained in closed form for vertically axisymmetric bodies:

$$R_m = \int_{-\pi/2}^{\pi/2} C_n \cos^{2n+1}\beta\, d\beta = \frac{2}{\pi}\, \frac{(2n!!)^2}{(2n+1)!!(2n-1)!!} \tag{3.5}$$

where $n!!=(n-2)!!n$ and $1!!=0!!\equiv 1$.

The spectrum of the slowly-varying drift force, S_F, can be expressed in terms of the wave spectrum for the preceding approximations. We rewrite (2.5) for $\tilde{F}(t)$ in the form:

$$\tilde{F}(t) = 2 \sum_{\substack{ij\\(i>j)}}\sum a_i a_j\, |D_{ij}| \cos[(\omega_i-\omega_j)t + \epsilon_i - \epsilon_j + \psi_{ij}]$$

with

$$D_{ij} = |D_{ij}|\, e^{i\psi_{ij}} \tag{3.6}$$

where the case i=j (i.e. $\bar{F}$) is not included here. The autocorrelation function $R_F(\tau)$ is then given by:

$$R_F(\tau) = \overline{F(t)F(t+\tau)} = 2 \sum_{\substack{ij \\ (i>j)}}\sum a_i^2 a_j^2 \; |D_{ij}|^2 \cos(\omega_i - \omega_j)\tau$$

$$= 8 \int_{\omega_j}^{\infty} d\omega_i \int_0^{\infty} d\omega_j \; S(\omega_i)S(\omega_j) \; |D(\omega_i,\omega_j)|^2 \cos(\psi_i - \psi_j)\tau \tag{3.7}$$

After a change of variables ($\omega_i - \omega_j = \mu$, $\omega_j = \omega$) and using the Wiener-Kinchin relation, we obtain the spectrum of the exact $\tilde{F}(t)$:

$$S_F(\mu) = 8 \int_0^{\infty} S(\omega)S(\omega+\mu) \; |D(\omega,\omega+\mu)|^2 \, d\omega \tag{3.8}$$

For the index approximation (2.8), we can follow a similar procedure and obtain the spectrum:

$$S_F(\mu) \simeq 2 \int_0^{\infty} S(\omega)S(\omega+\mu) \; [D(\omega,\omega)+D(\omega+\mu,\omega+\mu)]^2 \, d\omega \tag{3.9}$$

In the case of <u>multidirectional</u> seas, the time-averaged autocorrelation function $R_F(\tau)$ for (2.10) is still a function of the phases. Thus if we take ensemble average over the random phases, and using the symmetry relation (2.11), we obtain the ensemble-mean autocorrelation function:

$$E[R_F(\tau)] = 2 \sum_{\substack{ijkl \\ (i>j)}}\sum\sum\sum a_{ik}^2 a_{jl}^2 \; |D_{ijkl}|^2 \cos(\omega_i - \omega_j)\tau$$

$$= 8 \int_{\omega_j}^{\infty} d\omega_i \int_{0}^{\infty} d\omega_j \int_{0}^{2\pi} d\beta_k \int_{0}^{2\pi} d\beta_l \; S(\omega_i,\beta_k) S(\omega_j,\beta_l) \; |D(\omega_i,\omega_j,\beta_k,\beta_l)|^2 \cos(\omega_i-\omega_j)\tau \tag{3.10}$$

The spectrum of the exact $\tilde{F}(t)$ is then given by:

$$S_F(\mu) = 8 \int_{0}^{\infty} d\omega \int_{0}^{2\pi} d\beta_k \int_{0}^{2\pi} d\beta_l \; S(\omega,\beta_k) \; S(\omega+\mu,\beta_l) \; |D(\omega,\omega+\mu,\beta_k,\beta_l)|^2 \tag{3.11}$$

Corresponding results for the double index approximation (2.14) as well as our present approximation (2.15) are respectively:

$$S_F(\mu) \simeq 2 \int_{0}^{\infty} d\omega \int_{0}^{2\pi} d\beta_k \int_{0}^{2\pi} d\beta_l \; S(\omega,\beta_k) \; S(\omega+\mu,\beta_l) [D(\omega,\omega,\beta_k,\beta_k)+D(\omega+\mu,\omega+\mu,\beta_l,\beta_l)]^2 \tag{3.12}$$

and

$$S_F(\mu) \simeq 2 \int_{0}^{\infty} d\omega \int_{0}^{2\pi} d\beta_k \int_{0}^{2\pi} d\beta_l \; S(\omega,\beta_k) S(\omega+\mu,\beta_l) \{ |D(\omega,\omega,\beta_k,\beta_l)|^2 + |D(\omega+\mu,\omega+\mu,\beta_l,\beta_k|^2$$
$$+ 2 \; |D(\omega,\omega,\beta_k,\beta_l)| \; |D(\omega+\mu,\omega+\mu,\beta_l,\beta_k)| \cos[\phi(\omega,\omega,\beta_k,\beta_l)+\phi(\omega+\mu,\omega+\mu,\beta_l,\beta_k)] \tag{3.13}$$

Provided that the wave spectrum is narrow-banded in frequency, the approximation (3.13) gives reasonable results for small μ for all directional spreadings. When one is interested in the response spectra of lightly-damped low-natural-frequency systems, the prediction based on (3.13) is even more reliable since the transfer function of the system can be expected to filter out the relatively poorly approximated higher-frequency range.

4. APPLICATION TO STORM-SWELL MIXED SEAS

The approximation (2.15) allows us to study the slowly-varying forces on a body due to the simultaneous presence of seas from different directions. Grancini et al(1984) reported an interesting field observation of the SALS mooring system and a tanker ship installed in the Sicily Channel, where large dynamic roll motions were observed when combined storm and swell seas from different directions were present. To characterize such sea conditions, we write the total spectrum of the mixed seas as a sum of two spectra:

$$S(\omega,\beta) = S_1(\omega,\beta) + S_2(\omega)\delta(\beta-\beta_0) \tag{4.1}$$

where S_1 is the spectrum of a short-crested storm sea, and S_2 that of a long-crested swell with direction β_0. From (2.7) and (2.13), the mean drift force in waves specified by (4.1) can be obtained by simply superposing each contribution:

$$E(\bar{F}) = 2\int_0^\infty d\omega\int_0^{2\pi} d\beta\; S_1(\omega,\beta)\; D(\omega,\omega,\beta,\beta) + 2\int_0^\infty d\omega\; S_2(\omega)\; D(\omega,\omega,\beta_0,\beta_0) \tag{4.2}$$

This superposition is, however, no longer valid for the spectrum or the variance of $\tilde{F}(t)$. Using spectrum (4.1) in (3.11), we obtain the spectrum of the slowly-varying force $\tilde{F}(t)$ in the storm-swell irregular seas:

$$S_F(\mu) = S_{F_{11}}(\mu) + S_{F_{22}}(\mu) + S_{F_{12}}(\mu) \tag{4.3}$$

where

$$S_{F_{11}}(\mu) = 8\int_0^\infty d\omega\int_0^{2\pi} d\beta_k\int_0^{2\pi} d\beta_l\; S_1(\omega,\beta_k)\; S_1(\omega+\mu,\beta_l)\; |D(\omega,\omega+\mu,\beta_k,\beta_l)|^2 \tag{4.4}$$

$$S_{F_{22}}(\mu) = 8 \int_0^\infty d\omega \; S_2(\omega)\, S_2(\omega+\mu)\, |D(\omega,\omega+\mu,\beta_0,\beta_0)|^2 \tag{4.5}$$

$$\begin{aligned} S_{F_{12}}(\mu) = 8 \int_0^\infty d\omega \int_0^{2\pi} d\beta \; & [S_1(\omega,\beta)\, S_2(\omega+\mu)\, |D(\omega,\omega+\mu,\beta,\beta_0)|^2 \\ & + S_1(\omega+\mu,\beta)\, S_2(\omega)\, |D(\omega,\omega+\mu,\beta_0,\beta)|^2] \end{aligned} \tag{4.6}$$

The first and second terms of (4.3) are respectively contributions from the storm and swell alone, while the last term represents the additional contribution to the spectrum due to the interaction between the storm and swell. Because of this third term, the variance of $\tilde{F}(t)$ in a storm-swell mixed sea is always greater than that obtained from direct superposition of the individual contributions. If the storm and swell spectra do not overlap and are not close in frequency, (4.6) shows that the interaction effect is confined to large μ and is therefore relatively unimportant to low-natural-frequency systems. On the other hand, a change to S_F near μ=0 is critical to slowly-varying response. In this sense, usual low-frequency swells are less important than those whose frequency is within the energy band of the storm waves. Confining ourselves to this case, the narrow frequency band approximations of the previous sections can be applied directly. For the double index approximation (3.12), the interaction term can be written as:

$$\begin{aligned} S_{F_{12}}(\mu) = 2 \int_0^\infty d\omega \int_0^{2\pi} d\beta \; \{ & S_1(\omega+\mu,\beta)\, S_2(\omega)\, [D(\omega,\beta_0)+D(\omega+\mu,\beta)]^2 \\ & + S_1(\omega,\beta)\, S_2(\omega+\mu)\, [D(\omega,\beta)+D(\omega+\mu,\beta_0)]^2 \} \end{aligned} \tag{4.7}$$

while the approximation (3.13) gives:

$$S_{F_{12}}(\mu) = 2 \int_0^\infty d\omega \int_0^{2\pi} d\beta \, \{ \, [S_1(\omega+\mu,\beta)S_2(\omega)+S_1(\omega,\beta)S_2(\omega+\mu)] \bullet [|D(\omega,\omega,\beta_0,\beta)|^2$$
$$+|D(\omega+\mu,\omega+\mu,\beta,\beta_0)|^2 + 2|D(\omega,\omega,\beta_0,\beta)||D(\omega+\mu,\omega+\mu,\beta,\beta_0)| \bullet$$
$$\cos(\psi(\omega,\omega,\beta_0,\beta)+\psi(\omega+\mu,\omega+\mu,\beta,\beta_0))] \, \} \tag{4.8}$$

Since (4.8) is not restricted to narrow spreading, it is of interest to investigate the dependence of S_F on different incidence directions, β_0, of the swell with respect to the storm waves. The results clearly depend on the behavior of the QTF in $\beta_k-\beta_l$ space as well as the shape of the input directional spreading. As will be shown in our numerical results, the interaction effect is sensitive to changes in the direction of the swell, and large amplifications of the slowly-varying force is often possible. This phenomenon has important implications for the operation and safety of moored or dynamically-positioned vessels in mixed seas.

5. STATISTICS OF SLOWLY-VARYING DRIFT FORCES

In addition to quantities such as mean, variance and frequency spectrum, the probability distribution and in particular the extreme values of the slowly-varying drift forces are of engineering importance. For general nonlinear Volterra systems, a probability theory was developed in communication theory (e.g., Bedrosian & Rice; 1971), and was first applied to second-order wave forces by Neal(1974). In contrast to time-invariant linear systems, the second-order force in a Gaussian sea is in general not a Gaussian process, so that information on the force spectrum alone is of limited usefulness. For the index and envelope approximations, the probability density function (PDF) of $\tilde{F}(t)$ can be obtained in closed form, while for the exact QTF, the PDF must be calculated numerically.

<u>Index Approximation Method</u>

Applying the index approximation, the summations in (2.8) and (2.14) become separable, and the PDF of $\tilde{F}$ can be obtained analytically. The following approach was essentially followed in Vinje(1983), which unfortunately contains an error in the starting assumption in applying Newman's index approximation to both sum- and difference-frequency terms (his Eqs.4 & 5) leading to incorrect results.

If we define the Hilbert transfom pairs (x,X) and (y,Y):

$$\begin{Bmatrix} x \\ X \end{Bmatrix} = \sum_j a_j \begin{Bmatrix} \cos \\ \sin \end{Bmatrix} (\omega_j t+\epsilon_j); \qquad \begin{Bmatrix} y \\ Y \end{Bmatrix} = \sum_i a_i D_{ii} \begin{Bmatrix} \cos \\ \sin \end{Bmatrix} (\omega_i t+\epsilon_i) \tag{5.1}$$

then (2.8) can be written in the form:

$$F(t) = x(t)y(t) + X(t)Y(t) \tag{5.2}$$

where x,X,y and Y are zero-mean Gaussian random variables. The covariance matrix of these four variables is given by:

$$\mathrm{Cov}(x,y,X,Y) = \begin{bmatrix} \sigma_x^2 & m & 0 & 0 \\ m & \sigma_y^2 & 0 & 0 \\ 0 & 0 & \sigma_x^2 & m \\ 0 & 0 & m & \sigma_y^2 \end{bmatrix} \tag{5.3}$$

where

$$\sigma_x^2 = \sigma_X^2 = \int_0^\infty S(\omega)\, d\omega \tag{5.4}$$

$$\sigma_y^2 = \sigma_Y^2 = \int_0^\infty S(\omega)\; D^2(\omega,\omega)\; d\omega \tag{5.5}$$

and

$$m = E(xy) = E(XY) = \int_0^\infty S(\omega)\; D(\omega,\omega)\; d\omega \tag{5.6}$$

The mean value of $\tilde{F}(t)$ is then:

$$E(\tilde{F}) = E(xy) + E(XY) = 2m \tag{5.7}$$

and is identical to (2.7). Noting that xy and XY are independent random variables whose covariance is zero, the variance of $\tilde{F}$ is simply:

$$\sigma_F^2 = \sigma_{xy}^2 + \sigma_{XY}^2 \; ; \quad \text{with} \quad \sigma_{xy}^2 = \sigma_{XY}^2 = \sigma_x^2\sigma_y^2 + m^2 \tag{5.8}$$

This result can also be derived from (3.9). It is convenient to introduce the normalized Gaussian random variables z_+ and z_-, which are mutually independent:

$$z_{\pm} = [\; x/\sigma_x \pm y/\sigma_y \;] \; / \sqrt{2(1 \pm \rho)} \tag{5.9}$$

where

$$\rho = \text{cov}(xy)/\sigma_x\sigma_y \tag{5.10}$$

is the correleration coefficient of x,y. Defining the nondimensional force $f_1 \equiv xy/\sigma_x\sigma_y$, we can express it in terms of z_+ and z_-:

$$f_1 = z_+^2(\rho+1)/2 + z_-^2(\rho-1)/2 \tag{5.11}$$

$z_\pm^2/2$ have Gamma distributions whose characteristic functions are given by $(1-i\theta)^{-1/2}$. Eq. (5.11) is a special case of Bedrosian & Rice's general theory, where the corresponding equation contains an infinite sum of Gamma distribution variables. From the independence of z_+ and z_-, the characteristic function of f_1 can be shown to be equal to:

$$\Pi_{f_1}(\theta) = \{ [1-i(\rho+1)\theta] \; [1-i(\rho-1)\theta] \}^{-1/2}$$

A similar analysis can also be performed for the random variable $f_2 \equiv XY/\sigma_x\sigma_y$. Using the independence of xy and XY, we obtain finally the characteristic function of the random variable defined by $f \equiv \tilde{F}/\sigma_x\sigma_y = (xy+XY)/\sigma_x\sigma_y$:

$$\Pi_f(\theta) = \{ [1-i(\rho+1)\theta] \; [1-i(\rho-1)\theta] \}^{-1} \tag{5.12}$$

Taking the inverse Fourier transform of (5.12), we obtain a remarkably simple form for the probability density function p(f) which depends on the single parameter ρ:

$$p(f) = \frac{1}{2} \exp \{ - \frac{|f|}{1 \mp \rho} \}; \qquad f \lessgtr 0 \tag{5.13}$$

It is interesting to note that there is a small but nonzero probability of negative f which is confirmed by direct numerical simulation. In the limit of an extremely narrow-banded input spectrum ($\rho \rightarrow 1$), (5.13) is simply the exponential distribution and f is always positive as is expected for the case of drift force due to a single regular wave. The parameter ρ can be obtained from (5.10), or equivalently from the result of spectral analysis:

$$\rho = E(\tilde{F}) \; [2\sigma_F^2 - E^2(\tilde{F})]^{-1/2}$$

Note that since by definition, $|\rho| \leq 1$, it follows that the inequality,

$\sigma_F^2 \geq E^2(F)$, is always true.

For multidirectional seas, the foregoing analysis can be extended in a straight-forward manner using the Hilbert transform pairs (x,X) and (y,Y) defined as:

$$\begin{Bmatrix} x \\ X \end{Bmatrix} = \sum_{j}\sum_{l} a_{jl} \begin{Bmatrix} \cos \\ \sin \end{Bmatrix} (\omega_j t+\epsilon_{jl}); \qquad \begin{Bmatrix} y \\ Y \end{Bmatrix} = \sum_{i}\sum_{k} a_{ik} D_{iikk} \begin{Bmatrix} \cos \\ \sin \end{Bmatrix} (\omega_i+\epsilon_{ik}) \tag{5.14}$$

and identical results are reached upon substituting the following for (5.4~6):

$$\sigma_x^2 = \sigma_X^2 = \int_0^\infty d\omega \int_0^{2\pi} d\beta \; S(\omega,\beta); \qquad \sigma_y^2 = \sigma_Y^2 = \int_0^\infty d\omega \int_0^{2\pi} d\beta \; S(\omega,\beta) \; D^2(\omega,\omega,\beta,\beta) \tag{5.15}$$

and

$$m = E(xy) = E(XY) = \int_0^\infty d\omega \int_0^{2\pi} d\beta \; S(\omega,\beta) \; D(\omega,\omega,\beta,\beta) \tag{5.16}$$

Envelope Approximation Method

When the envelope approximation is used, the requisite result for the PDF can be obtained using multiple transforms of the local variables. If we redefine the Hilbert transform pair:

$$\begin{Bmatrix} \varsigma(x,t) \\ \eta(x,t) \end{Bmatrix} = a(x,t) \begin{Bmatrix} \cos \\ \sin \end{Bmatrix} \theta(x,t) = \sum_i a_i \begin{Bmatrix} \cos \\ \sin \end{Bmatrix} [(\omega_i-\omega_p)t-(k_i-k_p)x+\epsilon_i] \tag{5.17}$$

the covariance matrix of the four slowly-varying Gaussian random variables, $\varsigma, \eta, \varsigma_t$ and η_t, can be written as:

$$\mathrm{cov}(\varsigma,\eta,\varsigma_t,\eta_t) = \begin{bmatrix} m_o & 0 & 0 & m_1 \\ 0 & m_o & -m_1 & 0 \\ 0 & -m_1 & m_2 & 0 \\ m_1 & 0 & 0 & m_2 \end{bmatrix} \tag{5.18}$$

where the n-th central moment m_n is defined as:

$$m_n = \int_0^\infty (\omega-\omega_p)^n \, S(\omega) \, d\omega \qquad (5.19)$$

The choice of the carrier-wave frequency, ω_p, is arbitrary at this point, and we can diagonalize the covariance matrix by selecting ω_p so that the first central moment m_1 is zero. Thus, we set $\omega_p = M_1/M_0$, where the moment M_n is defined as:

$$M_n \equiv \int_0^\infty \omega^n \, S(\omega) \, d\omega \qquad (5.20)$$

Then, from the independence of the variables ζ, η, ζ_t and η_t, the joint distribution can be found easily:

$$p(\zeta,\eta,\zeta_t,\eta_t) = \frac{1}{4\pi^2 \, m_o m_2} \, e^{-\left[(\zeta^2+\eta^2)/m_o \, + \, (\zeta_t^2+\eta_t^2)/m_2 \right]/2} \qquad (5.21)$$

Transforming these variables to the set, $\{a, a_t, \theta, \theta_t\}$, and integrating with respect to the dummy variables a_t and θ, we obtain the joint distribution of a and θ_t :

$$p(a,\theta_t) = \frac{a^2}{m_o \sqrt{2\pi m_2}} \, e^{-(a^2/m_o \, + \, a^2\theta_t^2/m_2)/2} \qquad (5.22)$$

Integration of (5.22) with respect to θ_t yields the well known Rayleigh distribution. Upon further transformation of (5.22) into variables $\tilde{F}$ and ω_L, we finally obtain the joint distribution for the slowly-varying drift force and local frequency:

$$p(\tilde{F},\omega_L) = \frac{\sqrt{\tilde{F}}}{2\sqrt{2\pi m_2}\, m_o D(\omega_L)^{1.5}} \exp\{ \frac{-\tilde{F}}{2D(\omega_L)} [1/m_o + (\omega_L - M_1/M_o)^2/m_2]\} \tag{5.23}$$

Formula (5.23) was also obtained by Langley(1984). However, his choice of $\omega_p=\sqrt{(M_2/M_0)}$, which do not diagonalize (5.18), led to an incorrect later result for $p(\tilde{F})$. Integrating (5.23) with respect to ω_L (or $\tilde{F}$) yields the PDF of $\tilde{F}$ (or ω_L):

$$p(\tilde{F}) = \int_{-\infty}^{\infty} p(\tilde{F},\omega_L)\, d\omega_L \tag{5.24}$$

$$p(\omega_L) = \frac{1}{2m_o\sqrt{m_2}} [1/m_o + (\omega_L - M_1/M_o)^2/m_2]^{-3/2} \tag{5.25}$$

The cumulative density function of ω_L is given by:

$$\text{prob}(\omega_L \le \omega) = (1 + \epsilon_\omega/\sqrt{1+\epsilon_\omega^2})/2 \; ; \quad \text{where } \epsilon_\omega = \sqrt{m_o/m_2}\,(\omega - M_1/M_o) \tag{5.26}$$

From (5.25) we note that there is finite probability of negative ω_L, which is non-physical and for which $\tilde{F}\equiv 0$, so that there is an integrable singularity in the probability distribution of $\tilde{F}$ (Eq.5.24) at $\tilde{F}=0$. Since there is not an explicit relationship between the local frequency and local wavenumber, a direct transformation of (5.23) or (5.25) cannot be used to obtain the PDF for k_L. If the probability density for k_L is desired, it is convenient to start with variables ζ,η,ζ_x and η_x instead. The covariance matrix can then be diagonalized by selecting wavenumber of the carrier wave $k_p = M_2/M_0 g$:

$$\mathrm{cov}(\zeta,\eta,g\zeta_x,g\eta_x) = \begin{bmatrix} M_o & 0 & 0 & 0 \\ 0 & M_o & 0 & 0 \\ 0 & 0 & \sigma^2 & 0 \\ 0 & 0 & 0 & \sigma^2 \end{bmatrix} = \mathrm{diag}\ [M_o,M_o,\sigma^2,\sigma^2] \tag{5.27}$$

where

$$\sigma^2 = \int_o^\infty S(\omega)\ (\omega^2-\omega_p^2\ )^2\ d\omega = M_4 - M_2^2/M_o \tag{5.28}$$

and deep water is assumed. Note that for the Pierson-Moskowitz spectrum (3.4), the moment M_4 is unbounded and a suitable spectral cut-off is in general required (see §6). A similar procedure leads to the joint probability distribution of $\tilde{F}$ and k_L:

$$p(\tilde{F},k_L) = \frac{g\sqrt{\tilde{F}}}{2\sqrt{2\pi}\ m_o\sigma D(k_L)^{1.5}}\ \exp\{\frac{-\tilde{F}}{2D(k_L)}\ [1/m_o + g^2(k_L-M_2/gM_o)^2/\sigma^2]\} \tag{5.29}$$

and the PDF of $\tilde{F}$ and k_L are given respectively by:

$$p(\tilde{F}) = \int_{-\infty}^{\infty} p(\tilde{F},k_L)\ dk_L \tag{5.30}$$

$$p(k_L) = \frac{g}{2m_o\sigma}\ [1/m_o + g^2(k_L-M_2/gM_o)^2/\sigma^2]^{-3/2} \tag{5.31}$$

Similar to (5.24), $p(\tilde{F})$ in (5.30) contains an integrable singularity at $\tilde{F}$ =0. The cumulative density of k_L can be obtained from the integration of (5.31), and is given by (5.26) with ϵ_ω replaced by ϵ_k defined as:

$$\epsilon_k = g\sqrt{M_o}\ \ (k-M_2/gM_o)/\sigma \tag{5.32}$$

For multidirectional seas, the foregoing analysis can be extended by using the Hilbert transform pair:

$$\begin{Bmatrix}\zeta(x,t)\\ \eta(x,t)\end{Bmatrix} = a(x,t) \begin{Bmatrix}\cos\\ \sin\end{Bmatrix} \theta(x,t) = \Sigma\Sigma_{ik} a_{ik} \begin{Bmatrix}\cos\\ \sin\end{Bmatrix} [(k_i-k_p)\bullet x-(\omega_i-\omega_p)t+\epsilon_{ik}] \tag{5.33}$$

If we choose the direction and wavenumber of the carrier wave as $\beta_p=0$, and

$$k_p = M^C_{2,1}/gM_o$$

where

$$\begin{Bmatrix}M^C_{ij}\\ M^S_{ij}\end{Bmatrix} = \int_0^{\infty} d\omega \int_0^{2\pi} d\beta\ S(\omega,\beta)\ \omega^i \begin{Bmatrix}\cos^j\beta\\ \sin^j\beta\end{Bmatrix} \tag{5.34}$$

the covariance matrix of the six variables, $\{\zeta,\zeta_x,\zeta_y,\eta,\eta_x,\eta_y\}$ can again be diagonalized to yield:

$$\mathrm{cov}(\zeta,\eta,g\zeta_x,g\zeta_y,g\eta_x,g\eta_y) = \mathrm{diag}[M_o,M_o,\sigma_1^2,\sigma_2^2,\sigma_1^2,\sigma_2^2] \tag{5.35}$$

where

$$\sigma_1^2 = M^C_{4,2} - (M^C_{2,1})^2/M_o\ ; \qquad \sigma_2^2 = M^S_{4,2} \tag{5.36}$$

and again deep water and symmetry of the directional spreading are assumed. The joint distribution of these six variables are:

$$p = \frac{1}{(2\pi)^3 M_o\sigma_1^2\sigma_2^2} \exp\{-[(\zeta^2+\eta^2)/2M_o+g^2(\zeta_x^2+\eta_x^2)/2\sigma_1^2+g^2(\zeta_y^2+\eta_y^2)/2\sigma_2^2]\} \tag{5.37}$$

Transforming (5.37) to the variables $\{a,a_x,a_y,\theta,\theta_x,\theta_y\}$, and integrating with respect to the variables a_x,a_y and θ, we have:

$$p(a,\theta_x,\theta_y) = \frac{g^2a^3}{2\pi M_o\sigma_1\sigma_2} \exp\{-a^2[1/M_o+g^2\theta_x^2/\sigma_1^2+g^2\theta_y^2/\sigma_2^2]/2\} \tag{5.38}$$

Integrating (5.38) with respect to θ_x and θ_y yields the same Rayleigh distribution as (5.22), and transformation into the variables, $\tilde{F},k_L,\beta_L$ gives the joint distribution:

$$p(\tilde{F},k_L,\beta_L) = \frac{g^2 k_L \tilde{F}}{4\pi M_o \sigma_1 \sigma_2 D(k_L,\beta_L)\,|D(k_L,\beta_L)|} \cdot$$

$$\exp\{ - \frac{\tilde{F}}{2D(k_L,\beta_L)} [1/M_o + g^2(k_p - k_L\cos\beta_L)^2/\sigma_1^2 + (gk_L\sin\beta_L)^2/\sigma_2^2]\} \qquad (5.39)$$

where $\tilde{F}$ must have the same sign as $D(k_L,\beta_L)$. The result (5.39) was also obtained by Vinje(1985) via a much more indirect way. Integrating (5.39) with respect to k_L and β_L leads finally to the PDF of $\tilde{F}(t)$:

$$p(\tilde{F}) = \int_0^{\infty} dk_L \int_0^{2\pi} d\beta_L \; p(\tilde{F},k_L,\beta_L) \qquad (5.40)$$

Note that there is no singularity at $\tilde{F}=0$ in the above PDF since there is no finite region in k_L-β_L space for which $\tilde{F}\equiv 0$.

For vertically axisymmetric bodies, the result is simplified:

$$p(\tilde{F},k_L,\beta_L) = \frac{g^2 k_L |\tilde{F}|}{4\pi M_o \sigma_1 \sigma_2 D^2(k_L)\cos^2\beta_L} \exp\{- \frac{\tilde{F}\, Q(k_L,\beta_L)}{2D(k_L)\cos\beta_L}\} \qquad (5.41)$$

where $Q(k_L,\beta_L)$ is a quadratic polynomial given by:

$$Q(k_L,\beta_L) = \alpha_o - \alpha_1 k_L \cos\beta_L + \alpha_2 k_L^2 \cos^2\beta_L + \alpha_3 k_L^2$$

with

$$\alpha_o = M^C_{4,2}/q \;; \quad \alpha_1 = 2gM^C_{2,1}/q \;; \quad \alpha_2 = g^2(M_o/q - 1/M^S_{4,2}) \;; \quad \alpha_3 = g^2/M^S_{4,2}$$

and $$q = M_o M^C_{4,2} - (M^C_{2,1})^2 \qquad (5.42)$$

The joint distribution of k_L and β_L can be obtained from (5.41):

$$p(k_L,\beta_L) = g^2 k_L \;/\; \pi M_o \sigma_1 \sigma_2 Q^2 \qquad (5.43)$$

Integrating with respect to k_L gives the PDF of β_L:

$$p(\beta_L) = \frac{g^2}{\pi M_0 \sigma_1 \sigma_2} \{ 2/\Delta + 2\alpha_1 \Delta^{-1.5} \cos \beta_L \, [\pi/2 - \tan^{-1}(-\alpha_1 \cos \beta_L/\sqrt{\Delta})] \}$$

$$\Delta \equiv 4\alpha_0\alpha_3 + (4\alpha_0\alpha_2 - \alpha_1^2) \cos^2\beta_L \tag{5.44}$$

which is the probability distribution of the direction of the slowly-varying drift forces acting on an axisymmetric body.

For numerical integration of (5.24) and (5.30), it is convenient to subdivide the domain of integration into three parts, so that for (5.30) for example, we write:

$$p(\tilde{F}) = \left\{ \int_{-\infty}^{0} + \int_{0}^{\epsilon} + \int_{\epsilon}^{\infty} \right\} dk_L \; p(\tilde{F},k_L) \;\; \equiv \;\; p_1(\tilde{F}) + p_2(\tilde{F}) + p_3(\tilde{F})$$

In the first interval, $-\infty \leq k_L \leq 0$, $D(k_L)$ is identically zero, and the integral can be obtained analytically:

$$p_1(\tilde{F}) = \lim_{\delta \to 0} \frac{1}{2M_0\delta} \, e^{-\hat{F}/2M_0\delta} \; \mathrm{erf}[-(M_2/\sigma M_0) \sqrt{\tilde{F}/\delta} \tag{5.45}$$

Thus, $p_1(\tilde{F})$ behaves like a delta function at $\tilde{F}=0$, and the contribution of $p_1(\tilde{F})$ to the cumulative density of $\tilde{F}$ can be obtained from the probability $P(k_L \leq 0)$ in (5.32). In the second interval, $0 \leq k_L \leq \epsilon$, $D(k_L)$ is typically small and p_2 depends on the asymptotic behavior of $D(k_L)$ for $k_L \ll 1$. For uniform vertical cylinders (see Appendix D), $D(k_L)$ decreases as k_L^3 for $k_L \ll 1$, so that $p_2(\tilde{F})$ has contributions only near $\tilde{F}=0$ and decreases exponentially for $\tilde{F} > O(\epsilon^3)$. The range of p_2 can be limited near 0+ by choosing a sufficiently small ϵ, and the cumulative density obtained from $P(0 \leq k_L \leq \epsilon)$. The integrand in p_3 is regular and the integral is readily obtained by direct quadrature (Romberg quadrature is used here).

Similar analyses and numerical procedure are used for (5.40, 41) where both the limits $k_L \to 0$ and $\beta_L \to \pi/2$ are treated asymptotically. In this case, negative values of $\tilde{F}$ are possible when $|\beta_L| \geq \pi/2$ and there is no singularity at $\tilde{F}=0$ since $\tilde{F}$ is not identically zero in any interval of k_L and β_L.

6. NUMERICAL RESULTS AND DISCUSSION

With the preceding formulation, the exact mean and approximate slowly-varying drift forces and statistics can be obtained for unidirectional and short-crested irregular seas. For simplicity, we consider a vertically axisymmetric body in deep water. Specifically, we choose a uniform vertical cylinder of radius a=10m, and a wind speed of U=30 knots in the Pierson-Moskowitz spectrum (3.4). To ensure the narrow-bandedness of the spectrum, the wave energy is assumed to be zero for frequencies $\omega \leq .3s^{-1}$ and $\omega \geq 1.3s^{-1}$. In general, the narrow-bandedness can be quantified by the parameter $q_s^2 \equiv 1-M_1^2/M_0M_2$, where q_s^2 is equal to 0 for monochromatic seas. For the present truncated spectrum, the value of q_s is 0.27, whereas a typical value for a North Sea wave spectrum is $q_s=0.3$.

In this case, the monochromatic bidirectional QTF, D_{ijkl}, can be obtained analytically and is presented in the Appendix D. Table 1 shows the values of $D_x(\omega,\omega,\beta_k,\beta_l)$ for a range of incidence angles β_k and β_l, and frequency ω^2a/g $k_0a=0.5$. Along the diagonal ($\beta_k=\beta_l$), the real part of D_x (or D_y) has cosine (or sine) behavior, and the imaginary part is zero since the single-wave QTF is real. It is interesting to note that the magnitude of D_{ijkl} for different incident angles $\beta_k \neq \beta_l$ can be several times greater than that for a narrow directional spreading case.

Table 1. Quadratic transfer function, $D_{iikl}=D(\omega,\omega,\beta_k,\beta_l)$, for the drift force in the x direction in the presence of two incident waves, frequency $\omega^2a/g=k_0a=0.5$, and incidence angles β_k and β_l. The results are normalized by ρga. Note that $D_{iikl}=D_{iilk}^*$.

Real(D_{iikl}):

β_l/π	β_k/π = -1	-.75	-.5	-.25	0	.25	.5	.75	1
-1	-.286	-.214	-.083	-.012	.000	-.012	-.083	-.214	-.286
-.75		-.202	-.089	.000	.012	.000	-.029	-.118	-.214
-.5			.000	.089	.083	.029	.000	-.029	-.083
-.25				.202	.214	.118	.029	.000	-.012
0					.286	.214	.083	.012	.000
.25						.202	.089	.000	-.012
.5							.000	-.089	-.083
.75								-.202	-.214
1									-.286

Imag(D_{iikl}):

β_l/π	β_k/π = -1	-.75	-.5	-.25	0	.25	.5	.75	1
-1	.000	-.032	.152	.665	.962	.665	.152	-.032	.000
-.75		.000	-.077	.215	.665	.681	.275	.000	.032
-.5			.000	-.077	.152	.275	.000	-.275	-.152
-.25				.000	-.032	.000	-.275	-.681	-.665
0					.000	.032	-.152	-.665	-.962
.25						.000	.077	-.215	-.665
.5							.000	.077	-.152
.75								.000	.032
1									.000

Given two <u>regular</u> waves of the same frequency, the mean drift force on the body is in general a function of the wave amplitudes (a_1,a_2), phases (ϵ_1,ϵ_2), and incident angles (β_1,β_2). Fixing the wave frequency at

$k_0a=0.5$ and amplitude $a_1=a_2$, we show in Figures 1a and b the mean drift force in the x and y direction respectively as a function of the difference in phase $\Delta\epsilon\equiv\epsilon_2-\epsilon_1$, for the different incident angles $\beta_1=0$, and $\beta_2/\pi=0,.25,.5,.75$ and 1. For the main direction steady drift force $\bar{F}_x$, the maximum amplitude for $\beta_2=\pi$, depending on relative phases, is almost twice as large as that for $\beta_2=0$. As expected, the drift force is always positive for two incident waves in the same direction, whereas $\bar{F}_x$ is an odd function of $\Delta\epsilon$ for waves in opposing directions. Thus the (phase ensemble-averaged) mean steady force is still largest for $\beta_2=0$. For the transverse drift force, we note another interesting result in that the maxima for any $\Delta\epsilon$ occur when β_2 is at an obtuse angle $3\pi/4$ rather than at the normal incidence of 90°. These observations are, however, directly dependent on the frequency of the incident waves. This is shown in Figures 2, where the maximum (over all $\Delta\epsilon$) of the drift force in the longitudinal and transverse directions respectively for $\beta_2=0$ and π, and $\beta_2=\pi/2$ and $3\pi/4$, are compared over a range of wavenumbers k_0a. In both cases, the incident waves at obtuse angles have greater maximum $\bar{F}$ in the long-wave range ($k_0a < \sim 2/3$), whereas the opposite is true for shorter waves. These deterministic results have much relevance to the case of multi-directional irregular incident waves as will be discussed later. When the directional spreading is small, the double-index and envelope approximations give reasonable estimates, but fail as the directional speading increases. Consequently, the interesting dual wave interaction results above are not predicted by these methods. For example, Figure 3 shows the maximum (over all phase combinations) x-direction drift force as a function of the second incident wave angle β_2. Our exact result shows a minimum at $\beta_2 \sim 80^\circ$, but a maximum F_x of over 1.6 times its value at $\beta_2=0$ when the waves are from opposite directions. As expected, the predictions based on narrow-spreading approximations are poor except for small values of β_2.

We next consider the time series of the slowly-varying drift force. For these simulations, the input wave spectrum is subdivided into N=K=25 segments in both the frequency and directional domains. A sampling interval of $\Delta t = 2$ seconds is used which satisfies the Nyquist criterion. First we show the results for unidirectional seas (Figures 4) using the envelope approximation, the index method, and an Inverse Discrete Fast Fourier Transform (IDFFT) method suggested by Oppenheim & Wilson(1980). The method of envelope always gives non-negative forces, and remains zero whenever the local frequecy (or wavenumber) becomes negative. This is a numerical confirmation of the integrable singularity observed earlier in the PDF of $\tilde{F}$ at $\tilde{F}=0$. The index approximation, on the other hand, gives negative values, and although the time history qualitatively resembles that of the envelope method, the amplitudes in general tend to be somewhat smaller. In contrast, the results from IDFFT using the spectrum of $\tilde{F}$ are unacceptable since the second-order force is in fact not a Gaussian process and only the freguency of $\tilde{F}$ can be preserved by this method. Similar results for short-crested seas with a directional spreading of $\cos^2\beta$ are shown in Figures 5. In this case, the envelope method gives negative values whenever $|\beta_L| \geq \pi/2$, and as pointed out earlier, has a finite PDF at $\tilde{F}=0$. The results from all three approximation methods (envelope, index and the present one) are qualitatively similar, with the present method predicting the smallest amplitudes, which is also indicated in the later spectral analysis results.

Using the time history data, the statistics of the slowly-varying drift force can be calculated numerically. This is shown in Table 2 where the results are compared to statistics obtained from the power spectra (Eqs. 3. 9,12,13). Note that since the multidirectional simulations are in general not ergodic, eight simulations with different sets of random phases are made in each case, and the ensemble averages are used for these and later results. From Table 2, we see that the statistics from numerical simulations and theoretical predictions are in good agreement. Envelope approximation overpredicts both the mean and variance of $\tilde{F}_x$, whereas the present method for short-crested waves is overestimated by the index method for the main direction mean force, but underestimated for the transverse mean force.

Table 2. Mean, $E(\tilde{F})$, and standard deviation, σ, of slowly-varying drift forces obtained from time simulations and from theoretical power spectra. All values are normalized by ρga and given in units of m^2. Results from power spectra are in brackets ([...]).

Unidirectional seas

	$E(\tilde{F})$	σ_F
envelope approximation	.942	1.167
index approximation	.803 [.804]	.961 [.932]

$\cos^2\beta$ directional spread seas

	$E(\tilde{F}_x)$	$E(\tilde{F}_y)$	σ_{Fx}	σ_{Fy}
envelope approximation	.749	-.012	.902	.388
index approximation	.666 [.683]	-.014 [0]	.776 [.801]	.375 [.369]
present method	.680 [.683]	-.003 [0]	.696 [.746]	.444 [.422]

The spectrum of the slowly-varying drift force in a multidirectional sea can be obtained in terms of the wave spectrum from (3.12) & (3.13) for the index and present approximation respectively. These are plotted in Figures 6 for directional spreadings of $\cos^2\beta$ and $\cos^8\beta$. As the waves become more short-crested, the longitudinal force results deviates more from the unidirectional force spectrum. In all cases, the present approximation predicts lower main direction but higher transverse direction force amplitudes at all slowly-varying frequencies μ.

When the directional spreading of the incoming seas is not small, the index or envelope approximations are no longer valid and the present method must be used. To illustrate this, we consider the important case of the simultaneous presence of storm and swell seas from different directions. For definiteness, the storm sea is assumed to be given by (3.4) (m_0=1.55 m^2) with a $\cos^2\beta$ directional spreading about x=0, and the swell is approximated as a long-crested monochromatic waves of frequency ω_0=.6 rad/s and amplitude $a_0=\sqrt{2m_0}$, so that the storm and swell overlap in wave frequency and have the same total energy. Eq.(4.1) for the swell spectrum is now simply:

$$S_2(\omega) = (a_0^2/2)\ \delta(\omega-\omega_0)$$

In this case, our approximation (4.8) reduces to a single integral with respect to β. Five incidence angles of the swell, β_0/π=0,.25,.5,.75 and 1 are considered. In Figures 7, we plot that part of the longitudinal and transverse force spectra due to the interaction of the storm and swell waves (Eq.4.3) for the different swell angles. Comparing to Figure 6a, we note that the interaction spectra are typically much greater than that due to the storm waves alone. The large amplification of the spectrum in Figures 7 for certain obtuse values of β_0 especially for small μ is most noteworthy. For example, in the case of the x-direction slowly-varying force, the increase in the force magnitude near $\mu \simeq 0$ due to storm-swell interaction can be up to 4 and over 5 times larger for the case when the swell seas are incident at 135° and 180° to the main direction of the storm waves than when they are arriving from the same direction. For the tranverse slowly-varying force, we again observe the interesting result that the interaction contribution is actually larger for a 135° swell angle than one at 90° to the main storm direction. These observations are also confirmed by direct simulations of (2.15). We remark that although the variance of the slowly-varying forces due to storm-swell interactions are greater for certain opposing swell angles, the net <u>mean</u> drift forces are always greatest for the case of $\beta_0=0$ and $\beta_0=\pi/2$ for the longitudinal and transverse directions respectively. These results have important implications for ocean operations under storm and swell conditions such as those reported by Grancini et al(1984).

Although the results of Figures 7 are anticipated from our earlier deterministic calculations, we note that existing approximations such as the index method are incapable of making such predictions because of the narrow directional spreading assumptions. Thus a direct calculation of the storm-swell interaction effect based on the double-index approximation (4.7) leads to qualitatively incorrect results except for small values of β_0 (see Figure 8).

We now turn to the probability distribution of the slowly-varying forces in unidirectional and short-crested seas. Figure 9 shows the index approximation PDF and CDF for the main direction drift force $\tilde{F}_x$ for three different directional spreadings. For the short-crested waves used, the probability densities are qualitatively similar and tend towards the long-crested result as the spreading is decreased. As expected, the probabilty of extreme values of $\tilde{F}_x$ are higher for smaller directional spreadings. As pointed earlier, there is a small probability for the drift force to be negative. These theoretical PDF's are also confirmed by direct numerical simulations of the time-varying drift force. This is shown in Figures 10 where there is good comparison between simulated histograms and the PDF's.

The results using the envelope method are likewise obtained. For unidirectional seas (Figures 11), there is a finite probability for negative values of the local frequency ω_L or wavenumber k_L, which results in an integrable singularity in $p(\tilde{F})$ at $\tilde{F}=0$. The histograms obtained from simulations are also shown in Figures 11, and the comparisons are satisfactory for all three local variables (amplitude, frequency and wavenumber). The PDF and CDF of the slowly-varying force for different directional spreadings are plotted in Figure 12. The probability of extreme values are generally somewhat higher than those predicted by the index approximation. (For example, for $\cos^2\beta$ seas, the probability $P(\tilde{F}\geq 4)$ is .012 for the envelope method but only .006 for the double-index approximation.) For unidirectional waves $\tilde{F}_x$ is always positive, while for short-crested seas, the probabilty of negative force is nonzero corresponding to the situation where the absolute value of the local direction is greater than $\pi/2$. The PDF for $\tilde{F}_x$ for uni- and multidirectional seas, and for the local direction β_L, i.e. the instantaneous direction of the drift force in short-crested waves, are compared to simulated histograms for the envelope method in Figures 13. The comparisons, including the prediction of negative values in directional seas, are quite reasonable.

Although the theoretical methods for unidirectional waves may still be useful, a statistical theory for second-order forces in general directional seas has yet to be developed and is a subject of current research. In this chapter, we show only comparisons of the theoretical PDF's of $\tilde{F}_X$ obtained from the envelope and double-index approximations which assume narrow directional spreading to the simulated histograms using the present arbitrary-spreading approximation. This is shown in Figure 14 for the case of a $\cos^2\beta$ spreading. It appears that the envelope method overpredicts the probability near the peak at 0, but underestimates the probability of neagtive values. Overall, the histogram from the present approximation is closer to and compares fairly well to the double-index result.

7. CONCLUSION

A new method for the calculation of slowly-varying wave drift forces in short-crested irregular seas is presented and compared with existing theories based upon envelope and index approximations. These methods assume both a narrow band in the frequency of the waves and a narrow spreading in wave directionality. The present method retains Newman's narrow-band assumption of the wave frequency, but allows for arbitrary directional speading which is treated exactly. For typical short-crested storm waves with $\cos^{2n}\beta$ spreadings, the present thoery predicts respectively lower and higher amplitudes for the main and transverse direction slowly-varying forces. For wide directionally spread waves, such as in the important case of the simultaneous presence of both storm and swell seas from different directions, the existing approximations are invalid and the present approach must be used. For the examples we consider, surprising results are found which indicate that the slowly-varying forces can be several times larger in the main direction when the storm and swell are incident from opposite directions than when they are from the same direction. Similarly, for the slowly-varying drift force transverse to the main storm wave direction, the largest amplitude is reached not when the swell is incident at 90° but when the swell is coming from an obtuse angle.

For the probability distribution of second-order slowly-varying forces in unidirectional and short-crested seas, existing results[15,16,19] for the index and envelope approximations are reexamined and in several cases corrected and generalized. These theoretical probability densities are shown to compare well with numerically simulated histograms.

For general wave frequencies and directions, a complete analysis will require not only the exact bifrequency bidirectional quadratic transfer functions (QTF), but also a probabilistic theory for these processes.

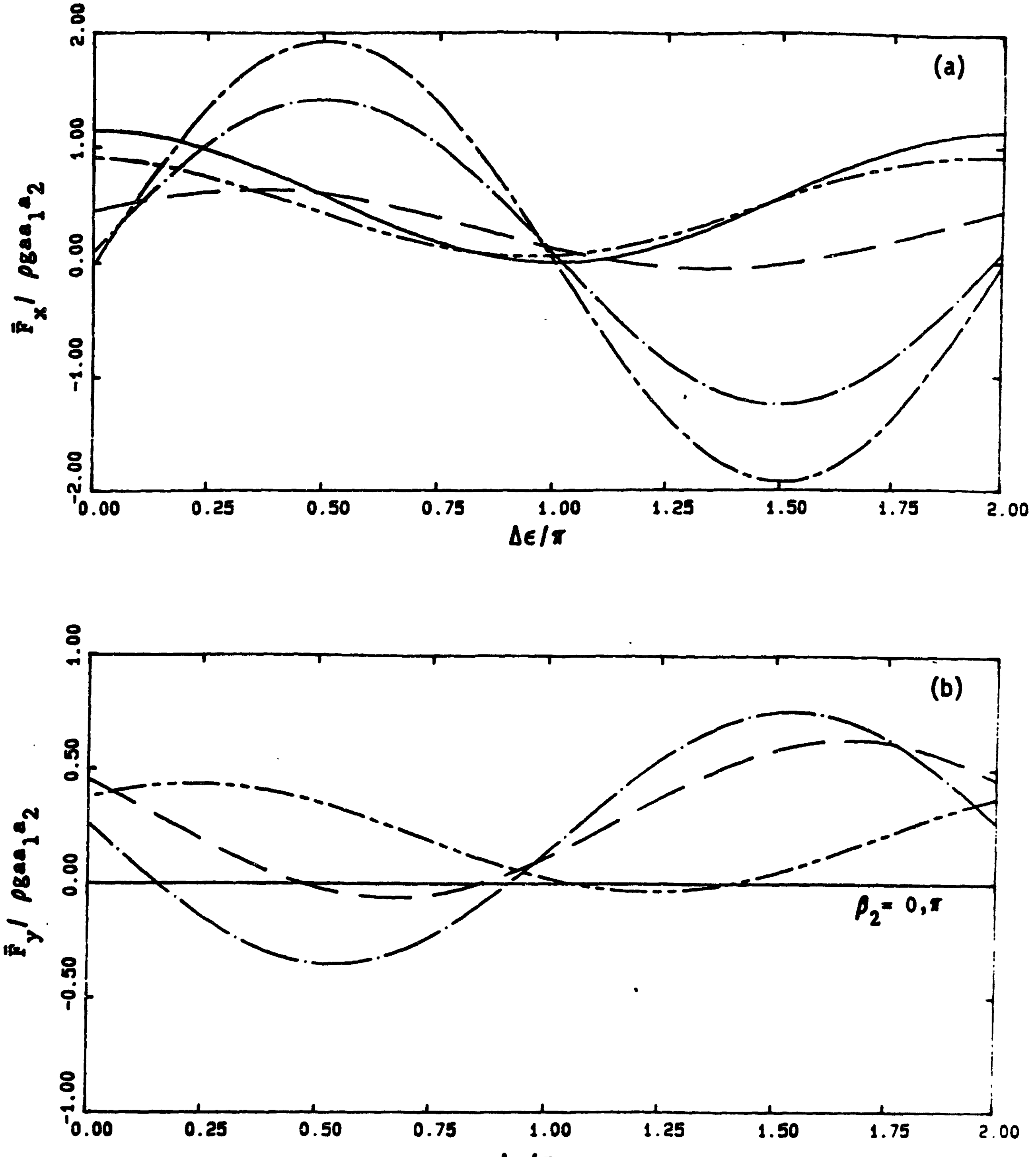

Figure 1. Mean drift force on a uniform vertical cylinder (radius a) in the presence of two regular waves, frequency $\omega^2 a/g=k_o a=.5$, amplitudes a_1 and a_2, and phases ϵ_1 and ϵ_2. The results are shown for (a) x-direction force; and (b) y-direction force; as a function of the phase difference $\Delta\epsilon \equiv \epsilon_1-\epsilon_2$, for incident angles $\beta_1=0$ and $\beta_2/\pi = 0$ (————); .25 (—— - - ——); .5 (—— —— ——); .75 (—— • ——); 1 (—— - ——).

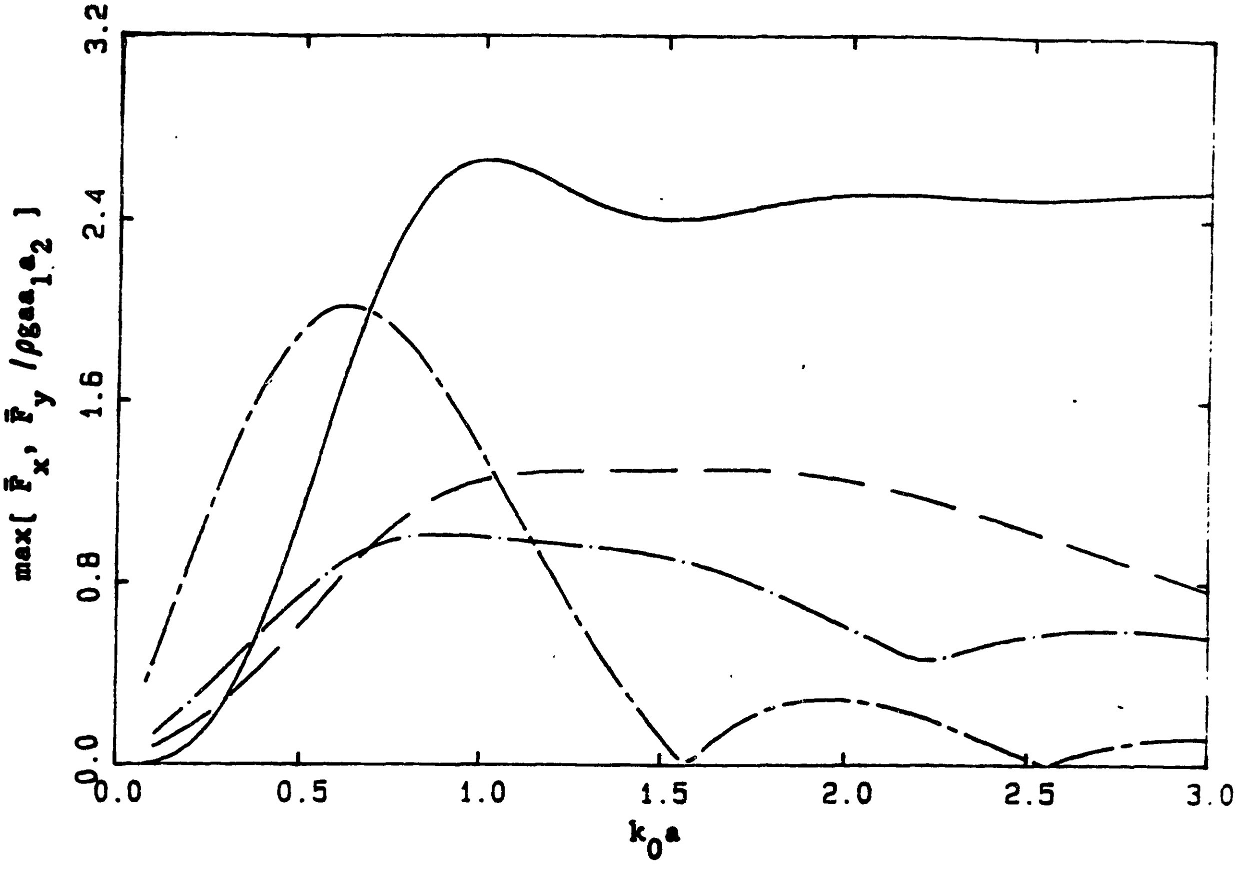

Figure 2. Maximum mean drift force (over all possible phase combinations) on a uniform vertical cylinder (radius a) in the presence of two regular waves, amplitudes a_1 and a_2, as a function of the common wavenumber k_0a. The curves shown are for (i) the x-direction force for incidence angles $\beta_1=0$ and $\beta_2 = 0$ (———) and π (—— – ——); and (ii) the y-direction force for $\beta_1=0$ and $\beta_2 = \pi/2$ (—— —— ——) and $3\pi/4$ (—— • ——).

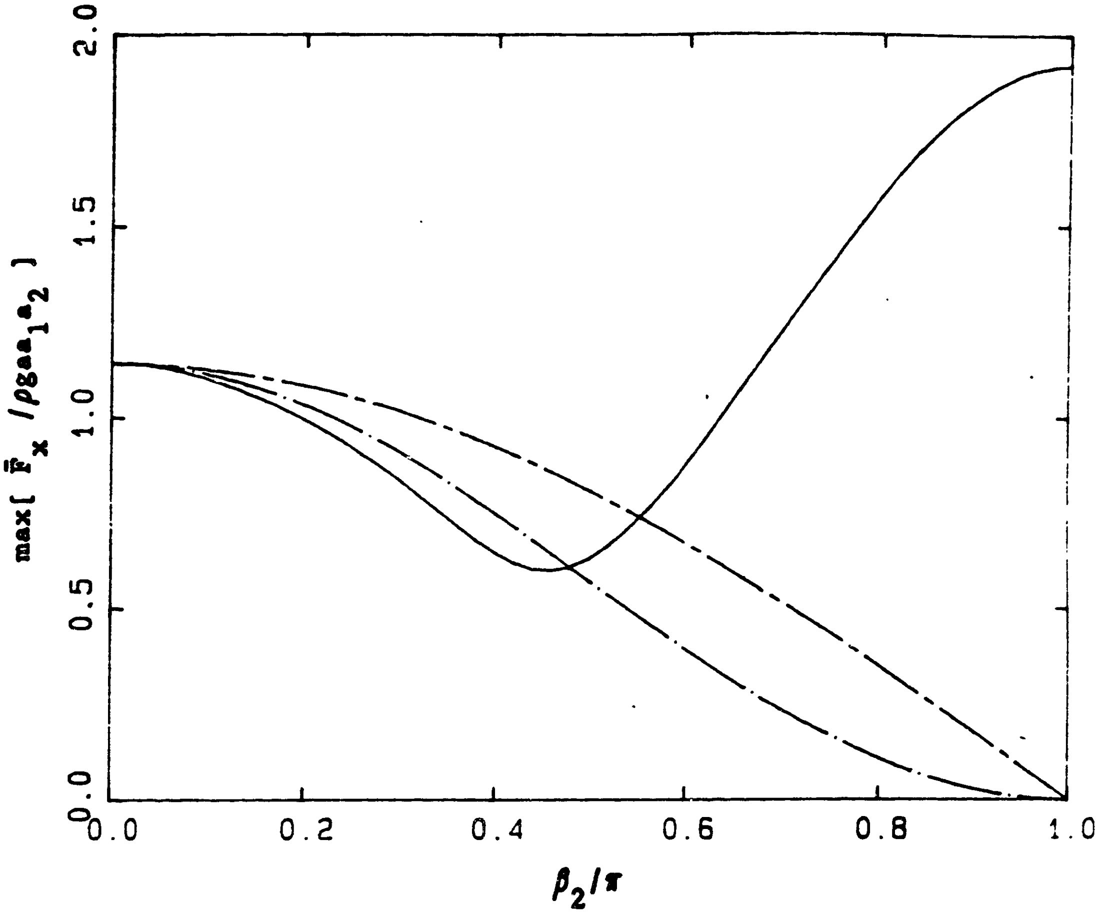

Figure 3. Maximum x-direction mean drift force (over all possible phase combinations) on a uniform vertical cylinder (radius a) in the presence of two regular waves, amplitudes a_1 and a_2, and wavenumber $k_0a=.5$, as a function of incidence angle β_2 ($\beta_1=0$). Three results obtained using respectively the (i) index approximation (—— • ——); (ii) envelope approximation (—— – ——); and (iii) present method (————) are shown.

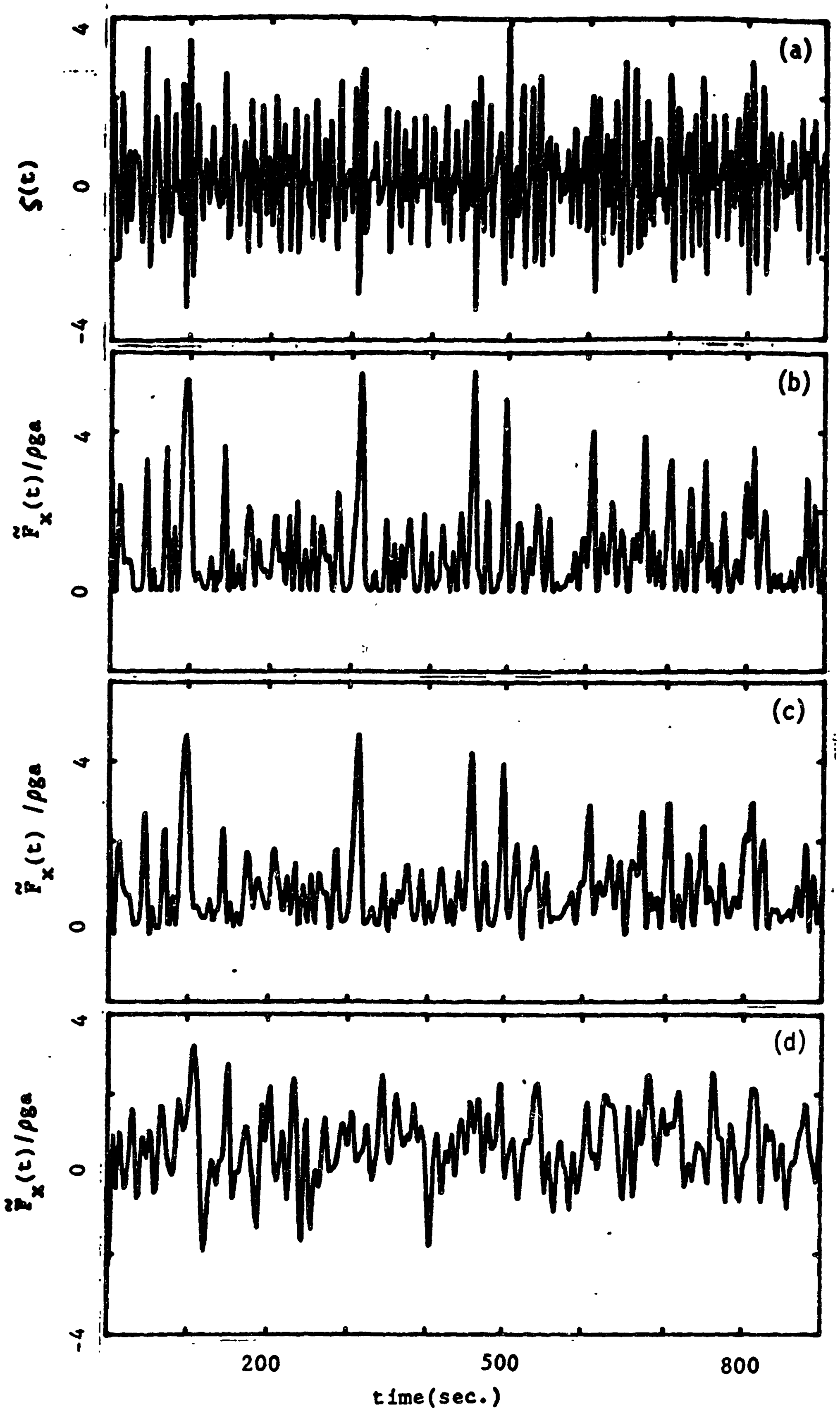

Figure 4. Simulated time histories for the case of unidirectional seas incident on a uniform vertical cylinder for (a) the free surface elevation; and slowly-varying drift force obtained using (b) the envelope approximation; (c) the index approximation; and (d) inverse discrete FFT from power spectrum of the slowly-varying force.

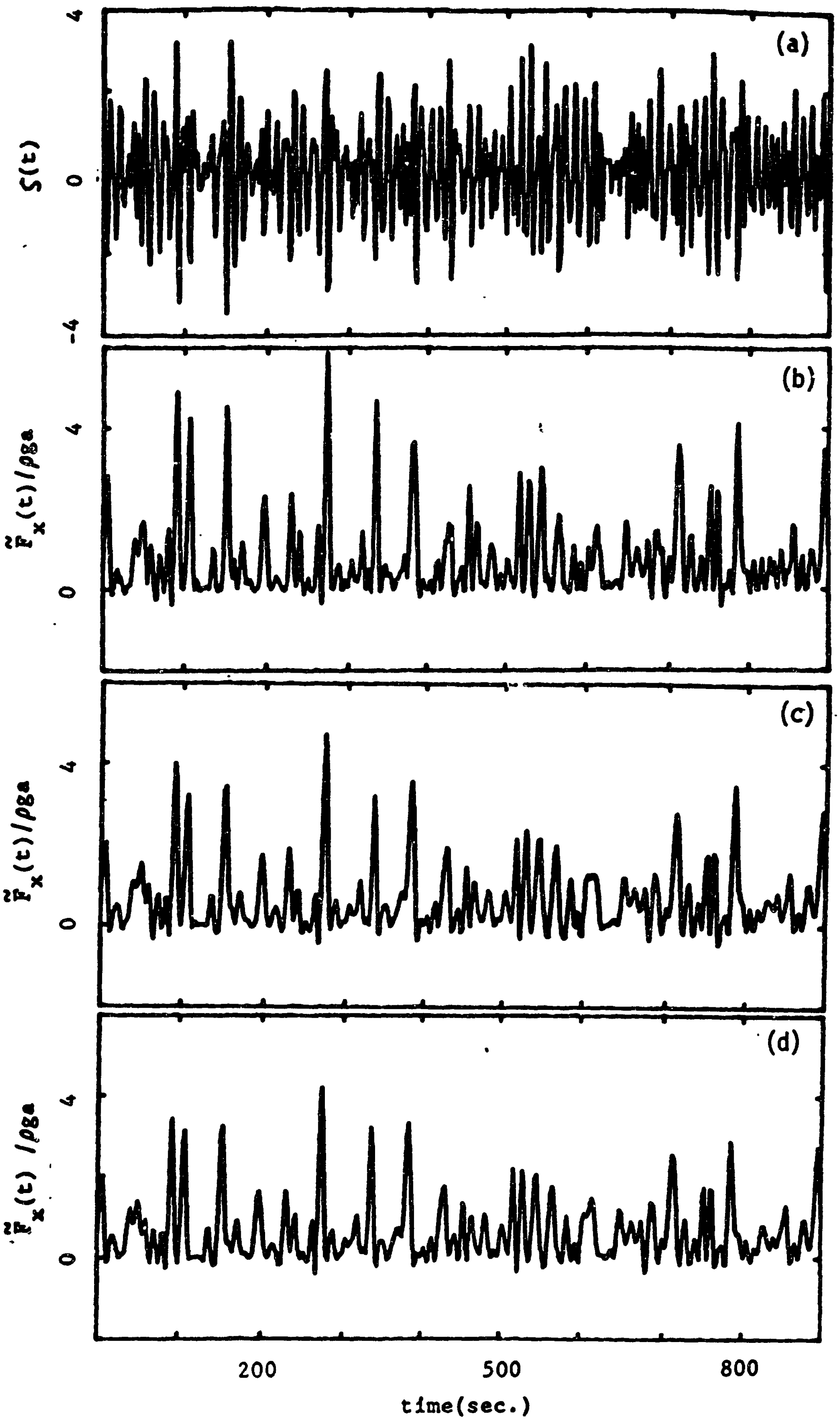

Figure 5. Simulated time histories for the case of directional seas ($\cos^2\beta$ spreading) incident on a uniform vertical cylinder for (a) the free surface elevation; and slowly-varying main direction drift force obtained using (b) the envelope approximation; (c) the double-index approximation; and (d) the present method.

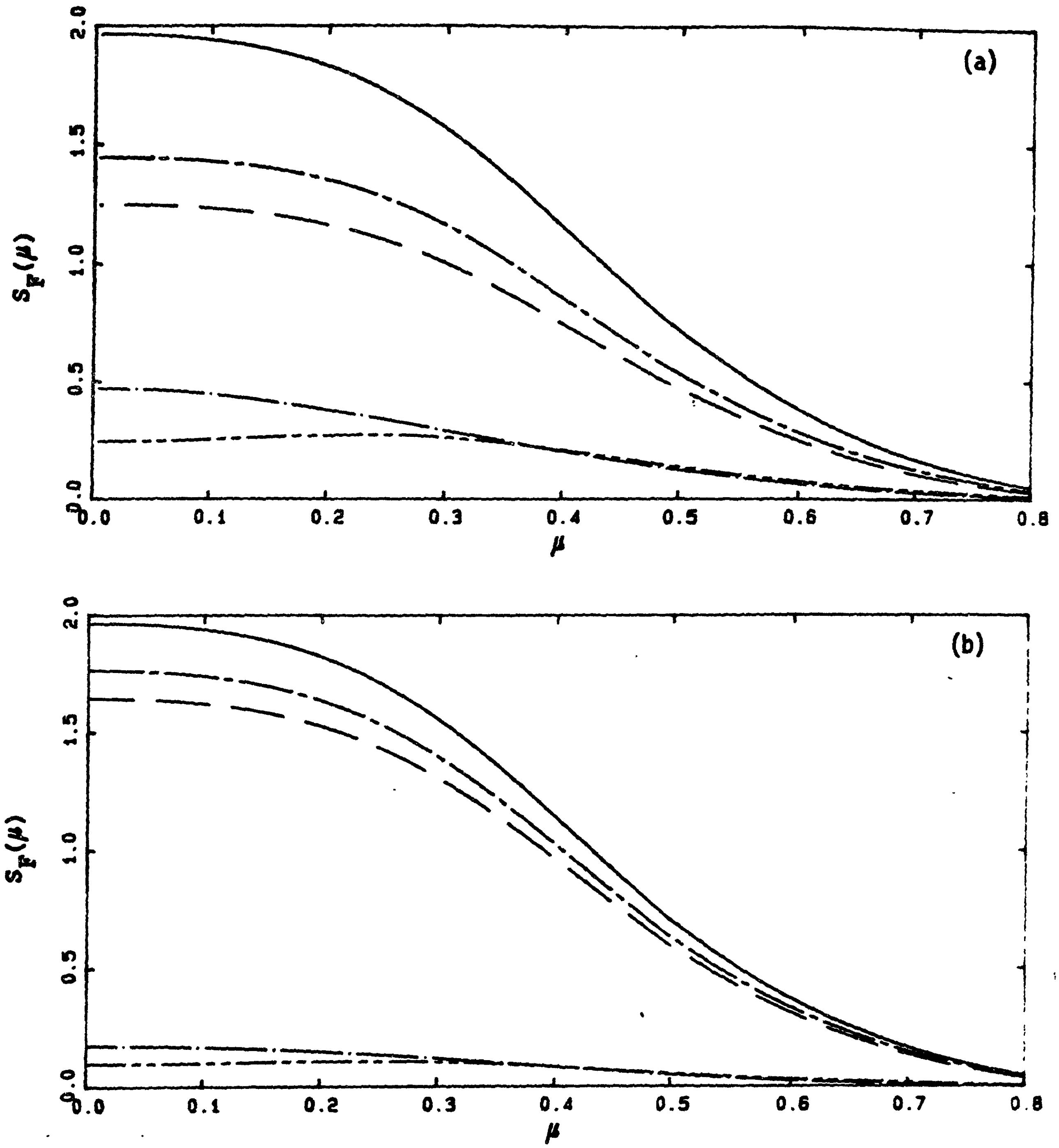

Figure 6. Power spectra of the slowly-varying drift force as a function of the slowly-varying frequency μ. Two short-crested seas with directional spreading (a) $\cos^2\beta$; and (b) $\cos^8\beta$ are considered. The curves shown correspond to results for x-direction force for (i) unidirectional seas (————); (ii) present method (—— —— ——); (iii) index approximation (—— – ——); and for y-direction force for (iv) present method (—— • ——); and (v) index approximation (—— – – ——).

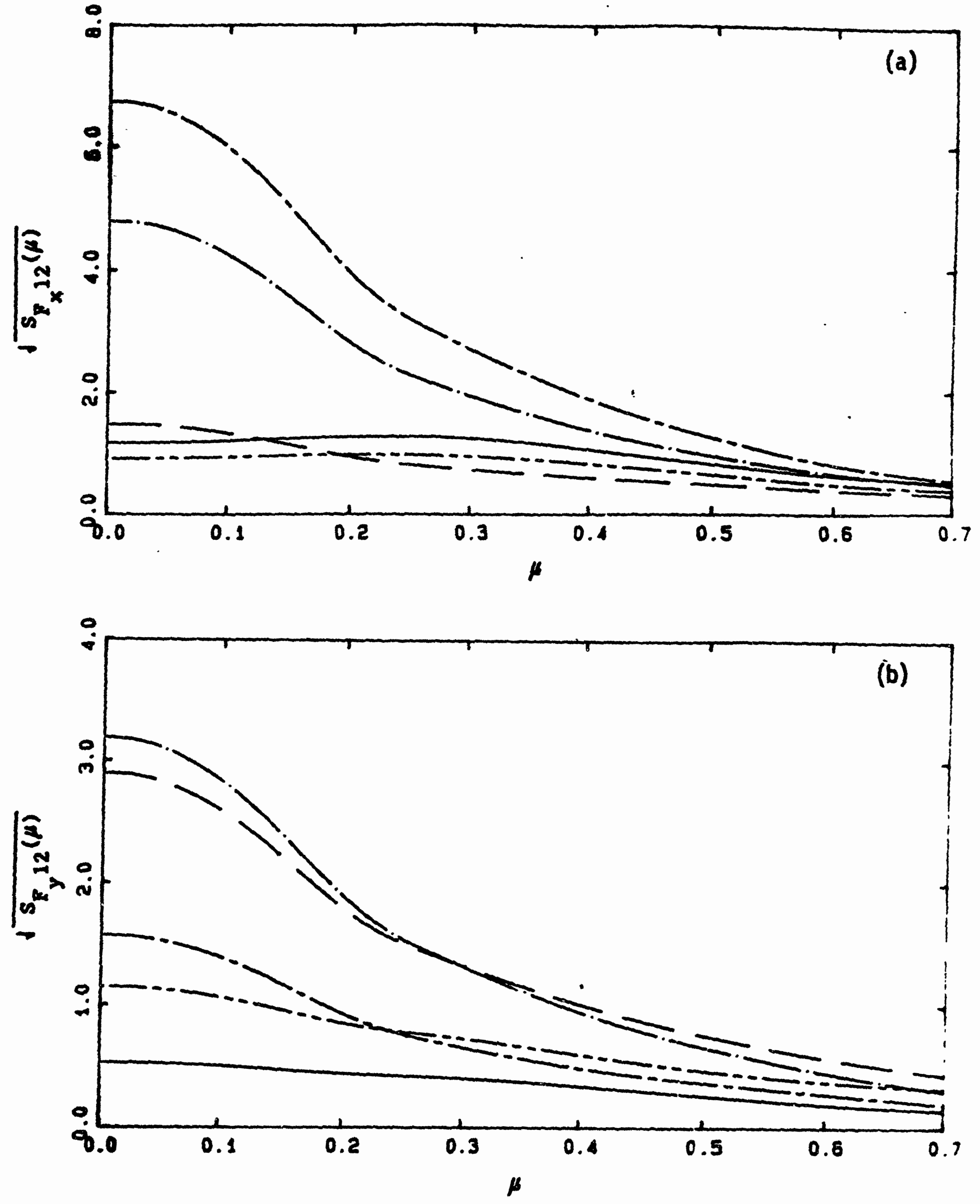

Figure 7. Interaction component of the power spectrum of the slowly-varying drift force due to the presence of combined storm and swell seas as a function of the slowly-varying frequency μ. The results are obtained using the present method for (a) the x-direction force; and (b) the y-direction force for storm wave main direction β_1=0, and swell incident angle of β_2/π = 0 (————); .25 (— — — —); .5 (—— —— ——); .75 (—— • ——); 1 (—— - ——).

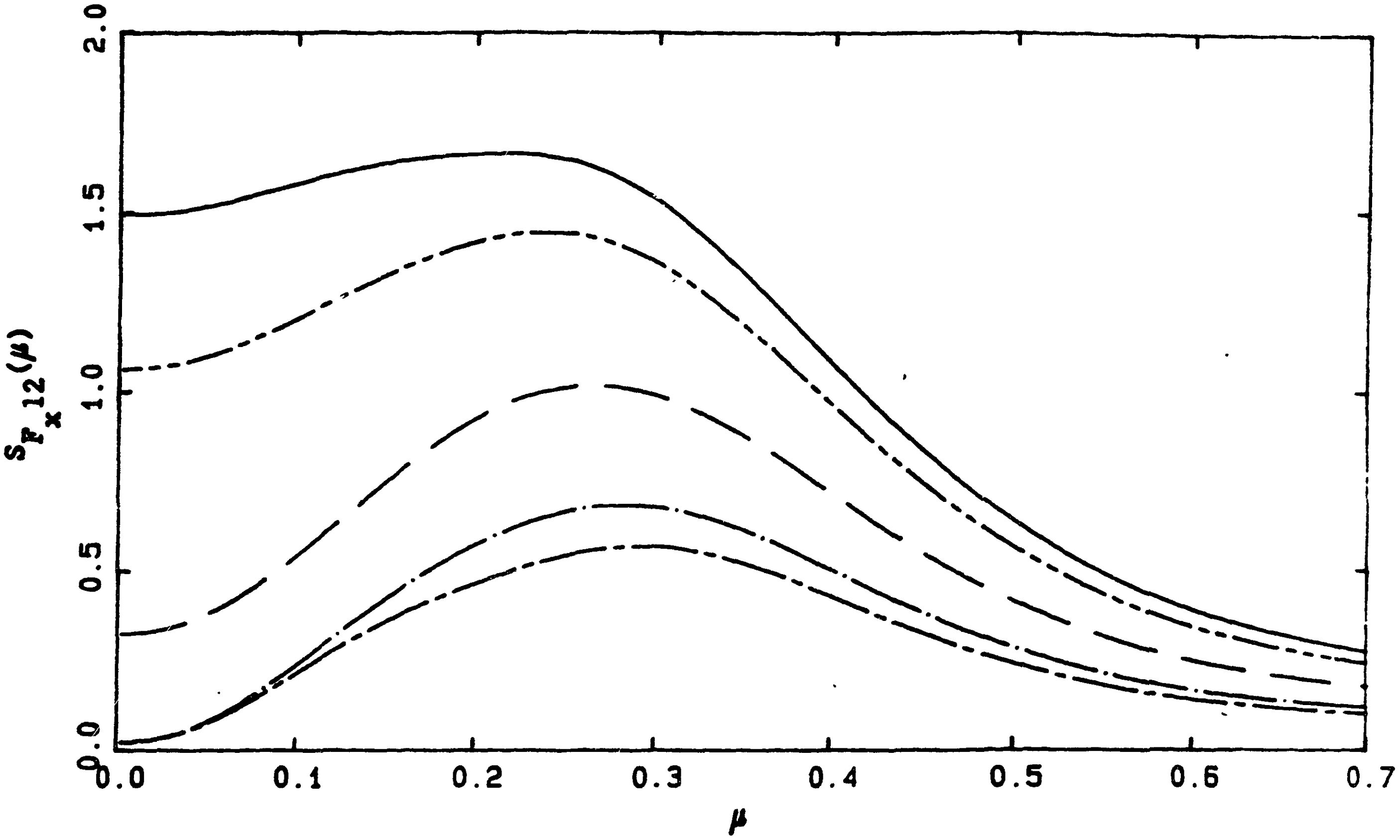

Figure 8. Interaction component of the power spectrum of the x-direction slowly-varying drift force due to the presence of combined storm and swell seas as a function of the slowly-varying frequency μ. The results are obtained by the double-index approximation for the x-direction force for storm wave main direction of $\beta_1=0$, and swell incident angle of β_2/π = 0 (————); .25 (—— – – ——); .5 (—— —— ——); .75 (—— • —— • ——); 1 (—— – ——).

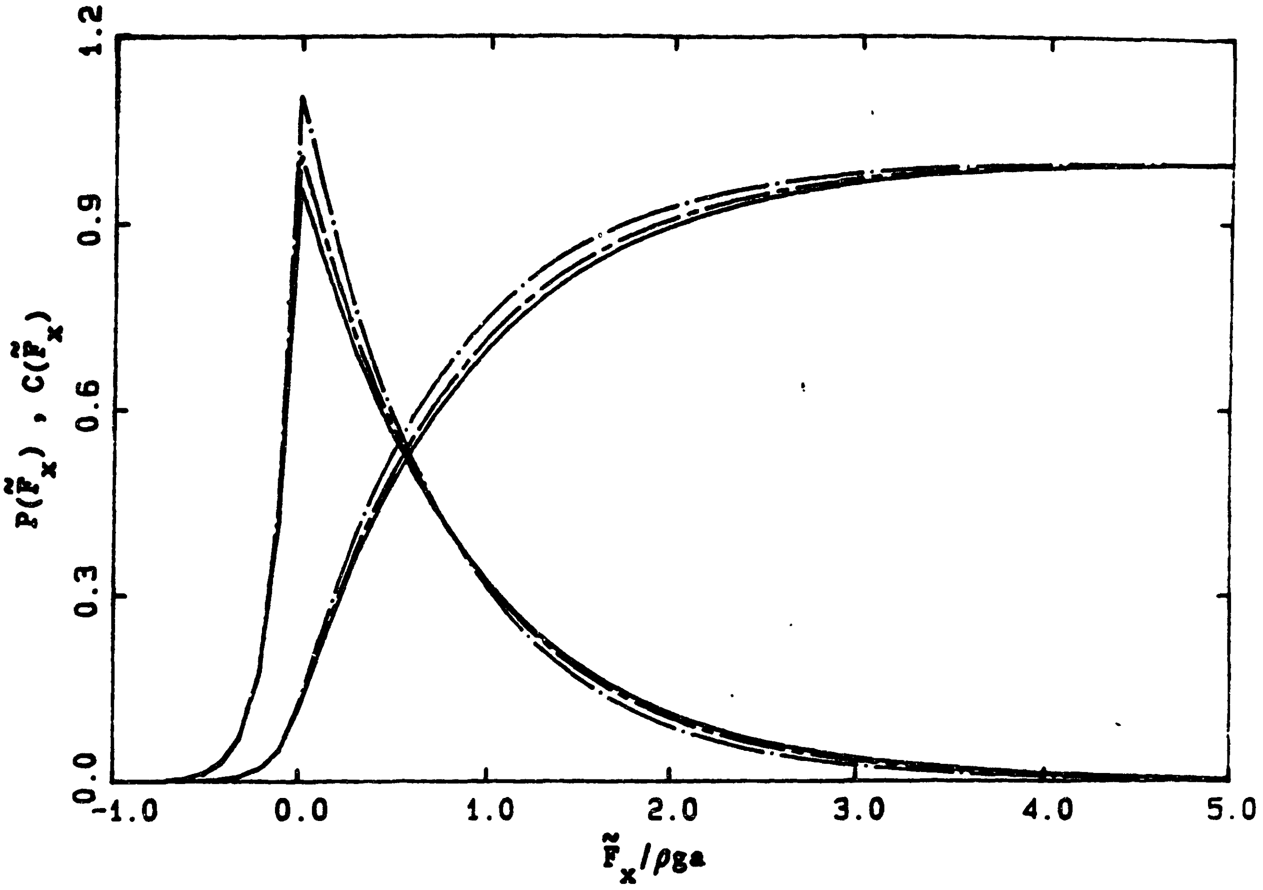

Figure 9. Probability density function and cumulative density function of the main direction slowly-varying drift force of the index approximation method. The results are for (a) long-crested waves (————); (b) $\cos^2\beta$ spread directional seas (—— • ——); and (c) $\cos^8\beta$ spread directional seas (—— – ——).

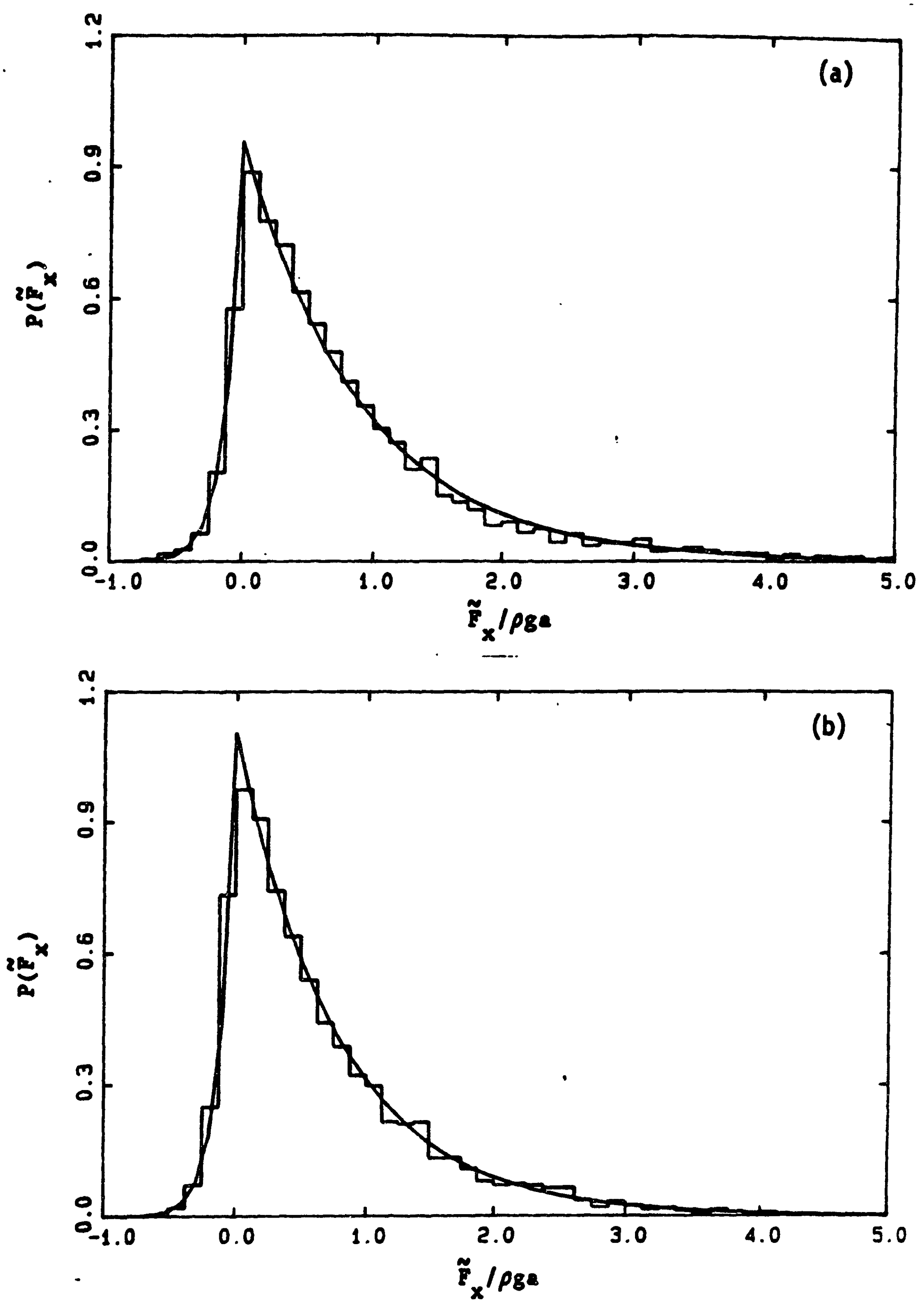

Figure 10. Comparisons between the theoretical probability density function and that obtained from numerical simulation of the main direction slowly-varying drift force using the index approximation method. The results are for (a) long-crested waves; and (b) $\cos^2\beta$ spread directional seas.

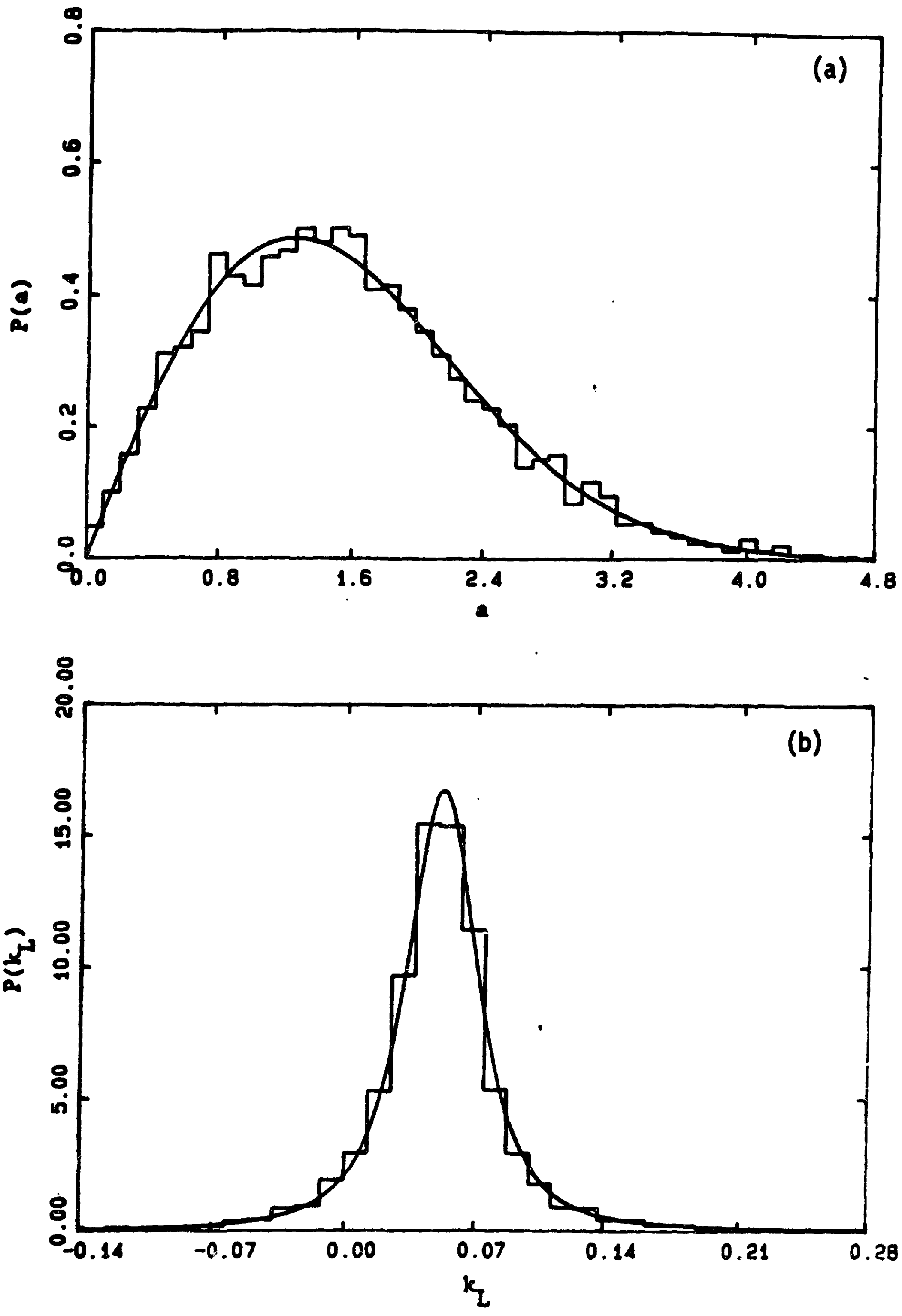

Figure 11. Comparisons between the theoretical probability density function and that obtained from numerical simulation of local random variables of the envelope approximation method in unidirectional seas. The results are for (a) local amplitude; (b) local wavenumber; and (c) local frequency.

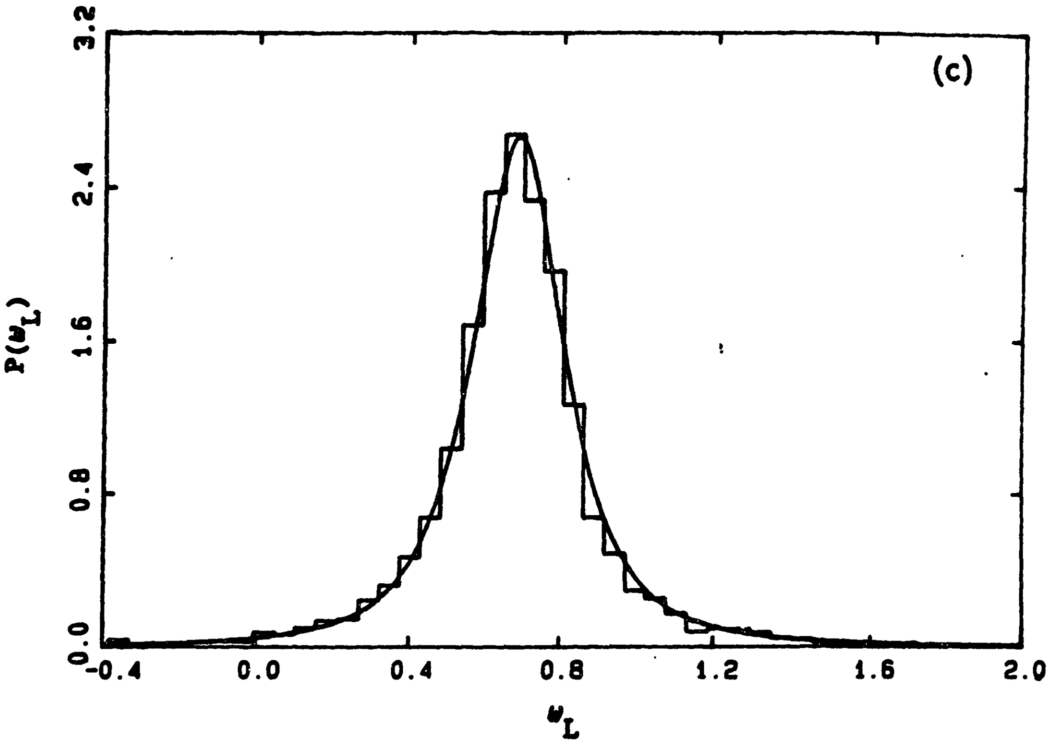

Figure 11. Comparisons between the theoretical probability density function and that obtained from numerical simulation of local random variables of the envelope approximation method in unidirectional seas. The results are for (a) local amplitude; (b) local wavenumber; and (c) local frequency.

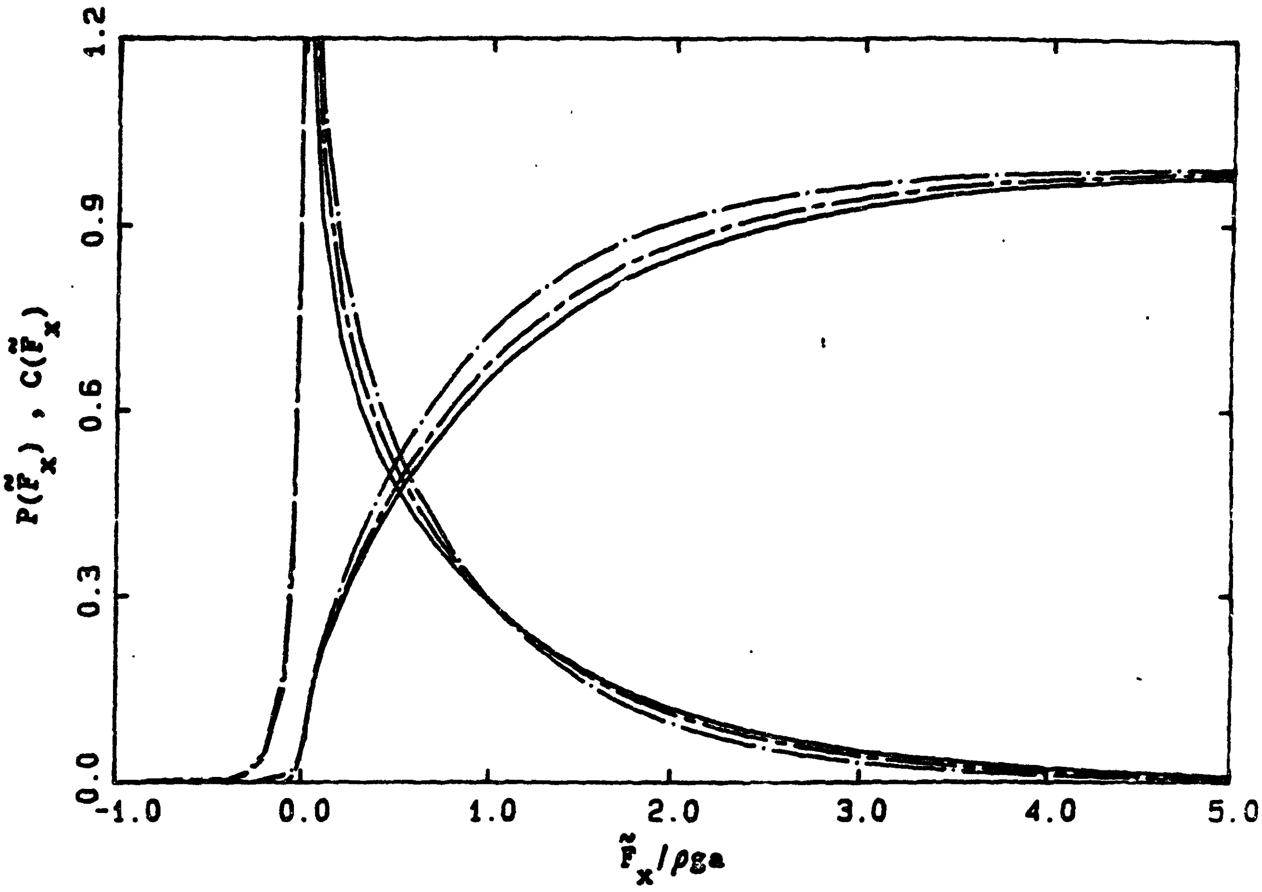

Figure 12. Probability density function and cumulative density function of the main direction slowly-varying drift force of the envelope approximation method. The results are for (a) long-crested waves (————); (b) $\cos^2\beta$ spread directional seas (—— • —— • ——); and (c) $\cos^8\beta$ spread directional seas (—— – —— –).

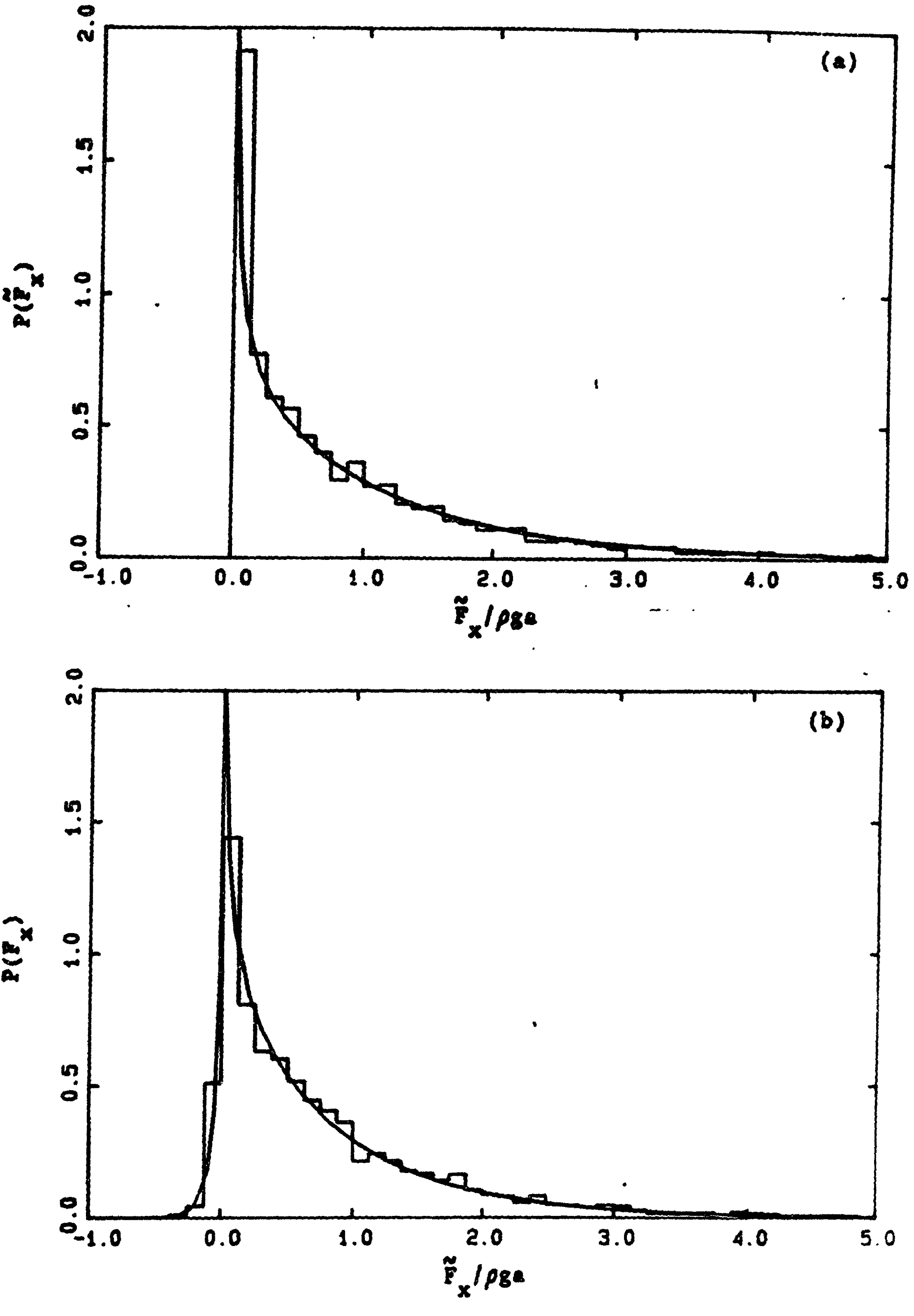

Figure 13. Comparisons between the theoretical probability density function and that obtained from numerical simulation of the slowly-varying drift force using the envelope approximation method. The results are for the force magnitude for (a) long-crested waves; (b) $\cos^2\beta$ spread directional seas; and (c) the direction of the force in $\cos^2\beta$ spread directional seas.

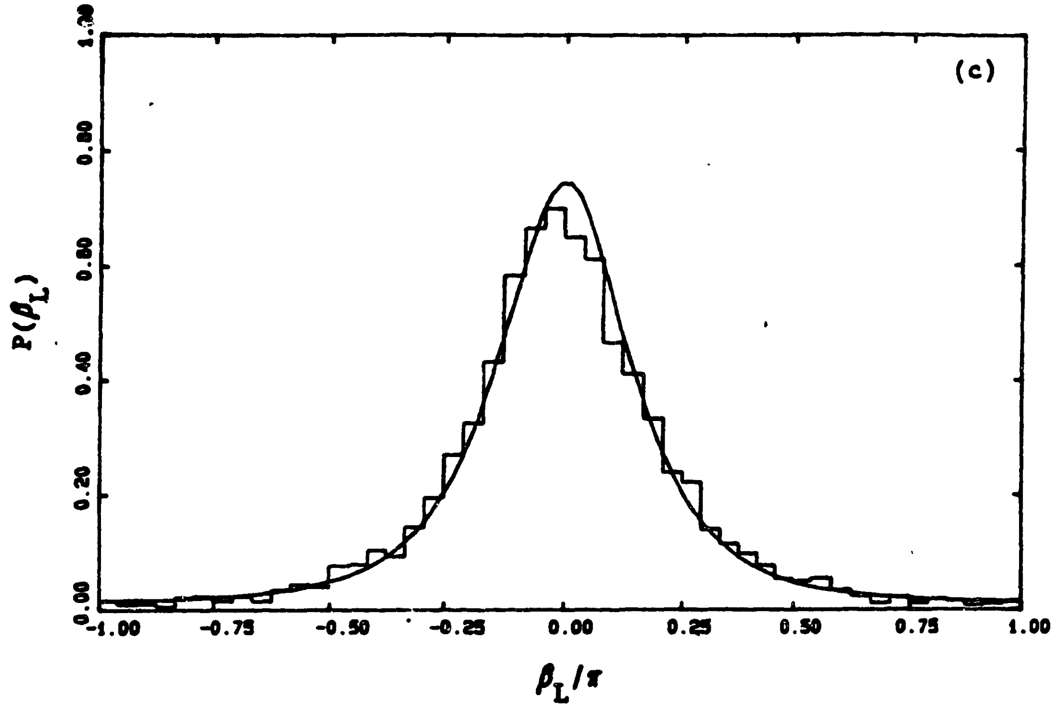

Figure 13. Comparisons between the theoretical probability density function and that obtained from numerical simulation of the slowly-varying drift force using the envelope approximation method. The results are for the force magnitude for (a) long-crested waves; (b) $\cos^2\beta$ spread directional seas; and (c) the direction of the force in $\cos^2\beta$ spread directional seas.

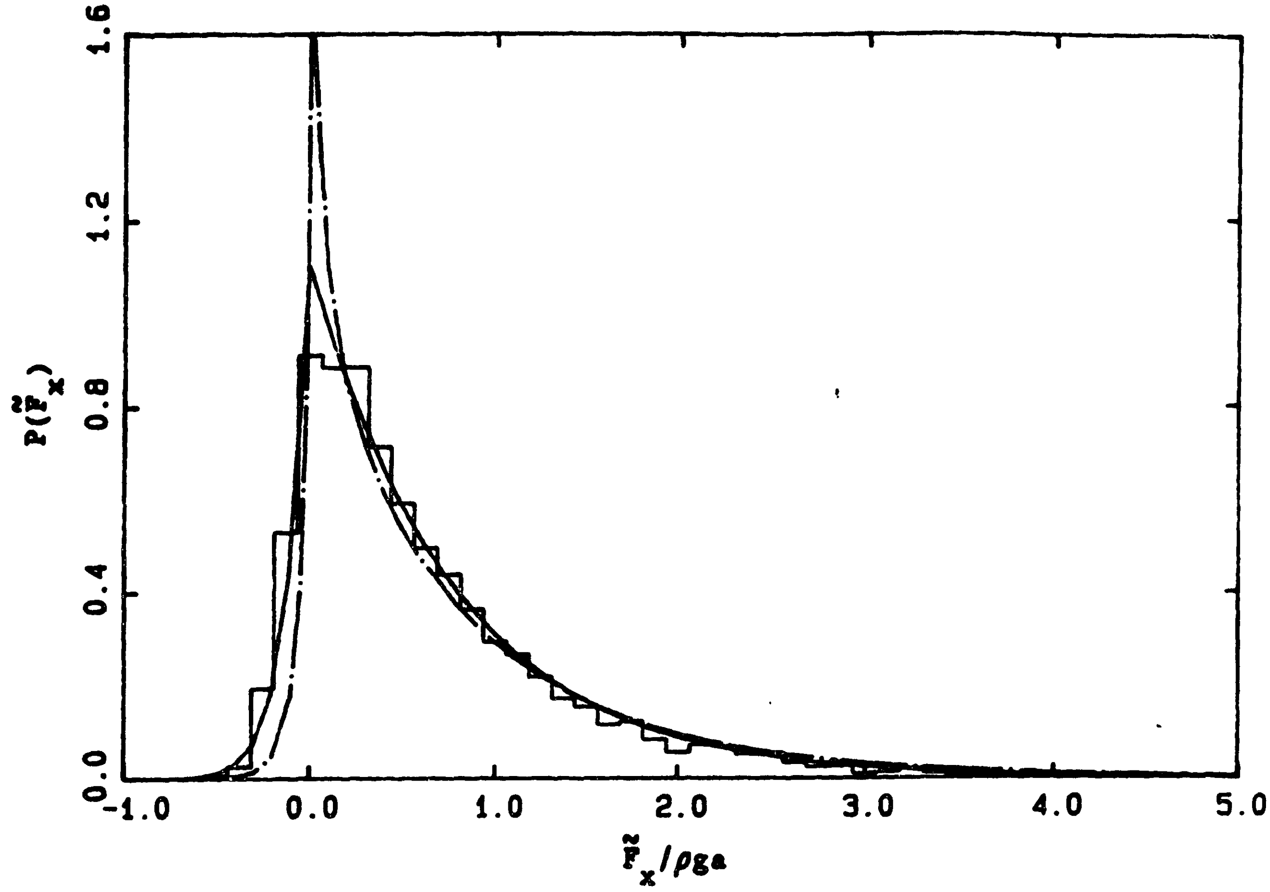

Figure 14. Probability density function of the main direction slowly-varying drift force in $\cos^2\beta$ spread directional seas. The histogram obtained from numerical simulation of the present approximation is compared to the theoretical distributions of (i) the index approximation (————); and (ii) the envelope approximation (—— • —— • ——).

CHAPTER VI. CONCLUDING REMARKS

> **Like all other arts, the Science of Deductin and Analysis is one which can only be acquired by long and patient study, nor is life long enough to allow any motal to attain the highest possible perfection in it.** **- Sir Arthur Conan Doyle -**

In this thesis, the second-order wave effects on a large body are studied both in the presence of regular and irregular waves. The only assumption made is that the body is vertically axisymmetric. The theory is otherwise complete in the context of second-order diffraction theory.

The second-order sum- and difference-frequency potentials are obtained explicitly by a ring-source integral equation method. An important part of the solution is the development of the local-wave-free method for the efficient and accurate evaluation of the slowly-convergent free-surface integrals. For irregular seas, explicit results for the spectra and probability distributions of the second-order forces are obtained using a two term Volterra model.

The accuracy and efficacy of the numerical method are established through systematic convergence tests and comparisons to available semi-analytic solutions. Detailed computations are performed for bottom-mounted and truncated vertical cylinders, conical gravity platforms, and fixed and freely-floating hemispheres.

From our numerical examples, a number of important second-order phenomena, which have not been reported previously, are found:

(1) The second-order sum-frequency diffraction potential penetrates deep especially at the weather side of a body and when the two frequencies are close. As a result of this, a number of existing approximation methods

which exclude this contribution may greatly underestimate the second-order sum-frequency wave loads and resonant responses of large-draft offshore platforms.

(2) When the body side walls are outward sloping towards the bottom, such as in the case of a vertical cone, second-order excitations and run-up are amplified and may indeed be greater than first-order quantities for moderately steep incident waves.

(3) Body boundary terms due to linear motions and free-surface forcing pressures in the boundary value problem of the second-order diffraction potential contribute significantly to the total sum-frequency excitations. These are, however, not so important in the difference-frequency problem.

(4) Comparisons of the probability density functions and spectra of the second-order wave loads obtained from the present complete QTF's to those calculated from approximated QTF's show that the extreme and rms second-order forces in irregular seas can be severely underestimated by approximation methods.

(5) Our preliminary study of the slowly-varying wave forces for multidirectional seas reveals that unidirectionality is not necessarily a conservative assumption when second-order wave effects are included.

When second-order wave effects play an important role, the necessity of a complete second-order theory for the safe design of large offshore structures is underscored.

For numerical efficiency, we have only considered axisymmetric bodies in this work. The present method, however, can readily be generalized for arbitrary three-dimensional bodies using a three-dimensional source potential and associated two-dimensional integral equation. The local-wave-free method for the free-surface integrals is still applicable in this case.

For general three-dimensional bodies, the two-dimensional free-surface integral has the form:

$$I(x') = \iint_{S_F} q(x)\, G(x;x')\, dx \,, \tag{1}$$

where q is the free-surface inhomogeneity, and the linear potential $\phi^{(1)}$ can be given, say, by a source distribution on the body:

$$\phi^{(1)}(x) = \iint_{S_B} \sigma(x')\, G(x;x')\, dx' \,. \tag{2}$$

Using the far-field asymptotic of G (see 2.32 of Chapter I), and the addition theorem for Hankel functions, we have after a simple expansion:

$$\begin{Bmatrix} G \\ \phi^{(1)} \end{Bmatrix} \sim \sum_{n=0}^{\infty} H_n(k\rho) \begin{Bmatrix} g_{Cn}(x') \cos n\theta + g_{Sn}(x') \sin n\theta \\ L_{Cn} \cos n\theta + L_{Sn} \sin n\theta \end{Bmatrix} , \quad k\rho \gg 1, \tag{3}$$

where g_{Cn}, g_{Sn} are known functions of the point, x', on the body, and L_{Cn}, L_{Sn} are the Kochin functions:

$$\begin{Bmatrix} L_{Cn} \\ L_{Sn} \end{Bmatrix} = \iint_{S_B} \sigma(x') \begin{Bmatrix} g_{Cn}(x') \\ g_{Sn}(x') \end{Bmatrix} dx' . \tag{4}$$

Using (2)-(4) in (1) in the local-wave-free farfield, the θ integral can be integrated explicitly, and (1) reduces to sums of one-dimensional integrals over the radial coordinate ρ, and the method of Appendix A is directly applicable.

REFERENCES

Abramovitz, M. & Stegun, I.A. (1964). Handbook of mathematical functions. Government Printing Office, Washington.

Abul-Azm, A.G. & Williams, A.N. (1988). Second order diffraction loads on two uniform vertical cylinders. Proc. 7th OMAE, Houston, **2**: 131-138.

Bedrosian, E. & Rice, S.O. (1971) The output properties of Volterra systems (nonlinear systems with memory) driven by harmonic and Gaussian inputs. Proc. of IEEE, **59**: 1688-1707.

Benschop, A., Hermans, A.J., & Huijsmans, R.H.M. (1987). Second order diffraction forces on a ship in irregular waves. Applied Ocean Research, **9**; 96-104.

Black, J.L. (1975). Wave forces on vertical axisymmetric bodies. Journal of Fluid Mechanics, **67**: 369-376.

Chakrabarti, S.K. (1978). Comments on second-order wave effects on large diameter vertical cylinder. Journal of Ship Research, **22**: 266-268.

Chau, F.P. & Eatock Taylor, R. (1988). Second order velocity potential for arbitrary bodies in waves. 3rd. Intl. Workshop on Water Waves & Floating Bodies, Woods Hole. 15-19.

Chen, M.C. & Hudspeth, R.T. (1982). Nonlinear diffraction by eigenfuntion expansions. J. Waterways Port Coastal & Ocean Div., ASCE, **108**: 306-325.

De Boom, W.C., Pinkster, J.A., & Tan, S.G. (1983). Motion and tether force prediction for a deep water Tension Leg Platform. Proc. Offshore Technology Conf., OTC, Houston, #4487.

Eatock Taylor, R. & Hung, S.M. (1987). Second order diffraction forces on a vertical cylinder in regular waves. Applied Ocean Research, **9**: 19-30.

Eatock Taylor, R., Hung, S. M., & Mitchell, K. L. (1988). Advances in the prediction of low frequency drift behavior. Proc. Behavior of Offshore Structures, BOSS, Norway, 651-666.

Faltinsen, O.M. & Loken, A.E. (1978a). Drift forces and slowly-varying horizontal forces on a ship in waves. Proc. Symp. Applied Math., Delft.

Faltinsen, O.M. & Loken, A.E. (1978b). Slow drift oscillations of a ship in irregular waves. Applied Ocean Research, **1**: 21~.

Fenton, J.G. (1978). Wave forces on vertical bodies of revolution. Journal of Fluid Mechanics, **85**: 241-255.

Fernandes, A.C. (1983). Analysis of an axisymmetric pneumatic buoy by reciprocity relations and a ring source method. Ph.D. Thesis. MIT. Dept. of Ocean Engineering.

Finkelstein, A.B. (1957). The initial value problem for transient water waves. Communications Pure & Applied Mathematics, 10: 511-522.

Gradshteyn, I.S. & Ryzhik, I.M. (1980) Tables of integrals, series and products. Academic Press.

Grancini, G., Iovenitti, L.M. & Pastore, P. (1984) Moored tanker behavior in crossed seas: Field experiences and model tests. Symp. on Description and Modeling of Directional Seas, Copenhagen.

Herfjord, K. & Nielsen, F.G. (1986). Nonlinear wave forces on a fixed vertical cylinder due to the sum frequency of waves in irregular seas. Applied Ocean Research, 8: 8-21.

Hsu, F.H. & Blenkarn, K.A. (1970) Analysis of peak mooring forces caused by slow vessel drift oscillations in random seas. Offshore Technology Conference, No. 1159.

Hulme, A. (1983). A ring source integral equation method for the calculation of hydrodynamic forces exertied on floating bodies of revolution. Journal of Fluid Mechanics, 128: 387-412.

Hung, S.M. & Eatock Taylor, R. (1987). Second order time harmonic forces on bodies in waves. 2nd. Intl. Workshop on Water waves & Floating bodies, Bristol, England.

Hunt, J.N. & Baddour, R.E. (1981). The diffraction of nonlinear progressive waves by a vertical cylinder. Quart. Journal of Mechanics and Applied Mathematics, 34: 69-87.

Issacson, M.Q. (1977). Nonlinear wave forces on large offshore structures. J. Waterways, Port, Coastal & Ocean Div., ASCE, 103: 166-170.

Jamieson, W.W., Mansard, E.P.D. & Mogridge, G.R. (1985) Wave loading on a Conical Gravity Platform. Proc. BOSS '85, Netherlands.

Jefferys, E.R. (1987). Directional seas should be ergodic. Applied Ocean Research, 9: 186~.

John, F. (1950) On the motion of floating bodies; 2. Communications on Pure and Applied Mathematics, 3: 45-101.

Jonsson, J.G. (1978) A new approach to oscillatory rough turbulent boundary layers. Series paper 17 Hydrodynamics and hydraulic Eng., Technical University of Denmark.

Kac, M. & Siegert, A.J.F. (1947) On the theory of noise in radio receivers with square-law detectors. Journal of Applied Physics, **18**, 383-397.

Kagemoto, H. & Yue, D.K.P. (1986). Interactions among multiple three-dimensional bodies in water waves: an exact algebraic method. Journal of Fluid Mechanics, **166**: 189-209.

Kaplan, P. (1982) Comment on Oppenheim and Wilson: "Continuous digital simulation of the second order slowly varying wave drift force". Journal of Ship Research, **26**: 36~.

Kim, M.H. (1987). Second-order diffracted waves around an axisymmetric body. The 2nd. Intl. Workshop on Water Waves & Floating Bodies, Bristol.

Kim, M.H. & Yue, D.K.P. (1988a) Slowly varying wave drift forces in short-crested irregular seas. Applied Ocean Research. (In Press)

Kim, M.H. & Yue, D.K.P. (1988b) The nonlinear sum-frequency wave excitation and response of a tension-leg platform. 5th International Conf. Behavior Offshore Structures, BOSS, Norway.

Kim, M.H. & Yue, D.K.P. (1988c) The complete second-order diffraction solution for an axisymmetric body. Part I. Monochromatic incident waves. Journal of Fluid Mechanics. (In Press)

Kim, M.H. & Yue, D.K.P. (1988d) The complete second-order diffraction /radiation solution for an axisymmetric body. Part II. Bichromatic incident waves. (Submitted for Publication)

Kim, M.H. & Yue, D.K.P. (1988e) The complete sum- and difference-frequency wave force Quadratic Transfer Functions for an axisymmetric body. 3rd. Intl. Workshop on Water Waves & Floating Bodies, Woods Hole.

Korsmeyer, F.T. (1988) The first- and second-order transient free-surface wave radiation problems. Ph.D. Thesis. MIT. Dept. of Ocean Engineering.

Langley, R.S. (1984) The statistics of second order wave forces. Applied Ocean Research, **6**: 182-186.

Langley, R.S. (1987). Second-order frequency domain analysis of moored vessels. Applied Ocean Research, **9**: 7-18.

Lighthill, M. J. (1979). Waves and hydrodynamic loading. Proc. 2nd International Conf. Behavior Offshore Structures, BOSS, London, 1-40.

Lin, Y.K. (1967). Probabilistic theory of structural dynamics. McGraw-Hill Press.

Loken, A.E. (1986). Three dimensional second order hydrodynamic effects on ocean structures in waves. University of Tronheim. Dept. of Marine Technology. Report UR-86-54.

Longuet-Higgins, M.S. (1984). Statistical properties of wave groups in a random sea state. Phil. Trans. Lond., A312, 219~.

Luke, Y.L. (1975). The special functions and their approximations. Academic Press, New York.

Marthinsen, T. (1983a) Calculation of slowly varying drift forces. Applied Ocean Research, 5: 141-144.

Marthinsen, T. (1983b) The effect of short crested seas on second order forces and motions. International workshop on ship and platform motions, Berkeley.

Matsui, T. (1988). Computation of slowly varying second order hydrodynamic forces on floating structures in irregular waves. Proc. Offshore Mechanics & Arctic Engineering. OMAE, Houston, 1: 117-124.

Mei, C.C. (1978). Numerical methods in water-wave diffraction and radiation. Annual Review of Fluid Mechanics, 10, 393-416.

Mei, C.C. (1983). The applied dynamics of ocean surface waves. Wiley Press.

Miloh, T. (1980). Irregularities in solutions of nonlinear wave diffraction problem by vertical cylinder. J. Waterways Port Coastal & Ocean dev., ASCE # WW2, 279-284.

Molin, B. (1979). Second order diffraction loads upon three dimensional bodies. Applied Ocean Research, 1: 197-202.

Molin, B. (1983). On second order motion and vertical drift forces for three dimensional bodies in regular waves. Intl. Workshop Ship & Platform Motions, Berkeley, 344-362.

Molin, B. & Fauveau, V. (1984). Effect of wave-directinality on second-order loads induced by the set-down. Applied Ocean Research, 6.

Molin, B. & Marion, A. (1986). Second order loads and motions for floating bodies in regular waves. Proc. Offshore Mechanics & Arctic Engineering, OMAE, Tokyo, 1: 353-360.

Naess, A. (1985). Statistical analysis of second-order response of marine structures. Journal of Ship Research, 29; 270-284.

Naess, A. (1986). The statistical distribution of second-order slowly-varying forces and motions. Applied Ocean Research, 8: 110-118.

Neal, E. (1974) Second order hydrodynamic forces due to stochastic excitation. Proc. 10th Symp. on Naval Hydrodynamics.

Newman, J.N. (1967). The drift force and moment on ships in waves. Journal of Ship Research, 11: 51-60.

Newman, J.N. (1974). Second order slowly varying forces on vessels in irregular waves. Symp. on Dynamics of marine vehicles and structures in waves, London.

Newman, J.N. (1977). Marine Hydrodynamics. MIT Press.

Newman, J.N. (1985a). Algorithms for the free surface Green function. Journal of Engineering Mathematics, 19: 57-67.

Newman, J.N. (1985b). Transient axisymmetric motion of a floating cylinder. Journal of Fluid Mechanics, 157; 17-33.

Newman, J.N. (1988). Second-harmonic wave diffraction at large depth. (Submitted for publication)

Nordgren, R.P. (1986). Analysis of high frequency vibration of tension leg platforms. Proc. 5th OMAE, Tokyo, 3: 149-156.

Ogilvie, T.F. (1983). Second order hydrodynamic effects on ocean platforms. Intl. Workshop Ship & Platform Motion, Berkeley, 205-265.

Oppenheim, B.W. & Wilson, P.A. (1980) Continuous digital simulation of the second order slowly varying wave drift force. Journal of Ship Research, 24: 181~.

Pearcy, H.H. (1979). Some observations on fundamental features of wave induced viscous flows past cylinders. Mecanics of wave induced forces on cylinders, Pitman Publ.

Peters, A.S. & Stoker, J.J. (1957). The motion of a ship, as a floating rigid body, in a seaway. Comm. Pure & Applied Math., 10: 399-490.

Petrauskas, C. & Liu, S.V. (1987). Springing force response of a tension leg platform. Proc. Offshore Technology Conf., OTC, Houston, #5458.

Pinkster, J.A. (1976). Low frequency second order wave forces on vessels moored at sea. Proc. of the 11th Symp. on Naval Hydrodynamics.

Pinkster, J.A. (1980). Low frequency second order wave exciting forces on floating structures. NSMB Rep. No. 650.

Rahman, M. (1983). Wave diffraction by large offshore structures; an exact second order theory. Applied Ocean Research, 6: 90-100.

Sabuncu, T. & Goren, O. (1985). Second-order vertical and horizontal wave forces on a circular dock. Ocean Engineering, 12; 341-361.

Sarpkaya, T. & Isaacson, M. (1981). Mechanics of wave forces on offshore structures. Van Nostrand Reinhold, New York.

Sclavounos, P.D. (1988). Radiation and diffraction of second-order surface waves by floating bodies. Journal of Fluid Mechanics, 196; 65-91.

Standing, R.G. & Dacunha, N.M.C. (1982). Slowly varying and mean second-order wave forces on ships and offshore structures. Proc. 14th Symp. on Naval Hydrodynamics, Ann Arbor.

Stoker, J.J. (1957) Water waves. Interscience, New York.

Teigen, P.S. (1983) The response of a TLP in short crested waves. Offshore Technology Conference, No. 4642.

Tucker, M.J., Challenor, P.G. & Carter, D.J.T. (1984) Numerical simulation of a random sea: a common error and its effect upon wave group statistics. Applied Ocean Research, 6: 118~.

Vinje, T. (1983) On the statistical distribution of second order forces and motions. International Shipbuilding Progress, 30: No. 343.

Vinje, T. (1985) On the statistical distribution of second order forces. VERITEC report # 2.6.

Wang, P.F. (1987). The radiation condition and numerical aspects of second order surface wave radiation and diffraction. Ph.D. Thesis. MIT. Dept. of Ocean Engineering.

Wehausen, J.V. (1980). Perturbation methods in diffraction. Journal AWaterways Port Coastal & Ocean Div., ASCE, 106: 290-291.

Watson, G.N. (1952). A treatise on the theory of Bessel functions. Cambridge University Press.

APPENDIX A: EVALUATION OF THE TRIPLE-HANKEL INTEGRALS

We consider, as an example, the integral:

$$I^1_{lmn}(x_o) = \int_{x_o}^{\infty} x\, H_l(x)\, H_m(x)\, H_n(\alpha x)\, dx, \tag{A.1}$$

where $x_o \equiv kb$, and $\alpha \equiv k_2/k$. To evaluate (A.1), we expand each Hankel function in polynomials of x_o/x, whose coefficients can be determined from an equivalent Chebyshev polynomial expansion for a specified equal-ripple error (Luke, 1975):

$$H_n(x) = \sqrt{\frac{2}{\pi x}}\; e^{i(x-\gamma_n)} \sum_i C_{ni}(x_o/x)^i, \qquad i=1,2,\ldots \tag{A.2}$$

where $\gamma_n \equiv (n/2+1/4)\pi$. The integral (A.1) can then be written as a triple sum:

$$I^1_{lmn} = A_{lmn} \sum_i \sum_j \sum_k C_{li} C_{mj} C_{nk} \alpha^{-k} x_o^{i+j+k} \int_{x_o}^{\infty} \frac{e^{i(2+\alpha)x}}{x^{i+j+k+1/2}}\, dx, \tag{A.3}$$

where $A_{lmn} \equiv \dfrac{2\sqrt{2}}{\pi\sqrt{\pi\alpha}}\, e^{-i(\gamma_l+\gamma_m+\gamma_n)}$.

Using a change of variable, $y=(2+\alpha)x$, we obtain

$$I^1_{lmn} = B_{lmn} \sum_i \sum_j \sum_k \alpha^{-k} y_o^{i+j+k}\, C_{li} C_{mj} C_{nk} U(i+j+k), \tag{A.4}$$

where $y_o \equiv (2+\alpha)x_o$, $B_{lmn} \equiv (2+\alpha)^{-1/2} A_{lmn}$, and U is defined to be the definite integral

$$U(n) \equiv \int_{y_0}^{\infty} \frac{e^{iy}}{y^{n+1/2}}\, dy. \tag{A.5}$$

Upon integration by part in (A.5), the following recurrence formula for U(n) can be derived:

$$U(n) = \frac{e^{iy_0}}{(n-\frac{1}{2})\, y_0^{n-1/2}} + \frac{i}{n-\frac{1}{2}}\, U(n-1), \qquad n=1,2,... \tag{A.6}$$

The starting value U(0) is given from Fresnel integrals (Abramowitz & Stegun, 1964):

$$U(0) = \sqrt{2\pi}\, [\tfrac{1}{2}(1+i) - C_2(y_0) - iS_2(y_0)]. \tag{A.7}$$

The recurrence formula (A.6) is stable in the forward direction. Since U(n) decreases rapidly with n, to avoid underflow cancellation in computations, it is convenient to define $\bar{U}(n) \equiv \Gamma(n+1/2)U(n)$, which has the neutrally stable forward recurrence formula

$$\bar{U}(n) = \Gamma(n-1/2)e^{iy_0}y_0^{1/2-n} + i\bar{U}(n-1), \qquad n=1,2,..., \tag{A.8}$$

with the starting value $\bar{U}(0)=\sqrt{\pi}\, U(0)$. The use of $\bar{U}$ in (A.4) is numerically more robust and preferred. In practice, the summations in (A.4) are truncated for a prescribed equal-ripple tolerance according to the magnitudes of the original Chebyshev coefficients. The other integrals in (2.41) of Chapter I are evaluated in a similar manner.

To give an indication of the accuracy of the present method, we calculate (A.1) for two partition points x_1, x_2 according to (A.4), and compare their difference to that computed by numerical Romberg quadrature over (x_1,x_2). The results for a range of orders l,m,n are given in Table A. The accuracy is satisfactory but diminishes somewhat with increasing orders due to round-off cancellations associated with the slow convergence of (A.4).

Table A. Numerical verification of (A.4) for evaluating the integral of triple products of Hankel functions, (A.1). The difference $I_{lmn}^{1}(x_2)-I_{lmn}^{1}(x_1)$ obtained from two evaluations of (A.4) and from direct Romberg quadrature (tolerance 10^{-6}) over the interval (x_1,x_2) are compared for $x_1=10$, $x_2=11$, and $\alpha=4$.

l	m	n	Eq.(A.4)	Romberg quadrature
1	2	3	(0.001886, 0.003742)	(0.001886, 0.003742)
5	3	6	(-0.006758, 0.002120)	(-0.006758, 0.002120)
9	9	12	(-0.011812,-0.034072)	(-0.011812,-0.034072)
11	11	14	(0.109891, 0.000471)	(0.109891, 0.000471)
14	9	17	(-0.361132, 0.022987)	(-0.361132, 0.022987)
12	12	15	(-0.040432,-0.246567)	(-0.040433,-0.246565)
13	13	17	(-0.240835, 0.712153)	(-0.240853, 0.712166)

APPENDIX B: SEMIANALYTIC SOLUTIONS FOR THE SECOND-ORDER FORCES AND MOMENTS ON A BOTTOM-MOUNTED VERTICAL CYLINDER

The solution for the second-order horizontal force on a bottom-seated vertical cylinder has been studied by Molin (1987) and Eatock Taylor & Hung (1987). We extend the results to the second-order overturning moment also. The first-order total potential is:

$$\phi^{(1)} = \frac{-igA}{\omega} \frac{\cosh k(z+h)}{\cosh kh} \sum_{n=0}^{\infty} \epsilon_n i^n [J_n(k\rho) - \frac{J_n'(ka)}{H_n'(ka)} H_n(k\rho)] \cos n\theta, \qquad \text{(B.1)}$$

and the first-order forces and moments are given in closed form.

From (3.6) and (3.7) of Chapter I, the component of the second-order mean and double-frequency horizontal force and overturning moment (about the center of the cylinder bottom) due to quadratic products of the first-order potential can be evaluated:

$$\frac{F_{x1}^{(2)}}{\rho_0 gaA^2} = \frac{2i}{\pi(ka)^2} \sum_{n=0}^{\infty} \frac{(-1)^n}{H_n'(ka)H_{n+1}'(ka)} [3 - \frac{2kh}{\sinh 2kh} + \frac{n(n+1)}{(ka)^2}(1+\frac{2kh}{\sinh 2kh})] , \qquad \text{(B.2)}$$

$$\frac{M_{y1}^{(2)}}{\rho_0 gahA^2} = \frac{4i}{\pi(ka)^2} \sum_{n=0}^{\infty} \frac{(-1)^n}{H_n'(ka)H_{n+1}'(ka)} \{1 + \frac{2kh}{\sinh 2kh}[(\frac{n(n+1)}{(ka)^2}+1)Z(kh) - \frac{1}{2}]\} , \qquad \text{(B.3)}$$

$$\frac{\bar{F}_x^{(2)}}{\rho_0 gaA^2} = \frac{4}{\pi^2(ka)^3} (1+\frac{2kh}{\sinh 2kh}) \sum_{n=0}^{\infty} \frac{[1-n(n+1)/(ka)^2]^2}{[J_n'^2(ka)+Y_n'^2(ka)][J_{n+1}'^2(ka)+Y_{n+1}'^2(ka)]} , \qquad \text{(B.4)}$$

$$\frac{\bar{M}_y^{(2)}}{\rho_0 gahA^2} = \mathrm{Re}\{\frac{-4i}{\pi(ka)^2} \sum_{n=0}^{\infty} \frac{1}{H_n'(ka)H_{n+1}'^{*}(ka)} [-1+\frac{2kh}{\sinh 2kh}((\frac{n(n+1)}{(ka)^2}+1)Z(kh)-\frac{1}{2})]\} , \qquad \text{(B.5)}$$

where $Z(kh) \equiv 1/4+(2kh \sinh 2kh - \cosh 2kh +1)/8(kh)^2$, and the Wronskian $J_n(ka)H_n'(ka)-J_n'(ka)H_n(ka)=2i/\pi ka$ is used.

From (3.5) of Chapter I, the second-order potential forces and moments ($F_2^{(2)}$) have components which depend on the second-order incident wave $\phi_I^{(2)}$ ($F_{2I}^{(2)}$) and diffracted wave $\phi_D^{(2)}$ ($F_{2D}^{(2)}$) respectively. Expanding the incident wave potential into partial waves, the Froude-Krylov components can be readily calculated:

$$\frac{F_{x2I}^{(2)}}{\rho_o g a A^2} = \frac{-3i\pi J_1(2ka)}{2 \sinh^2 kh} \tag{B.6}$$

$$\frac{M_{y2I}^{(2)}}{\rho_o g a h A^2} = \frac{-3i\pi \tanh kh}{2 \sinh^4 kh} J_1(2ka) \left[\frac{\sinh 2kh}{2} - \frac{\cosh 2kh-1}{4kh}\right] \tag{B.7}$$

The diffraction component can be obtained via (3.14) of Chapter I in terms of assisting radiation potentials for horizontal translation (ϕ_1) and pitch rotation (with respect to the bottom) (ϕ_5). These potentials are given by:

$$\begin{bmatrix}\phi_1\\ \phi_5\end{bmatrix} = \cos\theta \left\{\begin{bmatrix}\Lambda_{1o}\\ \Lambda_{5o}\end{bmatrix} \frac{\cosh k_2(z+h)}{k_2} \frac{H_1(k_2\rho)}{H_1'(k_2a)} + \sum_{m=1}^{\infty} \begin{bmatrix}\Lambda_{1m}\\ \Lambda_{5m}\end{bmatrix} \frac{\cos \kappa_{2m}(z+h)}{\kappa_{2m}} \frac{K_1(\kappa_{2m}\rho)}{K_1'(\kappa_{2m}a)}\right\} \tag{B.8}$$

The coefficients Λ_1, Λ_5 are obtained by integrating the vertical eigenfunctions with 1 and (z+h) respectively in z:

$$\Lambda_{1m} = \frac{4 \sinh k_{2m}h}{2k_{2m}h + \sinh 2k_{2m}h},$$

$$A_{5m} = \frac{4(k_{2m}h \sinh k_{2m}h - \cosh k_{2m}h + 1)}{k_{2m}(2k_{2m}h + \sinh 2k_{2m}h)} , \qquad m=0,1,2,... \qquad (B.9)$$

where $k_{20} \equiv k_2$, $k_{2m} \equiv i\kappa_{2m}$, $m=1,2,...,$ and κ_{2m} are the real roots of (2.31) of Chapter I with ω replaced by 2ω.

From (3.14) of Chapter I, the diffraction components are given by:

$$\begin{bmatrix} F_{x2D}^{(2)} \\ M_{y2D}^{(2)} \end{bmatrix} = \begin{bmatrix} F_{x2H}^{(2)}+F_{x2P}^{(2)} \\ M_{y2H}^{(2)}+M_{y2P}^{(2)} \end{bmatrix} = 2i\rho_o\omega a\int_{-h}^{0} dz\int_{0}^{2\pi} d\theta \begin{bmatrix} \psi_1 \\ \psi_5 \end{bmatrix} \frac{\partial\phi_I^{(2)}}{\partial\rho} + \frac{2i\rho_o\omega}{g} \int_{0}^{2\pi} d\theta\int_{a}^{\infty} \rho d\rho \; q\begin{bmatrix} \psi_1 \\ \psi_5 \end{bmatrix}_{z=0} \qquad (B.10)$$

Using (B.8), the first term can be integrated to yield:

$$\begin{bmatrix} F_{x2H}^{(2)}/\rho_o gaA^2 \\ M_{y2H}^{(2)}/\rho_o gahA^2 \end{bmatrix} = \frac{3\pi ik^2\tanh kh \; J_1'(2ka)}{\sinh^4 kh} \left\{ \begin{bmatrix} A_{1o} \\ A_{5o} \end{bmatrix} \frac{\Pi_o H_1(k_2a)}{k_2H_1'(k_2a)} + \sum_{m=1}^{\infty} \begin{bmatrix} A_{1m} \\ A_{5m} \end{bmatrix} \frac{\Pi_m K_1(\kappa_{2m}a)}{\kappa_{2m}K_1'(\kappa_{2m}a)} \right\} \qquad (B.11)$$

where

$$\Pi_m = \frac{1}{2} \left[\frac{\sinh(2k+k_{2m})h}{2k+k_{2m}} + \frac{\sinh(2k-k_{2m})h}{2k-k_{2m}} \right], \qquad m=0,1,2,... . \qquad (B.12)$$

The second term of (B.10) represents the contribution due to ϕ_P and is simplified somewhat after integration in θ:

$$\begin{bmatrix} F_{x2P}^{(2)}/\rho_o gaA^2 \\ M_{y2P}^{(2)}/\rho_o gahA^2 \end{bmatrix} = 8\pi i \int_{ka}^{\infty} d(k\rho) \; k\rho \; \bar{q}_1 \begin{bmatrix} \psi_1/a \\ \psi_5/ah \end{bmatrix}_{z=0,\theta=0} , \qquad (B.13)$$

where

$$\bar{q}_1 = \sum_{n=0}^{\infty} (-1)^n \{\Upsilon_n'(k\rho)\Upsilon_{n+1}'(k\rho) - J_n'(k\rho)J_{n+1}'(k\rho) + [\Upsilon_n(k\rho)\Upsilon_{n+1}(k\rho) - J_n(k\rho)J_{n+1}(k\rho)] \, [\frac{n(n+1)}{(k\rho)^2} - \frac{1}{2} + \frac{3}{2} \tanh^2 kh]\} \, , \tag{B.14}$$

and $\Upsilon_n(k\rho) \equiv J_n(k\rho) - (J_n'(ka)/H_n'(ka))H_n(k\rho)$. The free-surface integral in (B.13) can be evaluated as described in Appendix A.

APPENDIX C: SEMIANALYTIC SOLUTIONS FOR SUM- AND DEFFERENCE-FREQUENCY FORCES ON THE BOTTOM MOUNTED VERTICAL CYLINDER

Here, we consider the second-order sum- and difference- frequency forces on the bottom-mounted vertical cylinder in the presence of bichromatic waves. These solutions can be obtained following the formula given in Chapter II with the analytic first-order potential:

$$\phi_j^{(1)} = \frac{-igA_j}{\omega_j} \frac{\cosh k_j(z+h)}{\cosh k_j h} \sum_{n=0}^{\infty} \epsilon_n i^n \left[J_n(k_j\rho) - \frac{J'_n(k_ja)}{H'_n(k_ja)} H_n(k_j\rho) \right] \cos n\theta \tag{C.1}$$

where (') represents differentiation with respect to arguments. Substituting (C.1) into (4.19) and (4.20) of Chapter II and performing θ integration, $f_{qjl\pm}$ are given respectively by:

$$\frac{f^+_{qjl}}{\rho g A_j A_l} = \frac{2i}{\pi(k_ja)(k_la)} \sum_{n=0}^{\infty} (-1)^n \Omega^+_{njl} \left[1 + \frac{(k_jh)(k_lh)}{\omega_j\omega_l h/g} \frac{(I^- + I^+ n(n+1)/(k_ja)(k_la))}{\cosh k_jh \cosh k_lh}\right] \tag{C.2}$$

$$\frac{f^-_{qjl}}{\rho g A_j A_l^*} = \frac{-2i}{\pi(k_ja)(k_la)} \sum_{n=0}^{\infty} \Omega^-_{njl} [\, 1 - \frac{(k_jh)(k_lh)}{\omega_j\omega_l h/g} \frac{(I^- + I^+ n(n+1)/(k_ja)(k_la))}{\cosh k_jh \cosh k_lh} \tag{C.3}$$

where

$$\Omega^+_{njl} = \frac{1}{H'_{n+1}(k_ja)\, H'_n(k_la)} + \frac{1}{H'_n(k_ja)\, H'_{n+1}(k_la)} \tag{C.4}$$

$$\Omega^-_{njl} = \frac{1}{H'_{n+1}(k_ja)\, H'^{*}_n(k_la)} - \frac{1}{H'_n(k_ja)\, H'^{*}_{n+1}(k_la)} \tag{C.5}$$

$$I^{\pm} = \frac{1}{2} \left[\frac{\sinh k^+h}{k^+h} \pm \frac{\sinh k^-h}{k^-h} \right] \tag{C.6}$$

The second-order Froude-Krilov type excitation QTF can be obtained from the first integral of (4.21) of Chapter II, which leads:

$$f^{\pm}_{Ij1} = \pi a\rho\omega^{\pm} \begin{matrix}(\gamma^{+}_{j1} + \gamma^{+}_{1j})\\ (\gamma^{-}_{j1} + \gamma^{-*}_{1j})\end{matrix} \frac{\tanh k^{\pm}h}{k^{\pm}} J_1(k^{\pm}a) \tag{C.7}$$

where $\gamma_{j1\pm}$ are given in (2.6) and (2.7) of Chapter II. The diffraction component can be evaluated via (4.23) of Chapter II in terms of sum- and difference-frequency assisting radiation potentials for horizontal translation, $\Phi_{x\pm}$, which have following explicit expressions:

$$\Phi^{\pm}_{x} = \cos\theta \left[B^{\pm}_{0} \frac{\cosh k^{\pm}_{2}(z+h)}{k^{\pm}_{2}} \frac{H_1(k^{\pm}_{2}\rho)}{H'_1(k^{\pm}_{2}a)} + \sum_{m=1}^{\infty} B^{\pm}_{m} \frac{\cos \kappa^{\pm}_{2m}(z+h)}{\kappa^{\pm}_{2m}} \frac{K_1(\kappa^{\pm}_{2m}\rho)}{K'_1(\kappa^{\pm}_{2m}a)} \right] \tag{C.8}$$

where K is the second kind modified Bessel function, and the coefficients, $B^{\pm}$, in (C.8) are given by:

$$B_m = \frac{4 \sinh k^{\pm}_{2m}h}{2k^{\pm}_{2m}h + \sinh 2k^{\pm}_{2m}h} \qquad (\ m=0,1,2,\cdots\ ) \tag{C.9}$$

where $k_{20}=k_2$, $k_{2m}=i\kappa_{2m}$, and κ_{2m} represents evanescent mode and is given by the real roots of the following equation:

$$\omega^{\pm 2} = -\kappa^{\pm}_{2m} g \tan \kappa^{\pm}_{2m} h \quad , \qquad (m-1/2)\pi \le \kappa^{\pm}_{2m} h \le m\pi \tag{C.10}$$

Upon integrating the first integral of (4.23) of Chapter II, the body forcing contribution is obtained in explicit form as follows:

$$f^{\pm}_{Bj1} = -\pi\rho a\omega^{\pm} \begin{bmatrix}(\gamma^{+}_{j1} + \gamma^{+}_{1j})\\ (\gamma^{-}_{j1} + \gamma^{-*}_{j})\end{bmatrix} \frac{k^{\pm}h\ J'_1(k^{\pm}a)}{\cosh k^{\pm}h} \left[B^{\pm}_{0}\Pi^{\pm}_{0} \frac{H_1(k^{\pm}_{2}a)}{k^{\pm}_{2}\ H'_1(k^{\pm}_{2}a)} + \sum_{m=1}^{\infty} B^{\pm}_{m}\Pi^{\pm}_{m} \frac{K_1(\kappa^{\pm}_{2m}a)}{\kappa^{\pm}_{2m}\ K'_1(\kappa^{\pm}_{2m}a)} \right] \tag{C.11}$$

where

$$\Pi_m^\pm = \frac{1}{2}\left[\frac{\sinh(k^\pm + k_{2m}^\pm)h}{k^\pm + k_{2m}^\pm} + \frac{\sinh(k^\pm - k_{2m}^\pm)h}{k^\pm - k_{2m}^\pm}\right] \quad , \quad m=0,1,2,\cdots \tag{C.12}$$

From (3.4a) of Chapter II and (C.1), the sum- and difference-frequency free-surface forcing for n=1 are given respectively by:

$$q_{Ijl}^\pm = \frac{2g^2 A_j A_l k_j^2}{\omega_j} \sum_{m=0}^{\infty} \begin{bmatrix} (-1)^m \\ 1 \end{bmatrix} \left[\left(\Lambda_{jl} + \frac{k_l}{k_j} \frac{m(m+1)}{(k_j\rho)(k_l\rho)} \right) \Gamma_m^\pm + \frac{k_l}{k_j} \hat{\Gamma}_m^\pm \right] \tag{C.13}$$

where Λ_{jl} is given in (3.16) of Chapter II and

$$\Gamma_m^+ = Z_{m+1}^j Z_m^l + Z_m^j Z_{m+1}^l - J_{m+1}^j J_m^l - J_m^j J_{m+1}^l \tag{C.14}$$

$$\hat{\Gamma}_m^+ = Z_{m+1}^{'j} Z_m^{'l} + Z_m^{'j} Z_{m+1}^{'l} - J_{m+1}^{'j} J_m^{'l} - J_m^{'j} J_{m+1}^{'l} \tag{C.15}$$

$$Z_m^j = J_m(k_j\rho) - \frac{J_m'(k_j a)}{H_m'(k_j a)} H_m(k_j\rho) \tag{C.16}$$

The corresponding difference-frequency terms in (C.14 & 15) can be obtained by taking complex conjugate for each term containing superscript l. Finally free-surface forcing contributions are given by the infinite line integral:

$$f_{Fjl}^\pm = \frac{i\pi\rho\omega^\pm}{g} \int_a^\infty d\rho\, \rho\, Q_I^\pm \left[\Psi_x^\pm\right]_{z=0,\theta=0} \tag{C.17}$$

This free-surface integral can be evaluated as described in Appendix A.

APPENDIX D. DERIVATION OF THE MONOCHROMATIC-BIDIRECTIONAL QTF.

The QTF, D_{iikl}, for a general body in arbitrary water depth for monochromatic bidirectional dual waves is derived using the far-field method (Newman, 1967). In the presence of two incident waves, wavenumber k_o, and incident angles β_k and β_l, the far-field asymptotic forms of the incident(ϕ_I) and diffracted (ϕ_D) potentials can be written as:

$$\phi_I \sim -(ig/\omega)f(z) \; [\; A_k e^{ik_o r \cos(\theta-\beta_k)} + A_l e^{ik_o r \cos(\theta-\beta_l)} \;] \tag{D.1}$$

$$\phi_D \sim -(ig/\omega)f(z) \sqrt{k_o/2\pi r} \; [\; A_k K_k(\pi+\theta) + A_l K_l(\pi+\theta) \;] \; e^{i(k_o r+\pi/4)} \tag{D.2}$$

for $k_o r >> 1$, and $f(z) \equiv \cosh k_o(z+h)/\cosh k_o h$. Here, A_k, A_l are the complex amplitudes of the incident waves, and K_k, K_l the Kochin functions defined by:

$$K_j(\theta) = \iint\limits_{body} dS \left(\frac{\partial \phi_{Dj}}{\partial n} - \phi_{Dj} \frac{\partial}{\partial n} \right) f(z) \; e^{ik_o(x\cos\theta + y\sin\theta)} \tag{D.3}$$

$j=k,l$, where ϕ_{Dj} is the diffracted potential associated with the j^{th} incident wave alone. Using momentum conservation for the fluid volume, the mean force on the body can be expressed in terms a far-field integral given by:

$$\begin{Bmatrix} F_x \\ F_y \end{Bmatrix} = G(k_o h) \frac{\rho}{8k_o} \; [\int_0^{2\pi} d\theta \; r \begin{Bmatrix} \cos\theta \\ \sin\theta \end{Bmatrix} \left[\frac{1}{r^2} \frac{\partial\phi}{\partial\theta}\frac{\partial\phi^*}{\partial\theta} - \frac{\partial\phi}{\partial r}\frac{\partial\phi^*}{\partial r} - k_o^2 \phi\phi^* \right]_{z=0}$$
$$+ \int_0^{2\pi} d\theta \begin{Bmatrix} \sin\theta \\ \cos\theta \end{Bmatrix} \left[\frac{\partial\phi}{\partial r}\frac{\partial\phi^*}{\partial\theta} + \frac{\partial\phi}{\partial\theta}\frac{\partial\phi^*}{\partial r} \right]_{z=0}] \tag{D.4}$$

where $\phi=\phi_I+\phi_D$, and $G(k_o h) \equiv \tanh(k_o h)+k_o h \operatorname{sech}^2 k_o h$, is a depth factor which goes to unity as $k_o h \to \infty$. Substituting (D.1,D.2) into (D.4), and using the method of stationary phase for the resulting integral, we obtain the drift force QTF:

$$\begin{Bmatrix} D_{x_{kl}} \\ D_{y_{kl}} \end{Bmatrix} = - \frac{\rho g k_o G(k_o h)}{8\pi} \int_o^{2\pi} K_k(\pi+\theta) K_l(\pi+\theta) \begin{Bmatrix} \cos\theta \\ \sin\theta \end{Bmatrix} d\theta$$

$$- \frac{i\rho g}{4} G(k_o h) \left[\left(K_k(\pi+\beta_l) \begin{Bmatrix} \cos\beta_l \\ \sin\beta_l \end{Bmatrix} - K_l^*(\pi+\beta_k) \begin{Bmatrix} \cos\beta_k \\ \sin\beta_k \end{Bmatrix}\right]\right. \qquad \text{(D.5)}$$

which satisfies the symmetry relationship $D_{kl} = D_{lk}^*$. The QTF is related to the mean drift force by:

$$F_{x,y} = \sum_{k=1}^{2} \sum_{l=1}^{2} A_k A_l^* D_{x,y_{kl}} \qquad \text{(D.6)}$$

For vertically axisymmetric body geometries, the Kochin functions K_k need to be calculated only for one incident wave angle, since $K_k(\theta)=K_l(\theta+\beta_l-\beta_k)$, and the computational effort is greatly reduced.

In the special case of a uniform vertical cylinder (radius a), the total potential ϕ_j and hence the QTF can be expressed in closed form:

$$\phi_j = - \frac{igA_j}{\omega} f(z) \sum_{n=0}^{\infty} e_n i^n \left[J_n(k_o r) - \frac{J_n'(k_o a)}{H_n'(k_o a)} H_n(k_o r)\right] \cos n(\theta-\beta_j) \qquad \text{(D.7)}$$

where J_n, H_n are Bessel and Hankel functions of the first kind, primes denote derivatives with respect to argument, and $e_o=1$, $e_n=2$ for $n \geq 1$. Substituting ϕ_{Dj} in (D.7) into (D.3), the Kochin function can be evaluated to be:

$$K_j(\pi+\theta) = \frac{2i}{k_o} \sum_{n=0}^{\infty} e_n \cos n(\theta-\beta_j)\; J_n'(k_o a)/H_n'(k_o a) \tag{D.8}$$

Using (D.8) in (D.5), we have finally:

$$\begin{Bmatrix} D_{x_{kl}} \\ D_{y_{kl}} \end{Bmatrix} = \frac{\rho g a G(k_o h)}{k_o a \tanh k_o h} \sum_{n=0}^{\infty} \Big[\frac{e_n}{2} \cos n(\beta_k-\beta_l) \Big(\begin{Bmatrix} \cos\beta_k \\ \sin\beta_k \end{Bmatrix} T_n(k_o a) + \begin{Bmatrix} \cos\beta_l \\ \sin\beta_l \end{Bmatrix} T_n^*(k_o a) \Big)$$
$$- \begin{Bmatrix} \cos[(n+1)\beta_k - n\beta_l] \\ \sin[(n+1)\beta_k - n\beta_l] \end{Bmatrix} R_n(k_o a) - \begin{Bmatrix} \cos[(n+1)\beta_l - n\beta_k] \\ \sin[(n+1)\beta_l - n\beta_k] \end{Bmatrix} R_n^*(k_o a) \Big] \tag{D.9}$$

where the functions T_n and R_n are defined by:

$$T_n(k_o a) = J_n'(k_o a) \;/\; H_n'^{*}(k_o a)$$

$$R_n(k_o a) = J_{n+1}'(k_o a)\; J_n'(k_o a) \;/\; H_{n+1}'(k_o a)\; H_n'^{*}(k_o a) \tag{D.10}$$

In the special case of a single incident wave ($\beta_k=\beta_l=\beta$), the single frequency and direction QTF, $D(\omega,\omega,\beta,\beta)$, reduces to the familiar result:

$$\begin{Bmatrix} D_{x_{kk}} \\ D_{y_{kk}} \end{Bmatrix} = \frac{2\rho g a G(k_o h)}{k_o a \tanh k_o h} \begin{Bmatrix} \cos\beta \\ \sin\beta \end{Bmatrix} \sum_{n=0}^{\infty} \Big[\frac{e_n}{2} \,\mathrm{Real}\{T_n(k_o a)\} - \mathrm{Real}\{R_n(k_o a)\} \Big] \tag{D.11}$$

which has the asymptotic value of $(2/3)\rho g a\{\cos\beta,\sin\beta\}$ in the limit of short waves ($k_o a, k_o h \to \infty$); and the long-wave ($k_o a, k_o h \to 0$) asymptote of:

$$\begin{Bmatrix} D_{x_{kk}} \\ D_{y_{kk}} \end{Bmatrix} \sim \frac{5\pi^2}{8}\, \rho g a (k_o a)^3 \begin{Bmatrix} \cos\beta \\ \sin\beta \end{Bmatrix} \tag{D.12}$$